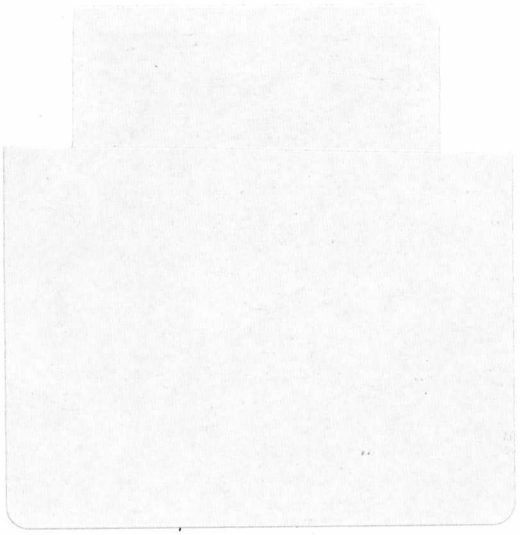
Low Temperature Sintering of Solid Oxide Fuel Cell Electrolytes

Gene Stacey Lewis

A thesis submitted for the degree of Doctor of Philosophy of the University of London and for the diploma of Imperial College of Science, Technology and Medicine



Department of Materials,
Imperial College of Science, Technology and Medicine,
Prince Consort Road,
London,
SW7 2BP.

July 2002

to my father.....

"Remember folks, you gotta go owww"
Moriarty, The Goons

Abstract

Solid oxide fuel cells provide a clean and efficient means to produce electricity. Gadolinium oxide doped ceria is considered to be an ideal electrolyte material for SOFC's operating at temperatures between 500-600°C. Typically, this material is sintered to high density at approximately 1300°C. Reducing this temperature to ~1000°C will enable ferritic stainless steel to be used as a cell supporting material, thus significantly reducing cost and potentially enhancing the mechanical reliability of the stack.

The aim of this study is to devise a method for sintering Gd doped ceria to high density at temperatures between 900-1000°C with no detrimental effects on its electrical properties. A number of experimental techniques were employed to characterise the sintering process and the resulting materials including, a.c. impedance spectroscopy, dilatometry, four-point d.c resistivity, Raman spectroscopy, transmission electron microscopy and x-ray photoelectron spectroscopy.

Gd doped ceria was successfully sintered to high density at <1000°C by additions of cobalt oxide. A 2cat%Co addition to commercially available 10mol%Gd doped ceria reduced the 'gas tight' densification temperature to 930°C. Furthermore, the Co addition was not detrimental to the electrical properties of Gd doped ceria under SOFC operating conditions at 500-600°C. Copper oxide was also shown to be a suitable sintering aid. The mechanism of enhanced sintering rate has been explored in detail and does not conform to any of the standard models. Evidence is presented to indicate that redistribution of the Gd dopant is also involved. The Co addition reduces the grain size of the sintered product, but this is mainly due to the reduced sintering temperature and not to reduced grain boundary mobility by the additive which is preferentially segregated to the grain boundaries. By careful control of the amount of additive and the heat treatment schedule it has proved possible to actually improve the ionic conductivity of Gd doped ceria, probably by optimising the lattice parameter. Co was also found to be effective in reducing the sintering temperature of yttria-stabilised zirconia.

Acknowledgments

I would like to thank my supervisors, Prof. Alan Atkinson and Prof. Brian Steele, for their guidance and all round encouragement that was fundamental in helping me complete my postgraduate studies at Imperial College.

There are many staff at Imperial that I owe a considerable debt of gratitude: Firstly, I would like to thank Mr. Bob Rudkin for his technical help/advice, and more importantly his patience. Thanks likewise go to the 6th floor characterisation 'mafia' consisting of Mr. Richard Sweeney (possibly the nicest Arsenal fan I ever met) and Mr. Mike Haddon. I would also like to thank Prof. John Kilner, Dr. Ahmet Selçuk, Mr. Nick Royale, Dr. Stephen Skinner, Dr. Mark Tyrer and Mr. Karol Senwic. A special thanks also goes to Prof. John Drennan's microscopy research group at the University of Brisbane, Australia.

There are many friends who have enriched my time at Imperial. I would especially like to thank (and in no particular order!) Ms. Awla Alibia, Dr. Cynthia Shaw, Ms. Tania Ramos, Dr. Phil Vickers, Dr. Nick Zaphouropoulous and Dr. Jon Wells. Special thanks go to my very good friend Mr. Sean Mcloughlin. One of life's true spirits.

I would also like to thank EPSERC for their financial support of this study. I would likewise like to thank the Institute of Materials, The Royal Academy of Engineering and the trustees of the Hilary Bowerman fund for enabling me to attend two international conferences.

I would like to thank my family. Their consistent support, love and guidance, a source of strength (especially the last six months!). Lastly, I would like to thank Idit Yehezkely. She convinced me, what now seems a long time ago, in the middle of the Amazon that a Ph.D. seemed a good idea. How right she was. Thank you for *always* being there.....

Thank you all

Table of Contents

Abstract 2

Acknowledgments 3

Table of Contents 4

Abbreviations, Symbols and Constants 10

List of Figures 14

List of Tables 17

Section 1: General Introduction and Review of Literature 18

Chapter 1. Introduction 19

1.1. Introduction 19

1.2. Aims of my Research 20

1.3. Outline of the Thesis 20

1.4. Raw Materials Used in this Study 21

1.5. Nomenclature 22

Chapter 2. The Fuel Cell 23

2.1. Principle of Operation 23

2.2. The Alkaline Fuel Cell (AFC) 24

2.3. The Phosphoric Acid Fuel Cell (PAFC) 24

2.4. The Polymer Electrolyte Membrane Fuel Cell (PEMFC) 24

2.5. The Molten Carbonate Fuel Cell (MCFC) 25

2.6. The Solid Oxide Fuel Cell (SOFC) 25

Chapter 3. The Solid Oxide Fuel Cell 27

3.1. Introduction 27

3.2. Operating Principle of the SOFC 27

3.3. Efficiency of the SOFC 28

3.4. Components in a SOFC 30

3.4.1. The Electrolyte 31

3.4.1.1. $LaGaO_3$ 33
3.4.1.2. δ-Bi_2O_3 33
3.4.1.3. Doped CeO_2 33
3.4.1.4. Interlayers 34
3.4.2. The Anode 35
3.4.3. The Cathode 35
3.4.4. The Interconnect (or Biopolar Plate) 37
3.5. Designs of a SOFC 38
3.5.1. Tubular Design 38
3.5.2. Planar Design 39
3.6. Summary 41

Chapter 4. Properties of Doped Ceria and YSZ 44
4.1. Introduction 44
4.2. Defect Types 44
4.3. Defect Association 46
4.4. Lattice Ionic Conductivity of Doped Ceria 46
4.5. Ionic Conductivity in Doped Zirconia 48
4.6. Grain Boundary Ionic Conductivity of Doped Ceria and YSZ 48
4.7. Effect of Grain Size on Grain Boundary Ionic Conductivity 50
4.8. Electronic Conductivity in Doped Ceria 51
4.9. Summary 52

Chapter 5. Fabrication of Electrolyte Films 54
5.1. Introduction 54
5.2. Chemical Vapour Deposition (CVD) 54
5.3. Electrochemical Vapour Deposition (EVD) 55
5.4. Tape Casting 56
5.5. Calendering 57
5.6. Screen Printing 57
5.7. Sol-gel Fabricated Thin Films 58
5.8. Summary 59

Chapter 6. Sintering of SOFC Electrolytes 61
6.1. General Introduction 61
6.2. Powder Processing and Preparation 61
6.2.1. Solid State Sintering 62
6.2.2. The Driving Force for Sintering 63
6.2.3. Factors Effecting Homogeneous Compaction 64
6.2.4. Solid State Technique 66
6.2.5. The Co-Precipitation Technique 67
6.2.6. Sol-gel Prepared Powders 67
6.2.7. Hydrothermal Synthesis 68
6.2.8. Grain Growth Considerations 69
6.2.9. Powder Processing and Preparation – Summary 70
6.3. Sintering Aids 71
6.3.1. Dopant Additions and the Effect on Grain Boundary Mobility 71
6.3.2. Low Temperature Solid State Sintering by Dopant Addition 73
6.3.3. Liquid Phase Sintering 75
6.3.4. Driving Force of Densification in Liquid Phase Sintering 76
6.3.5. Stages of Liquid Phase Sintering 76
6.3.5.1. Rearrangement 77
6.3.5.2. Solution-Precipitation 77
6.3.5.3. Ostwald Ripening 78
6.3.6. Liquid Phase Sintering of Doped Ceria and Related Materials 78
6.3.7. Sintering Aids – Summary 83

Section 2: Experimental 87

Chapter 7. Experimental 88
7.1. Introduction 88
7.2. Calcium-Gallate Glass Preparation 88
7.3. Solid State Dopant Addition of Cu and Co to CGO 89
7.4. Precipitation Dopant Addition of Cu and Co to CGO 89
7.5. Cobalt Nitrate Addition to CGO 89
7.6. Consolidation of Powders 90
7.7. A.C. Impedance Spectroscopy 90

7.8. Density Measurements 91
7.9. Dilatometry (Sintering) 92
7.10. Dilatometry (Thermal Expansion) 92
7.11. Four-Point D.C Resistivity 93
7.12. Particle Size Analysis 94
7.13. Raman Spectroscopy 94
7.14. Scanning Electron Microscopy (SEM) 95
7.14.1. Grain Size Determination Using SEM 95
7.15. Transmission Electron Microscopy (TEM) 95
7.16. Thermal Analysis 96
7.17. X-ray Photoelectron Spectroscopy (XPS) 96
7.18. X-Ray Diffraction (XRD) 97

Section 3: Results and Discussion 99

Chapter 8. Development of Procedure to Densify CGO at Low Temperature 100
8.1. Introduction 100
8.2. CaO-Ga_2O_3 Sintering Aids 100
8.3. Solid State Dopant Addition of Cu and Co to CGO 101
8.4. Precipitation Dopant Addition of Cu and Co to CGO 102
8.5. Cobalt and Copper Nitrate Addition to CGO 103
8.6. Summary 104

Chapter 9. Sintering of CGO with Sintering Aids 106
9.1. Introduction 106
9.2. Dilatometry 106
9.2.1. Co Additions to CGO: CHR Dilatometry 108
9.2.2. Cu Additions to CGO: CHR Dilatometry 111
9.2.3. Fe Additions to CGO: CHR Dilatometry 114
9.3. Evidence for Liquid Phase Sintering of CoCGO 114
9.4. Densification Mechanisms from CHR Dilatometry of CGO and 2CoCGO 115
9.5. TEM of 2CoCGO 120

9.6. Lattice Parameter Measurements of CGO and 2CoCGO 123
9.7. Densification of Gd Doped Ceria 127
9.8. Oxygen Vacancy Concentration of CGO and 2CoCGO 128
9.9. Solubility of Co in CGO 130
9.10. Co Additions to CGO20: CHR Dilatometry 133
9.11. Co Oxide Phase Change: Influence on Densification of CoCGO 135
9.12. Grain Growth of CGO and 2CoCGO 137
9.13. Summary 139

Chapter 10. Electrical Properties of CoCGO and CuCGO 142
10.1. Introduction 142
10.2. A.C. Impedance Spectroscopy of Polycrystalline Materials 142
10.3. A.C. Impedance Spectroscopy of Materials in this Study 145
10.3.1. Electrical Conductivity of CoCGO 146
10.3.2. Electrical Conductivity of CuCGO 150
10.4. Effect of Grain Size on the Conductivity of 2CoCGO 152
10.5. 4 Point D.C. Conductivity of CoCGO 155
10.6. Effect of Sintering Time and Temperature on the Conductivity of 2CoCGO 158
10.7. Summary 161

Chapter 11. Factors Affecting Consolidation and Densification of 2CoCGO 163
2CoCGO
11.1. Introduction 163
11.2. Effect of Powder Calcination Temperature on Densification of 2CoCGO 163
11.3. Effect of Isostatic Pressure on Densification of 2CoCGO 165
11.4. Effect of Particle Size on Densification of CGO and 2CoCGO 168
11.5. Thermal Expansion Coefficient (TEC) of CGO and 2CoCGO 171
11.6. Tape Casting Thick Films of 2CoCGO 172
11.7. Screen Printing Thick Films of 2CoCGO 174
11.8. Summary 176

Chapter 12. Co Additions to 8YSZ: Effect on Densification and Electrical Properties 177

12.1. Introduction 177

12.2. Commercially Supplied YSZ 177

12.3. CHR Dilatometry of Co Additions to 8YSZ 177

12.4. A.C Impedance Spectroscopy of Co Additions to 8YSZ 181

12.5. Effect of Sintering Temperature on the Conductivity of Co8YSZ 183

12.6. Lattice Parameter Measurements Resulting from Co Additions to 8YSZ 184

12.7. Summary 185

Section 4: Conclusions and Future Work 187

Conclusions 188

Suggestions for Further Work 191

References are included at the end of each chapter

Abbreviations, Symbols and Constants

A.C	Alternating current
AFC	Alkaline fuel cell
APU	Auxiliary power unit
ASR	Total cell area specific resistance
CGO	$Gd_{0.9}Gd_{0.1}O_{1.95}$
CGO20	$Gd_{0.8}Gd_{0.2}O_{1.90}$
CHP	Combined heat and power
CHR	Constant heating rate
CVD	Chemical vapour deposition
D.C.	Direct current
DTA	Differential thermal analysis
EDXS	Energy dispersive x-ray spectroscopy
EPD	Electrophoretic deposition
EVD	Electrochemical vapour deposition
EXAFS	Extended x-ray absorption fine structure spectroscopy
ICP	Inductively coupled plasma
ITSOFC	Intermediate temperature solid oxide fuel cell
KD1	Polyester resin
LSC	$La_{1-x}Sr_xCoO_{3-\delta}$
LSCF	Sr-doped $La(Co,Fe)O_3$
LSGM	$La_{1-x}Sr_xGa_{1-y}Mg_yO_{3-0.5(x+y)}$
LSM	$La_{1-x}Sr_xMnO_3$
MCFC	Molten carbonate fuel cell
Ni/CGO	Composite Ni-CGO anode
Ni/YSZ	Composite Ni-YSZ anode
PAFC	Phosphoric acid fuel cell
PBT	Poly butyl phthalate
PEG	Poly ethylene glycol
PEMFC	Polymer electrolyte membrane fuel cell
PEN	Positive electrolyte negative
PVB	Poly vinyl butyral
SEM	Scanning electron microscope
SGO	$Sr_2Ga_2O_5$
SOFC	Solid oxide fuel cell
S-W	Siemens-Westinghouse
TEC	Thermal expansion coefficient
TEM	Transmission electron microscope
TGA	Thermogravimetric analysis
YSZ	Yttria stabilised zirconia
XPS	X-ray photoelectron spectroscopy
XRD	X-ray diffraction

T	Temperature (K)
ΔH	Enthalpy change (J mol^{-1})
ΔG	Free energy change (J mol^{-1})
ΔS	Entropy change (J K^{-1} mol^{-1})
E_{rev}	Open circuit cell e.m.f. (V)
R_{ele}	Electrical resistance of the electrolyte (V/A)
R_a	Electrical resistance of the anode (V/A)
R_c	Electrical resistance of the cathode (V/A)
I	Current (A)
η_a	Activation polarisation of the anode (V/A)
η_c	Activation polarisation of the cathode (V/A)
δ_a	Concentration polarisation of the anode (V/A)
δ_c	Concentration polarisation of the cathode (V/A)
σ	Ionic (or electronic) conductivity (S m^{-1})
A	Pre-exponential Arrhenius term
ΔE_a	Activation energy for conductivity (J mol^{-1})
ΔH_m	Enthalpy of motion of an oxygen vacancy (J mol^{-1})
ΔH_a	Enthalpy of association of an oxygen vacancy and impurity (J mol^{-1})
σ_{sgb}	Specific grain boundary conductivity (S m^{-1})
δ_{gb}	Grain boundary thickness (m)
d	Grain size (m)
σ_{tgb}	Total conductivity (S m^{-1})
μ	Chemical potential (J mol^{-1})
i	Particle sort
E_s	Molar surface free energy (J mol^{-1})
A	Particle radius (m)
γ_{sv}	Specific surface energy (J mol^{-1})
V_m	Molar volume (m^3)
c	crystallite size (m)
ΔG_F	Free energy change of Frenkel defect pair formation (J mol^{-1})
ΔG_S	Free energy change of Schottky defect pair formation (J mol^{-1})
K_F	Reaction constant of Frenkel defect pair formation
K_S	Reaction constant of Schottky defect pair formation
T_m	Temperature of maximum rate of shrinkage (s^{-1})
r	Spherical pore radius in a liquid (m)
ΔP	Pressure difference across curved surface (N/m^2)
γ_{lv}	Surface energy of the liquid/vapour interface (J m^{-2})
ρ_b	Bulk density (kg m^{-3})
$\rho_{water/T}$	Specific gravity of distilled water at temperature, T
M_{air}	Dry sample weight (kg)
M_{water}	Immersed (in distilled water) sample weight (kg)
M_{wire}	Immersed (in distilled water) wire weight (kg)
$M_{wet/air}$	Wet sample weight (kg)
A	Cross sectional area of sample (m^2)
L	Length between the two potential wires (m)
R_T	Measured resistance of sample (V/A)
ρ_r	Relative density (kg m^{-3})
ρ_o	Initial relative density (kg m^{-3})
ΔL	Change in length of sample (m)
L_o	Initial length of sample (m)

A_o	Material parameter
m	Material sintering exponent
Q_s	Apparent activation energy for initial stage sintering (J mol^{-1})
C	Heating rate in CHR dilatometry (K s^{-1})
T_p	Temperature for maximum in derivative of ρ_r with respect to temperature (K)
σ_{TS}	Tensile fracture strength of a ceramic (Pa)
a	Inherent flaw size (m)
K_{IC}	Fracture toughness of a ceramic (Pa)
t	Time (s)
n	Grain growth exponent
K	Rate constant for grain growth
K_o	Pre-exponential grain growth constant
Q	Activation energy of grain growth (J mol^{-1})
V_t	Sinusoidal voltage (V)
I_t	Sinusoidal current (A)
ϕ	Phase angle
Z	Impedance (ohm)
Z'	'Real' impedance (ohm)
Z''	'Imaginary' impedance (ohm)
V_o	Amplitude of the voltage
I_o	Amplitude of the current
R_T	Resistance component (parallel) of the impedance (ohm)
C_T	Capacitance component (parallel) of the impedance (F)
τ_l	Lattice relaxation time constant (s)
R_l	Resistance of the lattice (ohm)
C_l	Capacitance of the lattice (F)
σ_l	Electrical conductivity of the lattice (S m^{-1})
ε_l	Relative dielectric constant of the lattice (dimensionless)
τ_{gb}	Grain boundary relaxation time constant (s)
R_{gb}	Resistance of the grain boundary (ohm)
C_{gb}	Capacitance of the grain boundary (F)
ε_{gb}	Grain boundary relative dielectric constant (dimensionless)
d_{Ce}	Room temperature lattice parameter of ceria solid solutions (m)
Δd_{Ce}	Difference in lattice parameter compared to that of ceria at room temperature (m)
Δr_k	Difference in ionic radius of the dopant (r_k) and the Ce cation (m)
Δz_k	Difference in valence of the dopant (z_k) and the Ce cation
m_k	Cation percent of the dopant

Avogadro's number, N	0.6023×10^{24} mol^{-1}
Boltzmann's constant, k	13.81×10^{-24} J/K
Planck's constant, h	0.6626×10^{-33} J s
Gas constant, R	8.314 J/(mol K)
Faraday constant, F	96490 C mol^{-1}
Permittivity of free space, ε_o	8.854×10^{-12} C V^{-1} m^{-1}

The table below lists the different elements, atomic species, ions and oxides (and others) in this study;

Element	Atomic species	Ion	Oxides and others
Aluminium	Al		
Bismuth	Bi		Bi_2O_3, $BiGaO_3$
Carbon	C		CO, CO_2
Calcium	Ca	Ca^{2+}	CaO, $CaCO_3$
Cerium	Ce	Ce^{3+}, Ce^{4+}	CeO_2, $Ce_{0.9}Gd_{0.1}O_{1.95}$, $Ce_{0.8}Gd_{0.2}O_{1.90}$, $Ce_{0.9}Gd_{0.09}Ca_{0.01}O_{2-X}$, $Ce(NO_3)_3.6H_2O$, $Ce_{0.8}Sm_{0.2}O_{1.9}$, $CeO_{0.94}SmO_{0.04}Y_{0.02}$
Cobalt	Co	Co^{2+}, Co^{3+}	CoO, Co_2O_3, $Co(NO_3)_2{\cdot}6H_2O$)
Chromium	Cr		
Copper	Cu	Cu^{2+}	CuO, Cu_2O, $Cu(NO_3)_2.xH_2O$
Erbium	Er		Er_2O_3
Iron	Fe		Fe_2O_3, $Fe(NO_3)_3.9H_2O$
Gallium	Ga	Ga^{3+}	Ga_2O_3
Gadolinium	Gd	Gd^{3+}	Gd_2O_3 $Gd_2Ti_2O_7$, $Gd_{0.6}Sr_{0.4}CoO_3$
Hydrogen	H	H^+	H_2
Potassium	K		
Lanthanum	La	La^{3+}	$LaCrO_3$, $LaGaO_3$, $LaMnO_3$, $La_2Zr_2O_7$
Magnesium	Mg	Mg^{2+}	
Manganese	Mn		MnO_2
Nitrogen	N		N_2, NO_x
Sodium	Na		Na_2O
Niobium	Nb	Nb^{5+}	
Neodymium	Nd		$Nd_{0.7}Sr_{0.3}MnO_3$
Nickel	Ni		NiO
Oxygen	O	O^{2-}	
Palladium	Pd		
Praseodymium	Pr	Pr^{4+}	Pr_6O_{11}, $Pr_{0.7}Sr_{0.3}MnO_3$
Platinum	Pt		
Sulphur	S		SO_x
Scandium	Sc	Sc^{3+}	
Silicon	Si		SiO_2
Samarium	Sm		$Sm(NO_3)_3.6H_2O$, $Sm_{0.5}Sr_{0.5}CoO_3$
Tin	Sn		SnO_2
Strontium	Sr	Sr^{2+}	SrO, $Sr_2Ga_2O_5$, $Sr_3Ga_2O_6$, $Sr_4Ga_4O_9$
Terbium	Tb		
Titanium	Ti	Ti^{4+}	TiO_2
Yttrium	Y	Y^{3+}	Y_2O_3
Zirconium	Zr	Zr^{4+}	ZrO_2

List of Figures

Figure 2.1 Basic operation of the fuel cell.
Figure 3.1 Schematic diagram of reactions in a SOFC.
Figure 3.2 Temperature dependant efficiencies of a heat engine and a fuel cell.
Figure 3.3 Polarisation losses in a fuel cell.
Figure 3.4 Resistance of various electrolytes as a function of temperature and thickness.
Figure 3.5 The Siemens-Westinghouse tubular SOFC.
Figure 3.6 The SOFC planar design.
Figure 5.1 Basic CVD operation; (A) heterogeneous precipitation (B) homogeneous precipitation.
Figure 5.2 The principle of EVD.
Figure 5.3 The tape casting process.
Figure 6.1 Transport mechanisms for grain growth and densification.
Figure 6.2 Development of the ceramic microstructure during sintering: (a) loose powder particles, (b) initial stage, (c) intermediate stage and (d) final stage.
Figure 6.3 Effect of crystallite size (c) on the sintering profile of ceria.
Figure 6.4 An agglomerate of dense polycrystalline primary particles.
Figure 6.5 (a) Sintering dilatometry of Co additions to SnO_2 (b) Shrinkage rate of Co additions to SnO_2.
Figure 6.6 The different stages of liquid phase sintering.
Figure 6.7 (a) Sintering dilatometry of transition metal oxide additives (1%) to CGO20 (b) Shrinkage rate of Co additives to CGO20.
Figure 7.1 Percentage of nominal applied pressure in a unidirectional single ended pressed die.
Figure 7.2 Diagram to show sample in dilatometer.
Figure 7.3 Plan view of 4 point D.C. conductivity test sample.
Figure 8.1 Phase diagram of $CaO\text{-}Ga_2O$.
Figure 8.2 Sintering time versus bulk density for CGO, 1CoCGO and 1CuCGO at 1000°C (air). The transition metal oxides were added by powder mixing.
Figure 8.3 Bulk density versus Co and Cu addition to CGO sintered at 1000°C for 1 hour (air).
The sintering aids were added by precipitation.
Figure 8.4 DTA/TG (air) of $Co(NO_3)_2.6H_2O$ dissolved in ethanol and dried at 50°C.
Figure 8.5 Co and Cu addition to CGO via 'nitrate addition' as a function of bulk density (1000°C for 1 hour (air)).
Figure 9.1 Linear shrinkage versus temperature for CGO at 10K/min.
Figure 9.2 Relative density from dilatometry data (10K/min), bulk density and TG as a function of temperature for CGO.
Figure 9.3 Relative density of Co additions to CGO as a function of temperature by CHR dilatometry (10K/min).
Figure 9.4 (a) SEM image of CGO agglomerate (dispersed in ethanol, air dried, calcined at 650°C for 30 minutes and sieved) (b) SEM image of 2CoCGO agglomerate.
Figure 9.5 Linear differential shrinkage as a function of temperature for Co additions to CGO.
Figure 9.6 Relative density of CuCGO as a function of temperature by CHR dilatometry (10K/min).
Figure 9.7 DTA/TG of 2CuCGO at 10K/min in air.
Figure 9.8 Linear differential shrinkage as a function of temperature for Cu additions to CGO.
Figure 9.9 Relative density of Fe additions to CGO as a function of temperature by CHR dilatometry (10K/min).

Figure 9.10 Relative density of CGO and 2CoCGO as a function of temperature by CHR dilatometry at 2K/min, 10K/min and 20K/min.
Figure 9.11 $\ln(\Delta L/L_o)T$ versus lnC for CGO between 830-870°C.
Figure 9.12 $\ln(\Delta L/L_o)T$ versus lnC for 2CoCGO between 830-870°C.
Figure 9.13 Arrhenius plot of $\Delta L/L_o$ for CGO at CHR of 2K/min, 10K/min and 20K/min.
Figure 9.14 Arrhenius plot of $\Delta L/L_o$ for 2CoCGO at CHR of 2K/min, 10K/min and 20K/min.
Figure 9.15 The derivatives of relative densities with respect to temperature versus temperature for CGO and 2CoCGO at a CHR of 10K/min.
Figure 9.16 TEM micrograph of 1CoCGO sintered to full density at 1000°C for 1 hour in air.
Figure 9.17 TEM micrograph of 2CoCGO sintered to full density at 930°C for 4 hours in air.
Figure 9.18 (a) TEM micrograph of grain in 2CoCGO fired at 980°C for 12 hours and furnace cooled (b) EDX map of Co X-rays inside box area in (a) (c) EDX line scan of Co and Gd concentration across grain in (a).
Figure 9.19 Typical XRD trace for CGO.
Figure 9.20 Lattice parameter of CGO and CoCGO powder (1-4%) after decomposition of ethanol/nitrate at 650°C for 1 hour.
Figure 9.21 XPS spectrum for CGO and 2CoCGO powder calcined at 650°C for 2 hours and furnace cooled.
Figure 9.22 Lattice parameter of CGO and 2CoCGO powder calcined for 2 hours in air at the indicated temperature and furnace cooled.
Figure 9.23 Linear differential shrinkage of CGO and CGO20 as a function of temperature fired at a CHR of 2K/min in air.
Figure 9.24 Raman spectra (400-750cm^{-1}) of (a) CGO and (b) 2CoCGO pellet fired at 750°C, 850°C, 950°C and 1050°C (2 hours in air and furnace cooled).
Figure 9.25 Raman spectra (520-720cm^{-1}) of (a) CGO and (b) 2CoCGO pellet fired at 750°C, 850°C, 950°C and 1050°C (2 hours in air and furnace cooled).
Figure 9.26 Raman spectra of CGO pellet fired at 750°C, 850°C, 950°C and 1050°C (2 hours in air and ice quenched).
Figure 9.27 XPS spectra of CGO and 2CoCGO powder (1000°C for 2 hours and furnace cooled).
Figure 9.28 XPS spectra of CGO and 2CoCGO powder (1000°C for 2 hours and quenched in air).
Figure 9.29 Raman spectra of CGO pellet fired at 750°C, 850°C, 950°C and 1050°C (2 hours in air and ice quenched).
Figure 9.30 Relative density of Co additions to CGO20 by CHR dilatometry (10K/min).
Figure 9.31 Linear shrinkage rate as a function of temperature for Co additions to CGO20.
Figure 9.32 DTA of $Co(NO_3)_2.6H_2O$ dissolved in ethanol and dried at 50°C when fired in air and argon.
Figure 9.33 Linear shrinkage rate as a function of temperature for 2CoCGO fired in air and argon at a CHR of 2K/min.
Figure 9.34 SEM micrograph of 2CoCGO fired at 1500°C for 1 hour.
Figure 9.35 The plots of LnD versus Lnt (a) CGO (b) 2CoCGO.
Figure 9.36 The plots of LnD^n versus 1/T to calculate Q for (a) CGO and (b) 2CoCGO.
Figure 10.1 Impedance spectrum at 163°C for CGO fired at 1350°C for 4 hours in air and equivalent R-C circuit.
Figure 10.2 Arrhenius graph of the lattice conductivity of CGO and CoCGO.
Figure 10.3 EDXS spectrum for point analysis in TEM of Co content in the grain boundary and lattice of 2CoCGO sintered at 980°C for 12 hours and furnace cooled.
Figure 10.4 Arrhenius graph of the grain boundary conductivity of CGO and CoCGO.
Figure 10.5 Arrhenius graph of the total conductivity of CGO and CoCGO.
Figure 10.6 Arrhenius graph of the lattice conductivity of CGO and CuCGO.
Figure 10.7 Arrhenius graph of the grain boundary conductivity of CGO and CuCGO.
Figure 10.8 Arrhenius graph of the total conductivity of CGO and CuCGO.

Figure 10.9 SEM micrographs of (a) CGO (1450°C for 4 hrs) (b) 2CoCGOL (1300°C for 0 hrs).
Figure 10.10 Arrhenius graph of lattice and grain boundary (GB) conductivity of CGO, 2CoCGOS and 2CoCGOL.
Figure 10.11 Arrhenius graphs of (a) lattice and (b) grain boundary relaxation time (τ) of CGO, 2CoCGOS and 2CoCGOL.
Figure 10.12 Total conductivity of CGO, 2CoCGO and 4CoCGO in air (AC and DC).
Figure 10.13 Total D.C. conductivity of CGO, 2CoCGO and 4CoCGO versus pO_2 at 750°C.
Figure 10.14 Graph showing the P(-) value for CGO and 2CoCGO at 750°C.
Figure 10.15 Total conductivity of 2CoCGO versus pO_2 at four different temperatures (°C).
Figure 10.16 Arrhenius plot of the (a) lattice conductivity and (b) grain boundary conductivity of 2CoCGO sintered at 930°C for different periods of time.
Figure 10.17 Arrhenius plot of the (a) lattice conductivity and (b) grain boundary conductivity of 2CoCGO sintered at 980°C for different periods of time.
Figure 10.18 Lattice and grain boundary conductivities of 2CoCGO at 200°C sintered at 930°C and 980°C (0-4 hours) as a function of bulk density.
Figure 11.1 CRH of 2CoCGO calcined at 400°C for 30 minutes (2CoCGOLC) and 650°C for 30 minutes (2CoCGOHC) (5K/min to 800°C and 2K/min to 1000°C (argon)).
Figure 11.2 Isothermal sintering of 2CoCGOLC and 2CoCGOHC at 1000°C (argon).
Figure 11.3 Green density (%bulk) of CGO and 2CoCGO isostatically pressed at different pressures.
Figure 11.4 CRH dilatometry of 2CoCGO powder isostatically pressed at different pressures (5K/min to 800°C and 2K/min to 1000°C (argon)).
Figure 11.5 Isothermal sintering at 1000°C of 2CoCGO powder isostatically pressed at different pressures (argon).
Figure 11.6 Green density (bulk) of bimodal mixture of CGO powder (Praxair added to Rhodia).
Figure 11.7 The particle size distribution for (a) CGOR and (b) CGOP (both powders ultrasonically dispersed in distilled water for 15 minutes).
Figure 11.8 CRH dilatometry of CGOR, CGOP, CGORP, 2CoCGOR, 2CoCGOP and 2CoCGORP (5K/min to 800°C and 2K/min to 1000°C (argon), powder calcined at 400°C for 30 minutes).
Figure 11.9 Isothermal sintering at 1000°C of CGOR, CGOP, CGORP, 2CoCGOR, 2CoCGOP and 2CoCGORP (argon).
Figure 11.10 Schematic flow diagram for tape casting of 2CoCGO.
Figure 11.11 SEM images of fracture surface of 2CoCGO tape fired at 1000°C for 4 hours (argon).
Figure 11.12 Fracture surface of 2CoCGO thick film (supported on porous LSCF) by screen printing (a-b) at 1000°C for 4 hours (argon) and (c-d) 1100°C for 4 hours (argon).
Figure 12.1 Relative density of Co additions to 8YSZ as a function of temperature by CHR dilatometry (10K/min).
Figure 12.2 The particle size distribution for 8YSZ (powders ultrasonically dispersed in distilled water for 15 minutes).
Figure 12.3 Linear differential shrinkage of Co8YSZ as a function of temperature.
Figure 12.4 Bulk density after sintering 1Co8YSZ for 1 hour at the indicated temperature.
Figure 12.5 Arrhenius graph of the lattice conductivity of 8YSZ and Co8YSZ.
Figure 12.6 Arrhenius graph of the grain boundary conductivity of 8YSZ and Co8YSZ.
Figure 12.7 Arrhenius graph of the total conductivity of 8YSZ and Co8YSZ.
Figure 12.8 Lattice conductivity of YSZ and 1Co8YSZ fired at 3 different temperatures (°C).
Figure 12.9 Grain Boundary conductivity of YSZ and 1Co8YSZ fired at 3 different temps (°C).
Figure 12.10 Lattice parameter of 8YSZ and 1Co8YSZ powder calcined for 2 hours in dry air at the indicated temperature and furnace cooled.

List of Tables

Table 1.1 Chemical and powders (supplier and purity) used in this study.

Table 6.1 Grain boundary mobility of undoped and doped ceria.

Table 8.1 Glasses fabricated from the CaO-Ga_2O system.

Table 8.2 ICP of $Co(NO_3)_2.6H_2O$ dissolved in ethanol added as a sintering aid to CGO.

Table 9.1 T_{max} and $(d(\Delta L/L_o)/dT)$ at T_{max} for Co additions to CGO powders.

Table 9.2 T_{max} and $(d(\Delta L/L_o)/dT)$ at T_{max} for Cu additions to CGO powders.

Table 9.3 The values of m for CGO and 2CoCGO between 830-870°C.

Table 9.4 T_{max} of CoCGO20 from CHR dilatometry at 5K/min and 10K/min.

Table 11.1 TEC's of CGO and 2CoCGO (20-950°C).

Table 11.2 Mass of additives used to make 2CoCGO tape cast slurry: polyester resin (KD1), poly (vinyl butyral) (PVB), poly (ethylene glycol) (PEG) and poly (butyl phthalate) (PBT).

Table 12.1 T_{max} and magnitude for Co additions to 8YSZ powders.

Section 1

General Introduction

And

Review of Literature

Chapter 1 – Introduction

1.1. Introduction

In the early 1970's, oil accounted for approximately 50% of the world's total energy demand. By 1994 this figure was reduced to around 40% and is expected to remain at this level until the year 2010. Due to development and population growth in the third world it is expected that the world's consumption of oil will significantly increase. Predictions forecast that unless new oil reserves are discovered, depleting oil reserves would force production down in 2035. Negating the well documented environmental concerns associated with the combustion of oil, the economic and political instability that may result over the next two generations due to plummeting oil reserves is a daunting prospect for world peace and security [1].

The need for power sources that require alternative/less fossil fuels and compete economically with traditional power sources presents a major challenge to society. For the past five decades nuclear energy has been exploited as a means of supplying power. The industry, however, suffered a major setback as a result of the Chernobyl disaster and continues to attract significant opposition due to safety concerns ranging from waste removal to possible terrorist attack. Renewable energy sources such as solar, wind and geothermal power are currently very much in vogue with environmental lobby groups. It is considered unrealistic that these sources could deliver the massive quantities of energy the world needs.

The scientific and engineering community is currently placed under immense pressure to devise and manufacture a power source that produces clean and abundant energy. One such device being considered is the fuel cell.

In its simplest form, the fuel cell consists of an electrolyte sandwiched between two electrodes, often referred to as a positive electrolyte negative (PEN) assembly. Supplying fuel and oxygen to the electrodes results in electrochemical reactions that conduct ions through the electrolyte and produce electricity, heat and water (and CO_2 if using hydrocarbon fuels).

1.2. Aims of My Research

For approximately the last 10 years, the Department of Materials has pursed a research program with the aim of scaling up a novel ITSOFC that operates between 500-600°C. The Imperial College planar ITSOFC design takes advantage of the almost identical thermal expansion coefficients of Gd doped ceria and ferritic stainless steel, allowing the thick film PEN structure to be supported on a porous stainless steel foil. The incorporation of the stainless steel substrate should enhance the mechanical strength and significantly reduce production and material costs.

Typically, bulk Gd doped ceria is sintered to high density (>95%) at approximately 1300-1400°C. The electrodes, owing to their large porosity content, can be fired at 900-1000°C. The aim of my studies has been to find a method of lowering the sintering temperature of Gd doped ceria to between 900-1000°C without any deleterious effect on its electrical properties. The primary aim of lowering the sintering temperature is to enable ferritic stainless steel to be incorporated into the Imperial ITSOFC design. In order to limit oxidation of the stainless steel during densification of the electrolyte, it is necessary to minimise the time required to densify the material at maximum firing temperature. Acceptable levels of oxidation on the stainless steel have been reported when isothermally held at 1000°C for 1 hour in reducing conditions [2]. Therefore, it is required that the electrolyte achieves high density (no connected porosity) under similar conditions. Sintering at lower temperature may also enhance the properties of the electrolyte. Grain growth and impurity segregation, generally considered deleterious to the mechanical and electrical properties, are significantly reduced when electrolyte materials are sintered at lower temperature. For similar reasons, it would also be beneficial to lower the sinter temperature of YSZ.

1.3. Outline of the Thesis

The thesis begins with an introduction to the fuel cell, followed by a more in-depth look at the most promising of the fuel cells, the solid oxide fuel cell (SOFC). The emphasis then focuses on material selection for the different components within the SOFC, particularly for SOFC electrolytes operating at reduced temperature. The design and fabrication of operating SOFC systems is likewise discussed. The majority of the literature review is dedicated to the low temperature sintering of SOFC electrolytes. The

experimental section encompasses a discussion on the different powder synthesis and characterisation techniques employed to obtain data presented in this study. The results and discussion section are split into five chapters. The first describes the development of a technique that enabled a commercially supplied doped ceria powder to be sintered to high density at the annealing temperature of ferritic stainless steel. The next two chapters discuss the densification and electrical properties of these materials. A chapter is dedicated to ways in which different firing conditions can be manipulated to enhance the densification of these materials. Based on the findings for low temperature densified doped ceria electrolytes, the final chapter of the results and discussion section comments on the ability to densify yttria stabilised zirconia electrolytes at reduced temperature. Finally, there are some general conclusions and suggestions for future work.

1.4. Raw Materials Used in this Study

Table 1.1 lists the chemicals and powders (supplier and purity) used in this study;

Material	Supplier	Purity (%)
CGO	Rhodia	99.999
CGO	Praxair	99.999
CGO20	Rhodia	99.999
8YSZ	Tosoh	99.999
Ga_2O_3	Aldrich Chemical Co.	99.99
$CaCO_3$	Aldrich Chemical Co.	99.9
Bi_2O_3	Aldrich Chemical Co.	99.99
CuO	Aldrich Chemical Co.	99.99+
Co_3O_4	Aldrich Chemical Co.	99.995
$Cu(NO_3)_2.xH_2O$	Aldrich Chemical Co.	99.999
$Co(NO_3)_2.6H_2O$	Aldrich Chemical Co.	99.999
$Fe(NO_3)_3.9H_2O$	Aldrich Chemical Co.	99.99+
Ethanol 'AnalR'	Merck	96
Ammonia 'AnalR'	Merck	35
Ag paint	Leitsilber	99
KD1	Avecia Ltd.	97-99
PVB	Aldrich Chemical Co.	99
PEG400	Aldrich Chemical Co.	99
PBT	Aldrich Chemical Co.	99

Table 1.1 Chemical and powders (supplier and purity) used in this study.

1.5. Nomenclature

The bulk of the studies presented in this thesis involve adding metal oxides to the host electrolyte materials: CGO, CGO20 and 8YSZ. Additive level is expressed in cation% unless stated otherwise. Examples of nomenclature used in the results and discussion section of this thesis are as follows;

1. CGO + 2cation%Co = 2CoCGO
2. CGO20 + 2cation%Co = 2CoCGO20
3. CGO + 4cation%Cu = 4CuCGO
4. 8YSZ + 1cation%Co = 1Co8YSZ

When describing a range of concentration of a particular additive to a host electrolyte, the cation% of the additive is omitted (i.e. 0.1CoCGO to 4CoCGO is expressed simply as CoCGO.

References

1. Hubbert's Peak; The Impending World Oil Shortage. K.S.Deffeyes. Princeton University Press, 2001.
2. R.Rudkin. Private Communications.

Chapter 2 - The Fuel Cell

2.1. Principle of Operation

The fuel cell, invented in 1839 by the British scientist William Grove, is a highly efficient device for the production of electricity. Using similar principles as a conventional alkaline battery, the fuel cell converts chemical energy directly into electricity. However, unlike a battery, the reactants are supplied continuously. The fuel cell consists of two electrodes (anode and cathode) which are separated by an ionic conducting electrolyte. The cells are electrically connected to form a fuel cell stack. Fuels, such as hydrogen, are fed to the anode and oxidised. Electrons are released to the external circuit. Oxidant, typically oxygen, is fed to the cathode and is reduced by acceptor electrons from the external circuit. Ions are then conducted through the electrolyte to the anode for completion of the circuit. Products of the chemical reactions are water and, depending on the fuel source, carbon dioxide. By nature of its operation, the system is virtually free from noxious emissions of NO_x, SO_x and CO. Another positive environmental aspect of the fuel cell is an absence of mechanically moving parts thus facilitating silent operation.

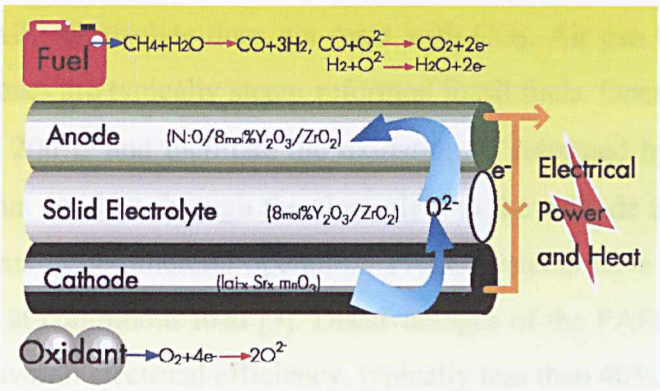


Figure 2.1 Basic operation of the fuel cell [1].

A fuel cell is a thermodynamic device and converts chemical energy directly to electrical energy. The process, unlike the internal combustion engine, does not transfer chemical energy via heat and mechanical energy and thus has higher theoretical efficiencies. There are, however a number of irreversible losses in a fuel cell which limit its efficiency, these are reviewed in chapter 3.

There are a number of different fuel cell systems under development; each classified by the type of electrolyte incorporated in the cell.

2.2. The Alkaline Fuel Cell (AFC)

Although fuel cells have existed in concept from 1839, it was not until NASA in the 1960's demonstrated their potential in providing power by the incorporation of the AFC in the famed Apollo missions. Concentrated liquid potassium hydroxide is most often used as the electrolyte whilst electrodes are fabricated from porous nickel or carbon in PTFE. The hydroxide ion is the ionic conductor species and forms by reaction of oxygen and water at the cathode. The AFC operates at low temperatures (60-120°C) and produces relatively high current densities. A major disadvantage of AFC systems is that the electrolyte reacts with CO_2 contained in both the fuel and air to form insoluble potassium carbonate. High purity inlet gasses and expensive materials required for this cell have limited its application primarily to power sources on board space vehicles [2].

2.3. The Phosphoric Acid Fuel Cell (PAFC)

The PAFC uses a phosphoric acid (H_3PO_4) electrolyte immobilised in a PTFE bonded SiC matrix. The gas diffusion electrodes consist of PTFE-bonded nanosized Pt crystallites dispersed on carbon supported by a carbon paper substrate. Unlike the AFC electrolyte, the PAFC electrolyte does not react with CO_2. Air can thus be used as an oxidant and fuel gases are typically steam-reformed fossil fuels. Operating temperatures are approximately 200°C and facilitate the oxidation of reformed hydrocarbon fuel to produce H^+ ions that conduct through the electrolyte to the cathode and form water. Of the fuel cell systems in commercial operation, PAFC systems have recorded the most hours in operation at continuous load [3]. Disadvantages of the PAFC are high running costs and the low overall electrical efficiency, typically less than 40%.

2.4. The Polymer Electrolyte Membrane Fuel Cell (PEMFC)

Initially developed in the 1950's by General Electric for the Gemini space program, fuel cells containing a solid polymer electrolyte membrane were considered inferior in performance to the AFC. In the 1980's Ballard Power developed the PEMFC,

incorporating an electrolyte fabricated from Nafion^{TM}, for the automobile market. The electrolyte, on a molecular level, has a tubular structure which contains functional acid groups $(SO_3)^{2-}$. These are present on the inner surface of the tubes and are capable of exchanging cations and anions. Water is added to expand the system. Hydrogen ions are then conducted through the membrane, which accumulates water molecules that also conduct. The electrodes are made from a porous carbon cloth support, which has a fine dispersion of carbon loaded with nanosized Pt crystallites [3]. A major problem associated the use of hydrogen rich gasses is the sensitivity of the anodic-catalysts to traces of CO [2]. The other main disadvantage is the high cost of materials currently used to construct the cell. Despite these drawbacks, the relatively high power densities ($1.5W/cm^2$) at low temperatures (~80°C) make the PEMFC an attractive alternative to the internal combustion engine.

2.5. The Molten Carbonate Fuel Cell (MCFC)

The MCFC incorporates a molten salt electrolyte consisting of K_2CO_3-Li_2CO_3, which is immobilised in a porous lithium aluminate ceramic matrix. Operating at 650°C, the electrolyte conducts CO_3^{2-} ions. This high temperature allows internal reforming of the hydrocarbon fuels, thus significantly reducing plant cost and increasing the efficiency of the cell. High temperatures also accelerate both the chemical and physical processes. Although the cost of materials is high, the system is relatively cheap to scale up by the use of techniques such as tape casting. One significant disadvantage of the MCFC is the deterioration of the cathode and biopolar plate due to the corrosive nature of the electrolyte. The system is also susceptible to sulphur poisoning from impurities in the fuel [3].

2.6. The Solid Oxide Fuel Cell (SOFC)

The SOFC is considered to be the fuel cell in its earliest stages of commercialisation. It is an all-ceramic ensemble that was originally conceived to operate at 1000°C which, integrated with coal gasification plants, could produce multi-MW of power [2]. Coupled with mixed conducting ceramic electrodes, zirconia has traditionally been the electrolyte of choice due to its high oxygen ion conducting ability. In recent years the development of ceramic electrolytes with superior ionic conductivity has enabled lower operating temperatures. This has changed the perceived commercialisation strategy of

the SOFC and opened a new market for the intermediate temperature SOFC (ITSOFC) operating between 500-800°C. The evolution of the SOFC shall be discussed more in detail in chapter 3. Advantages of the SOFC include; a solid electrolyte minimises corrosion and is relatively stable at operating temperature. As with the MCFC, the high operating temperature enables internal reforming of the hydrocarbon fuels and thus significantly reducing operational costs. The SOFC is also more impervious to poisoning from impurities contained within the fuel or air. Disadvantages at present are the high cost of the ceramic materials and problems associated with sealing and balance of plant equipment.

References

1. www.isis.rl.ac.uk/ISIS98/ Cryst_4.jpg
2. Science and Technology of Fuel Cells. N.Q.Minh and T.Takahashi. Elsevier Press, 1995.
3. B.C.H.Steele. J.Mater.Sci. **36**, (2001), 1053.

Chapter 3 – The Solid Oxide Fuel Cell

3.1. Introduction

The previous chapter briefly introduced the four different fuel cell systems. Of the four, the SOFC is in the earliest stages of commercialisation [1]. New designs and materials have enhanced SOFC performance considerably over the past decade, making the SOFC arguably the most attractive fuel cell system being developed. Extensive academic research plus the financial backing of large multi-national companies intend to exploit the versatile nature of the SOFC to produce energy for a wide range of applications.

The rest of this chapter will discuss in more detail the operation of the SOFC and its electrical efficiency. The different components that comprise the SOFC are described with particular emphasis on material development for the ITSOFC. The final section will look at SOFC designs currently being developed.

3.2. Operating Principle of the SOFC

As previously discussed in chapter 2, the electrical generation mechanism of a SOFC is based on the electrochemical combustion of the fuel. Typically, oxygen is used as the oxidant gas and is reduced at the cathode whilst syngas, produced by reforming a hydrocarbon fuel, is oxidised at the anode. Oxygen ions are generated at the cathode and migrate through an ionically conducting electrolyte. After passing through the electrolyte they release electrons at the anode and water and CO_2 are produced as the reaction products. The driving force for oxygen ion migration is the difference in oxygen partial pressure between the electrodes. Electrons are released to the external circuit producing direct current (D.C). For practical power generation applications the D.C. electricity is converted to alternating current (A.C) by means of an inverter. To scale up the voltage output of the SOFC, cells are stacked in series to produce the designated voltage requirement. Figure 3.1 is a schematic diagram of the reactions in a SOFC.

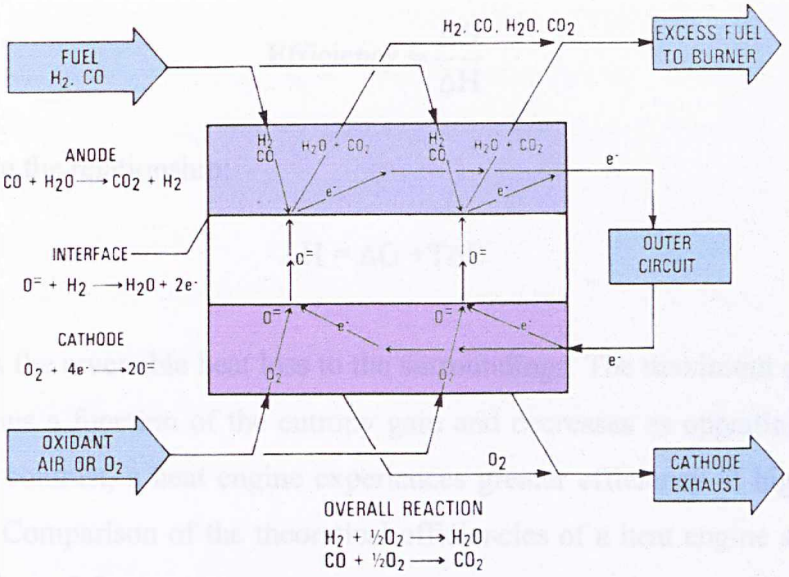


Figure 3.1 Schematic diagram of reaction in a SOFC [1].

3.3. Efficiency of the SOFC

The theoretical thermodynamic derivation of the Carnot cycle shows that even under ideal conditions, a heat engine cannot convert all the heat energy supplied into mechanical energy. In an internal combustion chamber, the engine accepts heat from a source at a high temperature (T_1) converts part of the energy into mechanical work and rejects the remainder to a heat sink at a lower temperature (T_2). The greater the difference between T_1 and T_2, the greater the efficiency (Equation 3.1):

$$\text{Maximum efficiency of heat engine} = \frac{(T_1 - T_2)}{T_1} \qquad (3.1)$$

Being an electrochemical device the SOFC efficiency is not related to the Carnot cycle. The relationship between the heat of combustion of the fuel (ΔH) and the energy produced by the device can be used to calculate the efficiency:

$$\text{Efficiency} = \frac{\text{Useful energy output}}{\Delta H} \qquad (3.2)$$

In ideal SOFC conditions (unattainable in reality), all the free energy change (ΔG) is available as electrical energy. At a specified temperature, the maximum efficiency is given by:

$$\text{Efficiency} = \frac{\Delta G}{\Delta H} \tag{3.3}$$

substituting in the relationship:

$$\Delta H = \Delta G + T\Delta S \tag{3.4}$$

where $T\Delta S$ is the reversible heat loss to the surroundings. The maximum efficiency of a fuel cell is thus a function of the entropy gain and decreases as operating temperature increases. In contrast, a heat engine experiences greater efficiency at higher operating temperature. Comparison of the theoretical efficiencies of a heat engine and a fuel cell is shown in figure 3.2.

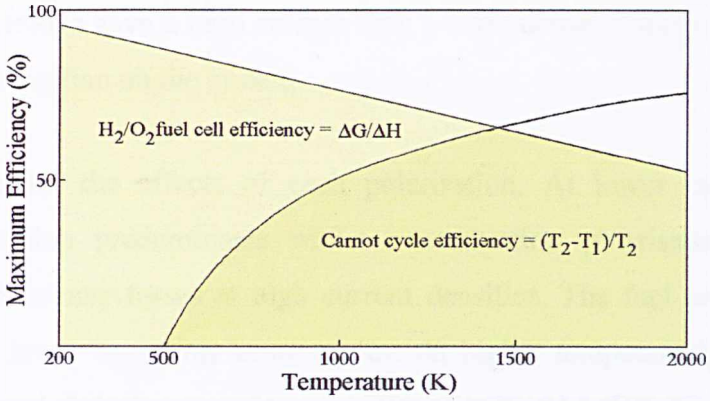


Figure 3.2 Temperature dependant efficiencies of a heat engine and a fuel cell [2].

Theoretical maximum efficiency of a fuel cell, allowing for slight differences in fuel and oxygen mixtures is approximately 95%. However, when a current is drawn from a fuel cell, the cell voltage decreases. Irreversible heat losses, termed polarisation losses, reduce the working efficiency to around 55% [2].

The polarisation losses are either ohmic or non-ohmic. The voltage of the cell can thus be expressed as:

$$E_{cell} = E_{rev} - I(R_{ele} + R_a + R_c) - (\eta_{a+c} + \delta_{a+c}) \tag{3.5}$$

where E_{rev} is the open circuit cell e.m.f. and R_{ele}, R_a and R_c are the electrical resistances of the electrolyte, anode and cathode respectively. η_{a+c} and δ_{a+c} are the total activation polarisation (anode and cathode) and the total concentration polarisation (anode and cathode) respectively.

Ohmic polarisation losses result from the different electrically conducting components within the cell and their associated resistive coefficients. Ohmic polarisation is minimised by selecting materials with high conductivity and small current path lengths. Electrochemical reactions involve an energy barrier that must be overcome by the reacting species. This barrier, called the activation energy, results in the activation polarisation and can be regarded as the extra potential needed to reduce the barrier of the rate-determining step of the reaction to a value such that the electrode reaction proceeds at a desired rate. Increasing the area or catalytic activity of the electrodes can reduce the activation polarisation.

Concentration polarisation occurs when the electrode reaction is hindered by mass transport of reactants to, or products away from, the active sites of the electrodes. Ensuring the electrodes have a high surface area (~70% dense) minimises the effect of concentration polarisation on the system.

Figure 3.3 illustrates the effects of each polarisation. At lower current densities, activation polarisation predominates whilst concentration polarisation is primarily responsible for efficiency losses at high current densities. The fuel cell, in theory, is more efficient at lower operating temperatures. At higher temperature, however, ions are more mobile and diffusion rates increase. Hence reduced polarisation and electrical resistance with increasing temperature results in an increase in power output.

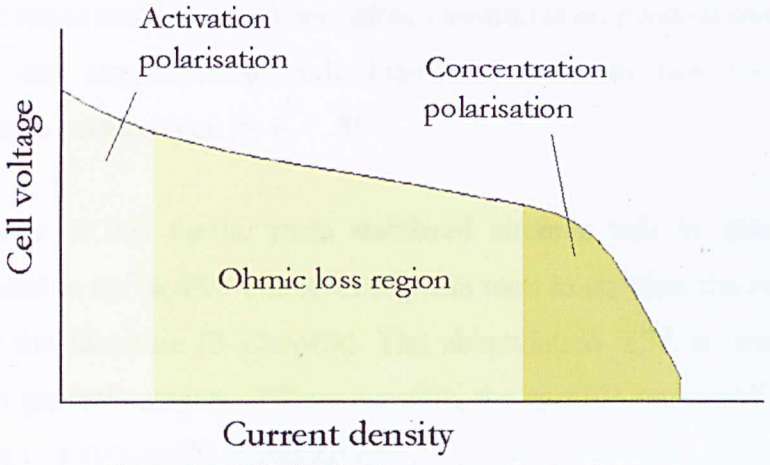


Figure 3.3 Polarisation losses in a fuel cell [2].

3.4. Components in a SOFC

The four main components in a fuel cell are the electrolyte, anode, cathode, and interconnects. Apart from each component requiring high strength and toughness,

similar thermal expansion coefficients and low cost there are other specific criteria that must be met.

3.4.1. The Electrolyte

The electrolyte has often been considered the most important part of the SOFC. The temperature at which the SOFC operates, and thus optimisation and fabrication of other components within the cell, is ultimately governed by the electrolyte's ability to effectively conduct ions between the anode and cathode. The electrolyte must be stable in both low and high oxygen partial pressures, have excellent ionic conductivity in the dual atmosphere at operating temperature, have negligible electronic conductivity and be sufficiently dense so as to prevent mixing of the air and fuel.

Oxide ions can migrate in an oxygen lattice via oxide ion vacancies, and oxides in which electrical charges are mainly carried by oxide ions are called oxide ion conductors. Traditionally, yttria stabilised zirconia has been the material selected as the electrolyte in the SOFC. Early SOFC designs required that the electrolyte operate at approximately 1000°C to achieve sufficient conductivity within the cell [3]. Siemens-Westinghouse have developed large SOFC stacks integrated with gas turbines that operate at 850°C to produce multi-kW of power with efficiencies of approximately 70% [4]. Problems associated with operating at high temperatures are excessive heating and cooling times between stand-still and operation, constraints on material selection for the interconnectors and electrolyte/electrode interfacial reactions that form insulating phases that degrade performance [5, 6, 7, 8].

For the remainder of this thesis, yttria stabilised zirconia will be discussed as an electrolyte material in the SOFC. The level of yttria used to stabilise the zirconia varies considerably in the literature (3-12mol%). The abbreviation YSZ is used to refer to materials in this general category. Where possible, the specific yttria addition is stated (i.e. 8YSZ refers to $8Y_2O_3$mol% doped ZrO_2).

In the last 10 years there has been a concerted drive to lower the operating temperature of the SOFC in order to exploit lucrative markets that require small-scale power applications (~1kW), that are not integrated with gas turbines (e.g. automobiles and houses). This has led to the development of the ITSOFC operating between 500-800°C.

Reducing the operating temperature could overcome many of the problems associated with the SOFC operating at high temperature. Importantly, functioning at below 750°C would enable stainless steel to replace many of the expensive and fragile ceramic components within the cell [9]. Above this temperature stainless steel oxidises too quickly and is considered a poor material selection.

The thinner the electrolyte, the lower the temperature at which the electrolyte can effectively operate due to reduced ohmic polarisation losses. Steele [10] stated that the electrolyte component should not contribute more than $0.15\Omega cm^2$ to the total cell area specific resistance (ASR). Films below about 15μm are prone to gas permeation, which complicates the design and fabrication process. From figure 3.4, the minimum theoretical operating temperature of a YSZ supported electrolyte is approximately 700°C [3]. Such operational temperatures have been reported for laboratory based stacks with a YSZ electrolyte thickness of 10μm [11].

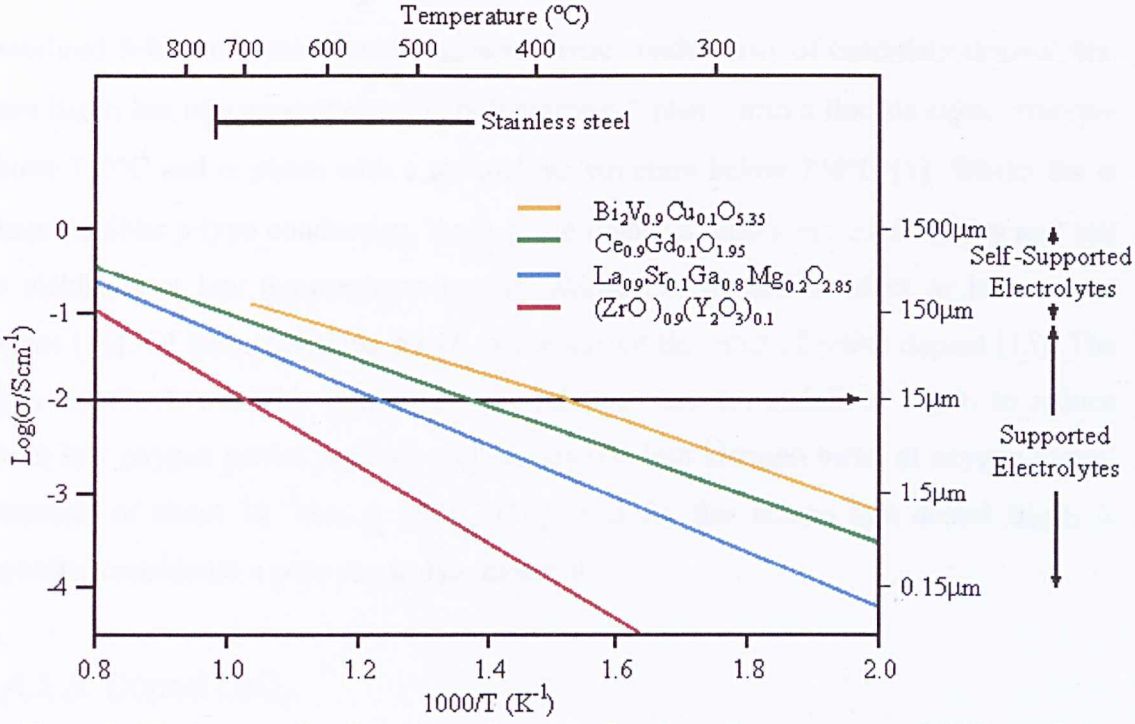


Figure 3.4 Resistance of various electrolytes as a function of temperature and thickness [3].

To enable the inclusion of stainless steel in the stack, perceived by many as the key to commercialisation of the ITSOFC, thus requires new electrolytic materials with acceptable ionic conductivity between 500-750°C. As illustrated in figure 3.4, this includes SrO and MgO doped $LaGaO_3$, δ-Bi_2O_3 and doped ceria.

3.4.1.1. $LaGaO_3$

Perovskite oxides, ABO_3, have stable crystal structures, which by the partial substitution of the A and B cation with lower valence cations can introduce a large number of oxygen vacancies. In 1994, Ishihara et al. [12] first reported on the highly ionic conducting material $La_{1-x}Sr_xGa_{1-y}Mg_yO_{3-0.5(x+y)}$ (LSGM). The material exhibited purely ionic conductivity in the fuel cell working environment up to 1000°C ($pO_2=10^{-20}$ to 1atm). Recent studies by Ishihara et al. [13] have found that doping LSGM on the B site with Co (<10%) and Ni (<10%) increases the ionic conductivity due to the improved mobility of the oxide ions within the defect structure. However, it has not yet proved possible to find suitable stable electrode materials to combine with LSGM electrolytes [3].

3.4.1.2. δ-Bi_2O_3

Stabilised δ-bismuth oxide has the greatest ionic conductivity of candidate electrolytes. Pure Bi_2O_3 has two crystallographic polymorphs: δ phase with a fluorite cubic structure above 730°C and α phase with a monoclinic structure below 730°C [1]. Whilst the α phase exhibits p-type conduction, the δ phase displays high ionic conductivity and can be stabilised at low temperatures by the addition of certain trivalent or hexa-valent oxides [14]. Of these additions, Er_2O_3 is considered the most effective dopant [15]. The main drawback with this material is the relative ease for stabilised Bi_2O_3 to reduce under low oxygen partial pressure and decompose into bismuth metal at oxygen partial pressures of about 10^{-13}atm at 600°C [16]. It is for this reason that doped Bi_2O_3 is currently considered a poor electrolyte material

3.4.1.3. Doped CeO_2

Similar to zirconia, ceria doped with divalent and trivalent oxides produces excellent oxygen-ion conductors. Doping with aliovalent cations introduces oxygen vacancies into the host lattice that make these materials potential electrolytes operating at approximately 500°C. Of the dopants, Sm and Gd are currently receiving the most attention. Apart from the high ionic conductivity, these material have a thermal expansion coefficient that closely matches ferritic stainless steel (~$12x10^{-6}K^{-1}$), the

implications of this will be discussed later in this chapter. Similar to stabilised bismuth oxide, the use of doped ceria as an electrolyte has been excluded for many years as it is well known that ceria becomes a mixed conductor in reducing atmospheres due to the formation of electronic charge carriers associated with the partial reduction of ceria. These charge carriers act to partially short the cell and thus reduce its efficiency. It has been shown that the electrolytic domain of this material increases as the operating temperature decreases. Steele has demonstrated that at 500°C under realistic anodic SOFC conditions, the doped ceria electrolyte has sufficiently high ionic conductivity to be considered an effective electrolyte [10].

Arguably, the best electrolyte material for ITSOFC operation is $Ce_{0.9}Gd_{0.1}O_{1.95}$ (CGO). The abbreviation CGO in this thesis relates solely to this composition. Gd doped ceria which varies from this stoichiometry is likewise given the abbreviation CGO but the different doping level is stated (i.e. CGO20 refers to $Ce_{0.8}Gd_{0.2}O_{1.90}$). The electrical properties of these materials will be reviewed in more depth in chapter 4.

3.4.1.4. Interlayers

In order to lower the operating temperature of the SOFC it is necessary to keep polarisation losses to a minimum. Various reports exist in the literature suggesting that placing very thin layers between doped ceria and the electrodes reduces polarisation losses. Inoue et al. [17] coated a thin film of stabilised zirconia on to the fuel side of a Sm doped ceria disk. The zirconia coating acted to suppress the reduction of the Sm doped ceria electrolyte. Decreasing the reduction of Ce^{4+} to Ce^{3+} limits the amount of electrons that act to short the cell. Lower internal resistances and higher current densities were reported. Similar results were obtained when a 1μm film of stabilised zirconia was sputtered onto the fuel side of an yttria doped ceria electrolyte [18]. Wachsman et al. [19] coated a thin bismuth oxide layer on to the fuel side of ceria and reported a 33% increase in power density. Another potentially positive aspect of composite electrolytes is enhanced mechanical strength. Atkinson and Selçuk [20] laminated a thin layer of YSZ onto Gd doped ceria and reported an increase in strength by a factor of between 1.75 and 4.06.

3.4.2. The Anode

The main function of the anode is to provide reaction sites for the electrochemical oxidation of the fuel, thus permitting the oxygen ions from the electrolyte to combine with the hydrogen to produce water and release electrons to the external circuit. Material requirements are; stable in reducing conditions (10^{-19}atm), undergo no second phase transformations during processing or operation, good electronic conductivity, sufficient porosity to allow gas transport to the reaction sites, high catalytic activity and be tolerant to impurities that may be present in the fuel [1].

Compared to the energy material scientists expend in trying to discover and optimise electrolyte and cathode materials, development of the anode often appears to have been overlooked. Composite Ni /YSZ anodes have long been a feature of high-temperature SOFC stacks [9]. As YSZ is electronically insulating, the Ni phase must be present such that there is a continuous electron conducting pathway through the anode. The balance between matching thermal expansion coefficients and achieving sufficient conductivity results in Ni concentrations between 40-60vol% [21]. Steele comments that in ITSOFC systems, the Ni may oxidise to form NiO and degrade performance [22]. It has been shown that the composite Ni/CGO anode has excellent ITSOFC properties at 700°C [23]. It is thought that the partial reduction of Ce^{4+} to Ce^{3+} introduces more electrons into the system thus enhancing the electronic conductivity [24].

3.4.3. The Cathode

Over the past 10 years there has been much research activity in ceramic mixed conductors for cathode application for the SOFC. It is not in the scope of this thesis to review all these materials; these have been reviewed in the following publications [22, 23, 25, 26].

The cathode provides reaction sites for the electrochemical reduction of the oxidant and is thus subject to high oxygen partial pressures. One important difference between the cathode and anode is the higher polarisation losses experienced at the cathode. This is due to the relatively large activation energy required for the reduction of oxygen [27]. The cathode material must; be stable in oxidising conditions, have good electrical

conductivity, be sufficiently porous to allow gas transport to the reaction sites and have good catalytic activity to limit polarisation losses.

The perovskite based $La_{1-x}Sr_xMnO_3$ (LSM) for some years has been regarded a good cathode. The material is considered a relatively poor ionic conductor but has sufficiently high electronic conductivity. One problem associated with this material is the reaction at the LSM/YSZ interface that produces the insulating phase $La_2Zr_2O_7$. Skinner [26] emphasises the need to develop not only new materials but also low temperature fabrication routes to avoid such insulating phases on the cathode/electrolyte interface. Current research of rare-earth doped manganite cathodes has led to new promising materials such as $Pr_{0.7}Sr_{0.3}MnO_3$ and $Nd_{0.7}Sr_{0.3}MnO_3$ [28]. Both have superior conductivity to traditional LSM and importantly produce no detrimental reaction products when sintered at elevated temperature with doped ceria electrolytes [29].

The poorly associated ionic properties of LSM have instigated considerable interest in $La_{1-x}Sr_xCoO_{3-\delta}$ (LSC) perovskites, these materials have good ionic conductivity plus sufficient electronic conductivity [30]. It is believed that the inclusion of Co, compared to Mn in LSM, increases the catalytic activity and thus reduces polarisation losses [31]. Godickemeier et al. [32] noted that the insulating second phases at the LSC/YSZ electrolyte interface during fabrication and operation make this a poor electrolyte/cathode combination. Due to lower operating temperatures, LSC has been regarded as a suitable cathode for ceria based electrolytes. It has been shown that doping the A and B sites of LSC with $Sr_{0.4}$ and $Fe_{0.8}$ (LSCF) respectively produces a perovskite that is stable in contact with ceria and produces low electrode resistivity ($0.2\Omega cm^2$) at temperatures of 700°C [27]. Bae and Steele [33] applied a double layered cathode of LSCF on to a Gd-doped cerium oxide. Separating the dense electrolyte and thick porous cathode was a thin dense cathode. Application of the thin film was found to decrease the resistivity of the cathode and enhance the efficiency of the cell. Dusastre [34] investigated the electrochemical properties of the interface between porous cathode composites of LSCF/CGO and the electrolyte CGO at 500-700°C. It was reported that the ASR decreased by a factor of 4 for LSCF doped with 36vol% CGO compared to undoped LSCF. It is speculated, however, that trace impurities in doped ceria electrolytes could form detrimental insulating second phases when coupled with LSC [26]. Recent developments of $Sm_{0.5}Sr_{0.5}CoO_3$ and $Gd_{0.6}Sr_{0.4}CoO_3$ show these to be promising new cathode materials for operation at about 600°C [35].

3.4.4. The Interconnect (or Bipolar Plate)

The interconnect arguably faces the greatest materials challenge of all the fuel cell components due to the demanding mechanical, physical and electronic constraints placed upon it. The main purpose of the interconnect is to connect the anode of one cell to the cathode of the next cell in electrical series and separate the fuel and oxidant between adjoining cells in a stack. The interconnect must be stable in both high and low oxygen partial pressures, undergo no phase transformations, possess good electronic conductivity in the dual environments and be dense so as to prevent mixing of the gases.

The most commonly used interconnect material for high temperature SOFC stacks is based on the perovskite $LaCrO_3$. Steele [23] comments that the optimal composition to minimise the lattice expansion associated with the loss of oxygen and thermodynamic stability of SrO and CaO doped $LaCrO_3$ at the CO_2 partial pressures generated in the anode compartment remains unclear. The other major problem associated with this material is its high cost: if the SOFC is to be economically competitive with existing power sources a cheaper interconnect alternative must be found.

Ferritic stainless steel is one such material. Apart from fulfilling all the material requirements necessary of the interconnect, it is relatively cheap and easy to mass-produce. Of equal importance is its the virtually identical thermal expansion coefficient to Gd doped ceria ($12.5x10^{-6}K^{-1}$). It should be noted that the thermal expansion coefficients of LSGM [35] and YSZ [36] are both approximately $11x10^{-6}K^{-1}$. Being structurally more robust, this would significantly aid SOFC deigns for both stationary and moving applications. One significant problem associated with stainless steel is the tendency to form an oxide scale at high temperature, which is enhanced in oxidising environments (i.e. at the cathode). The oxide scale is a poor conductor and is prone to spalling and cracking during long term operation [24]. Commercially available ferritic stainless steels (Avesta, Sheffield) were heated at 700°C for 5000 hours in air [37]. A steel containing 17%Cr stabilised with Ti and Nb was found to have acceptable levels of oxidation.

3.5. Designs of a SOFC

There are currently 2 main designs of SOFC stacks, each has its own particular advantages and disadvantages. As SOFC technology is in the primary stages of commercialisation, designs that will eventually by economically successful are far from clear. Brief summaries are as follows;

3.5.1. Tubular Design

Among the different SOFC designs under development, the Siemens-Westinghouse (S-W) sealless tubular design, introduced in 1980, is recognised as the design that is closest to commercialisation [38]. This design incorporates a YSZ electrolyte that operates at approximately 1000°C. Specifically targeting the stationary >100kW power market, S-W are currently testing a 200kW SOFC/50kW micro-turbine system [39]. The S-W SOFC stack is assembled from a number of tubes, each being a single cell, which comprise the cell components. Each tube, typically 0.5-1.5m in length, is sealed at one end (Figure 3.5).

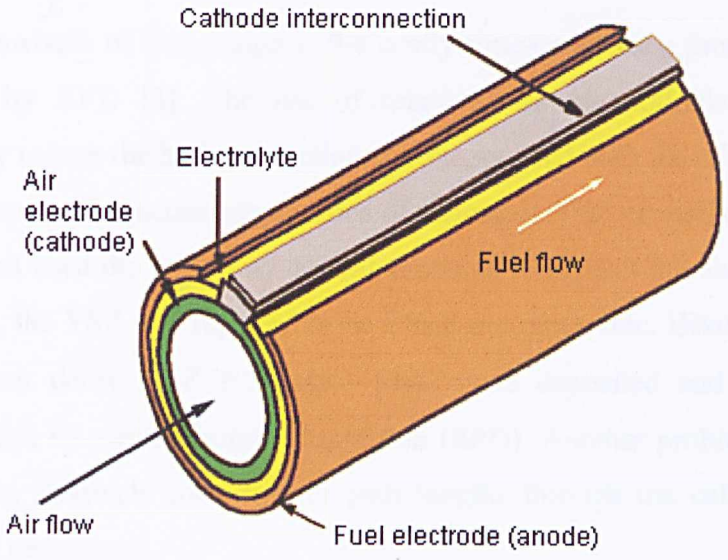


Figure 3.5 The Siemens-Westinghouse tubular SOFC [40].

An extrusion sintered porous cathode of LSM acts as the support. A 40μm dense layer of YSZ electrolyte is applied on top of the cathode by electrochemical vapour deposition (EVD), except for a strip along the active cell length. A gas tight interconnect layer, typically MgO doped $LaCrO_3$, is applied by plasma spraying onto the exposed cathode and sintered. The final step involves deposition of the Ni/YSZ

anode onto the electrolyte by slurry coating and final sintering. The oxidant flows into the tube whilst fuel gas is passed on the outside from the closed end to the open end. Depleted fuel and oxidant gases are combusted at the exhaust; heat is conserved and used to heat incoming gases.

Electrical connections are made on the anode side of each tube, this allows the use of low cost metals for cell to cell contacts and current collectors. Each tube is connected in series to others and forms a 'bundle' arrangement. Nickel felt connects the anode of one cell to the nickel plating on the interconnect of the next for series connection and the anode of one cell to the anode of the adjacent cell for parallel connection. The felt also acts to minimise stress on the stack during operation [1].

A significant advantage of the S-W tubular SOFC design is the absence of any high temperature sealants due to its closed end design. As the design is relatively flexible, any difference between thermal expansion coefficients of the different components can be designed into the cell and reduce the likelihood of mechanical failure. Other advantages include the relatively easy connection of the cells to form a stack, the integration of a high temperature heat exchanger and the absence of gas tight seals.

A major drawback of this design is the costly time-consuming fabrication of the YSZ electrolyte by EVD [3]. The use of relatively simple colloidal techniques could significantly reduce the high production costs associated with the tubular design. Swartz et al. [41] prepared aqueous suspensions of nanoscale YSZ crystallites by hydrothermal synthesis and used dip and spray coating methods to deposit the electrolyte onto LSM. After firing, the YSZ was reported to be dense and crack free. Basu et al. [42] reported that 10-50μm dense YSZ electrolyte films were deposited and fired onto porous $LaMnO_3$ tubes by electrophoretic deposition (EPD). Another problem with the tubular design is the relatively long current path lengths through the cell, resulting in high internal cell resistances.

3.5.2. Planar Design

The planar design, often termed 'flat-plate', can be produced by relatively cheap techniques such as tape casting, calendering and screen printing [5, 6 ,43 ,44 ,45]. It is

thus not surprising that most academic research groups, when testing new materials, use this design to evaluate the performance of new materials.

The electrolyte is either sintered and then co-sintered with the electrodes or can be sintered with both electrodes as green bodies in one step. The latter option being the ideal scenario as production costs are kept to a minimum. As the different materials at different rates this can introduce warping and cracking because of the large internal stresses that are generated [46]. Much care and attention is thus required in selecting materials and firing schedules. The interconnect, grooved to allow gas flow, is fabricated separately by either hot pressing or tape casting [2]. Components are stacked up on each other and connected in series, as depicted in figure 3.6.

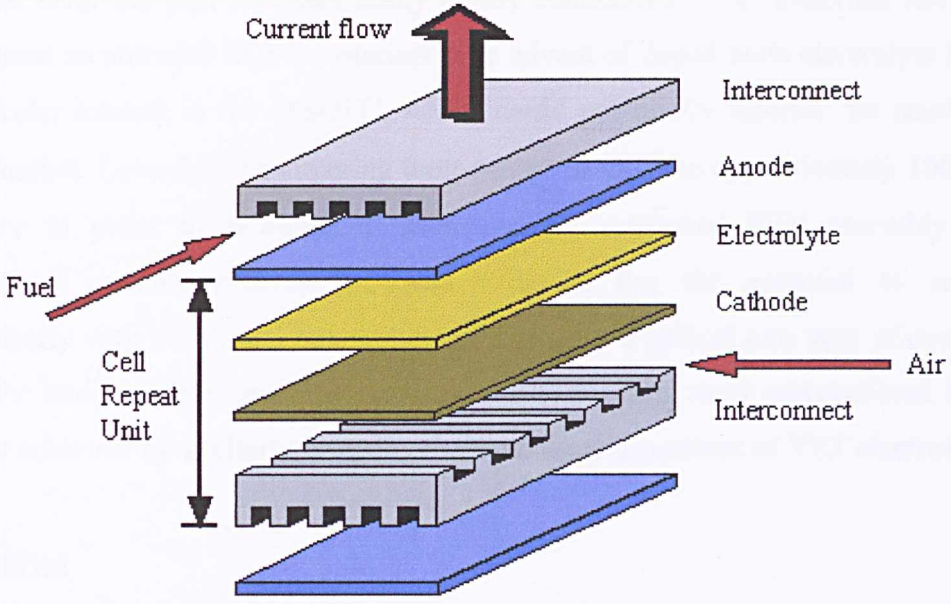


Figure 3.6 The SOFC planar design.

Advantages of this design are potential economic gains from the use of relatively simple, cheap and well practised ceramic fabrication routes. The design also allows much higher power densities than the tubular design, as internal losses are independent of cell area.

A drawback of this design is the need for high temperature gas seals at the edge of the plates. The planar design is also more susceptible to thermal and mechanical stresses compared to the tubular design. Atkinson [20, 47] comments on the difficulty in comparing strength values of flat plate ceramic components when processed by different methods. Results, for tape cast samples, indicate that flexural strength of YSZ decreases with increasing temperature. The effects of chemically induced stresses in

ionic conductors when subjected to a gradient in the thermodynamic activity of oxygen were also investigated. In doped ceria electrolytes, Ce^{4+} is reduced to Ce^{3+} at low oxygen partial pressures which increases the lattice parameter. The structure is thus subject to a differential strain across its thickness that can result in mechanical failure. It is predicted that the maximum 'safe' operating temperature that prevents failure of CGO20 is below 750°C. The advantages (and disadvantages) of the planar design thus make it subject to much interest from developers of the ITSOFC.

3.6. Summary

The SOFC is a highly efficient device that produces power by means of electrochemical reactions. Over the past 20 years many highly conducting novel materials have been investigated as potential SOFC materials. The advent of doped ceria electrolyte has led to particular interest in the ITSOFC, which could potentially saturate the small-scale power market. Lowering the sintering temperature of CGO to approximately 1000°C is necessary in order to fabricate a stainless steel supported PEN assembly using conventional ceramic processing. Such a device has the potential to compete economically with traditional power sources and offer a radical new way of supplying power for many applications. Cost reduction in fabricating more conventional SOFCs could be achieved by similarly lowering the sintering temperature of YSZ electrolytes.

References

1. Science and Technology of Fuel Cells. N.Q.Minh and T.Takahashi. Elsevier Press, 1995.
2. J.M.Ralph. Ph.D. Thesis. University of London, 1998.
3. B.C.H.Steele. J.Mater.Sci. **36**, (2001), 1053.
4. S.C.Singhal. Proc. of the 6th International Symposium on SOFC's. Eds. S.C.Singhal and M.Dokiya. The Electrochem.Soc. (1999), 39.
5. W.Schäfer, A.Koch, U.Herold-Schmidt and D.Stolten. Solid State Ionics. **86-88**, (1996), 1235.
6. M.Sahibzada, B.C.H.Steele, D.Barth, R.A.Rudkin and I.S.Metcalfe. Fuel. **78**, (1999), 639.
7. M.Liu and Z.Wu. Solid State Ionics. **107**, (1998), 105.
8. J.Van herle, R.Ihringer, N.M.Sammes, G.Tompsett, K.Kendall, K.Yamada, C.Wen,

T.Kawada, M.Ihara and J.Mizusaki. Solid State Ionics. **132**, (2000), 333.

9. B.C.H.Steele. Solid State Ionics. **129**, (2000), 95.
10. B.C.H.Steele. Proc. 1st European SOFC Forum. Ed. U.Bossel. (1994), 375.
11. S.De Souza, S.J.Visco and L.C.De Jonghe. Solid State Ionics. **98**, (1997), 57.
12. T.Ishihara. H.Matsuda and Y.Takita. J.Am.Chem.Soc. **116**, 9, (1994), 3801.
13. T.Ishihara, T.Shibayama, H.Nishiguchi and Y.Takita. J.Mater.Sci. **36**, (2001), 1125.
14. S.Takai, T.Kobayashi and T.Esaka. Solid State Ionics. **113-115**, (1998), 653.
15. M.J.Verkerk and A.J.Burggraaf. J.Electrochem.Soc. **128**, 1, (1981), 75.
16. T.Takahashi, T.Esaka and H.Iwahara. J.Appl.Electrochem. **7**, (1977), 303.
17. T.Inoue, T.Setoguchi, K.Eguchi and H.Arai. Solid State Ionics. **35**, (1989), 285.
18. H.Yahiro, Y.Baba, K.Eguchi and A.Arai. J.Electrochem.Soc. **135**, 8 (1988), 2077.
19. E.D.Wachsman, P.Jayaweera, N.Jiang, D.M.Lowe and B.G.Pound. J.Electrochem.Soc. **144**, 1, (1997), 233-236.
20. A.Atkinson and A.Selçuk. Solid State Ionics. **134**, (2000), 59.
21. D.W.Dees, T.D.Claar, T.E.Easler, D.C.Fee and F.C.Mrazek. J.Electrochem.Soc. **134**, 9, (1987), 2141.
22. B.C.H.Steele. Solid State Ionics. **86-88**, (1996), 1223.
23. B.C.H.Steele. Solid State Ionics. **134**, (2000), 3.
24. J.M.Ralph, A.C.Schoeler and M.Krumpelt. J.Mater.Sci. **36**, (2001), 1161.
25. J.A.Kilner. Bol.Soc.Esp.Cerám.Vidrio. **37**, 2-3, (1998), 247.
26. S.J.Skinner. J.Inorganic Materials. **3**, (2001), 113.
27. T.Inoue, K.Eguchi and H.Arai. Solid State Ionics. **40-41**, 1, (1990), 407.
28. Y.Sakaki, Y.Takeda, A.Kato, N.Imanishi, O.Yanamoto, M.Hattori, M.Iio, and Y. Esaki. Solid State Ionics. **118**, (1999), 187.
29. G.C.H.Kostogloudis and C.H.Ftikos. J.Eur.Ceram.Soc. **19**, (1999), 497.
30. S.B.Adler. Solid State Ionics. **111**, (1998), 125.
31. H.Taimatsu, K.Wada and H.Kanedo. J.Am.Ceram.Soc. **75**, 2, (1992), 401.
32. M.Godickemeier, K.Sasaki, L.J.Gauckler and I.Reiss. Solid State Ionics. **86-88**, (1996), 691.
33. J.M.Bae and B.C.H.Steele. Solid State Ionics. **106**, (1998), 247.
34. V.Dusastre and J.A.Kilner. To be published.
35. T.Ishihara, M.Honda, T.Shibayama, H.Minami, H.Nishiguchi and Y.Takita J.Electrochem.Soc. **145**, 9, (1998), 3177.
36. K.S.Mazzdiyasni, C.T.Lynch and J.S.Smith. J.Am.Ceram.Soc. **50**, (1967), 532.

37. D.Dulieu, J.Cotton, H.Greiner, K.Honegger, A.Scholten, M.Christie and T.Seguelong. Proc. 3rd European SOFC Forum. Ed. P.Stevens. (1998), 447.

38. S.C.Singhal. Proc. of the 5th International Symposium on SOFC's. Eds. U.Stimming, S.C.Singhal, H.Tagawa and W.Lehnert. The Electrochem.Soc. (1993), 37.

39. R.A.George. J.Power.Sources. **86**, (2000), 134.

40. http://www.siemens.dk/

41. S.L.Swartz, M.M.Seabaugh and W.J.Dawson. Proc. of the 6th International Symposium on SOFC's. Eds. S.C.Singhal and M.Dokiya. The Electrochem.Soc. (1999), 135.

42. R.N.Basu, C.A.Randall and M.J.Mayo. J.Am.Ceram. Soc. **84**, 1, (2001), 33.

43. G.Lindemann, H.Böder and H.Geier. Industrial Ceramics. **18**, 2, (1998), 99.

44. R.Doshi, V.L.Richards, J.D.Carter, X.Wang and M.Krumpelt. J.Electrochem.Soc. **146**, 4, (1999), 1273.

45. M.Sahibzada, B.C.H.Steele, K.Hellgardt, D.Barth, A.Effendi, D.Mantzavinos and I.S.Metcalfe. Chemical Engineering Science. **55**, (2000), 3077.

46. H.Ohrui, T.Matsushima and T.Hirai. J.Power Sources. **71**, (1998), 185.

47. A.Atkinson. Solid State Ionics. **95**, (1997), 249.

Chapter 4 – Properties of Doped Ceria and YSZ

4.1. Introduction

Over the past twenty years there has been considerable amount of literature published on zirconia and ceria based ionic conductors. Ultimately, the most important property of the electrolyte is its ability to effectively conduct oxygen ions with negligible electronic conductivity. The aim of this chapter, with particular emphasis on Gd doped ceria, is to briefly review the key factors affecting the ionic and electronic conductivity of these materials. Many of these issues are also of fundamental importance to the sintering process, which is the basis of this thesis. The following are comprehensive reviews on the properties of zirconia [1] and ceria-based [2, 3, 4, 5] electrolytes.

4.2. Defect Types

In an ideal crystal structure, ionic conduction is not possible, as all the atoms are tightly bonded and are not free to migrate. In real crystals and ceramics, however, structural imperfections known as defects control the rate at which matter is transported through the solid state and therefore determine a number of properties. The different types of structural defects can be classified into three groups: (i) point defects, (ii) line defects and (iii) planar defects. Point defects are missing atoms (vacancies), interstitial atoms occupying the interstices between atoms and substitutional atoms on sites that would normally be occupied by another type of atom. Line defects are characterised by displacements in the periodic structure of the lattice in certain directions and planar defects consist of stacking faults, internal interfaces and free surfaces [6]. Even though both line and planar defects significantly affect the properties of a ceramic material, it is the exploitation and manipulation of point defects that enable some ceramics to have excellent ionic conductivity.

In a pure compound (MO), intrinsic point defects can be introduced into the lattice by two relatively simple ways in order to maintain stoichiometry of the crystal. The first of these is known as the Schottky defect and is caused by the transfer of a cation and an

anion from their regular lattice sites to an external surface, leaving behind vacancies (standard Kröger-Vink notation is used throughout).

$$\text{null} \leftrightarrow V_M'' + V_O^{\cdot\cdot} \tag{4.1}$$

The second type is known as Frenkel disorder, which involves the formation of interstitial species. A cation leaves its regular lattice site and occupies an interstitial site, leaving behind a vacancy. Conversely if the anion forms an interstitial, this is known as an anti-Frenkel pair.

$$O_O^X \leftrightarrow O_i'' + V_O^{\cdot\cdot} \tag{4.2}$$

Concentrations of Schottky and Frenkel defects are highly temperature dependent, it is only near the melting point when a significant number of these defects are generated. It is generally accepted that oxygen vacancy formation occurs, as opposed to oxygen interstials, in non-stoichiometric CeO_2 together with electronic defects by partial reduction [2].

$$O_O^X \leftrightarrow V_O^{\cdot\cdot} + 2e' + \tfrac{1}{2}O_2 \tag{4.3}$$

In order to have a sufficient quantity of oxygen vacancies at fuel cell operating temperatures ceria is doped with aliovalent cations. The defect reactions for ceria doped with a cation with an effective 2+ charge can be written as:

$$MO \xrightarrow{CeO_2} M_{Ce}'' + V_O^{\cdot\cdot} + O_O^X \tag{4.4}$$

For dopants with an effective 3+ charge, the reaction can be written as:

$$M_2O_3 \xrightarrow{CeO_2} 2M_{Ce}' + V_O^{\cdot\cdot} + 3O_O^X \tag{4.5}$$

For dopants with an effective 5+ charge, the reaction can be written as:

$$M_2O_5 \xrightarrow{CeO_2} 2M_{Ce}^{\cdot} + 2e' + 4O_O^X + \frac{1}{2}O_2 \tag{4.6}$$

But this does not create oxygen vacancies. An alternative is;

$$M_2O_5 \xrightarrow{CeO_2} 2M_{Ce}^{\cdot} + 4O_O^X + O_i'' \tag{4.7}$$

But the energy for this reaction is thought to be prohibitively large [7]. Thus oxygen ion conductivity is generated by divalent and trivalent cation doping to produce oxygen vacancies. Similar reactions are possible in zirconia, although the reduction reaction has significantly higher energy.

4.3. Defect Association

It is assumed that at very low dopant concentrations, the defects are free to move within the lattice and not interact with other defects. However, the lower valent cations and the oxygen vacancies have opposite effective charge and so are attracted to each other. As dopant concentration increases, more defects are created and they begin to form bound pairs or larger clusters. It is generally accepted that simple associates of a single substitutional dopant cation to an oxygen vacancy are dominant. The formation of associates is significant because it reduces the ionic conductivity of the material. Thus a common trend observed in YSZ and doped ceria electrolytes is an almost linear increase in ionic conductivity as dopant concentration increases until a maximum is reached, after which the conductivity decreases. Initially, addition of dopant results in the creation of extra oxygen vacancies, a maximum occurs due to the increase in associates that reduces the number of free oxygen vacancies. Above this maximum, increased doping results in the formation of more complex associates that reduce the ionic conductivity despite the higher concentration of oxygen vacancies.

4.4. Lattice Ionic Conductivity of Doped Ceria

The ionic (or electronic) conductivity (σ) for a given temperature (T) for an electrolyte is usually represented by the following equation:

$$\sigma T = A\exp(-\Delta E_a/kT) \qquad (4.8)$$

where A is the pre-exponential term and ΔE_a is the activation energy. ΔE_a being equal to the sum of the enthalpy of motion (ΔH_m) and association (ΔH_a) of an oxygen vacancy. It has been found that this value depends strongly on the type of associate formed and the energy that binds the defects together [2]. There are two main contributions to the enthalpy of association. First is the coulombic interaction between the dopant cation and oxygen vacancy and second is the reduction of the elastic strain in the lattice caused by

the individual defects. The migration enthalpy in the fluorite structured oxides is very similar (CeO_2 = 0.61eV, ZrO_2 = 0.68eV) [5]. It thus follows that to maximise the ionic conductivity, ΔH_a must be kept to a minimum. The value of ΔH_a is strongly related to the ionic radii of the dopant ion.

Kim [8] studied the effect of ionic radii and valence of the dopant on the ionic conductivity of ceria. It was shown that elastic strain on the host lattice is minimised, when the dopant cation has an ionic radius that is slightly larger than the host. Of the divalent and trivalent dopant additions to ceria, Ca^{2+} and Gd^{3+} most closely match this requirement. Minervini et al. [9] used atomistic simulation based on energy minimisation techniques to study the energetics associated with M_2O_3 solution in CeO_2. Results indicate that charged defects are attracted to one another, and exhibit binding energies which are strong functions of dopant size. Both coulombic attraction and crystallographic relaxation effects control the atomic arrangement of the defects in the cluster. The dopant that exhibits the lowest binding energy and thus highest ionic conductivity in ceria is Gd^{3+}. It is now generally regarded that of all aliovalent dopants, Gd minimises structural disturbance of the ceria lattice and has the highest electrical conductivity. It is acknowledged that Sm is an effective dopant of ceria due to a similar ionic radius [10]. Zhan concluded that the optimum composition, in terms of total electrical conductivity, of Sm doped ceria to be $Ce_{0.8}Sm_{0.2}O_{1.9}$ [11]. It should be noted that the thermal expansion of $Ce_{0.8}Sm_{0.2}O_{1.9}$ is $11.4x10^{-6}K^{-1}$ [12] whilst the thermal expansion coefficient of Gd doped ceria (10-20mol%) is $12.5x10^{-6}K^{-1}$ [13], thus making Gd doped ceria mechanical more compatible with ferritic stainless steel.

It is accepted that the optimum Gd dopant level in ceria is between 10-20mol%. Steele [3] reviewed published literature and concluded that 10mol%Gd doping of ceria gave a better electrolyte than 20mol%Gd doped ceria. Researchers have commented on the better resistance to reduction of CGO compared to CGO20 at reduced oxygen partial pressures below 900°C [14, 15]. Wang et al. [16], however, compared the electrical performance of CGO and CGO20 and concluded that the latter material had slightly enhanced conductivity at ITSOFC operating temperatures. Ralph [5] compared the ionic conductivity of ceria as a function of Gd content and claimed 11mol% to be the optimum dopant level. Ralph also managed to exactly match the host ionic radii by co-doping Sm with Y, with the composition $CeO_{0.94}SmO_{0.04}Y_{0.02}$. The association enthalpy was reduced to below 0.1eV which resulted in a small enhanced conductivity below

350°C. As defects have dissociated at fuel cell operating temperatures, there was no reported increase in conductivity compared to Gd doped ceria of similar composition.

4.5. Ionic Conductivity in Doped Zirconia

The stabilisation of zirconia by the addition of dopants into the tetragonal or cubic fluorite structure at room temperature is well known. The addition of these aliovalent cations, in accordance with equations 4.1, 4.2 and 4.3 introduce charged defects into the structure that make doped zirconia an attractive material. Generally, dopants are added such that the fully stabilised (cubic) structure exists and thus avoid any problems that may arise from phase transformation in the partially stabilised (tetragonal) structure [17].

As previously mentioned for doped ceria, maximum ionic conductivity is established when the dopant ionic radii is slightly larger than the host. It is for this reason that Sc (0.87Å) is considered the best trivalent dopant at enhancing the ionic conductivity of Zr (0.84Å) [18]. Due to the availability and expense of Sc however, Y^{3+} (1.02Å) is generally selected. The optimal dopant level of Y_2O_3 in zirconia is ~8mol% [19].

4.6. Grain Boundary Ionic Conductivity of Doped Ceria and YSZ

The grain boundary conductivity discussed in this thesis is defined as "the reciprocal of the grain boundary contribution to the resistivity of a polycrystalline material". Often quoted in the literature is the specific grain boundary conductivity (σ_{sgb}) that corresponds to the conventional conductivity of a grain boundary considered as a homogeneous material of thickness, δ_{gb}. This is expressed as follows;

$$\sigma_{sgb} = \frac{\delta_{gb}\ \sigma_{tgb}}{d} \qquad (4.9)$$

where d is the grain size and it is assumed the grains are cubic and of equal size. Furthermore, it is assumed that there is a negligible contribution of conduction parallel to the grain boundary to the total conductivity (σ_{tgb}).

The deleterious effects of impurity grain boundary phases on the performance of ceramic electrolytes have been known for many decades. In order to minimise the large

elastic strain in the bulk, due to a mismatch in the ionic radii of the host and impurities, impurities segregate to the grain boundary. Thus the concentration of impurities at the grain boundary is considerably greater than in the lattice. The most common starting impurities detected in both powder and sintered doped ceria are Si, Ca, Na, Mg, K, Al and Fe. All these cations readily form oxides in the presence of oxygen and thus it must be concluded that all these oxides are present in the ceria [5]. Much data have been presented over the past two decades concerning the grain boundary conductivity of doped ceria. The author believes that much of the data are not representative of intrinsic behaviour due to the poor grade commercial powder that was available at the time. The transport processes taking place at the grain boundary are still far from understood due to the complex interaction of the trace impurities in a highly disordered region.

Of all the impurities present in the starting powder, silica is considered to have the most deleterious effects on the ionic conductivity at the grain boundary. Ralph [5] prepared samples of high purity CGO and CGO with deliberate silica 'impurity' additions. At 500°C no discrete grain boundary phase was detected in the clean samples, whilst in the silica doped samples grain boundary conductivity was considerably lower than the lattice conductivity up to 1000°C. Even in high purity powder, silica contamination present at the grain boundaries can reduce the grain boundary conductivity by orders of magnitude [20]. The addition of alumina to 8YSZ powder forms a non-wetting glassy phase with the silica impurities that enhances the total conductivity, the slight decrease in the lattice conductivity is compensated for by a large increase in the grain boundary conductivity [21, 22]. Steele [3] strongly recommends the use of clean powders (SiO_2<50ppm) in order to maximise grain boundary conductivity. These are now commercially available from suppliers such as Rhodia and Praxair.

The specific grain boundary resistivity of high purity CGO (SiO_2<50ppm) is still a couple of orders of magnitude greater than the lattice [5]. Similar observations were reported for high purity YSZ [20]. It has been proposed that the presence of a space-charge region at the grain boundary hinders the mass transport of vacancies across it and gives rise to the high specific resistivity of even "clean" grain boundaries.

Scanlon et al. [23] studied the surface composition of sintered specimens made from high purity CGO20 powder using XPS. The Ce/Gd ratio changes from 1 at the outermost surface to 4.2 in the bulk for samples sintered at 1300-1600°C. Similar

observations have been reported by others [7, 24]. The higher Gd concentration at the grain boundary would result in a lower conductivity because both Gd_2O_3 and highly doped ceria (>30mol%) are poor ionic conductors. Ohashi et al. [25] studied the local structures around Ce and Gd atoms in $Ce_{1-x}Gd_xO_{2-x/2}$ (x=0-0.30) by extended X-ray absorption fine structure spectrometry (EXAFS). Oxygen vacancies introduced into the ceria lattice (Equation 4.5) were located around both the Ce and Gd cations. As dopant concentration increased the interatomic distances of Ce-O and Gd-O decreased due to the oxygen ions surrounding the oxygen vacancies relaxing towards their adjacent vacancy. Any alteration in the defect structure as a function of sintering temperature has severe implications for both the ionic conductivity and the sintering process itself.

It should be noted that not all impurities and or dopants are detrimental to grain boundary conductivity of Gd doped ceria. Ralph [5] found that the grain boundary conductivity of $Ce_{0.9}Gd_{0.09}Ca_{0.01}O_{2-X}$ was approximately an order of magnitude higher than for CGO. Moure [26] and Eguchi [27] reported similar observations. The addition of 1%TiO_2 enhanced the grain boundary conductivity of CGO probably due to the presence of the pyrochlore $Gd_2Ti_2O_7$ phase, which is considered to be a good ionically conducting material. The presence of this phase redistributed silica to the triple points of the grain boundaries, further aiding the grain boundary conductivity. A slight increase in the lattice conductivity was likewise observed [28].

4.7. Effect of Grain Size on the Grain Boundary Ionic Conductivity

Badwal and Drennan [29] measured ionic conductivity as a function of grain size of 10YSZ. The lattice conductivity remained largely unaffected by any change in grain size. The grain boundary conductivity, however, was found to increase with increasing grain size. It was claimed that below 1400°C, impurities were present at the interface between grains. When the sintering temperature was >1400°C (resulting in significant grain growth) the impurity phase becomes less viscous (or liquid) and is squeezed into the triple points resulting in a "cleaner" grain boundary that has more grain to grain contact and thus enhanced specific grain boundary conductivity. It was noted, however, that the specific grain boundary conductivity for sub-micron grains was much greater than that of larger grains. Similar observations were recently reported by Kharton et al. for CGO [14].

Aoki et al. [30] studied the grain boundary conductivity as a function of grain size for 'clean' CaO doped YSZ (<80 ppm). The concentration of segregated silica increased at the grain boundaries as a function of grain size up to 4μm. Above this grain size, the silica content remained fixed at a coverage of approximately 1 monolayer thickness. Results further suggested that the segregation of Ca was linked to the segregation of Si up to a grain size of 4μm. For grains larger than 4μm, the total grain boundary conductivity increased as a function of grain size due to a decrease in the number of grain boundaries in series. As previously reported by Badwal and Drennan [29], the specific grain boundary conductivity was reportedly much higher in small grains. Similar observations were reported by Christie and Berkel [31] for studies on the effect of grain size on the conductivity of CGO20.

4.8. Electronic Conductivity in Doped Ceria

It is well known that the tendency of the cerium ion to reduce from Ce^{4+} to Ce^{3+} is the biggest disadvantage of this material for SOFC applications. Introducing electronic carriers into the electrolyte reduces both the electrical efficiency and mechanical stability. At 700°C, CGO and CGO20 change from predominately ionic to electronic conductivity at approximately $pO_2 = 10^{-20}$atm [4]. The electrolytic domain was found to increase in CGO20 with small additions of YSZ (1-5mol%) which increased the ionic domain from $pO_2 = 10^{-15}$ to 10^{-17}atm at 800°C [32].

Mogensen [33] argues that oxygen vacancies introduced through doping suppress the number of oxygen vacancies from the reduction of ceria. The reaction in equation 4.3 is driven further to the left as the dopant concentration increases, resulting in a lower electronic conductivity. Maricle [34] claimed that co-doping CGO with small quantities of Pr_6O_{11} induced electron trapping and significantly extended the ionic domain at 800°C. The Pr^{4+} 'electron trapping' cation was believed to reduce at a slightly higher potential than the cerium ion. The effective positive charge on the dopant attracts electrons, which reduces the dopant, trapping electrons and lowering their mobility. Measurements of the grain boundary and lattice conductivities suggest that an overall increase in conductivity was a result of the Pr addition lowering the grain boundary resistivity. Steele [3], however, claims that no redox reactions of the Pr ion occur and that any increase in ionic conductivity is due to grain boundary effects.

4.9. Summary

The careful addition of aliovalent dopants introduce charge compensating oxygen vacancies into the structure of ceria and zirconia that enhance the oxygen ion conductivity. It is generally considered that additions of Sm and Gd maximise the ionic conductivity due to minimised structural disruption. The presence of starting impurities has received considerable interest amongst the SOFC fraternity due to the deleterious effects on the grain boundary electrical properties. The role of these complex interactions is far from understood. Finally, the main drawback associated with doped ceria electrolyte is the reduction of the cerium 4+ cation concentration at low oxygen partial pressures which generates n-type electronic conduction and lowers the efficiency of the cell.

References

1. Science and Technology of Fuel Cells. N.Q.Minh and T.Takahashi. Elsevier Press, 1995.
2. M.Mogensen, N.M.Sammes and G.A.Tompsett. Solis State Ionics. **129**, (2000), 63.
3. B.C.H.Steele. Solid State Ionics. **129**, (2000), 95.
4. V.V.Kharton, F.M.Figueiredo, L.Navarro, E.N.Naumovich, A.V.Kovalevsky, A.A. Yaremchenko, A.P.Viskup, A.Carneiro, F.M.B.Marques and J.R.Frade. To be published.
5. J.M.Ralph. Ph.D. Thesis. University of London, 1998.
6. Ceramic Processing and Sintering. M.N.Rahaman. Marcel Dekker, 1995.
7. E.Ramirez-Cabrera. Ph.D. Thesis. University of London, 2001.
8. D-J.Kim. J.Am.Ceram.Soc. **72**, 8, (1989), 1415.
9. L.Minervini, M.O.Zacate and R.W.Grimes. Solid State Ionics. **116**, (1999), 339.
10. H.Yahiro, Y.Eguchi, K.Eguchi and H.Arai. J.Appl.Electrochem. **18**, (1988), 527.
11. Z.Zhan, T-L.Wen, H.Tu and Z-Y.Lu. J.Electrochem.Soc. **148**, 5, (2001), A427.
12. S.Sameshima, T.Ichikawa, M.Kawaminami and Y.Hirata. Materials Chemistry and Physics. **61**, (1999), 31.
13. H.Hayashi, M.Kanoh, C-J.Quan, H.Inaba, S.Wang, M.Dokiya and H.Tagawa. Solid State Ionics. **132**, (2000), 227.
14. V.V.Kharton, F.M.Figueiredo, L.Navarro, E.N.Naumovich, A.V.Kovalevsky, A.A.Yaremchenko, A.P.Viskup, A.Carneiro, F.M.B.Marques and J.R.Frade.

J.Mater.Sci. **36**, (2001), 1105.

15. L.Navarro, F.Marques and J.Frade. J.Electrochem.Soc. **144**, 1, (1997), 267.
16. S.Wang, T.Kobayashi, M.Dokiya and T.Hashimoto. J.Electrochem.Soc. **147**, 10, (2000), 3606.
17. N.Q.Minh. J.Am.Ceram.Soc. **76**, 3, (1993), 563.
18. M.O.Zacate, L.Minervini, D.J.Bradfield, R.W.Grimes and K.E.Sickafus. Solid State Ionics. **128**, (2000), 243.
19. M.Filal, C.Petot, M.Mokchah, C.Chateau and J.L.Carpentier. Solid State Ionics. **80**, (1995), 27.
20. X.Guo and J.Maier. J.Electrochem.Soc. **148**, 3, (2001), E121.
21. A.J.Feighery and J.T.S.Irvine. Solid State Ionics. **121**, (1999), 209.
22. A.Rizea, D.Chirlesan, F.Lacour-Laher, C.Petot and G.Petot-Ervas. To be published.
23. P.J.Scanlon, R.A.M.Bink, F.P.F.van Berkel, G.M.Christie, L.J.van Ijzendoorn, H.H.Brongersma and R.Gvan Welzenis. Solid State Ionics. **112**, (1998), 123.
24. P.Durán, C.Moure and J.R.Jurado. J.Mater.Sci. **29**, (1994), 1940.
25. T.Ohashi, S.Yamazaki, T.Tokunaga, Y.Arita, T.Matsui, T.Harami and K.Kobayashi. Solid State Ionics. 113-115, (1998), 559.
26. C.Moure, J.Tartaj, F.Capel and P.Duran. To be published.
27. K.Eguchi, T.Kunisaki and H.Arai. J.Am.Ceram.Soc. **69**, 11, (1986), 282.
28. J.R.Jurado. J.Mater.Sci. **36**, (2001), 1133.
29. S.P.S.Badwal and J.Drennan. J.Mater.Sci. **22**, (1987), 3231.
30. M.Aoki, Y-M.Chiang, I.Kosacki, L.J-R.Lee, H.Tuller and Y.Liu. J.Am.Ceram.Soc. **79**, 5, (1996), 1169.
31. G.M.Christie and F.P.F.van Berkel. Solid State Ionics. **83**, (1996), 17.
32. N.M.Sammes and Z.Cai. Solid State Ionics. **100**, (1997), 39.
33. M.Mogensen, T.Lindegaard, U.R.Hansen and G.Mogensen. J.Electrochem.Soc. **141**, 8, (1994), 2122.
34. D.L.Maricle, T.E.Swarr and S.Karavolis. Solid State Ionics. **52**, (1992), 173.

Chapter 5 – Fabrication of Electrolyte Films

5.1. Introduction

The components within each PEN structure consist of thick films layered on top of each other. The fabrication route must economically produce films that are flat, have uniform thickness and not alter the properties of the material. At present, there are many fabrication routes available to ceramists to produce electrolyte films. These can be separated into two different categories; vapour-assisted routes and conventional ceramic processing routes. A comprehensive literature review on all the techniques is beyond the scope of this thesis, nevertheless the rest of this chapter will review the most commonly associated fabrication routes that have been used to produce YSZ and doped ceria films.

5.2. Chemical Vapour Deposition (CVD)

In the 1980's, CVD was investigated for fabricating thin films of YSZ [1]. Figure 5.1 illustrates the basic operation of the CVD process.

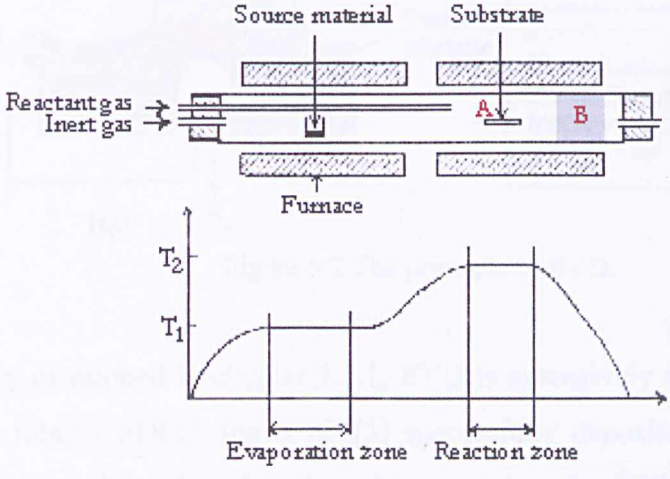


Figure 5.1 Basic CVD operation; (A) heterogeneous precipitation (B) homogeneous precipitation.

The precursor is initially evaporated and transported to the reaction chamber by a carrier gas. The reactions occur predominately by heterogeneous precipitation onto the substrate surface (e.g. cathode or anode support), and homogeneous precipitation in the gas phase, leading to the formation of particles which are detrimental to film formation

[2]. McAleese et al. [3, 4] conducted feasibility studies for producing CGO thin films by producing thin films of pure ceria and gadolinia on silicon wafers using CVD. The precursors for the ceria and gadolinia films were $Ce(fod)_4$ and $[\{Gd(tmhd)_3\}_2(tetraglyme)]$ respectively. For both systems, the evaporation and substrate temperatures were approximately 200°C and 300°C respectively. It was reported that the growth of the ceria films was very slow (3.5nm/min), highlighting the widely regarded fact that CVD is a slow and expensive technique.

5.3. Electrochemical Vapour Deposition (EVD)

EVD is a modified form of CVD that utilises an electrochemical potential gradient to grow thin, gas tight layers of either ionically or electronically conducting metal oxides on porous substrates. EVD is a two step process, the first involves pore closure by normal CVD type reaction between the reactant metal chlorides and water vapour. Once the pores are closed, film growth proceeds due to the presence of an electrochemical potential gradient across the deposited film. Oxygen ions diffuse through the thin film and react with metal chloride vapour to form a metal oxide product (Figure 5.2). Reactant concentration, reaction temperature and pressure control film growth.

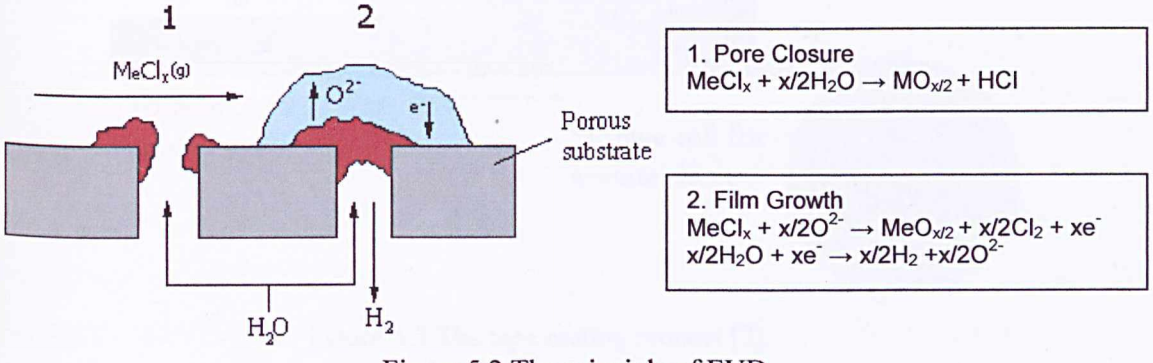


Figure 5.2 The principle of EVD.

As previously mentioned in chapter 3.5.1, EVD is extensively used to deposit films of YSZ for the tubular SOFC. Jue et al. [5] successfully deposited a thin film of dense ceria on a dense Y_2O_3 doped ceria substrate using the EVD process. By using a substrate of variable thickness they demonstrated that the kinetics of film deposition were controlled by oxygen ion diffusivity. It was commented that the EVD process would be an ideal technique to fabricate interlayers (section 3.4.1.4) between the electrolyte and electrodes.

5.4. Tape Casting

Tape casting is a relatively cheap, widely practised processing route for fabricating ceramic films. A ceramic powder is mixed with appropriate solvent and dispersant. After ball milling, the resulting slurry is mixed with a binder and plasticiser and further milled. The resulting slurry is then carefully bladed over a surface that has a removable plastic sheet (Figure 5.3). After drying, the tape is peeled off from the surface and cut to desired specifications. It is during this dying stage that the majority of the shrinkage occurs. Carefully controlled firing removes the organic additives and densifies the tape. The success of tape casting depends critically on the formulation of the slurry and the burnout of the organics. The solvent must be capable of dissolving all the organic additives in the system and have a fairly high vapour pressure to facilitate removal. The binder is typically of high molecular weight and has a low glass transition temperature to provide strength and flexibility to the dried tape.

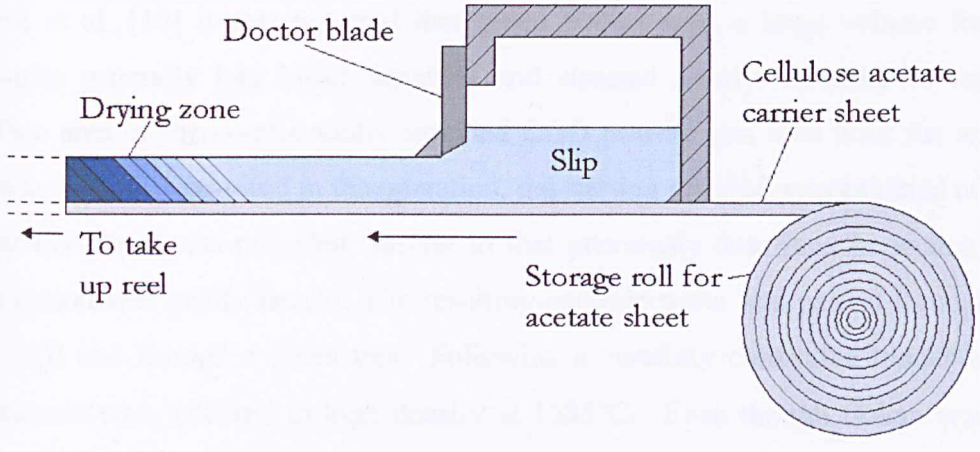


Figure 5.3 The tape casting process [2].

Herle [6] fabricated YSZ electrolytes via tape casting, hot pressing, vacuum plasma spraying and calendering. The electrolyte produced by the tape cast method had the best sinterability and ionic conductivity. The only significant drawback of the technique was the very slow heating cycle required to produce a non-warped sintered specimen. Similar observations on tape cast 9YSZ were reported by Lindemann [7]. Sahibzada et al. [8, 9] tape cast approximately 5-10μm of CGO onto one side of a Ni/YSZ anode disk. After densification of the CGO at 1400°C, a LSCF cathode layer was tape cast on top of the CGO and fired at 1280°C.

Ohrui et al. [10] successfully co-fired a LSM:8YSZ:Ni/YSZ PEN assembly by tape casting. Films were successfully layered on top of each other, fired to 360°C to burn out binders and fired to high density at 1300°C. It was reported that cracking and warping occurred in films that had higher binder content due to a greater shrinkage difference between components during the binder removal stage. By carefully controlling the binder additions and removal they demonstrated the flexibility of this technique for cheaply producing SOFCs.

5.5. Calendering

Calendering is comparable in principle to the tape casting process due to the similarity of slurry preparation. The main difference being an increased plasticiser and binder content, which gives the 'paste' a higher green strength that can be mechanically rolled into thin films prior to firing.

Őzkan [11] used this method to fabricate 200μm plates of CGO. In agreement with Ohrui et al. [10] it was reported that green bodies with a large volume fraction of organics generally had lower densities and sintered poorly. In order to reduce the surface area of the commercially supplied CGO powder and thus limit the amount of organic additives required in the operation, the starting material was calcined at 1100°C. After the slurry was prepared, similar to that previously described in section 5.4, the suspension was gently heated. The resulting ceramic paste was passed through a two-roll mill and formed a green tape. Following a carefully controlled binder burnt out specimens were sintered to high density at 1585°C. Even though Őzkan was able to produce dense films of CGO, the author feels that the technique would not be suitable for fabricating films at temperatures below 1000°C. The calcination of the starting powder is detrimental to the sintering process, as discussed in more depth in the next chapter.

5.6. Screen Printing

One of the simplest and least expensive techniques for producing doped ceria films is by screen-printing. The electrolyte powder is dispersed in an organic binder and forced through a screen onto a substrate of desired shape. The printed pattern is then dried and carefully heated to remove the organics. The green body can then be sintered to form a

film. Baumard [12] used this technique to produce flat films of ceria that were approximately 30μm in thickness. Schäfer et al. [13] used the screen printing process to fabricate all the components of the PEN arrangement: La(Ca)MnO_3:YSZ:Ni/YSZ.

5.7. Sol-Gel Fabricated Thin Films

Sol-gel processing has received much interest over the last 30 years as a technique that produces highly dense ceramics, which have excellent homogeneity at low sintering temperatures. A sol is a suspension of colloidal particles in a liquid or a solution of polymeric molecules. Typically, distilled water is added to a starting solution of metal alkoxides dissolved in alcohol. Controlling both temperature and pH promotes hydrolysis and condensation reactions that form polymeric inorganic chains. As chain development increases, the viscosity of the solution markedly decreases and a gel is eventually formed. The gel is carefully dried and sintered to high density at characteristically low temperatures. Water removal from the gel is the most time consuming and difficult step of the overall fabrication process. Drying the gel results in a large volume change that can result in mechanical failure of the material. Reducing the thickness of the gel decreases the risk of mechanical failure of the specimen.

Chen et al. [14] synthesised $(CeO_2)_{0.8}(SmO_{1.5})_{0.2}$ sol-gel films by a relatively simple and potentially inexpensive process. The technique involved the oxidation of ethylene glycol by nitric acid and metal ions. The formed oxalic acid reacts further with ethylene glycol to form the polyester, which chelates a homogenous distribution of the required metal cations. Distilled water, ethylene glycol and HNO_3 were added to reagent grade $Ce(NO_3)_3.6H_2O$ and $Sm(NO_3)_3.6H_2O$. The solution was heated to 80°C in order to evaporate the water and promote gelation. A conventional spin coating technique was used to form wet films on YSZ substrates, thicker films were made by multiple coatings (dried at 320°C). It was noted that the thickness of the deposited film increased with increasing viscosity of the solution and decreasing spinning speed and time. Highly viscous liquids, however, resulted in inhomogeneous films that had poor mechanical properties. It was reported that crack free films of 0.3μm thickness achieved high density when fired at 600°C.

Woodhead [15] produced highly dispersible ceria powders that had an average grain size of 100-200nm. The technique requires heating cerium (IV) oxide hydrate in the

presence of a deaggregating agent at 320°C to produce a nanocrystalline cerium oxide. The cerium oxide can be dispersed in distilled water to form a sol and applied to a substrate. After drying in air, the gel can fully densify at temperatures below 1000°C [16].

Czerwinski and Smeltzer [17] coated metal substrates with ceria by dipping the substrate into a high purity ceria sol. The coating gelled on the substrate was dried at room temperature for 20 hours prior to calcining at 300°C. Analysis revealed the existence of microcracks in coatings that were equal to or in excess of 100nm in thickness. Removal of the liquid creates large capillary forces that result in cracking and warping in the weak gel. The sol was reported to be fully crystalline at approximately 700°C and contained no connected porosity after annealing at 900°C for 50 hours. Xia et al. [18] report similar findings for 8YSZ coated NiYSZ.

As the CGO electrolyte is required to be ~15μm in thickness, the warping and cracking associated during the drying stage presents a major challenge for the sol-gel route.

5.8. Summary

Vapour deposition techniques are generally considered time consuming and expensive. It is for this reason that the ITSOFC developed at Imperial College seeks to use conventional ceramic processing routes. Literature suggests that producing thick films of electrolyte by sol-gel processing is not feasible. Tape casting and screen printing are techniques that could be used to produce thick films of dense electrolyte cheaply.

References

1. M.F.Carolan and J.N.Michaels. Solid State Ionics. **25**, (1987), 207.
2. Ceramic Processing and Sintering. M.N.Rahaman. Marcel Dekker, 1995.
3. J.McAleese, J.C.Plakatouras and B.C.H.Steele. Thin Solid Films. **280**, (1996), 152.
4. J.McAleese, J.C.Plakatouras and B.C.H.Steele. Thin Solid Films. **286**, (1996), 64
5. J-F.Jue, J.Jusko and A.V.Virkar. J.Electrochem.Soc. **139**, 9, (1992), 2458.
6. J.Van herle, T.Horita, T.Kawada, N.Sakai, H.Yokokawa and M.Dokiya. Ceramics International. **24**, (1998), 229.
7. G.Lindemann, H.Böder and H.Geier. Industrial Ceramics. **18**, 2, (1998), 99.

8. M.Sahibzada, B.C.H.Steele, D.Barth, R.A.Rudkin and I.S.Metcalfe. Fuel. **78**, (1999), 639.

9. M.Sahibzada, B.C.H.Steele, K.Hellgardt, D.Barth, A.Effendi, D.Mantzavinos and I.S.Metcalfe. Chemical Engineering Science. **55**, (2000), 3077.

10. H.Ohrui, T.Matsushima and T.Hirai. J.Power Sources. **71**, (1998), 185.

11. N.Őzkan and B.J.Briscoe. J.Mater.Res. **13**, 3, (1998), 665.

12. J.F.Baumard, C.Gault and A.Argoitia. J.of the Less-Common Metals. **127**, (1987), 125.

13. W.Schäfer, A.Koch, U.Herold-Schmidt and D.Stolten. Solid State Ionics. **86-88**, (1996), 1235.

14. C.C.Chen, M.M.Nasrallah and H.U.Anderson. J.Electrochem.Soc. **140**, 12, (1993), 3555.

15. J.L.Woodhead. U.S. Patent No. 4356106, (1981).

16. J.L.Woodhead. Private communications.

17. F.Czerwinski and W.W.Smeltzer. Oxidation of Metals. **40**, 5-6, (1993), 503.

18. C.Xia, S.Zha, W.Yang, R.Peng, D.Peng and G.Meng. Solid State Ionics. **133**, (2000), 287.

Chapter 6 – Sintering of SOFC Electrolytes

6.1. General Introduction

The term sintering can be defined as the process that turns a green powder compact into a dense microstructure made up of bonded grains. Arguably, sintering is one of the most complex areas of study for ceramicists. Over the past forty years different models have been presented in order to try and explain the microstructural evolution of a green body to a dense pore free article. It is out of the scope of this thesis to investigate the many competing processes that determine the ability of a system to sinter effectively. The aim of this chapter is to present the fundamental aspects of sintering that can be controlled so as to enhance the densification process.

As discussed in the previous chapter, conventional ceramic processing techniques are the preferred fabrication routes for the electrolyte in the planar ITSOFC design being developed at Imperial College. In order to lower the sintering temperature of the CGO electrolyte to 900-1000°C, there are two general approaches. The first is to improve the powder processing and preparation whilst the second is to add sintering aids. In many cases a combination of both methods is used to achieve the desired result. This chapter presents a discussion of the literature related to the low temperature sintering of CGO and related materials.

6.2. Powder Processing and Preparation

The characteristics of a powder, and thus its sinterability, depend strongly on the method used to prepare it. The main powder characteristics that influence sintering are: particle size, particle size distribution, particle shape, degree of agglomeration, chemical composition and purity [1]. The first half of this chapter will briefly review the stages of solid state sintering and the key factors effecting the densification of a powder. Finally, four powder preparation techniques used to synthesise ceria and related materials are reviewed.

6.2.1. Solid State Sintering

Polycrystalline ceramics sinter by the diffusional transport of matter along different paths. In an over simplification it can be considered that atoms move from regions of high chemical potential to regions of low chemical potential (i.e. down a chemical potential gradient). The chemical potential refers to the quantity $\partial G/\partial n_i$, which is the partial derivative of the free enthalpy with respect to the particle sort, i. The chemical potential, μ, is a measure of how much the free enthalpy (or the free energy) of a system changes (by dG_i) if you add or remove a number dn_i particles while keeping the number of the other particles (and temperature and pressure) constant:

$$dG_i = (\partial G/\partial n_i)dn_i \qquad (6.1)$$

The different possible transport mechanisms illustrated in figure 6.1 all lead to growth of necks between particles. Neck growth is responsible for the bonding of particles in the first stage of sintering and thus increases the strength of the consolidated powder. It must be noted however, that only mechanisms that have grain boundaries as sources of material result in densification. Mechanisms 4 and 5 remove matter from the grain boundaries to the pore whilst mechanism 6 from dislocations within the neck region.

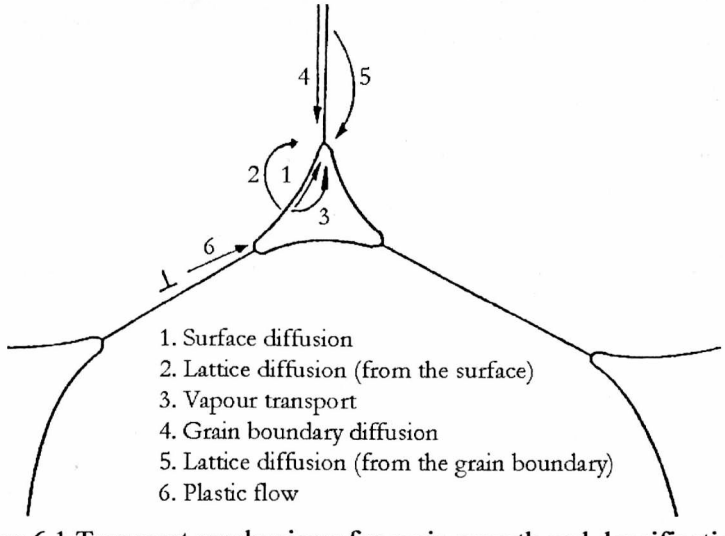


Figure 6.1 Transport mechanisms for grain growth and densification [1].

When a consolidated powder sample sinters there are three stages that occur prior to the densification of the article (Figure 6.2). In the initial stage, strong bonds and necks are formed at the contact points between particles. During the intermediate stage, the necks grow and the amount of porosity decreases rapidly, resulting in particles moving closer

together. Grain boundaries are formed at the necks and begin to move through the material. The intermediate stage is considered over when the open pore channels become isolated. In the final stage, where only a marginal density increase occurs, isolated pores are slowly eliminated. It is during this stage when grain growth becomes significant. As the densification process is nearly complete, the free energy of the system is lowered further by the reduction of the grain boundary area (i.e. grain growth). An electrolyte is acceptably dense when there is no connected porosity, this is typically achieved when the sample is >95% dense (i.e. high density).

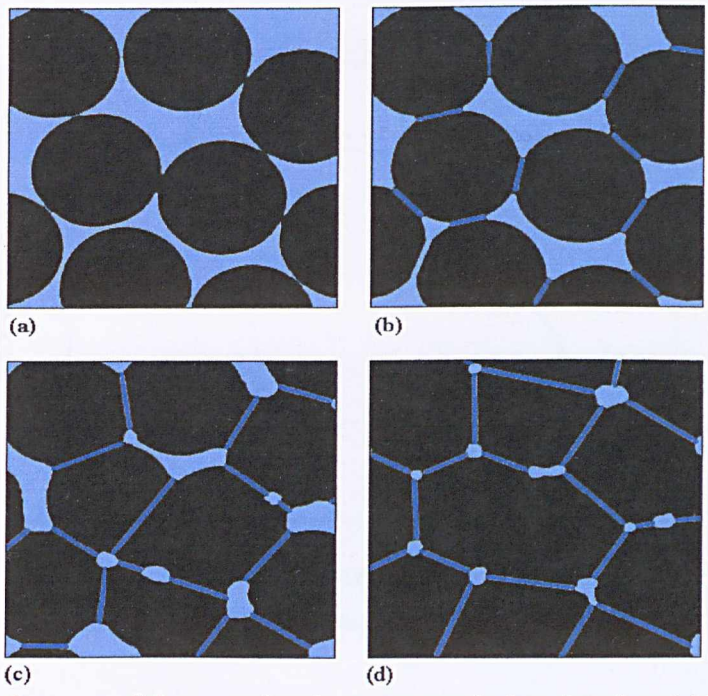


Figure 6.2 Development of the ceramic microstructure during sintering: (a) loose powder particles, (b) initial stage, (c) intermediate stage and (d) final stage [1].

6.2.2. The Driving Force for Sintering

As with all irreversible processes, sintering is accompanied by a lowering of the free energy of the system. Three factors influence the driving force for sintering a powder system, these are: curvature of the particle surface, applied external pressure on the powder body, and chemical reactions between particles at high temperature. The effect of particle curvature and thus size is controlled by the initial processing of the powder whilst the latter two factors are influenced during compaction and firing of the solid.

The molar surface free energy (E_s) associated with the size of particle radius (a), is related to the specific surface energy (γ_{sv}) and the molar volume (V_m) by;

$$E_s = 3\gamma_{sv}V_m/a \qquad (6.2)$$

A decrease in the particle radius increases the free energy of the system, thus enhancing the driving force for densification. This effect is well demonstrated by the sintering study of ceria performed by Inaba [2]. Compacted powder samples of different crystallite size were measured as a function of sintering temperature and time. It is shown in figure 6.3 that the finer particles densify at lower temperature due to the greater driving force associated with their larger surface area.

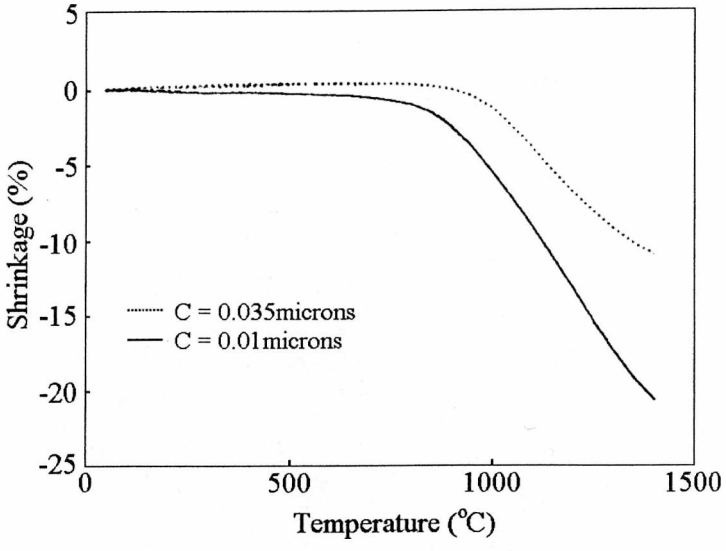


Figure 6.3 Effect of crystallite size (c) on the sintering profile of ceria [2].

Zhao and Harmer [3] proposed a model to describe the effect of pore size distribution on the final stage of sintering and predicted that increasing the number of pores per grain increased the densification rate, grain growth rate, and the ratio of relative densification rate/grain growth. In the comparative sintering study by Inaba [2], the finer ceria powder had an enhanced densification rate, grain growth rate, and ratio of relative densification rate/grain growth. It can thus be concluded that powder size strongly influences both aspects of sintering; densification and grain growth.

6.2.3. Factors Effecting Homogeneous Compaction

The simplest way to densify a powder material into a dense ceramic article is to consolidate the powder into a green body by an external force and fire at high temperature. Ceramists have long understood that effective particle packing of the green

body reduces the sintering temperature. The factors that most strongly influence powder packing are agglomeration, particle size and particle shape distribution.

In powder processing it is important to eliminate agglomerates as they reduce particle packing efficiency, suppress sintering activity and impair final properties due to the loss of microstructural homogeneity and crack like-void formation [4]. An agglomerate is a cluster of primary particles held together by surface forces, by liquid, or by a solid bridge (Figure 6.4). There are two types of agglomerates: soft and hard. Soft agglomerates are held together by fairly weak surface forces which can be overcome on compaction. Hard agglomerates, however, consist of primary particles that are chemically bonded. They are not broken down during compaction and can lead to incomplete densification and or strength limiting flaws.

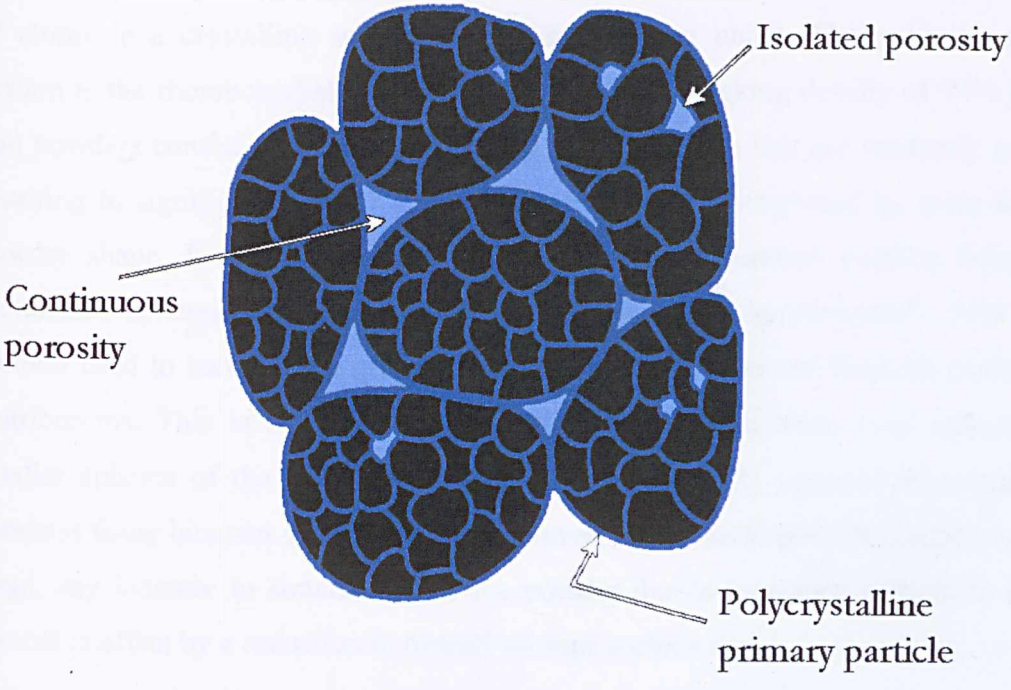


Figure 6.4 An agglomerate of dense polycrystalline primary particles [1].

Precipitation from aqueous solution is widely used in industry for producing ceramic oxide powders (e.g. co-precipitation and sol-gel). However, the nanocrystalline materials produced tend to form hard agglomerates even at relatively low calcination temperatures [5]. Kaliszewski and Heuer [6] described the mechanisms that produced soft agglomerates in aqueous precipitated YSZ powders. At the final stage of synthesis, the 'wet' powder was either washed in distilled water or ethanol. It was proposed that powders washed in ethanol form ethoxy surface groups on the surface of the powder, whereas water washed samples had hydroxyl groups. The latter readily allow Zr-O-Zr

bond formation between particles upon dehydration of the powder resulting in the formation of hard agglomerates. It was speculated that the ethoxy groups on the ethanol washed powders inhibit the close approach of particles and prevent the formation of Zr-O-Zr bonds between particles. Similar observations and conclusions were reported by Readey et al. [7] for MgO stabilised and MgO/Y_2O_3 stabilised ZrO_2 powder prepared by an aqueous precipitation method. It was reported that the green density and sinterability of powder washed in water was lower than that of powder washed in ethanol due to the presence of hard agglomerates.

It is generally accepted that the higher the green density, the lower the temperature needed to densify the material. This is due to greater initial particle to particle contact and a reduced pore size/particle size ratio [8]. If one assumes the powder particles are spherical and monosized, the powder packing arrangement is analogous to the packing of atoms in a crystalline solid (i.e. regular repeating units). The optimum packing system is the rhombohedral arrangement, which has a packing density of 74% [9]. All real powders consist of particles of varying size and shape that are randomly arranged resulting in significantly lower green densities. This is exacerbated by more irregular powder shape. It has been shown that the maximum random packing density for monosized spheres is independent of sphere size and is approximately 64% [1]. A method used to increase the green density of compacts is to use bimodal particle size distributions. This is achieved by filling the interstices between large spheres with smaller spheres of the same material [10]. Moskovits [11] reported increased green densities using bimodal 4YSZ powder. However, if the coarse powder component is too large, any increase in sinterability of the powder due to increased particle to particle contact is offset by a reduction in overall average surface area.

6.2.4. Solid State Technique

The solid state technique is considered the simplest and easiest way to produce CGO and related powders [12, 13, 14]. The ceria and gadolinia powders are mixed in the correct stichiometric proportions and are typically wet milled for a long period of time (~24 hours) to reduce particle size and to promote good homogeneous mixing. The milled powder is then dried and calcined at approximately 1000°C to form the solid solution. Finally, prior to consolidation, the powder is typically crushed and ground in a mortar and pestle.

Torrens et al. [15] characterised CGO20 synthesised using various techniques. The green density using powder produced by the solid state technique was relatively high due to good particle packing. However, samples that were sintered at 1650°C for 10 hours were only 86% the theoretical density. The term "theoretical density" is the true density of the solid phase alone (i.e. the mass of the specimen divided by only the volume of true solid material). It is generally regarded that of all powder synthesis techniques the solid state method produces the coarsest powders. Apart from a high sintering temperature, disadvantages of this technique include high impurity contamination, large average grain size, and the presence of hard agglomerates.

6.2.5. The Co-Precipitation Technique

The reverse strike co-precipitation technique is a relatively inexpensive process that can produce high purity, fine powders. Typically, $Ce(NO_3)_3$ and $Gd(NO_3)_3$ precursors of desired stoichiometric proportions are dissolved in water. Oxalic acid (~0.05M) is used as the precipitant, and the precipitation reaction is carried out by adding the nitrate solution to the precipitant. The careful addition of ammonia ensures neutral pH (6.6-6.9) during the course of the reaction. The resulting precipitate is repeatedly washed in ethanol, oven dried and calcined at approximately 500-700°C.

Compared to the solid state technique, powders produced by the co-precipitation technique tend to have a narrow and small particle size distribution and hence are considered more sinterable. Typically, the sintering temperature required to densify co-precipitated doped ceria powder to high density is approximately 1400-1500°C [15, 16, 17]. Reducing the calcination temperature decreases the sintering temperature needed to achieve high density as both particle size and the tendency for powder agglomeration are both minimised [18, 19]. The main disadvantage of this technique is poor chemical homogeneity that arises from the precipitation of the cations at different pH values.

6.2.6. Sol-Gel Prepared Powders

The sol-gel process was described in section 5.7. The gel, formed by hydrolysis and condensation reactions or peptisation of a precipitate, can be oven dried and ground down to form a very fine powder that can be processed by more conventional methods at significantly lower temperatures.

Huang et al. [20] synthesised solid solutions of $Ce_{1-x}Sm_xO_{2-x/2}$ (x=0-0.30) using a sol-gel method. The desired stoichiometric quantity of metal nitrate were separately dissolved in water, mixed and co-precipitated with ammonium hydroxide at pH=10. The precipitate was peptised by the addition of nitric acid at pH = 3.3. The resulting sol was dried in an oven (95°C) for 48 hours until a gel was formed. Calcination of the gel was performed at 1000°C. Samples were sintered to high density at approximately 1400°C. Similar observations were reported by Kai [21] for Sm doped ceria powder synthesised by a sol-gel method.

Huang et al. [22] fabricated spherical powders of CGO using a sol-gel process. The correct stoichiometric quantities of cerium and gadolinium nitrate were mixed together with ethylene glycol and heated at 80°C, whilst being continually stirred, for several hours. The solution eventually formed a gel that was subsequently oven dried (130°C) and calcined at 700°C. It was reported that the particle size of the powder, measured by transmission electron microscopy (TEM), was approximately 250nm. Consolidated powder was sintered at 1585°C to achieve high density. Using a similar technique, 3YSZ powder was prepared and sintered to high density at 1150°C [23]. More recently Durán et al. [24] prepared YSZ powder by a sol technique (surface area $>100m^2g^{-1}$) that sintered to high density at 1050°C after 5 hours. It appears likely that the CGO powder prepared by Huang et al. [22] would sinter to high density at temperatures significantly lower than that actually employed.

6.2.7. Hydrothermal Synthesis

The hydrothermal process involves heating reactants as a solution or a suspension at elevated temperature and pressure. Precipitation under these conditions can lead to an anhydrous powder that can have very fine size, narrow size distribution, single crystal particles, high purity and good chemical homogeneity (1).

Yamashita et al. [25] prepared precursor powders for hydrothermal synthesis by co-precipitation with ammonium hydroxide from aqueous solutions of cerium nitrate and nitrates or chlorides of the rare-earth and alkaline earth elements (Sm, Gd and Y) at pH=10. The precipitate, after filtration, was placed in a Teflon vessel without washing and hydrothermally treated with deionised water in a half-filled vessel at 220°C for several hours. The crystallised powder was repeatedly washed with deionised water,

filtered and freeze-dried. The crystallite size was approximately 10-20nm, however the presence of relatively large agglomerates (10μm) resulted in the samples having to be fired at 1450°C to achieve high density. Similar sintering temperatures were reported for Tb and Pr doped $Ce_{1-x}Sm_xO_{2-x/2}$ powder prepared by the same method [26]. Using the same technique, apart from hydrothermally treating at 260°C, Dikmen [27] synthesised $Ce_{1-x}Bi_xO_{2-\delta}$ (X=0-0.30) powder that had a crystallite size between 25-50nm. The presence of agglomerates was not reported and samples were sintered to high density at temperatures ranging from 900-1300°C.

Djuričić et al. [5] investigated the tendency of a powder to agglomerate as a result of the precipitating agent used. Of the agents investigated, the optimum method of avoiding hard agglomerates was to add hydrogen peroxide to the Ce(III) nitrate solution. The Ce cation is oxidised to a higher valence state, which initiates homogeneous precipitation resulting in the formation of dense spherical agglomerates. The precipitation process is completed by adding ammonium hydroxide, which breaks down the agglomerate. Hydrothermal treatment at 180°C produced a weakly agglomerated powder that had a uniform crystallite size of less than 5nm, unfortunately no sintering studies were performed on this ultrafine material.

6.2.8. Grain Growth Considerations

As previously discussed in chapter 4, the grain size has important consequences on the resulting properties of the material. In order to reduce polarisation losses, it is envisaged that the electrolyte will be ~15μm thick. It is desirable that the electrolyte have high toughness and strength. This can be achieved by reducing the grain size of the microstructure. From section 4.7, this enhancement in mechanical strength would be accompanied by reduction in the ionic conductivity from the grain boundaries. It is generally considered that any deleterious effect on the ionic conductivity due to a finer grain size is offset by gains in mechanical properties. It is thus considered desirable to minimise the grain size of the electrolyte. Knowledge of microstructure evolution is thus essential in order to produce a grain structure, which satisfies both electrical and mechanical requirements of the material.

The evolution of grains and their subsequent growth during sintering significantly influences the minimum temperature and time required to fabricate a highly dense

article. There are two types of grain growth, these are termed normal and abnormal. The former consists of grains that are uniform in size regardless of sintering time and temperature. Abnormal growth occurs when large grains grow rapidly at the expense of smaller grains. Over time the number of grains will vary markedly until the large grains begin to impinge.

Normal growth restricts pores to grain boundaries, from where they can be removed with relative ease due to the fast diffusion mechanisms associated with these highly disordered regions. The pores also act to 'pin' the grain boundaries, thus restricting grain growth and ensuring that densifying transport distances remain small thus aiding densification. If pore removal is too rapid during the early stages of sintering, pores become trapped within the abnormal grains that grow. These pores are more difficult to remove due to the relatively slow lattice diffusion.

Durán [16] reported that Gd doped ceria powders that were less agglomerated produced a more uniform microstructure. Microstructural analysis revealed that the densification process took place through the formation of regions with higher density than others, and these denser areas could cause the appearance of different populations of pores, neck sizes and abnormal growth.

Chen and Wang [28] devised a sintering schedule that densified Y_2O_3 at reduced temperature by carefully controlling the grain growth. Conventional sintering of Y_2O_3 (i.e. fixed heating rate and isothermal hold) at 1500°C for 1 hour was sufficient to densify the material. It was reported that during the latter stages of densification (70-100%) the grain size increased from 100nm to 400nm. The modified sintering cycle involved firing the material to approximately 75% theoretical density at 1250°C and lowering the temperature to 1150°C for 24 hours to achieve a highly dense specimen (100nm grain size). It is speculated that the grain boundary migration has an activation energy that is larger than the grain boundary diffusion for this to be successful.

6.2.9. Powder Processing and Preparation - Summary

Initially, the basic concepts and factors that influence the sintering of a powder have been reviewed. In order to lower the sintering temperature it is necessary that the powder has a small particle size and contains no hard agglomerates. It is likewise

necessary to maximise the green density of the consolidated body prior to firing. Four different powder preparation techniques were reviewed. Apart from powders produced by the solid state technique, all have produced highly sinterable powders. Commercially available CGO powders (Rhodia, Praxair) fall into this class. However, even these highly sinterable powders still require sintering at temperatures higher than the target of 1000°C. Therefore, it is necessary to explore the use of sintering aids to further increase the sinterability of CGO and related powders.

6.3. Sintering Aids

Deliberately adding impurities, sometimes referred to as dopants, can significantly enhance the sintering of ceramic systems in two very different ways. Firstly, the formation of a solid solution between host and dopant cations can enhance diffusion and hence sintering by changing the concentration of point defects and pinning the ground boundaries. Secondly, dopants are often added to ceramic systems to aid sintering by the formation of a liquid phase that facilitates both particle rearrangement and solution/precipitation.

It should be noted that controlling powder preparation is of critical importance for producing homogeneous fine powder that densifies by dopant addition. It is, however, the dopants that are considered to provide the actual mechanisms that aid densification and are thus solely discussed.

6.3.1. Dopant Additions and the Effect on Grain Boundary Mobility

As previously discussed in section 4.2, the addition of lower valency cations introduces oxygen vacancies that enhance the conductivity of the host material. As densification involves mass transport, it is therefore expected that the defect concentration will influence the sintering process.

Chen [29] noted that the grain boundary mobility in undoped ceria is higher in a less oxidising atmosphere. From the Schottky and Frenkel defect reactions (Equations 6.3 and 6.4 respectively):

$$\text{null} \xleftrightarrow{\Delta G_S} V_{Ce}^{''''} + 2V_{\ddot{O}} \qquad (6.3)$$

$$\text{null} \xleftrightarrow{\Delta G_F} V_{Ce}^{''''} + Ce_i^{\cdots\cdot} \tag{6.4}$$

we find:

$$\left[V_{Ce}^{''''}\right] = \left[V_O^{\cdot\cdot}\right]^{-2} \frac{K_F}{K_S} \exp\left(-\frac{\Delta G_F}{kT}\right) \tag{6.5}$$

$$\left[Ce_i^{\cdots\cdot}\right] = \left[V_O^{\cdot\cdot}\right]^{2} \frac{K_F}{K_S} \exp\left(-\frac{\Delta G_F - \Delta G_S}{kT}\right) \tag{6.6}$$

It was speculated that cation interstitial transport was the rate-limiting step in grain boundary mobility. From equation 6.6, an increase in oxygen vacancies likewise increases the concentration of cation interstitials.

In a subsequent study, Chen [30] studied the effects of a wide range of dopants on the grain boundary mobility of dense ceria. As discussed in chapter 4, additions of aliovalent dopants create charge-compensating defects on the oxygen sublattice of ceria (Equations 4.3, 4.4 and 4.5). It is thus not surprising that the grain boundary mobility in ceria is significantly affected by dopant addition (Table 6.1).

		Ionic (Å)	Mobility ($x10^{-16}m^2/(N.s)$)				Activation
(Ce^{3+}= 0.97Å)		Radius	1270°C	1320°C	1370°C	1420°C	energy (eV)
	CeO_2		10	36	169	551	6.16
0.1%	Mg^{2+}	0.89	70	250	700	1800	4.86
	Ca^{2+}	1.12	41	150	430	1171	5.02
	Sr^{2+}	1.26	29	110	330	1106	5.42
	Sc^{3+}	0.87	3.3	12	62	243	7.01
	Yb^{3+}	0.99	3.6	17	70	271	6.48
	Y^{3+}	1.02	27	72	229	446	4.88
	Gd^{3+}	1.05	33	100	247	509	3.79
	La^{3+}	1.16	9.3	26	136	361	6.19
	Ti^{4+}	0.74	48	140	365	1018	4.55
	Zr^{4+}	0.84	11	42	180	595	6.05
	Nb^{5+}	0.74	8	31	142	400	5.98
1.0%	Mg^{2+}	0.89	8.8	27.1	71	193	4.61
	Ca^{2+}	1.12	3.6	11	27	75	4.50
	Sc^{3+}	0.87	206	461	664	1045	2.37
	Yb^{3+}	0.99	1.4	3.1	12	24	4.51
	Y^{3+}	1.02	0.7	2.3	7.8	18	4.94
	Gd^{3+}	1.05	1.7	4.5	12	38	4.66
	La^{3+}	1.16	4.7	17	49	101	4.73
	Ti^{4+}	0.74	4.2	14	37	97	4.70
	Zr^{4+}	0.84	2.2	8.7	25	63	5.02
0.6%	Nb^{5+}	0.74	14	34	121	350	4.89

Table 6.1 Grain boundary mobility of undoped and doped ceria [29].

From table 6.1, at dilute concentrations (0.1%), minimal size misfit lower valency cation dopants create oxygen vacancies and thus increase grain boundary mobility. The Zr^{4+} cation gives similar mobility to undoped ceria.

Chen noted that when doping was not dilute but in the order of 1% for dopants of limited size misfit, doped ceria had a boundary mobility that was lower than undoped ceria. Even though more cation interstitials are available to enhance diffusivity, mobility of the boundary is reduced by the presence of a solute drag that did not exist at low dopant concentrations. Additives segregate to the grain boundary by coulombic attraction and decreasing elastic strain potential caused by dopant size mismatch and the segregation energy creates an effective "viscous" force on the moving boundary. Irregularities in the data were put down to the complex defect interactions occurring for additives with a greater ionic radius mis-match with the Ce^{4+} cation.

The larger value of densification/grain growth ratio of CGO20 compared to undoped ceria could be partly due to the presence of a solute drag [2]. It was claimed that the diffusion rate of oxygen in the bulk would be a rate-determining step in densification, since oxygen partial pressure in pores is considered to be limited by the diffusion of oxygen in the bulk. As the oxygen diffusion in fluorite materials is very fast, this explanation is considered wrong. As cation diffusion is the rate-limiting step for mass transportation, the creation of additional oxygen vacancies in ceria by substitution of Gd likewise increases the concentration of cation interstitials and thus explains the enhanced densification of CGO20 compared to ceria.

6.3.2. Low Temperature Solid State Sintering by Dopant Addition

The work by Chen [29, 30] indicates that both the grain boundary diffusivity and mobility can be manipulated by the addition of additives. In terms of the sintering process, both these factors are of extreme importance as they affect the rate of densification and grain growth. Recently, there has been considerable interest in the ability of additives to lower the sintering temperature of ionic conducting ceramic materials.

Baumand [31] reported that TiO_2 considerably aided densification of ceria. After firing at 1480°C for 15 hours ceria was 97% dense and had a mean average grain size of 13μm. Ceria doped with 0.1wt%Ti, however, achieved 99% density after being fired at 1200°C for 1 hour and had a mean average grain size of 2-3μm. As Ti^{4+} is neither an acceptor nor donor additive in ceria the mechanism is not clear: however, it was claimed that no liquid phase had formed during firing.

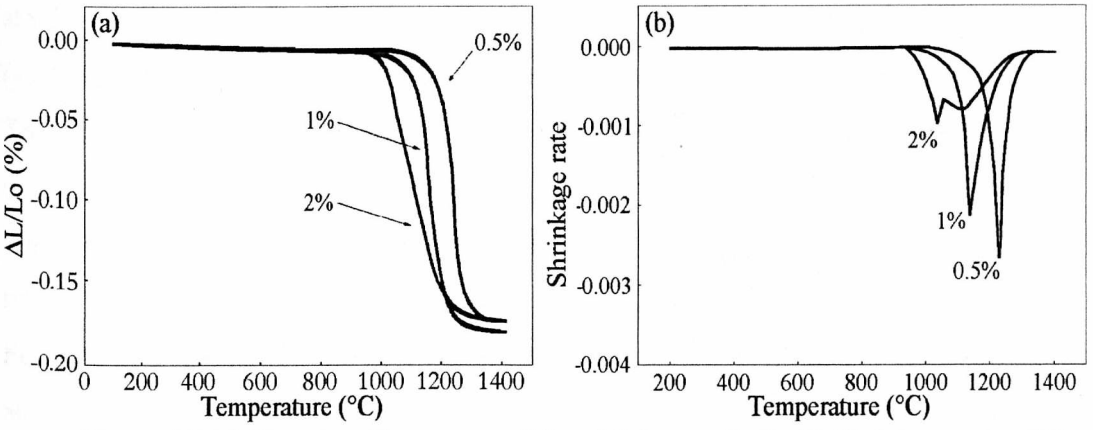


Figure 6.5 (a) Sintering dilatometry of Co additions to SnO_2 (b) Shrinkage rate of Co additions to SnO_2 [32].

Cerri et al. [32] studied the effect of CoO and MnO_2 additions on the sintering of SnO_2. A detailed study of the materials using high temperature XRD and DTA/TGA revealed that solid state densification was enhanced by the creation of additional oxygen vacancies. Of the two additions, CoO was the more effective sintering aid as expected from equation 4.3. Figure 6.5a shows that increased Co additions to SnO_2 decreased the sintering temperature, presumably due to the increased concentration of oxygen vacancies. Lange [33] suggested that densifying mechanisms dominate the sintering up to the temperature at which the maximum rate of shrinkage (T_m) occurs, and for temperatures above this value, the sintering is impaired by non-densifying mechanisms (i.e. grain growth). Figure 6.5b shows that T_m decreased as a function of Co addition (0.5-2%). Secondly, the linear shrinkage rate decreased faster after T_m for samples doped with less Co. It was concluded that the transition from densifying to impaired regions is more critical when SnO_2 is doped with a low concentration of dopant. It is more likely that increased Co content at the grain boundary establishes a solute drag effect that hinders grain growth and thus aids densification. Impedance spectroscopy performed by Muccillo et al. [34] on Co doped SnO_2 found that increased Co addition increased the electrical conductivity by 4-6 orders of magnitude due to the enhanced

conductivity associated with the presence of extra oxygen vacancies. Similar results were reported for Mn doped SnO_2 [35] and Mn doped CeO_2 [36].

Tianshu et al. [37] reported that additions of Fe were effective at reducing the sintering temperature of commercially available ceria by approximately 200°C. Fe doped ceria powders with atomic ratios of Fe/Ce ranging from 0 to 6% were synthesised by the solid state technique. XRD studies revealed that the solid solubility of Fe in ceria is very low (<2% at 1500°C), therefore it was assumed that not all of the Fe substitutes the Ce sites. The T_m value decreased whilst the corresponding maximum shrinkage rate was enhanced for increased additions of Fe up to 1%. It was noted that Fe doping shifts the maximum shrinkage rate towards the higher region of relative density during firing, this means that Fe doping delays the transition from the densification to the impaired region. Fe additions above 1% did not decrease the T_m value, presumably due to the limited solubility of Fe in ceria. Recently [38], it was reported that the addition of 2%Fe to ceria causes microcracking along grain boundaries at approximately 1400°C that results in an expansion of the sample and reduced relative density. The ability of Fe to promote sintering of ceria-stabilised zirconia has likewise been reported [39].

6.3.3. Liquid Phase Sintering

Liquid phase sintering is a common method used to lower the sintering temperature of many ceramics. Typically, the consolidated powder form for liquid phase sintering consists of a major component and a few percent of well-dispersed additive. On firing, the additive melts or reacts with a small amount of the major component to form a liquid. Assuming the liquid additive fully wets the powder, the particles will be separated by a liquid bridge that is significantly thicker than the grain boundary formed in solid state sintering. As diffusion through a liquid is much faster than in a solid, the bridge provides a faster diffusion path for matter transport. It also creates capillary pressure and lowers the friction between particles enabling more efficient packing. The remainder of this chapter will review the basic principles of liquid phase sintering and relevant literature concerning doped ceria and related materials.

6.3.4. Driving Force of Densification in Liquid Phase Sintering

The reduction of the liquid/vapour interfacial area provides a driving force for shrinkage and densification of the overall system. For a spherical pore of radius r in a liquid, the pressure difference (ΔP) across the curved surface is given by:

$$\Delta P = -\frac{2\gamma_{lv}}{r} \qquad (6.7)$$

where γ_{lv} is the surface energy of the liquid/vapour interface. The pressure in the liquid is lower than that in the pore, and this generates a compressive stress on the particles. This compressive stress due to the liquid is equivalent to placing the system under an external hydrostatic pressure that provides a fairly appreciable driving force for sintering [1].

6.3.5. Stages of Liquid Phase Sintering

Liquid phase assisted sintering consists of three stages that are identified by the dominant microstructure change occurring and have been reviewed in detail [1, 9].

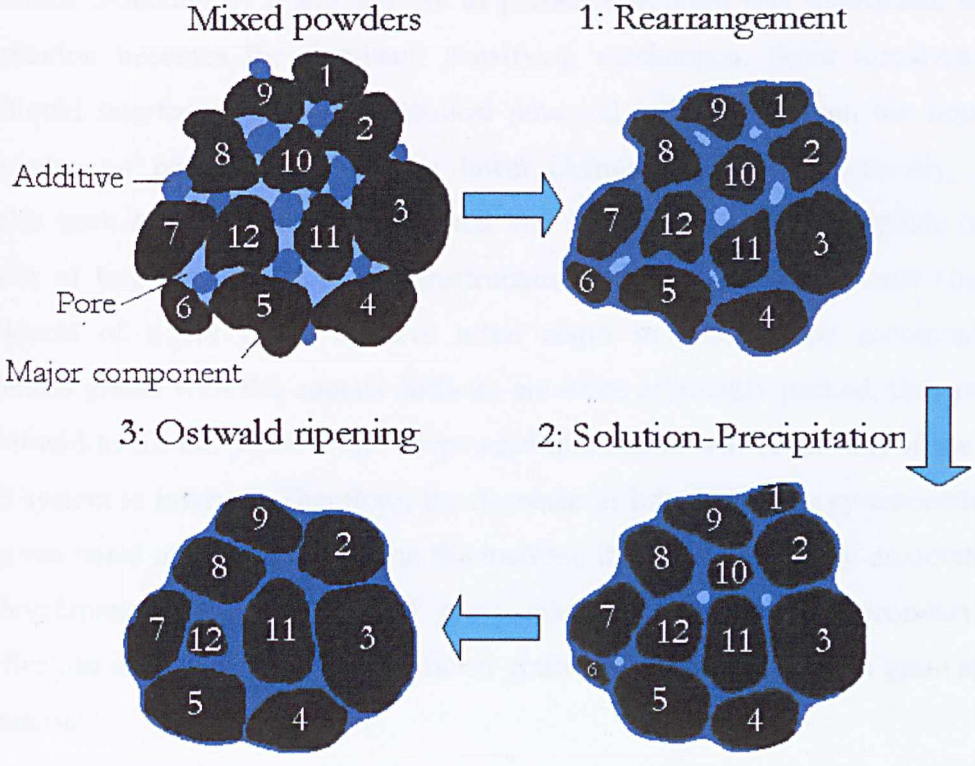


Figure 6.6 The different stages of liquid phase sintering.

6.3.5.1. Rearrangement

When the sample is fired the liquid additive will melt and wet the particles. The particles rearrange themselves under the action of surface tension forces to produce more stable packing [1]. Capillary stresses act to redistribute the liquid between particles and, if plentiful, into the pores. If the solid is soluble in the liquid, contact points between the agglomerates are dissolved due to reduction in interfacial energy resulting in smoother particle surfaces that reduce friction and further aid packing. The process of liquid redistribution and rearrangement continues until the liquid achieves a stable configuration. This initial stage occurs fairly rapidly and results in a large volume decrease of the sample. If a sufficient quantity of additive persists in the system, high density can be achieved during the rearrangement stage alone. However, as described in section 4.5, the presence of grain boundary phases are generally considered deleterious to the grain boundary conductivity. It is not the general practice to add large quantities of liquid phase additive to electroceramics and densify solely by rearrangement.

6.3.5.2. Solution-Precipitation

As volume reduction by rearrangement of particles becomes less significant, solution-precipitation becomes the dominant densifying mechanism. Solid dissolves at the solid/liquid interfaces with high chemical potential, diffuses through the liquid, and precipitates on particles that have a lower chemical potential. Generally, smaller particles have a higher chemical potential and are dissolved and precipitate onto the surfaces of larger particles. The microstructural development for systems containing low levels of liquid phase additive often result in grain shape accommodation. Polyhedral grains with flat contact surfaces are more efficiently packed, thus releasing more liquid to fill the pores. Grain shape accommodation will occur only if the energy of the system is lowered. Therefore, the decrease in interfacial energy associated with filling the pores must be greater than the increase in interfacial energy associated with the development of the polyhedral grain shape [1]. During the secondary stage, densification is accompanied by significant grain growth and changes in grain shape of the material.

6.3.5.3. Ostwald Ripening

During the latter stages of liquid phase sintering, densification becomes very slow and grain growth becomes the more dominant process. When the volume of additive is relatively low, solution-precipitation and grain shape accommodation remove any isolated porosity slowly due to large diffusional distances.

6.3.6. Liquid Phase Sintering of Doped Ceria and Related Materials

Suitable additives for liquid phase sintering must have low viscosity for rapid diffusion kinetics, a small dihedral angle and good solubility for the bulk material. The remainder of this chapter is dedicated to the low temperature sintering of doped ceria and related materials using additives to facilitate liquid phase sintering.

Earlier in this chapter, the enhanced sintering of SnO_2 by small amounts of CoO and MnO_2 was interpreted as being due to changes in the defect concentration. Varela [40] observed that 2% additions of Cu also promote a significant densification of SnO_2. It was suggested that a nonreactive liquid formed first that facilitated rearrangement during the initial stage of sintering. Later the dissolution of Cu into the SnO_2 creates lattice defects in SnO_2. Similar observations have likewise been reported by Zuca et al. [41].

Bi_2O_3 is a well known sintering aid for YSZ. Keizer [42] doped 8YSZ with additions of Bi (1-6%) and lowered the sintering temperature from 1697°C to 1077°C. The densification was explained by a liquid phase sintering mechanism. Kim and Kim [43] studied the effect on the microstructure and electrical conductivity of 3YSZ doped with 1.4-7%Bi. Analysis of sintered specimens revealed the residue of a Bi-containing liquid phase that aided densification. A dihedral angle greater than 90° indicated that the liquid had not penetrated all grain intersections and thus sintering was attributed to both liquid phase and solid state processes. It was noted that the phase stability of the cubic fluorite structure was affected by the additions of Bi and monoclinic and tetragonal minority phases were formed. The presence of a liquid phase that enhanced sintering of Bi additives to zirconia was reported by Chaim et al. [44]. However, Bi_2O_3 is a particularly reactive oxide and tends to form unwanted compounds with other materials in the SOFC, such as the electrodes.

Seidensticker and Mayo [45] investigated the claims by several authors that the beneficial effects of Cu additions on the sintering of 3YSZ reach a maximum around 0.3%Cu, beyond which sintered densities decrease markedly with further Cu additions. At 1038°C CuO transforms to Cu_2O and melts at 1144°C. This molten copper oxide reacts with the yttrium to form the liquid phase $Y_2Cu_2O_5$ and thus enhances sintering. Due to segregation of the dopant, an overall 0.3%Cu addition corresponds to a grain boundary composition of approximately 20%Cu for a 0.4μm grain size. It was presumed that the Cu has a higher solubility in 3YSZ at the grain boundary than in the bulk and that 20%Cu (overall 0.3%) could segregate at the grain boundary and not form a distinct phase. Above this doping level, it was speculated that the solubility of Cu at the grain boundary is exceeded and Cu not in solid solution reacts with Y_2O_3 to form a copper oxide rich liquid layer. This phase partially vaporises and is deleterious to the densification process by creating pressure within closed pores. Impedance spectroscopy of Cu additions to 2.5YSZ ceramics [46] revealed that the additive decreased both the lattice and grain boundary conductivities.

Shi et al. [47] studied the effects that CaO, Na_2O, Fe_2O_3, CuO (0.01-1wt%) additions had on the sintering of 3YSZ. The CuO additions, for reasons previously stated, enhanced the sintering. Additions of CaO and Fe_2O_3 were reported neither to enhance nor impede the densification process whilst Na_2O additions retarded the sintering of 3YSZ. Specific surface area and pore-size distribution measurements revealed the presence of large agglomerates in Na_2O doped 3YSZ that were detremental to the sintering process. Foschini et al. [48] reported that addition of 0.3% of transition metal oxides such as NiO, Fe_2O_3, CuO and MnO decrease the sintering temperature of Ce-stabilised ZrO_2 by up to 150°C when compared to undoped Ce-stabilised ZrO_2. The addition of the dopants enhanced the ionic conductivity of the lattice and grain boundary components. It was speculated that the grain boundary conductivity was enhanced due to the formation of a liquid phase that 'cleaned' the grain boundary by segregation of impurities at triple points.

The system SrO-Ga_2O_3 has a eutectic at 1270°C for the composition $Sr_2Ga_2O_5$ (SGO), which has the brownmillerite structure and is considered a potentially good ionic conducting material. On cooling, however, this phase dissociates to $Sr_3Ga_2O_6$ and $Sr_4Ga_4O_9$ [49]. Feng and Goodenough [50] prepared SGO by the solid state technique at 1210°C. XRD revealed that the majority of the material was indeed $Sr_4Ga_4O_9$. A 9YSZ

sample containing 3mol%SGO achieved 96% theoretical density at 1350°C, whereas the 9YSZ sample achieved only 94% theoretical density at 1450°C. The sample with additive had a slightly reduced lattice ionic conductivity, but higher grain boundary conductivity enhanced the overall total ionic conductivity by approximately 10% at 800°C. It was reported that the average grain size in the 9YSZ with additive (>10μm) was significantly larger than the 9YSZ without additive (~1μm). The large difference in grain size makes it difficult to ascertain whether any increase in the grain boundary conductivity is due to the presence of a highly conductive phase or by the reduction in the grain boundary surface area. Ralph [51] prepared SGO by a similar method and performed sintering studies of 3mol%SGO added to CGO. It was concluded that the additions failed to aid the densification of CGO as samples with additive failed to reach 95% theoretical density at 1300°C. It is speculated that the failure to isostatically press the CGO with additive resulted in consolidated green bodies with low densities that sintered poorly.

Ralph [51] unsuccessfully attempted to stabilise the brownmillerite structure SGO with boron additions. The small Ga^{3+} ion is considered to favour tetrahedral co-ordination as opposed to the octahedral co-ordination required to maintain the brownmillerite structure. As the boron ion is smaller than the gallium ion, it was speculated that boron could 'lock' the Ga^{3+} ion in its octahedral site. Trowbridge [52], in a continuation to the work initiated by Ralph, attempted to stabilise $Sr_2Ga_2O_5$ with $BiGaO_3$. XRD revealed that quenched glass samples of the oxide pre-cursor ratio $(Sr_2Ga_2O_5)_{0.9}$:$(BiGaO_3)_{0.1}$ had disproportionated to form the majority phase $Sr_3Ga_2O_6$. It was reported that Bi-strontium gallate additions to CGO proved ineffectual as sintering aids.

Jeevaratnam and Glasser's [53] study of the CaO-Ga_2O_3 system indicates that a eutectic exists at 1245°C between the compositions $3CaO$-Ga_2O_3 and CaO-Ga_2O_3. To the best of the author's knowledge, no literature exists on CaO-Ga_2O_3 materials as liquid phase sintering additives for CGO and related materials.

Yoshida et al. [54] investigated the effect that gallia had on the sintering behaviour of Sm doped ceria. Sm doped ceria densified at 1600°C whereas Sm doped ceria with gallia additions of 0.2-1% attained full theoretical density at 1450°C. It was reported that the additions significantly enhanced grain growth: however, samples in excess of 1% additive experienced a reduction in grain growth due to the presence of the second

phase $Ga_5Sm_3O_{12}$, which pinned grain boundaries. Importantly, the addition of the sintering aid was not detremental to the electrical conductivity of the material.

Recently, Kleinlogel and Gauckler have published a series of articles concerning the enhanced sinterability of CGO20 by the addition of various metal oxide additives (Co, Ni, Mn, Fe, Cu) with particular emphasis on Co [55, 56, 57, 58]. Commercially synthesised CGO20 with a specific surface area of $26m^2/g$ was initally soaked in ethanol. The desired amount of the dopant nitrate (e.g. $Co(NO_3)_2{\cdot}6H_2O$) was added to the CGO20/ethanol mixture and ground in an agate mortar. The doped powder was subsequently dried (120°C for 2 hours) and uniaxially (50MPa) and isostatically (840MPa) pressed. The green density of the pellets prior to sintering was in the order of 60% of the theoretical density.

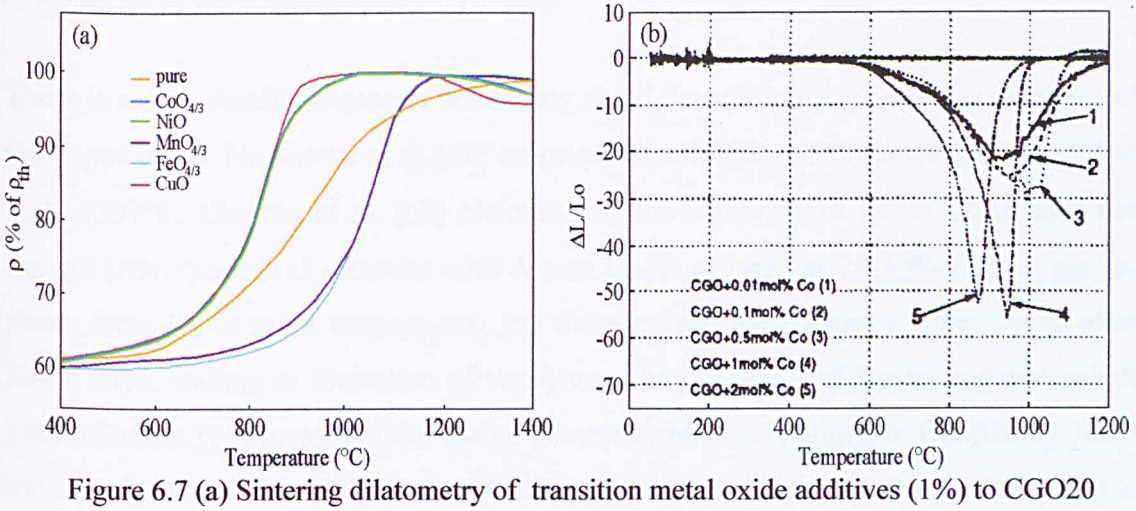


Figure 6.7 (a) Sintering dilatometry of transition metal oxide additives (1%) to CGO20 (b) Shrinkage rate of Co additives to CGO20 [55].

Figure 6.7a shows that all the dopants are effective in promoting the densification of CGO20. CGO20 sintered to high density at 1300°C, whilst 2% additions of NiO, CuO and Co_2O_3 reached high density at temperatures below 1000°C and 2% additions of MnO and Fe_2O_3 attained high density below 1100°C. It was reported that over sintering of dense samples leads to expansion. In the case of 2%Cu additive to CGO20 this was believed to be due to the phase transition of CuO to Cu_2O. Figure 6.7b shows the shrinkage rate versus temperature for Co added to CGO20. It indicates that Co is extremely effective in promoting the densification of CGO20 when exceeding an additive concentration of 0.5%. For example, CGO20 doped with 2%Co sintered to high density (>99%) at 900°C within 2 hours. Grain size measurements revealed that this sample had a grain size of 120nm whilst CGO20 without additive fired to

approximately the same density (at higher temperature) exhibited an average grain size of 2μm.

TEM analysis (2CoCGO20) of the grain boundaries on interrupting the sintering at 900°C after 10 minutes revealed an amorphous cobalt rich grain boundary film of 2-4nm width. The composition of the amorphous film analysised by electron energy loss spectroscopy was 60at%Co, 30at%Gd, 10at%Ce. It was speculated that the dopant layer present on the particle surface melts at temperatures below 900°C and facilitates densification via liquid phase sintering. TEM analysis of CGO20 with 5%Co additive sintered at 1400°C for 2 hours (furnace cooled) revealed that the Co rich film at the grain boundary had disappeared. It was speculated that sintering at higher temperature results in the formation of a solid solution of CoO in the CGO20 lattice, resulting in the disappearance of the grain boundary liquid.

There is a considerable degree of uncertanty about the solubility limit of Co in ceria and Gd doped ceria. Naumovic et al. [59] reported the solubility of Co in ceria to be <5% at 1127-1397°C. Kharton et al. [60] claimed that the solubility of Co in CGO does not exceed 10%. Quenched ceramics with dopant levels as large as 20-30% formed single-phase ceramics at room temperature; but these oxides were found to decompose after 30-60 days, leading to formation of two-phase fluorite type solid solutions and cobalt oxide. Sirman [61] measured the lattice parameter of Co_2O_3 added to CGO20 by XRD for samples sintered at 1400°C for 50 hours. It was concluded that the solubility of Co in CGO20 was 0.5mol%.

Kleinlogel and Gauckler commented that electronic conductivity was the principle mechanism of conduction at the grain boundary for samples that had the cobalt rich phase at the grain boundary (i.e. short sintering times). After annealing, it was reported that the conductive mechanism at the boundary changed and became predominately ionic due to the formation of a solid solution with the host. It was concluded that Co additions (<5%) neither enhanced nor impaired the ionic conductivity of CGO20 in fuel cell operating conditions when heat treated for sufficient time. Kharton et al. [60] reported that additions of Co to CGO (>5%) were deleterious to the electrical conductivity. It was claimed that the decrease was due to an increase in electronic conductivity resulting from the 'hopping' of electronic charge carriers between the variable valence cations. A decrease in ionic conductivity resulted from the blocking of

oxygen vacancies and or ions near the transition metal cations due to local distortions in the fluorite lattice.

Hartmonovà et al. [62] studied the relationship between lattice parameter and lattice conductivity of 12YSZ with additions of Co_2O_3 (0.1-0.5mass%). It was found that the lattice parameter decreased with additions below 0.2mass%Co_2O_3. This was interpreted as indicating a substitutional solid solution (Equation 6.8) as the Zr^{4+} cation was replaced with the smaller Co^{3+} cation. By substituting Co^{3+} for Zr^{4+} in the crystal matrix more oxygen vacancies would also be created and it was suggested that this might explain the increase observed in conductivity;

$$Co_2O_3 \longrightarrow 2Co'_{Zr} + V_O^{\cdot\cdot} + 3O_O^X \qquad (6.8)$$

Conversely, an increase in lattice parameter with additions between 0.3-0.5mass% Co_2O_3 was believed to be due to some of the Co entering the 12YSZ interstitially (Equation 6.9). The lattice conductivity of this material was greater than that of the 12YSZ but less than the 12YSZ with 0.2mass%Co_2O_3. This is possibly due to the filling of some oxygen vacancies by;

$$Co_2O_3 + 3V_O^{\cdot\cdot} \longrightarrow 2Co_i^{\cdot\cdot\cdot} + 3O_O^X \qquad (6.9)$$

6.3.7. Sintering Aids - Summary

It has been shown that the additions of sintering aids can significantly enhance the densification of CGO and similar materials. From the literature, additions of CaO-Ga_2O_3 or Co_2O_3 to commercial supplied CGO powders have the potential for reducing the sintering temperature to 900-1000°C.

References

1. Ceramic Processing and Sintering. M.N.Rahaman. Marcel Dekker, 1995.
2. H.Inaba, T.Nakajma and H.Tagawa. Solid State Ionics. **106**, (1998), 263.
3. J.Zhao and M.P.Harmer. J.Am.Ceram.Soc. **71,** 2, (1988), 113.
4. D-M.Liu, J-T.Lin and W.H.Tuan. Ceramics International. **25**, (1999), 551.
5. B.Djuričić and S.Pickering. J.Eur.Ceram.Soc. **19**, (1999), 1925.

6. M.S.Kaliszewski and A.H.Heuer. J.Am.Ceram.Soc. **73**, 6, (1990), 1504.

7. M.J.Readey, R-R.Lee, J.W.Halloran and A.H.Heuer. J.Am.Ceram.Soc. **73**, 6, (1990), 1499.

8. P-L.Chen and I-W.Chen. J.Am.Ceram.Soc. **79**, 12, (1996), 3129.

9. Introduction to Ceramics. W.D.Kingery, H.K.Bowen and D.R.Uhlmann. John Wiley and Sons, 1976.

10. R.J.Hellmig and H.Ferkel. J.Am.Ceram.Soc. **84**, 2, (2001), 261.

11. M.Moskovits, B.G.Ravi and R.Chaim. Nanostructured Materials. **11**, 2, (1999), 179.

12. H.Yahiro, Y.Baba, K.Eguchi and H.Arai. J.Electrochem.Soc. **135**, 8, (1988), 2077.

13. G.A.Tompsett and N.M.Sammes. J.Am.Ceram.Soc. **80**, 12, (1997), 3181.

14. S.Seike, H.Suwahara, T.Noguchi, C.Imazawa and M.Haba. Proc. of the 5th International Symposium on SOFCs. Eds. U.Stimming, S.C.Singhal, H.Tagawa and W.Lehnert. The Electrochem.Soc, (1997), 1096.

15. R.S.Torrens, N.M.Sammes and G.A.Tompsett. Solid State Ionics. **111**, (1998), 9.

16. P.Durán, C.Moure and J.R.Jurado. J.Mater.Sci. **29**, (1994), 1940.

17. J.Van herle, T.Horita, T.Kawada, N.Sakai, H.Yokokawa and M.Dokiya. Solid State Ionics. **86-88**, (1996), 1255.

18. Y.Gu, G.Li, G.Meng and D.Peng. Materials Research Bulletin. **35**, (2000), 297.

19. A.Tsoga, A.Naoumidis, W.Jungen and D.Stöver. J.Eur.Ceram.Soc. **19**, (1999), 907.

20. W.Huang, P.Shuk and M.Greenblatt. Solid State Ionics. **100**, (1997), 23.

21. J.Kai, M.Jian, H.E.Zhiqi, R.Yufang and S.U.Qiang. Science in China. **42**, 2, (1999), 160.

22. K.Huang, M.Feng and J.B.Goodenough. J.Am.Ceram.Soc. **81**, 2, (1998), 357.

23. W.Li, L.Gao and J.K.Guo. Nanostructured Materials. **10**, 6, (1998), 1043.

24. P.Durán, J.Tartaj, J.F.Fernández, M.Villegas and C.Moure. Ceramics International. **25**, (1999), 125.

25. K.Yamashita, K.V.Ramanujachary and M.Greenblatt. Solid State Ionics. **81**, (1995), 53.

26. W.Huang, P.Shuk and M.Greenblatt. Solid State Ionics. **113-115**, (1998), 305.

27. S.Dikmen, P.Shuk and M.Greenblatt. Solid State Ionics. **112**, (1998), 299.

28. I-W.Chen and X-H.Wang. Nature. **404**, 9, (2000), 168.

29. P-L.Chen and I-W.Chen. J.Am.Ceram.Soc. **77**, 9, (1994), 2289.

30. P-L.Chen and I-W.Chen. J.Am.Ceram.Soc. **79**, 7, (1996), 1793.

31. J.F.Baumard, C.Gault and A.Argoitia. J.of the Less-Common Metals. **127**, (1987), 125.

32. J.A.Cerri, E.R.Leite, D.Gouvêa and E.Longo. J.Am.Ceram.Soc. **79**, 3, (1996), 799.

33. F.F.Lange. Ceramic Transactions. **1**, (1989), 1069.

34. R.Muccillo, J.A.Cerri, E.R.Leite, E.Longo and J.A.Varela. Materials Letters. **30**, (1997), 125.

35. D.Gouvea, A.Smith, J.P.Bonnet and J.A.Varela. J.Eur.Ceram.Soc. **18**, (1998), 345.

36. Z.Tianshu, P.Hing, H.Huang and J.Kilner. Materials Science and Engineering. **B83**, (2001), 235.

37. Z.Tianshu, P.Hing, H.Huang and J.Kilner. J.Materials Processing Technology. **113**, (2001), 463.

38. Z.Tianshu, P.Hing, H.Huang and J.Kilner. J.Eur.Ceram.Soc. **21**, (2001), 2221.

39. P.A.P.Nascente and D.P.F.De Souza. Applied Surface Science. **144-145**, (1999), 228.

40. J.A.Varela, O.J.Whittemore and E.Longo. Ceram.Int. **16**, 3, (1990), 177.

41. S.Suca, Mterzi, M.Zaharescu and K.Matiasovsky. J.Mater.Sci. **26**, (1991), 1673.

42. K.Keizer and A.J.Burggraaf. J.Mater.Sci. **17**, (1982), 1095.

43. Y.H.Kim and H.G.Kim. J.Mater.Sci. **5**, (1994), 260.

44. R.Chaim and G.Basat and A.Kats-Demyanets. Materials Letters. **35**, (1998), 245.

45. J.R.Seidensticker and M.J.Mayo. J.Am.Ceram.Soc. **79**, 2, (1996), 401.

46. C.Bowen, S.Ramesh, C.Gill and S.Lawson. J.Mater.Sci. **33**, (1998), 5103.

47. J.L.Shi, T.S.Yen and H.Schubert. J.Mater.Sci. **32**, (1997), 1341

48. C.R.Foschini, D.P.F.Souza, P.I.P.Filho and J.A.Varela. J.Eur.Ceram.Soc. **21**, (2001), 1143.

49. V.P.Kobzareva, L.M.Kovba, L.M.Lopato, L.N.Lykova and A.V.Schevchenko. Russ.J.Inorg.Chem. **21**, 6, (1976), 903.

50. M.Feng and J.B.Goodenough. J.Am.Ceram.Soc. **77**, 7, (1994), 1954.

51. J.M.Ralph. Ph.D. Thesis. University of London, 1998.

52. G.Trowbridge. Private communications.

53. J.Jeevaratnam and F.P.Glasser. J.Am.Ceram.Soc. **44**, 11, (1961), 563.

54. H.Yoshida, K.Miura, J.Fujita and T.Inagaki. J.Am.Ceram.Soc. **82**, 1, (1999), 219.

55. C.Kleinlogel and L.J.Gauckler. Proc. of the 6th International Symposium on SOFC's. Eds. S.C.Singhal and M.Dokiya. The Electrochem.Soc. (1999), 225.

56. C.Kleinlogel and L.J.Gauckler. Solid State Ionics. **135**, (2000), 567.

57. C.Kleinlogel and L.J.Gauckler. J.Electroceramics. **5**, 3, (2000), 231.

58. C.Kleinlogel and L.J.Gauckler. Adv.Mats. **13**, 14, (2001), 1091.

59. E.N.Naumovic, V.V.Kharton, A.V.Kovalevsky, V.V.Samokhval. Proc. of the 17th

Riso International Symposium on Materials Science. Eds. F.W.Poulsen, N.Bonanos, S.Linderoth, M.Mogensen, B.Zachau-Christiansen, (1996), 375.

60. V.V.Kharton, F.M.Figueiredo, L.Navarro, E.N.Naumovich, A.V.Kovalevsky, A.A.Yaremchenko, A.P.Viskup, A.Carneiro, F.M.B.Marques and J.R.Frade. J.Mater.Sci. **36**, (2001), 1105.
61. J.D.Sirman, D.Waller and J.A.Kilner. Proc. of the 5th International Symposium on SOFCs. Eds. U.Stimming, S.C.Singhal, H.Tagawa and W.Lehnert. The Electrochem.Soc, (1997), 1159.
62. M.Hartmanová, F.Hanic, D.Tunega and K.Putyera. Chem.Papers. **12-15**, (1998), 12.

Section 2

Experimental

Chapter 7 – Experimental

7.1. Introduction

As previously discussed, the aim of my research was to develop a process to sinter commercially supplied CGO powder to high density between 900-1000°C without any deleterious effects on its electrolytic properties. Initial work concentrated on the addition of glass additives to facilitate enhanced densification via the liquid phase sintering of CGO. Reports midway through my first year indicated that Kleinlogel and Gauckler [1] had sintered CGO20 to high density below 1000°C by the addition of various transitions metal oxide additives. The emphasis of my research thus swiftly changed to investigate these additives as possible sintering aids to CGO. After a satisfactory doping technique had been developed, samples were characterised for their electrical and microstrucural properties. These techniques are briefly described in alphabetical order.

Unless stated otherwise, the commercial CGO powder used was supplied by Rhodia. Chemical analysis of the powders by the suppliers revealed that they contained minimal impurity levels (i.e SiO_2~30ppm) as recommended by Steele [2].

7.2. Calcium-Gallate Glass Preparation

As previously discussed in section 6.3.6, Jeevaratnam and Glasser [3] studied the CaO-Ga_2O_3 system. In a continuation to the work initiated by Ralph [4], two samples of eutectic composition ($3CaO\text{-}Ga_2O_3$ and $CaO\text{-}Ga_2O_3$ at 1245°C) were doped with Bi_2O_3. Prior to glass production, 5g of the starting precursors Ga_2O_3, $CaCO_3$ and Bi_2O_3 were calcined at 1000°C to ascertain any weight loss of the powders. Taking into account any change in weight, the appropriate quantities of the precursor materials were dry milled with alumina balls for 24 hours in a polyethylene container. The powder mixture was then heated to 1350°C for 1 hour in a platinum crucible. To avoid explosive shattering, the melt was cast onto a hot stainless steel plate (500°C). Samples were ground in a mortar and pestle to approximately 10μm prior to characterisation.

7.3. Solid State Dopant Addition of Cu and Co to CGO

The solid state technique was initially used to investigate the effect of Co and Cu on the sintering of CGO. The CuO and Co_3O_4 additions to CGO were ball milled in ethanol for 24 hours with CGO. After drying in an oven (50°C), the powder was ground in a mortar and pestle and sieved through a 38μm stainless steel mesh.

7.4. Precipitation Dopant Addition of Cu and Co to CGO

An alternative method of adding Co and Cu to CGO was by using the precipitation technique. The additive, in the form of a metal nitrate (e.g. $Co(NO_3)_2.6H_2O$), was dissolved in ethanol. The molarity of Co in solution was typically controlled to ~0.2M. This actual concentration was measured by inductively coupled plasma analysis (ICP) of the solution. The required stoichiometric quantity of additive and CGO were mixed in a beaker and agitated by a magnetic stirrer for approximately 30 minutes to promote good homogeneity. Dilute ammonia was added to precipitate the additive hydroxide at a pH of 10.5, and the slurry was subsequently centrifuged at 4500rpm for 5 minutes. Excess ammonia and water was discarded leaving a paste that was washed three times in ethanol. The paste was dried at 90°C and calcined at 650°C for 1 hour. The powder was then ground in a mortar and pestle and finally sieved through a 38μm stainless steel mesh.

7.5. Cobalt Nitrate Addition to CGO

The results achieved from the precipitation technique (section 7.4) proved encouraging. The fabrication route, however, was time consuming and involved many steps that increased the likelihood of contamination. An alternative approach was to dissolve the additive metal nitrate (e.g. $Co(NO_3)_2.6H_2O$) in ethanol and directly mix the solution with the electrolyte powder in a mortar and pestle (30 minutes). To ensure homogeneous distribution of the additive, the consistency of the powder and solution was controlled such that its viscosity was similar to that of cream. The molarity of the metal nitrate additive solution was determined by ICP. The resulting CGO/additive slurry was oven dried at 50°C. Unless stated otherwise, the powder was calcined at

650°C for 30 minutes. Post calcination, powders were ground in a mortar and pestle and sieved through a 38μm stainless steel mesh.

7.6. Consolidation of Powders

Many of the characterisation techniques employed in this thesis required the powder to be in a regular compact form. This was achieved by consolidating the powder into a cylindrical green body by applying uniaxial pressure, typically in the region of ~75MPa in a stainless steel die. Figure 7.1 illustrates the localised pressure gradients in a uniaxially pressed green body. Such localised variations occur due to friction at the die walls and can significantly affect the resulting properties of the material post firing. To avoid this problem, die pressed samples were placed in air tight rubber jackets and isostatically pressed in a liquid medium. The very high pressures acting in all directions limit any localised pressure differences and also increase the green density. Unless stated otherwise, consolidated powders were uniaxially (~75MPa) and isostatically (300MPa) pressed prior to firing.

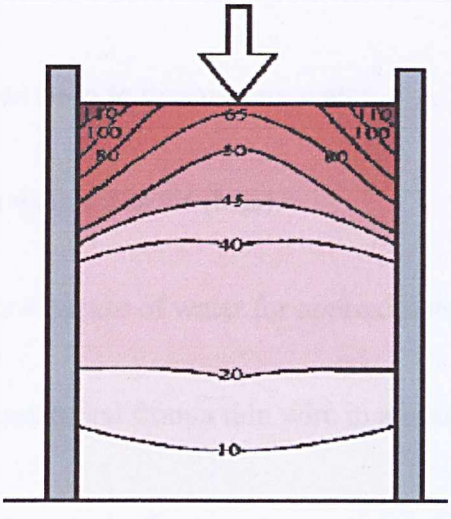


Figure 7.1 Percentage of nominal applied pressure in a unidirectional single ended pressed die [5].

7.7. A.C. Impedance Spectroscopy

A.C. impedance spectroscopy was used to characterise the electrical properties of different materials studied in this thesis. The sample, typically 10mm in diameter and 0.5mm in thickness after firing, was initially ground flat using 1200 grit SiC paper on each side, silver paint was then baked onto each side of pellet at 700°C for 30 minutes

to ensure good contact with the pellets. Electrical measurements were made via platinum wires attached to fine platinum meshes, which provided the current contacts to each electrode on the pellets. The pellets were held in position with springs, which applied a compressive force to the electrodes. Impedance spectra were obtained using a Solatron 1260 frequency response analyser over the frequency range 0.1-10^7Hz. Measurements were made in the temperature range 150-400°C in air. The amplitude of the applied excitation voltage was maintained at 50mV to ensure a linear response. Each spectrum showed two high frequency semi-circles that represent the response of the lattice and grain boundary of these materials. A.C. impedance spectroscopy theory and interpretation of the data is discussed in chapter 10.

7.8. Density Measurements

Bulk density (ρ_b) refers to the mass of the specimen divided by its total volume (i.e. the volume of solid material plus the volume of both open and closed porosity). The bulk density of samples was calculated using the Archimedes method described below (DD ENV 1389:1994):

1. The pellet is heated in an oven to remove any water.

2. The dried pellet is then weighed in air (M_{air}).

3. The pellet is placed into a beaker of water for approximately 1 hour.

4. The pellet is weighed suspended from a thin wire in a beaker of distilled water (M_{water}).

5. The wire suspended in the water is then weighed (M_{wire}).

6. The surface water is removed from the pellet and the pellet is re-weighed ($M_{wet/air}$).

$$\rho_b = \frac{M_{air}}{M_{wet/air} - (M_{water} - M_{wire})} \times \rho_{water/T} \qquad (7.1)$$

7.9. Dilatometry (Sintering)

The shrinkage behaviour of powders during firing was investigated using a Netzsch 402E horizontal dilatometer. A sample approximately 4mm in length was placed between two high purity alumina spacers (15mm). One of the spacers was in contact with a sprung loaded alumina push rod that pushed the other spacer tight against an alumina end plate (Figure 7.2). The spacers were a precaution to avoid contamination of the high purity alumina components in the dilatometer by cation diffusion at high temperature. As the sample was fired, shrinkage occurred resulting in displacement of the push rod. Data were recorded between 20-1400°C at various heating rates, isotherms and gas environments. Gas flow rate was kept below 100ml/min to prevent cooling of the sample during experimentation. The dilatometer software compensated automatically for the expansion of the holder.

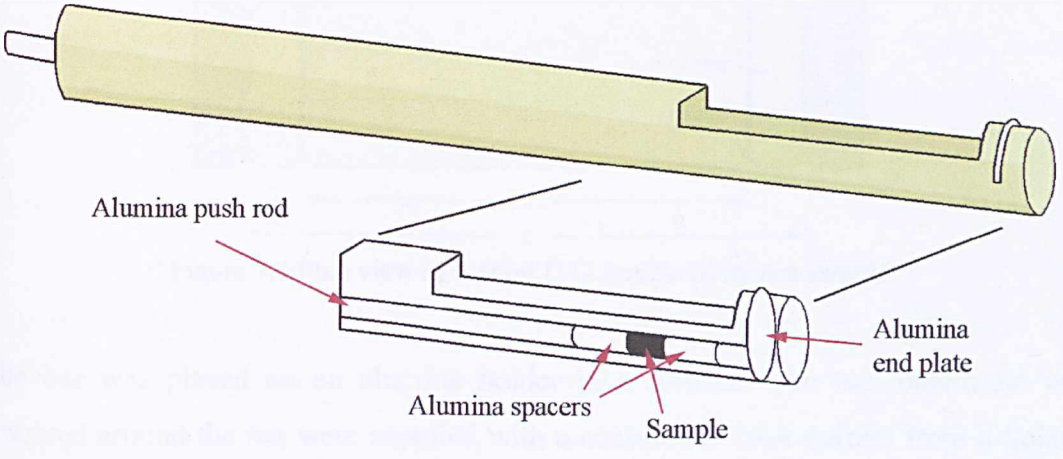


Figure 7.2 Diagram to show sample in dilatometer.

7.10. Dilatometry (Thermal Expansion)

The thermal expansion behaviour of CGO and 2CoCGO samples was measured using a Netzsch 402E horizontal dilatometer. Samples were consolidated in a bar die and then isostatically pressed. Sintered specimens (approximately 20mm x 5mm x 5mm) were loaded into the dilatometer as shown in figure 7.2. Data were recorded between 20-950°C at a fixed heating rate of 10K/min in air. The dilatometer software compensated for any expansion of the holder.

7.11. Four-Point D.C Resistivity

A 4-point D.C. resistivity technique was used to measure the electrical conductivity of CGO, 2CoCGO and 4CoCGO as a function of both temperature and oxygen partial pressure. Bar samples were prepared by consolidating powder in a bar die. Dense samples (>95%) were achieved by sintering the CGO and CoCGO samples at 1350°C for 4 hours and 1000°C for 2 hours respectively. Each bar was ground to produce flat, parallel faces with the approximate dimensions 3mm x 2mm x 20mm. Four platinum wires were then attached along the length of the bar. Each wire was tightly bound by making small notches in the bar and coated with platinum paste, which was fired at 850°C for 30 minutes to ensure good electrical contact with the sample (Figure 7.3). The precise distance between the central two wires and the dimensions of the bar sample were measured using a micrometer.

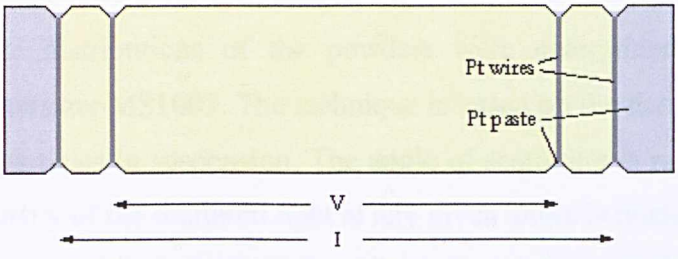


Figure 7.3 Plan view of 4 point D.C. conductivity test sample.

The bar was placed on an alumina holder in a furnace. The two outermost wires wrapped around the bar were supplied with a continuous 1mA current from a Solatron 1186 electrochemical interface. The two innermost wires were connected to a digital voltmeter to measure the potential difference. A thermocouple and zirconia oxygen probe were situated close to the sample. Mixing different ratios of CO_2 and H_2/N_2 at known flow rates with digital mass flow meters controlled the oxygen partial pressure inside the quartz envelope. To ensure equilibrium, the sample was kept at a particular temperature or pO_2 level for 24 hours before a measurement was made. This time factor reduced the number of samples that could be tested by this technique.

At a given temperature and pO_2, the conductivity (σ) can be calculated from equation 7.2:

$$\sigma = \frac{l}{R_T A} \tag{7.2}$$

where A is the cross sectional area of the bar, l is the length between the two potential wires and R_T is the measured resistance, which was calculated from Ohm's law (V=IR). The pO_2, at temperature, T, was calculated from the emf generated at the oxygen probe (E_r), using the Nernst equation:

$$E_r = \frac{RT}{4F} \ln \frac{pO_{2(c)}}{pO_2} \tag{7.3}$$

where R and F are the commonly used constants and $pO_2(c)$ is equal to 0.21atm.

7.12. Particle Size Analysis

The particle size distributions of the powders were determined using a Malvern Instruments Mastersizer MS1005. The technique is based on the fact that laser light will be scattered by particles in suspension. The angle of scattering is related to the particle size and the intensity of the scattered light at any given angle is related to the proportion of particles of that size in suspension. Prior to characterisation, powders were ultrasonically dispersed in distilled water (with a couple of pipette drops of Tepol surfactant) for 20 minutes to break down any soft agglomerates.

7.13. Raman Spectroscopy

CGO and 2CoCGO powders were pressed into pellets and fired at 750°C, 850°C, 950°C and 1050°C for 2 hours and either furnace or ice water quenched. The specimens were mounted in resin and polished to a ¼ μm finish using various grades of SiC paper and diamond paste. The Raman spectra were obtained using a Renishaw 2000 Micro Raman instrument in the Department of Physics, Imperial College. The spectra were excited with an argon ion laser that was operated at a wavelength of 514.5nm. Spectra from each sample presented are the average of 10 runs taken from 200-900cm^{-1} shift, each run lasting 10 seconds. The background in each spectrum has been subtracted and the data normalised to the peak intensity occurring at 460cm^{-1}.

7.14. Scanning Electron Microscopy (SEM)

A JEOL JSM-35CF SEM, in the secondary electron mode, was used to examine the morphology of various powders and dense ceramic materials. All samples were mounted onto aluminium stubs using a thin piece of carbon tape and coated with gold to avoid charging of the sample.

7.14.1. Grain Size Determination Using SEM

The majority of the SEM work presented in this thesis was used to investigate the grain growth in CGO and 2CoCGO. Samples were uniaxially (~75MPa) and isostatically (300MPa) pressed and fired to approximately 97% bulk density. This was performed to minimise the influence of porosity on grain growth. Each sample was broken into 4 segments and then heat treated at a specified temperature (1300°C, 1400°C and 1500°C) for different periods of time (1, 1.5, 3.375 and 38 hours). Heat treating at high temperature presented two problems with the 2CoCGO samples. Firstly, to prevent Co ion diffusion from the specimens each was surrounded by a quantity of its respective powder. Secondly, since Co loss at high temperature is by volatilisation as $Co(OH)_2$ vapour the heat treatment was carried out in dry air (BOC special gasses). Visual inspection of all 2CoCGO samples post firing indicated that these precautions had prevented significant loss of Co.

The specimens were mounted in resin and polished to a ¼ μm using various grades of SiC paper and diamond paste. Samples were then removed from the resin by soaking in ethanol overnight and thermally etched at 1250°C for 20 minutes in order to enhance grain features. The microstructures of the specimens were characterised by SEM. Using Adobe PhotoShop 5 software; the average linear intercept length of the grains was obtained for a minimum of 300 grains. The grain size was obtained by multiplying the average linear intercept length by 1.56 [6].

7.15. Transmission Electron Microscopy (TEM)

In order to investigate the microstructure of doped CGO samples that were sintered to high density at low temperature, TEM was performed. Samples were prepared at

Imperial College whilst characterisation was performed by Prof. John Drennan at the University of Queensland, Australia.

The TEM specimens were prepared from the sintered pellets using the following procedure. The pellet was first ground to between 150-200μm in thickness and then cut with a diamond impregnated wire saw into rectangular shaped pieces 2mm x 1.5mm. These pieces were then placed into a steel grid (non-magnetic) with a 3mm diameter and rectangular aperture in the centre for the ceramic sample. Araldite was used to fix the ceramic into the aperture of the metal grid and then the composite was ground further to reduce its thickness to between 80-100μm. The centre region of each sample was then thinned further by dimpling, using a Gatan 656 dimple grinder. The unpolished side was then dimpled and polished with 0.25μm diamond paste, to give a specimen thickness of 10-20μm. Ion beam thinning was then used to thin the centre of the sample to a thickness of 0-200nm for electron transparency. All ion beam thinning was conducted using a liquid nitrogen cooled stage in a Gatan Duomill 600. The ion beam gun voltage was set to 4keV and the current 1mA. Once the sample was perforated the gun voltage was lowered to 2keV and the sample thinned for approximately thirty minutes to remove contaminants and ion beam damage, a gun angle of 12° was used throughout. A Philips Tecnai 20 FEGTEM with a tungsten/zinc filament was used. It was equipped with an Oxford EDS detector and Moran Scientific analyser to give X-ray analysis with an approximate electron beam minimum spot size of around 5nm in diameter.

7.16. Thermal Analysis

A Stanton Redcroft Simultaneous (TGA/DTA) Thermal Analyser STA-780 Series was used to investigate the thermal characteristics of various materials in this study. Measurements were performed in both air and argon between 20-1350°C (10K/min), using platinum crucibles and an alumina reference for calibration.

7.17. X-ray Photoelectron Spectroscopy (XPS)

All XPS analysis was performed by Mr. Karol Senic in the Department of Chemical Engineering, Imperial College. The XPS spectra were acquired on a VG ESCALB

MKII spectrometer with a hemispherical electron analyser detector interfaced with a computer and using an AI Kα (1486.6eV) radiation source operated at 12kV and 20mA. Spectra were obtained operating the hemispherical detector with constant threshold pass energy of, 50eV, which gave a detector efficiency changing linearly with the inverse kinetic energy. The carbon 1s peak at 284.8eV was used to calibrate the binding energies. The base pressure during the acquisition was typically less than $1x10^{-8}$mbar.

Compressed powder specimens were mounted on a stainless steel stub and protected with a stainless steel lid having a small hole covered with aluminium foil. The powder specimens mounted on the stainless steel stub were introduced via a transfer device. The fast-entry chamber was purged using dry argon and evacuated to 10^{-3}mbar. Subsequently the sample was transferred via the preparation chamber (with a background pressure of 10^{-7}mbar) to the analysis chamber maintained under Ultra High Vacuum (UVH) conditions, where the lid was removed from the stub.

7.18. X-Ray Diffraction (XRD)

XRD was used to determine the lattice parameters of powder and sintered bodies. Samples were heated at 10K/min to temperatures between 650-1100°C for 2 hours in static air and furnace cooled. Post heat treatment, powder samples were ground in a mortar and pestle and sieved through a 38μm stainless steel mesh. The Co-free CGO powder, prior to heat treatment, was dispersed in ethanol and dried in an oven at 50°C. This was performed to ensure that any differences was solely due to the introduction of Co.

A Philips PW1720 diffractometer using Cu-Kα radiation was calibrated prior to data collection with a silicon reference and measurements of intensity versus 2θ were taken from 20 to 100° at 0.01° intervals every 5 seconds. Diffraction patterns were collected with the aid of Philips PC-APD software. CELREF, a crystal cell parameters program was used to determine the lattice parameters using a least squares refinement method.

References

1. C.Kleinlogel and L.J.Gauckler. Proc. of the 6th International Symposium on SOFC's. Eds. S.C.Singhal and M.Dokiya. The Electrochem.Soc. (1999), 225.

2. B.C.H.Steele. Solid State Ionics. **129**, (2000), 95.

3. J.Jeevaratnam and F.P.Glasser. J.Am.Ceram.Soc. **44**, 11, (1961), 563.

4. J.M.Ralph. Ph.D. Thesis. University of London, 1998.

5. Ceramic Processing and Sintering. M.N.Rahaman. Marcel Dekker, 1995.

6. M.I.Mendlson. J.Am.Ceram.Soc. **52**, 8, (1968), 443.

Section 3

Results

And

Discussion

Chapter 8 – Development of Procedure to Densify CGO at Low Temperature

8.1. Introduction

It was originally conceived that glass additions from the $CaO\text{-}Ga_2O_3$ system could act as liquid phase additives to commercially supplied CGO powder. It was during these initial studies that Prof. B. C. H. Steele discovered via private communication with Prof. L. G. Gauckler (Swiss Federal Institute of Technology, Switzerland) that Co and Cu additions could densify (>95%) CGO20 at temperatures below 1000°C. The emphasis of research thus changed and concentrated solely on addition of Cu and Co to CGO.

This chapter discusses the development of a technique that was successfully employed to densify CGO at reduced temperature.

8.2. $CaO\text{-}Ga_2O_3$ Sintering Aids

In accordance with the method detailed in section 7.2, table 8.1 lists the glasses that were produced around the eutectic composition of the $CaO\text{-}Ga_2O_3$ system (Figure 8.1). Due to the possible degradation of the platinum crucible by the high temperature reactions with Bi_2O_3, only two samples of Bi_2O_3 doped eutectic composition were produced.

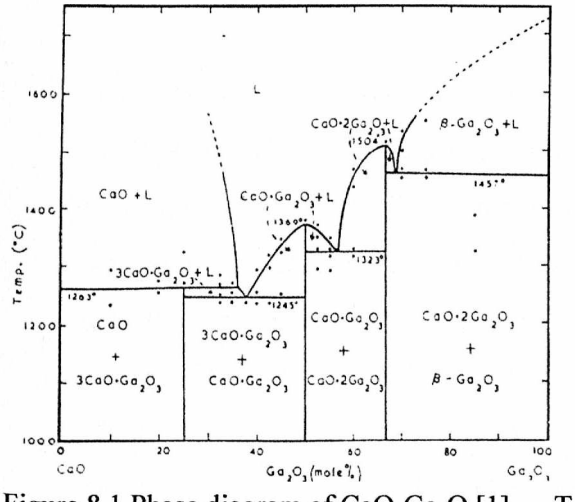


Figure 8.1 Phase diagram of $CaO\text{-}Ga_2O$ [1].

Sample no.	Glass (m%)
1	0.35 Ga_2O_3 : 0.65 CaO
2	0.363 Ga_2O_3 : 0.647 CaO
3*	0.375 Ga_2O_3 : 0.625 CaO
4	0.4 Ga_2O_3 : 0.6 CaO
5	0.425 Ga_2O_3 : 0.575 CaO
6	0.45 Ga_2O_3 : 0.55 CaO
7	0.9 Eutectic : 0.1 BiO
8	0.85 Eutectic : 0.15 BiO

Table 8.1 Glasses fabricated (3*=eutectic comp).

As predicted by Jeevaratnam and Glasser [1], all melts formed readily at 1350°C. When quenched, samples 1-6 formed highly fractured crystalline material whilst samples 7 and 8 were both crystalline and amorphous in appearance. It was noted during quenching that additions of Bi_2O_3 significantly decreased the viscosity of the melt. In a subsequent study of the glasses produced in table 8.1, DTA analysis revealed that Bi_2O_3 additions reduce the melting temperature of $CaO\text{-}Ga_2O_3$ materials. Sample 7 was reported to have a glass transition temperature at 645°C [2].

3 wt% of sample 7 was added to CGO in order to investigate its potential use as a sintering aid. The theoretical densities of the green bodies of CGO and CGO with additive were 60% and 49% respectively. After heating for 5 hours at 1250°C, CGO and CGO with additive were 95.6% and 93.9% dense respectively. The surface of the sintered CGO pellet was smooth and had a light yellow appearance. The doped material was significantly pitted and had a dark yellow and brown speckled appearance. Presumably, the glass additive was not sufficiently fine on addition, which resulted in a highly porous green body that sintered poorly.

8.3. Solid State Dopant Addition of Cu and Co to CGO

Samples were prepared by powder mixing in accordance with section 7.3. Figure 8.2 shows %bulk density as a function of sintering time at 1000°C in air for CGO, 1CoCGO and 1CuCGO. The most significant result is that both dopants enhanced the densification of CGO such that high density was achieved after only 1 hour. Increased firing time resulted in minimal change in the density of 1CoCGO, whilst the density of 1CuCGO markedly decreased. This phenomenon will be discussed in the next chapter.

Figure 8.2 shows that it is possible to produce dense (>95%) CGO without any sintering aids at 1000°C. The free standing sample achieved high density after 10 hours of sintering. In the Imperial College planar ITSOFC, the electrolyte will be layered on top of either an anode or cathode that is supported by ferritic stainless steel. During firing, densification processes that result in shrinkage of the CGO electrolyte will be constrained. Therefore, even though high density of a free standing body is achieved after 10 hours of firing, much longer sintering times would be expected for a thick supported film that would result in unacceptable levels of oxidation of the stainless steel support. As reported in the literature, the gradual increase in CGO density of as a

function of sintering time suggests solid state sintering mechanisms are responsible for densification [3].

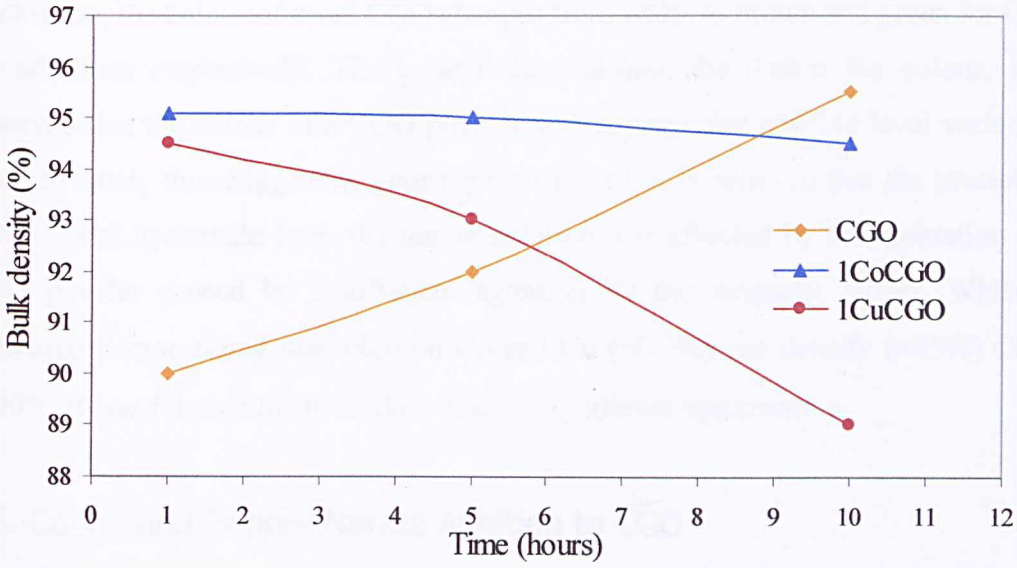


Figure 8.2 Sintering time versus bulk density for CGO, 1CoCGO and 1CuCGO at 1000°C (air). The transition metal oxides were added by powder mixing.

8.4. Precipitation Dopant Addition of Cu and Co to CGO

The encouraging results in the last section prompted the addition of Co and Cu to CGO by precipitating the additives onto CGO particles as described in section 7.4. It is generally regarded that this technique produces 'cleaner' powder that has enhanced sinterability when compared to powder made by the solid state technique.

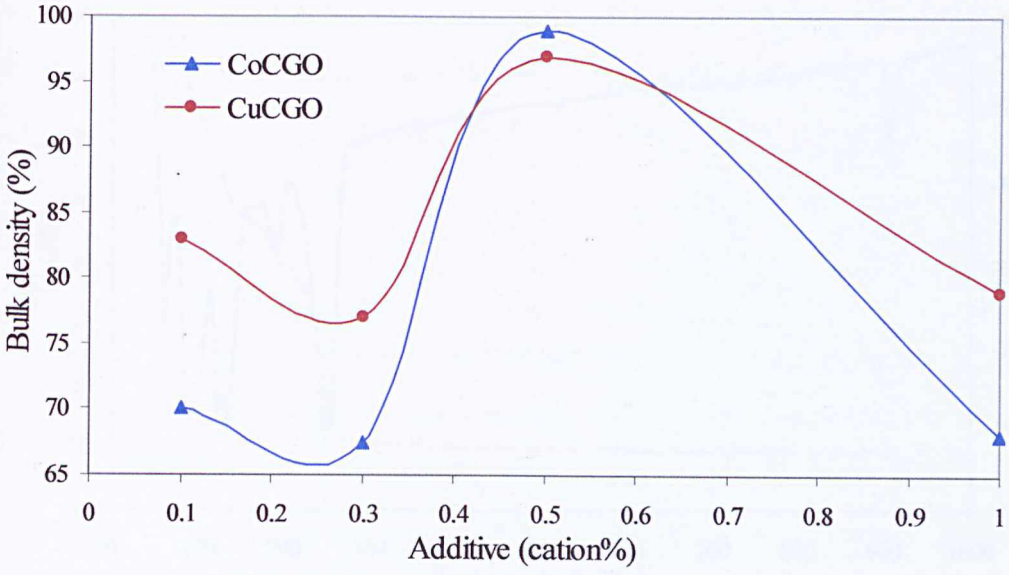


Figure 8.3 Bulk density versus Co and Cu addition to CGO sintered at 1000°C for 1 hour (air). The sintering aids were added by precipitation.

Figure 8.3 shows that 0.5% addition of both additive species densify CGO to high density at 1000°C. A CGO pellet fired in the same conditions was 88% dense. Pre-calcination, the colour of dried CGO changes from white to brown and green for Co and Cu additions respectively. The greater the addition, the darker the colour. It was observed that the colour of a CGO powder with a particular additive level varied from batch to batch, thus suggesting poor reproducibility. It is believed that the precipitation of the metal hydroxide from the nitrate solution was affected by sedimentation of the CGO powder caused by insufficient agitation by the magnetic stirrer. Whilst this technique demonstrated that addition Co and Cu (>0.5%) can densify (>95%) CGO at 1000°C it was felt that the procedure needed significant optimisation.

8.5. Cobalt and Copper Nitrate Addition to CGO

A much simpler additive technique involved addition of the unprecipitated Co/Cu nitrate precursors (dissolved in ethanol) directly to CGO, as described in section 7.5. Table 8.2 shows a typical ICP analysis of a nitrate solution used to add Co to CGO and indicates that impurity contamination is very low.

Element	Na	K	Ca	La	Cr	Fe	**Co**	Ni	B	Si
Amount (mg/ml)	0.01	0.01	0.1	0.015	0.02	0.05	**5200**	0.05	0.01	0.1

Table 8.2 ICP of $Co(NO_3)_2.6H_2O$ dissolved in ethanol added as a sintering aid to CGO.

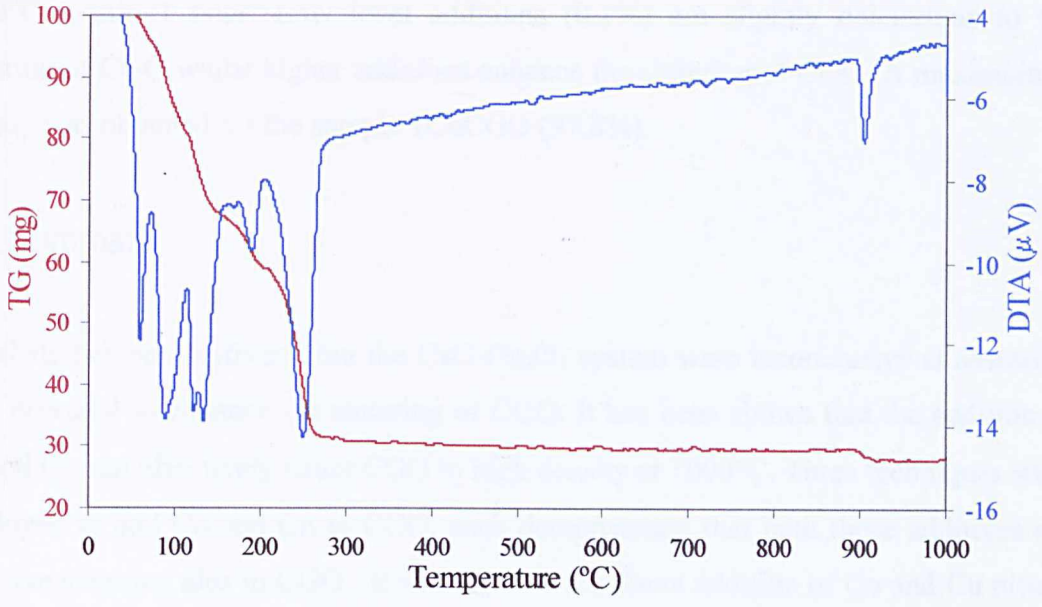


Figure 8.4 DTA/TG (air) of $Co(NO_3)_2.6H_2O$ dissolved in ethanol and dried at 50°C.

Prior to powder consolidation, it was necessary to remove water, ethanol and nitrate species from the doped powder surface. Figure 8.4 shows that the minimum calcination temperature required for CoCGO was 290°C, a similar temperature was found for CuCGO. The DTA graph for Co reveals an endothermic peak occurring at 906°C. This is due to the phase transformation of Co_2O_3 to CoO, the weight loss is due to the liberation of oxygen to the surroundings. The DTA graph also suggests that Co_2O_3 does not melt to form a liquid phase between 20-1000°C.

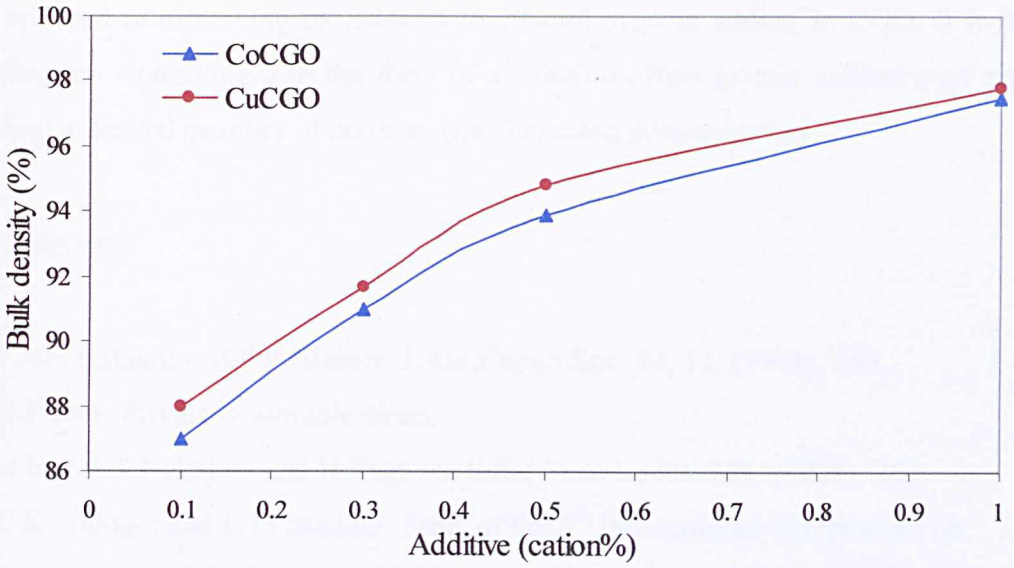


Figure 8.5 Co and Cu addition to CGO via 'nitrate addition' as a function of bulk density (1000°C for 1 hour (air)).

Figure 8.5 shows that nitrate addition of Cu or Co can densify CGO to high density at 1000°C within 1 hour. Low level additions (0.1%) are slightly deleterious to the sintering of CGO whilst higher additions enhance the sintering of CGO. A maximum in density was obtained for the sample 1CuCGO (97.8%).

8.6. Summary

Initial studies on additives from the CaO-Ga_2O_3 system were inconclusive at assessing their potential to enhance the sintering of CGO. It has been shown that the addition of Co and Cu can effectively sinter CGO to high density at 1000°C. Three techniques were employed to add Co and Cu to CGO, each demonstrated that both these additives are effective sintering aids to CGO. It was felt that the direct addition of Co and Cu nitrate precursors to CGO material was the best procedure. The process did not require many steps and thus reduced the risk of possible impurity contamination. For the remainder of

the work presented in this thesis, all electrolyte powders with additive were prepared using this technique.

Shortly after experiments had been performed that confirmed the reproducibility of powders prepared by this technique, Kleinlogel and Gauckler [4] first reported the use of Co (and other transition metal oxides) as sintering aids to CGO20 in the literature. The method used was almost identical to that developed in this study. The only difference being that they added the metal nitrate crystals to a CGO/ethanol suspension as opposed to dissolving the crystals in ethanol prior to adding to CGO. It is felt that adding the sintering aid in the form of a solution offers greater control over precisely adding a desired quantity of additive (i.e. increased homogeneity).

References

1. J.Jeevaratnam and F.P.Glasser. J.Am.Ceram.Soc. **44**, 11, (1961), 563.
2. B.Fisher. Private communications.
3. H.Inaba, T.Nakajma and H.Tagawa. Solid State Ionics. **106**, (1998), 263.
4. C.Kleinlogel and L.J.Gauckler. Proc. of the 6th International Symposium on SOFC's. Eds. S.C.Singhal and M.Dokiya. The Electrochem.Soc. (1999), 225.

Chapter 9 –Sintering of CGO with Sintering Aids

9.1. Introduction

In the last chapter it was established that both Cu and Co are effective sintering aids for CGO. The first half of this chapter discusses the effect that different levels of these additives have on the densification of CGO. This was investigated using dilatometry, a brief review of this technique will be presented at the start of this chapter. In the literature, it has been reported that Fe is a good sintering aid to ceria, and therefore its ability to enhance the densification of CGO was also investigated. The second half of this chapter presents an argument to explain why Co additives enhance the sintering of Gd doped ceria. Due to the complex nature of the densification process a variety of experimental techniques was used. Comparisons are made with the results of Kleinlogel and Gauckler for CoCGO20. Grain growth in CGO sintered to high density at low temperatures with Co additives was also investigated.

9.2. Dilatometry

Dilatometry is generally the method used to investigate the sinterability of ceramic powders. Two heating schedules were employed in the sintering studies performed in this thesis. In the first case, the powder compact was heated to a fixed sintering temperature and held at this allocated temperature for a specified time, and finally cooled to room temperature. This schedule is referred to as isothermal sintering. In the other case, referred to as constant heating rate (CHR) sintering, the compact is heated at a fixed rate to the required temperature, after which it is cooled. Theoretically, isothermal sintering is generally considered the better technique as data can be more easily compared to standard sintering models. CHR sintering is more difficult to analyze as the mechanisms of sintering may change over the temperature range studied. However, densification of a material fired from a green state to high density can be characterized easier using CHR dilatometry. Furthermore, as indicated in section 1.2, to reduce oxidation of the stainless steel support the CGO electrolyte is required to achieve high density after minimal time at maximum firing temperature (ideal scenario is high

density achieved after 0 hold time between 900-1000°C). It is for this reason that the majority of the sintering studies of CoCGO and CuCGO were performed using CHR dilatometry.

Figure 9.1 shows the linear shrinkage versus temperature for CHR sintering of CGO at 10K/min up to 1400°C. At temperatures below 600°C, there is no detectable shrinkage of the specimen. Above this temperature, there is an increase in shrinkage until a plateau is reached at high temperature. The onset of this plateau (~1200°C) is considered to be the point at which the sample has high density (>95%).

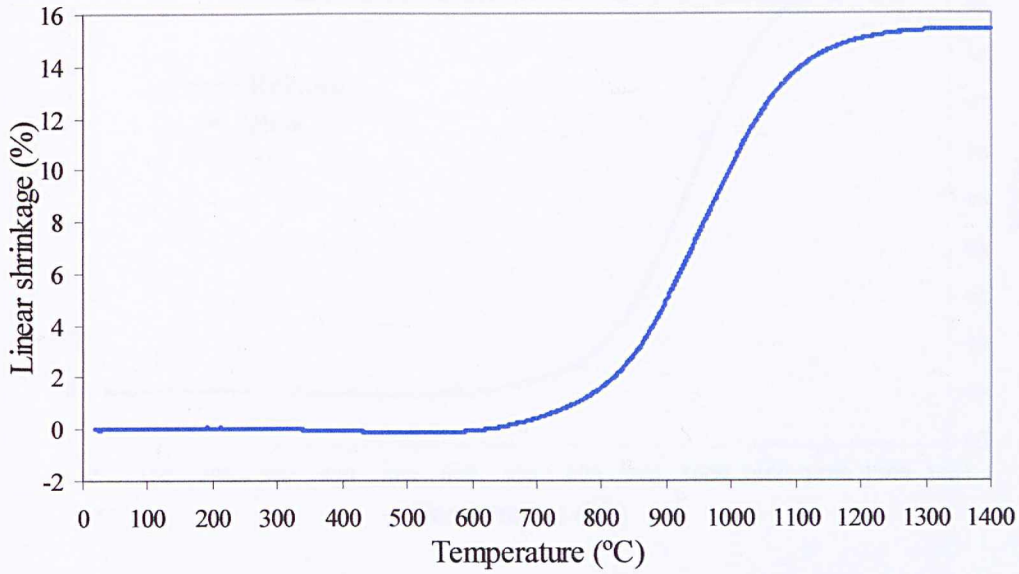


Figure 9.1 Linear shrinkage versus temperature for CGO at 10K/min in air.

The amount of linear shrinkage on completion of densification is inversely proportionally to the starting green density. It is of more practical value when comparing the sinterability of different powders to compare the relative density as a function of temperature. This enables the powders all to have a common reference point to which they can be compared.

If the mass of the powder compact remains constant and the shrinkage is isotropic, the relative density (ρ_r) can be determined from the dilatometry data using equation 9.1:

$$\rho_r = \frac{\rho_o}{(1 - \Delta L/L_o)^3} \qquad (9.1)$$

where ρ_o is the initial relative density of the compact, ΔL and L_o are the change and initial length of the sample respectively. Figure 9.2 shows that the relative density from the data presented in figure 9.1 is almost identical to the bulk density measured after samples were fired at the same heating rate (10K/min) to designated temperature and held for zero time prior to cooling at 10K/min. The excellent agreement between the density values and the fact that there is virtually no weight change during firing indicates that the shrinkage of CGO is isotropic. All materials studied in this thesis showed excellent agreement between calculated values of bulk and relative density.

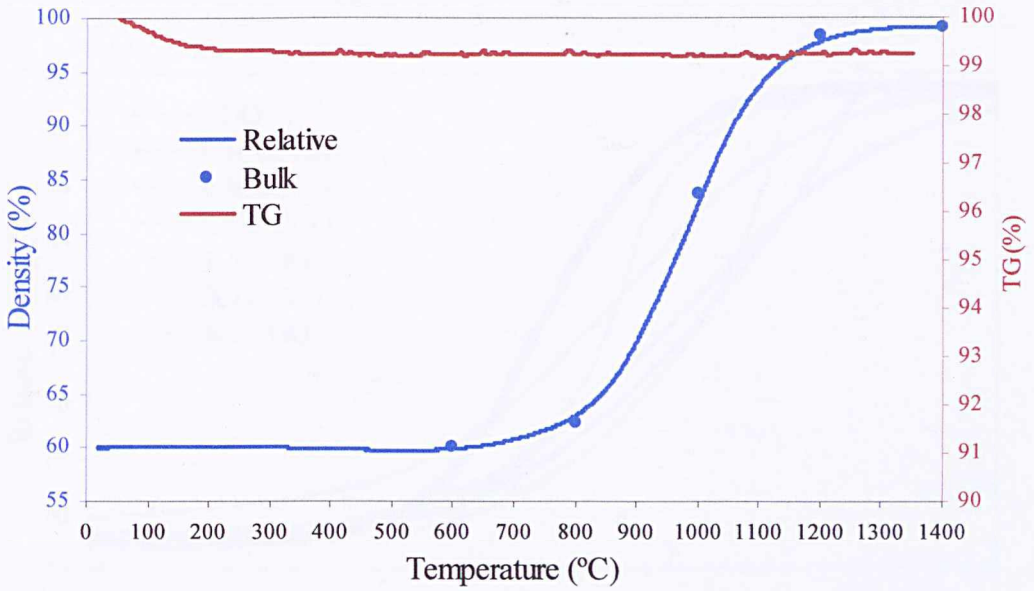


Figure 9.2 Relative density from dilatometry data (10K/min), bulk density and TG as a function of temperature for CGO.

9.2.1. Co Additions to CGO: CHR Dilatometry

Figure 9.3 is a plot of relative density as a function of temperature for Co additions to CGO powders fired in air. Additions of Co greater than 0.1% significantly enhance the densification of CGO (i.e. samples highly dense <1150°C). As the level of Co additive increases, so does the sinterability of the powder up to 2%. Compared to the 2%Co level, further Co additions do not enhance the densification.

Particle size measurements revealed that average particle size of CGO (dispersed in ethanol and heat treated at 650°C for 30 minutes) was 0.87μm. Whilst figure 9.4a indicates that the CGO powder consisted of agglomerates, it was found that they were broken down when ultrasonically dispersed prior to particle size analysis. The average

particle size of the as-received CGO and CGO dispersed in ethanol and treated at 650°C for 30 minutes were identical, thus indicating that these agglomerates were soft. Experimentally, it was found that the green density of both these materials (isostatically pressed at 300MPa) were the same (~60%). The average particle size of 0.1CoCGO and 0.3CoCGO powder calcined at 650°C was 0.91μm. The average particle size of CGO with additions of Co in excess 0.3% (calcined at 650°C) were approximately 0.94μm. This indicates that the addition of Co to CGO (calcined at 650°C) does not result in the formation of significant hard agglomerates.

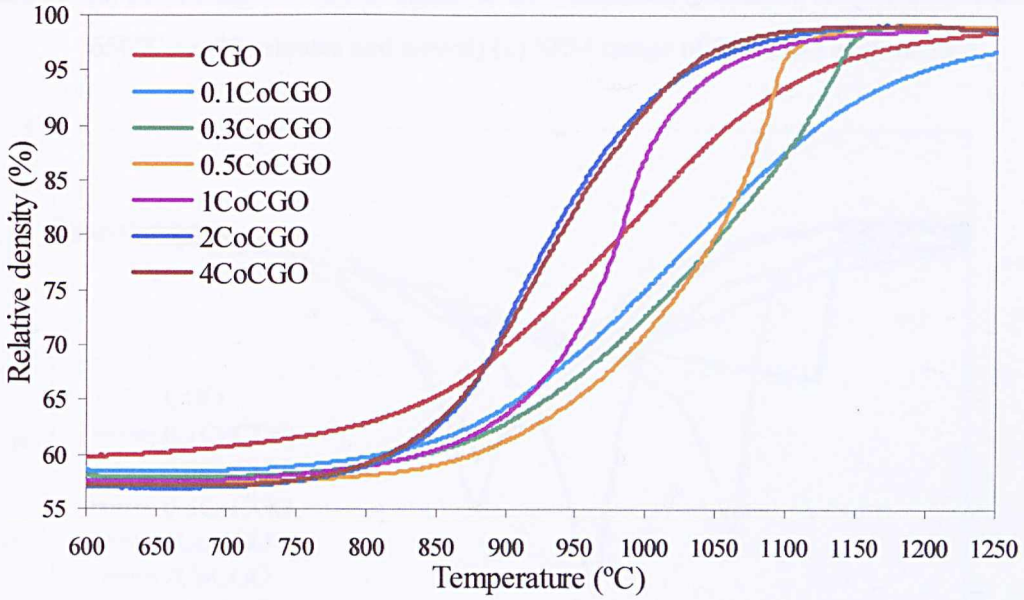


Figure 9.3 Relative density of Co additions to CGO as a function temperature by CHR dilatometry (10K/min).

Figure 9.4a shows that the surface of a CGO agglomerate has a relatively smooth surface compared to a similarly sized agglomerate from 2CoCGO powder (Figure 9.4b). As the only difference between the powders in figure 9.4 is the introduction of Co, the more irregular surface of 2CoCGO is believed to result from the Co addition. It is widely known that irregular shapes pack poorly due to interparticle friction. Therefore, it is suggested that the more irregular surfaces lower the green density of CoCGO compared to CGO without additive (Figure 9.3). The effect of agglomeration and green density on the densification of CGO and 2CoCGO will be discussed in more depth in chapter 11.

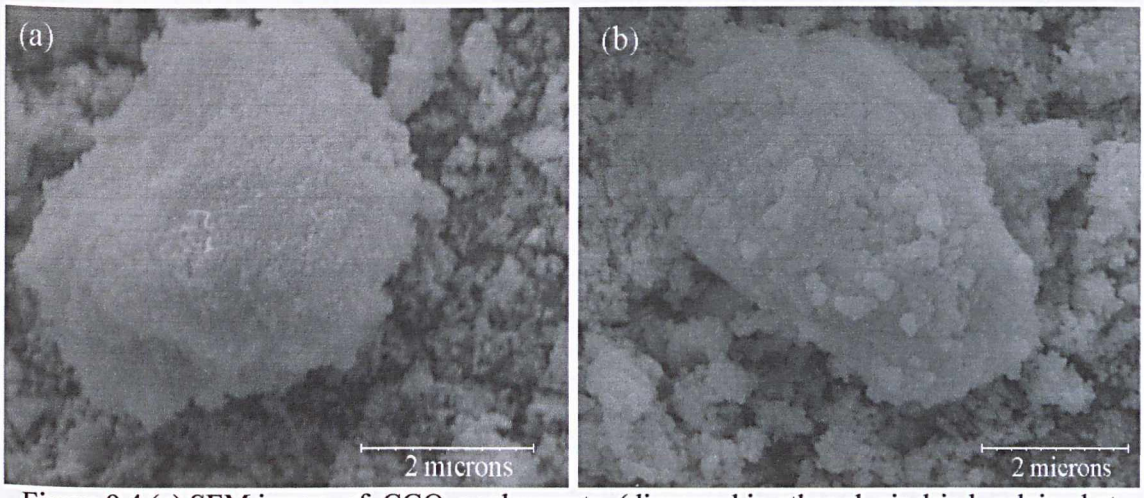


Figure 9.4 (a) SEM image of CGO agglomerate (dispersed in ethanol, air dried, calcined at 650°C for 30 minutes and sieved) (b) SEM image of 2CoCGO agglomerate.

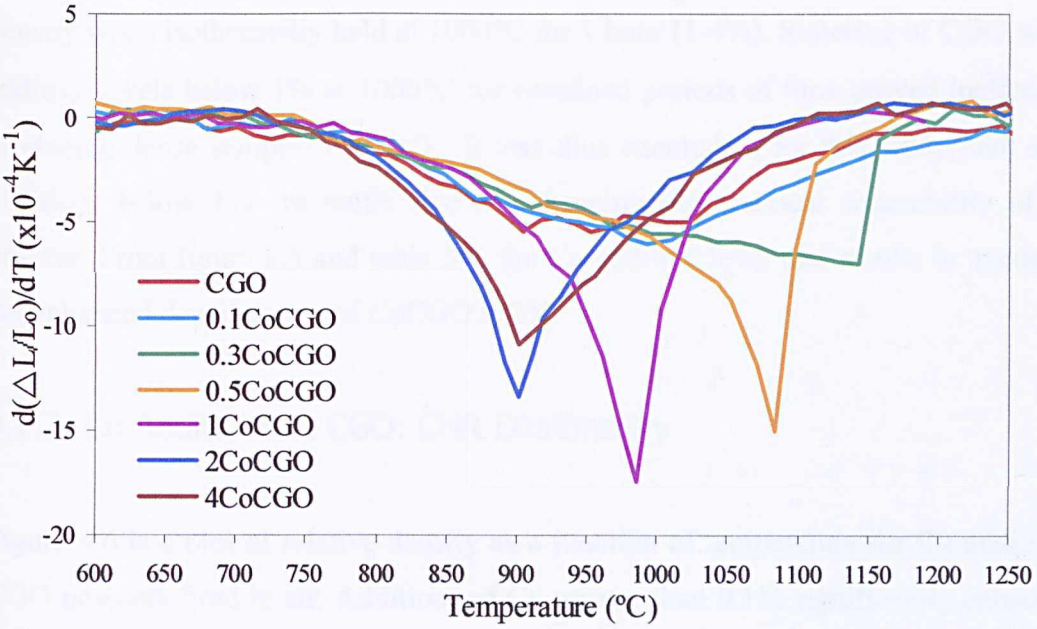


Figure 9.5 Linear differential shrinkage as a function of temperature for Co additions to CGO.

Co addition (%)	T_{max} (°C)	$(d(\Delta L/L_o)/dT)$ at T_{max} ($x10^{-4}K^{-1}$)
0	950	-5.4±0.1
0.1	993	-5.7±0.1
0.3	1143	-7.0±0.1
0.5	1084	-15.0±0.1
1	985	-17.4±0.1
2	902	-13.4±0.1
4	902	-10.8±0.1

Table 9.1 T_{max} and $(d(\Delta L/L_o)/dT)$ at T_{max} for Co additions to CGO powders.

Figure 9.5 shows the linear differential shrinkage ($d(\Delta L/L_o)/dT$) as a function of temperature for different Co additions to CGO. Lange [1] suggests that densifying mechanisms dominate the sintering up to the maximum shrinkage rate, and for densities above this value the sintering is influenced by nondensifying mechanisms, such as grain growth. It is observed in table 9.1 that the temperature of maximum differential shrinkage (T_{max}) depends on the concentration of Co additive. Moreover, it is observed that above T_{max}, the shrinkage rate decreases faster for decreasing Co additions (0.3-4% Co). This indicates that the transition from densifying processes to nondensifying processes is more critical when CGO has a low concentration of Co additive. Similar observations were reported for Ti additions to MnO_2 [2] and Co to CGO20 [3].

It was found that samples that had T_{max} values below 1000°C could be sintered to high density when isothermally held at 1000°C for 1 hour (1-4%). Sintering of CGO with Co additive levels below 1% at 1000°C for sustained periods of time proved ineffective at producing dense samples of CGO. It was thus concluded, for this study, that sample additions below 1% are ineffective at enhancing the practical sinterability of CGO powder. From figure 9.5 and table 9.1, the Co additive level that results in maximising the enhanced densification of CoCGO is 2%.

9.2.2. Cu Additions to CGO: CHR Dilatometry

Figure 9.6 is a plot of relative density as a function of temperature for Cu additions to CGO powders fired in air. Additions of Cu greater than 0.1% significantly enhance the densification of CGO. As the level of Cu additive increases, likewise does the sinterability of the powder upto 4%.

The green density of CuCGO samples was lower than the CoCGO samples for a similar additive level and the average particle size of CuCGO was slightly larger than for the corresponding CoCGO powder. For example, the average particle size of 2CoCGO and 2CuCGO (calcined at 650°C) were 0.94μm and 0.98μm respectively and the packing efficiency of CuCGO was lower. As previously mentioned in chapter 8, 'over firing' of CuCGO (0.3-4%) results in a reduction in the relative density. The temperature for the onset of this reduction in 0.5CuCGO and 1CuCGO-4CuCGO is 1100°C and 1030°C respectively. A similar trend was reported for 3YSZ with additions of Cu in excess of 0.3% [4]. The possible vaporisation of $Y_2Cu_2O_5$ was suggested to be responsible by

creating pressure within closed pores. DTA (Figure 9.7) shows an endothermic peak occurring in 2CuCGO at ~1040°C, which corresponds to the expected transformation temperature of CuO to Cu_2O in air [4]. The graph does not reveal the presence of a liquid phase. It was reported that 1%Fe additions to ceria enhanced its densification [5]. Overfiring of dense $FeCeO_2$ specimens reduced the relative density from 99% to ~90% (similar to the behaviour observed in figure 9.6) and microcracks were observed at the grain boundaries. Visual inspection of a 4CuCGO pellet fired at 1400°C for 5 hours also indicated the presence of microcracks on the surface.

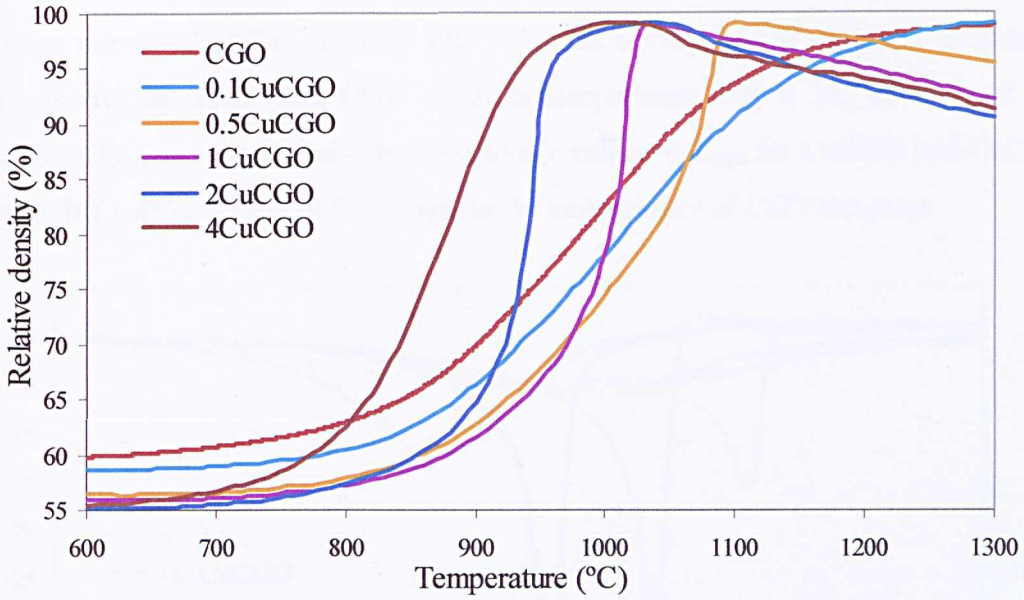


Figure 9.6 Relative density of CuCGO as a function of temperature by CHR dilatometry (10K/min).

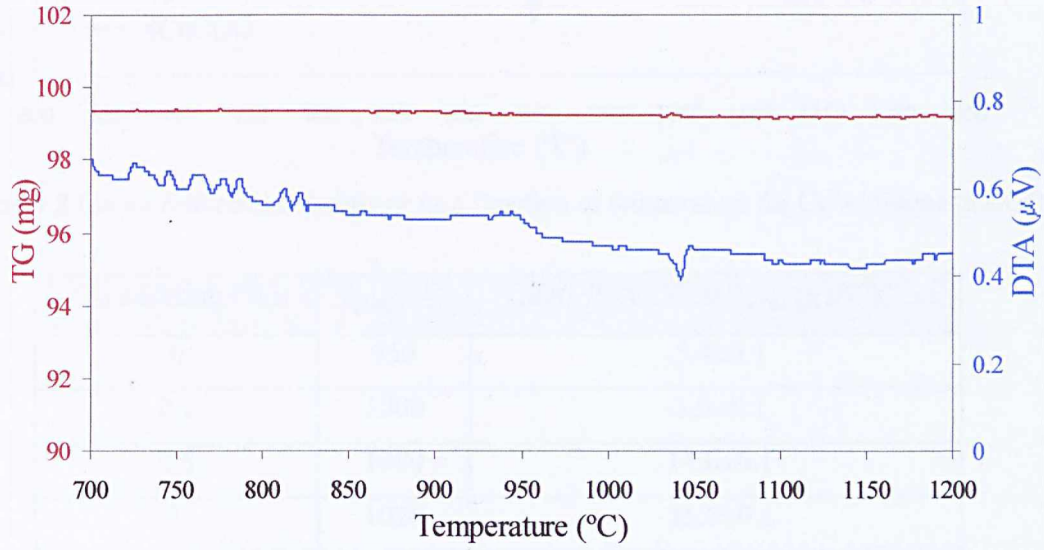


Figure 9.7 DTA/TG of 2CuCGO at 10K/min in air.

As observed for CoCGO, figure 9.8 indicates that the influence of nondensifying mechanisms is more critical when CGO has a low concentration of Cu additive. Table

9.2 shows that T_{max} and the magnitude of the shrinkage rate at T_{max} for CuCGO are comparable to CoCGO for additions below 1%. T_{max} for 1CuCGO and 2CuCGO are slightly higher than for their CoCGO counterparts. Whilst T_{max} indicates the temperature at which the maximum shrinkage rate occurs, the magnitude of shrinkage rate is significantly greater for 1CuCGO and 2CuCGO compared to adding the same amount of Co to CGO. A combination of both these factors must be considered when comparing the densification behaviour. For example, T_{max} of 2CoCGO is 902°C and has an associated shrinkage rate of $-13.51 \times 10^{-4} K^{-1}$. Whilst T_{max} of 2CuCGO is 950°C, the shrinkage rate associated with this temperature is $-39.14 \times 10^{-4} K^{-1}$. At 902°C, the shrinkage rate of 2CuCGO is $-7.45 \times 10^{-4} K^{-1}$, thus a 2% addition of Co is considered more effective at densifiying CGO at lower temperature than a 2% addition of Cu. Comparing T_{max} and the magnitude of shrinkage values at T_{max} for CoCGO and CuCGO suggests that a 4% addition of Cu enhances the sinterability of CGO the most.

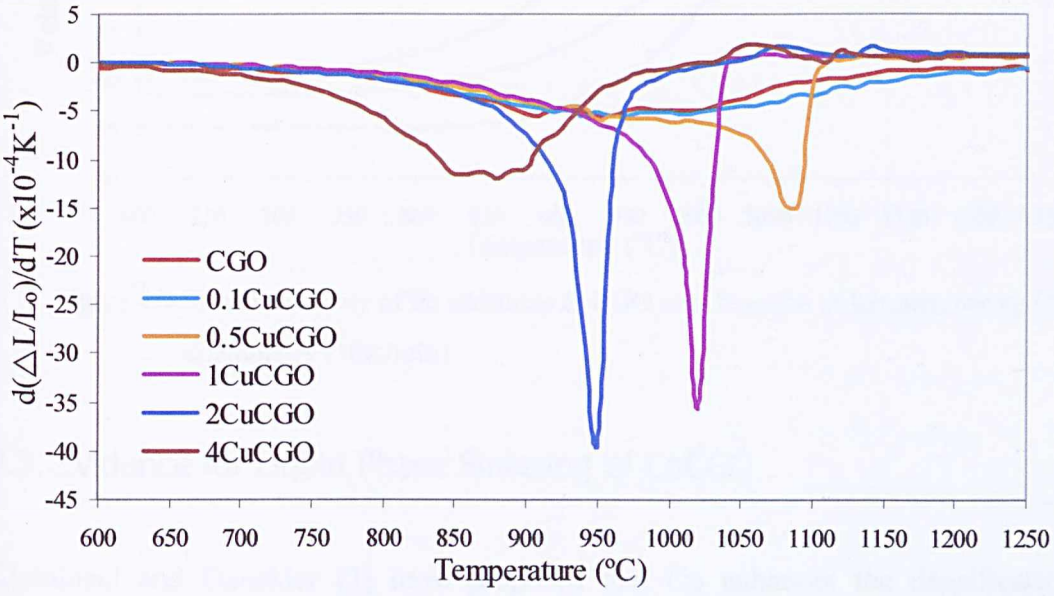


Figure 9.8 Linear differential shrinkage as a function of temperature for Cu additions to CGO.

Cu addition (%)	T_{max} (°C)	$(d(\Delta L/L_o)/dT)$ at T_{max} ($x10^{-4}K^{-1}$)
0	950	-5.4±0.1
0.1	1000	-5.0±0.1
0.5	1080	-14.6±0.1
1	1020	-35.6±0.1
2	950	-39.1±0.1
4	880	-12.0±0.1

Table 9.2 T_{max} and $(d(\Delta L/L_o)/dT)$ at T_{max} for Cu additions to CGO powders.

9.2.3. Fe Additions to CGO: CHR Dilatometry

Sintering studies of Fe additions to CGO were performed as previously discussed for CoCGO and CuCGO. Figure 9.9 indicates that Fe is not effective at enhancing the densification of CGO as high density (>95%) for 2FeCGO was only achieved at approximately the same temperature as CGO when heated at a CHR of 10K/min. Similar observations were reported by Kleinlogel and Gauckler [3] for 1FeCGO20.

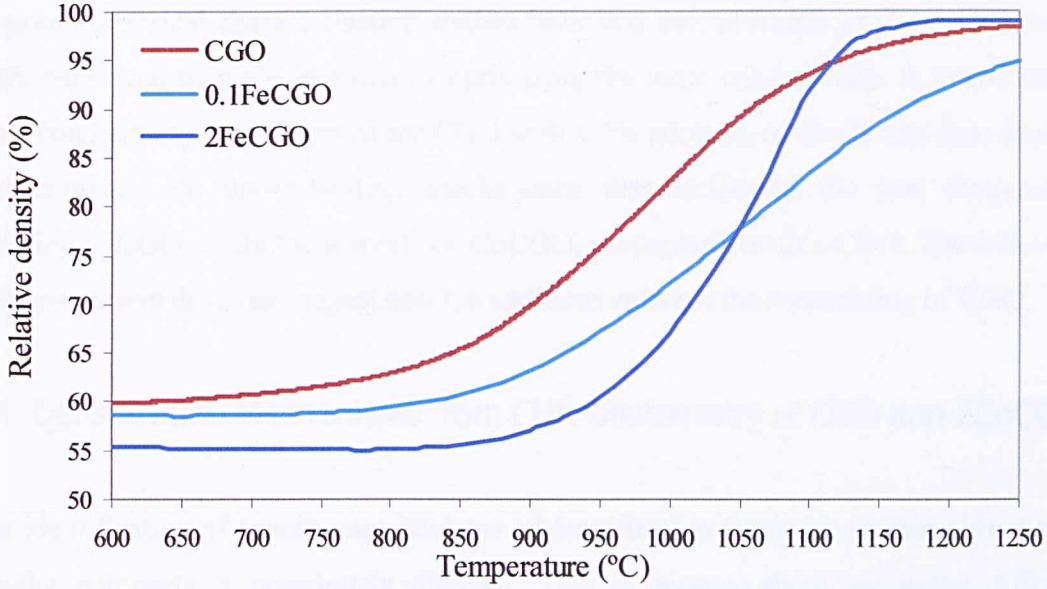


Figure 9.9 Relative density of Fe additions to CGO as a function of temperature by CHR dilatometry (10K/min).

9.3. Evidence for Liquid Phase Sintering of CoCGO

Kleinlogel and Gauckler [3] have proposed that Co enhances the densification of CGO20 by forming a liquid phase at approximately 850°C. They acknowledge that this temperature is significantly lower than the eutectic temperature in the CoCGO20 system (1420°C). They argued that since the Co is present as a thin coating on the surface of very small CGO20 particles the eutectic temperature will be lowered thus allowing the material to densify by a liquid phase mechanism. It is plausible to expect a reduction in the eutectic temperature by reducing particle or film thickness but this seems to be too large a reduction. Furthermore this does not explain why CGO can be sintered to >95% density at 1000°C by solid state addition of relatively coarse Co_2O_3 powder with an average particle size of ~2.5μm (section 8.3).

A series of thermal analysis (DTA) experiments was performed on CoCGO and CuCGO. No evidence of liquid phases was detectable between 20-1300°C. Similar observations were also recently reported for ceria with small additions of Co [6]. Kleinlogel and Gauckler, whilst claiming that liquid phase sintering was the method of densification for CoCGO20, have not presented any convincing experimental evidence for the existence of a liquid phase in the CoCGO20 system below 1000°C.

Whilst performing sintering studies on the enhanced sintering of CoCGO and CuCGO, on-going electrical characterisation studies indicated that additions of Co to CGO were more beneficial than Cu in terms of optimising the ionic conductivity. A maximum in ionic conductivity was observed for CGO with a 2% addition of Co. It was thus decided that emphasis on understanding mechanisms that facilitated the low temperature sintering of CGO would focus solely on CoCGO, particularly on 2CoCGO. The following sections present data that suggest how Co additions enhance the sinterability of CGO.

9.4. Densification Mechanisms from CHR Dilatometry of CGO and 2CoCGO

The identification of specific mechanisms of densification from the sintering kinetics of powder compacts is notoriously difficult. This is because there are many different microstructural configurations that change as a function of sintering time and temperature. These include powder morphology, grain size and elemental distributions. Many of these properties, however, do not significantly change during the initial sintering (i.e. low shrinkage values). It was observed in section 9.2.1 that additions of Co significantly aid densification of CGO from the onset of shrinkage. Therefore, analysis of the initial stage sintering can help identify why Co enhances the densification of CGO.

Bannister [7] suggested a general equation for isothermal initial-stage sintering:

$$\frac{d}{dt}(\Delta L/L_o) = A_o \exp\left(-\frac{Q}{RT}\right)/(\Delta L/L_o)^m \qquad (9.2)$$

where A_o is a constant depending only on material parameters. The exponent, m, has values of m=0 for a viscous flow mechanism, m=1 for a volume diffusion mechanism and m=2 for a grain boundary diffusion mechanism. Based on equation 9.2, Young and Cutler [8] developed the following equation under a CHR condition:

$$(\Delta L/L_o)/T = A_1 \exp\left[-\frac{Q}{(m+1)RT}\right] \quad (9.3)$$

The natural logarithmic form of equation 9.3 is:

$$\ln(\Delta L/L_o)/T = -\frac{Q}{(m+1)R}\frac{1}{T} + \ln A_1 \quad (9.4)$$

If m is known, the apparent activation energy, Q, can be calculated from the slope of $\ln[(\Delta L/L_o)/T]$ versus 1/T. Woolfrey and Bannister [9] suggested that m can be determined by integrating equation 9.2:

$$(\Delta L/L_o)_T = A_2 C^{-\frac{1}{m+1}} \quad (9.5)$$

where $(\Delta L/L_o)_T$ is relative shrinkage at a particular temperature and, C, is the heating rate. The natural logarithmic form of equation 9.5 is:

$$\ln(\Delta L/L_o)_T = -\frac{\ln C}{m+1} + \ln A_2 \quad (9.6)$$

Therefore, the gradient of $\ln(\Delta L/L_o)T$ versus lnC enables m to be determined from the slope [-1/(m+1)]. It was commented that the geometric models on which these initial-stage sintering equations are based break down at approximately 5-6% shrinkage [9].

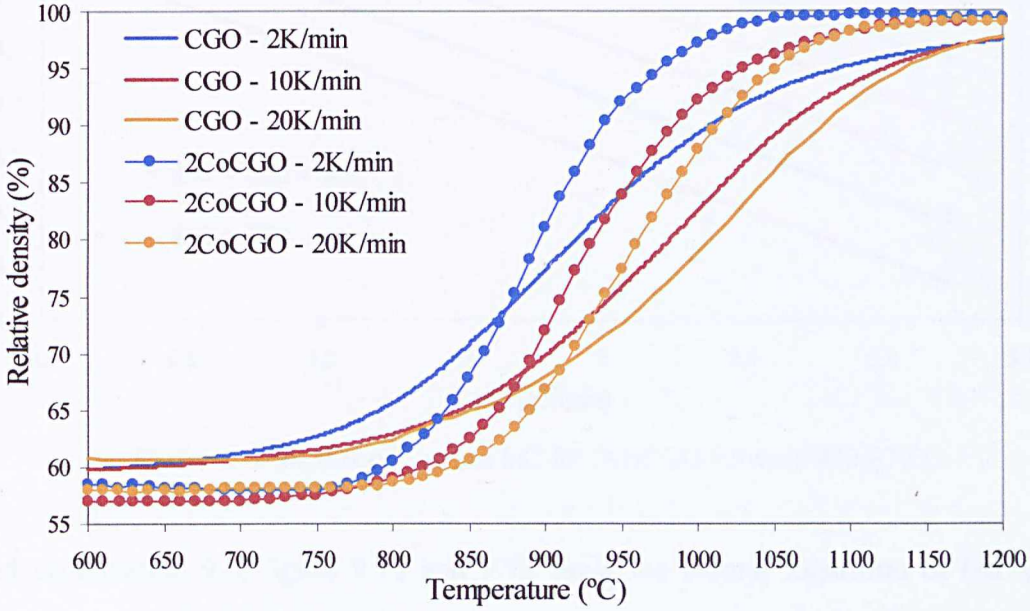


Figure 9.10 Relative density of CGO and 2CoCGO as a function of temperature by CHR dilatometry at 2K/min, 10K/min and 20K/min.

Figure 9.10 shows the relative density of CGO and 2CoCGO when fired at different values of C. The densification of both samples shifts to the left when C is reduced as the material has more time to densify at each indicated temperature.

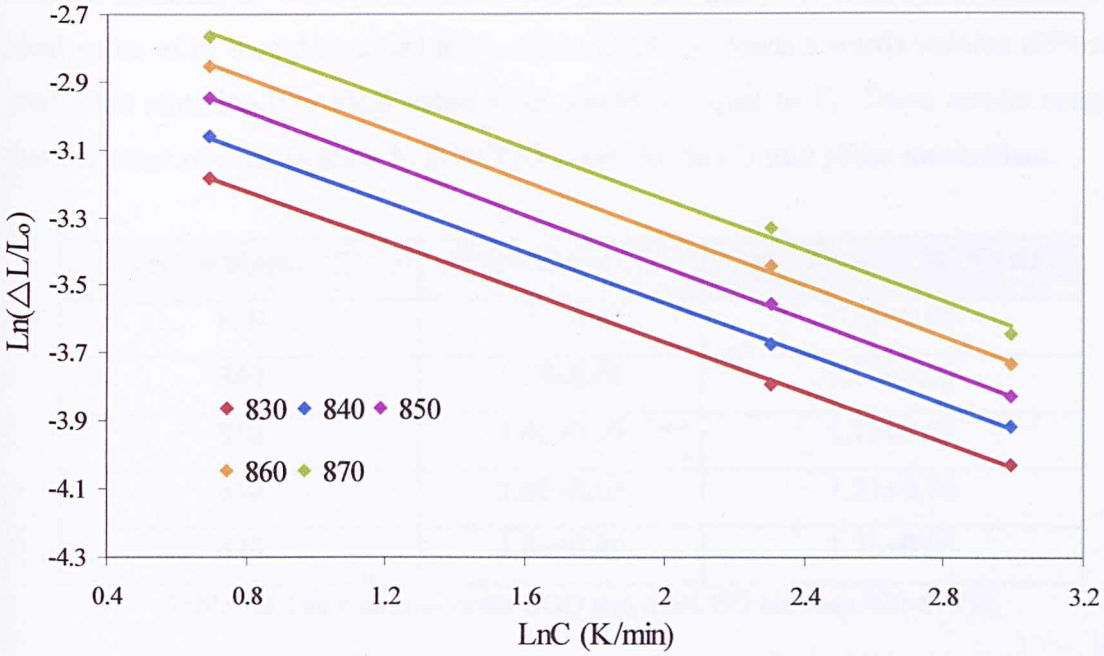


Figure 9.11 ln(ΔL/Lo)T versus lnC for CGO between 830-870°C.

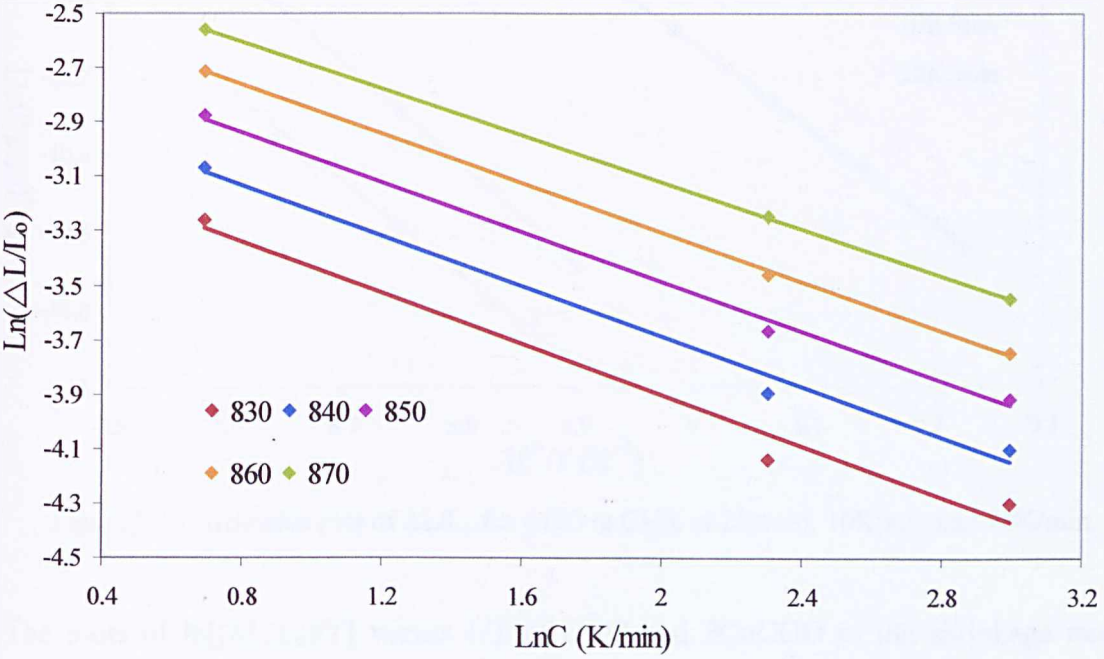


Figure 9.12 ln(ΔL/Lo)T versus lnC for 2CoCGO between 830-870°C.

Based on equation 9.6, figure 9.11 and 9.12 show the natural logarithm of $(\Delta L/L_o)_T$ versus natural logarithm of C for CGO and 2CoCGO respectively. The values of $(\Delta L/L_o)_T$, obtained from figure 9.10, corresponded to shrinkage values during initial

stages of densification. The values of m calculated from the slope of [-1/(m+1)] in figures 9.11 and 9.12 are listed in table 9.3. The average values of m between 830-870°C for CGO and 2CoCGO are 1.68±0.03 and 1.23±0.03 respectively. This suggests that the sintering of CGO tends towards a grain boundary controlled mechanism (the ideal value of m would be equal to 2) whilst 2CoCGO tends towards volume diffusion controlled sintering (the ideal value of m would be equal to 1). These results suggest that the onset of densification in 2CoCGO is not due to a liquid phase mechanism.

Temperature (°C)	m values for CGO	m values for 2CoCGO
830	1.71±0.05	1.13±0.05
840	1.68±0.05	1.17±0.05
850	1.62±0.05	1.18±0.05
860	1.62±0.05	1.21±0.05
870	1.66±0.05	1.33±0.05

Table 9.3 The values of m for CGO and 2CoCGO between 830-870°C.

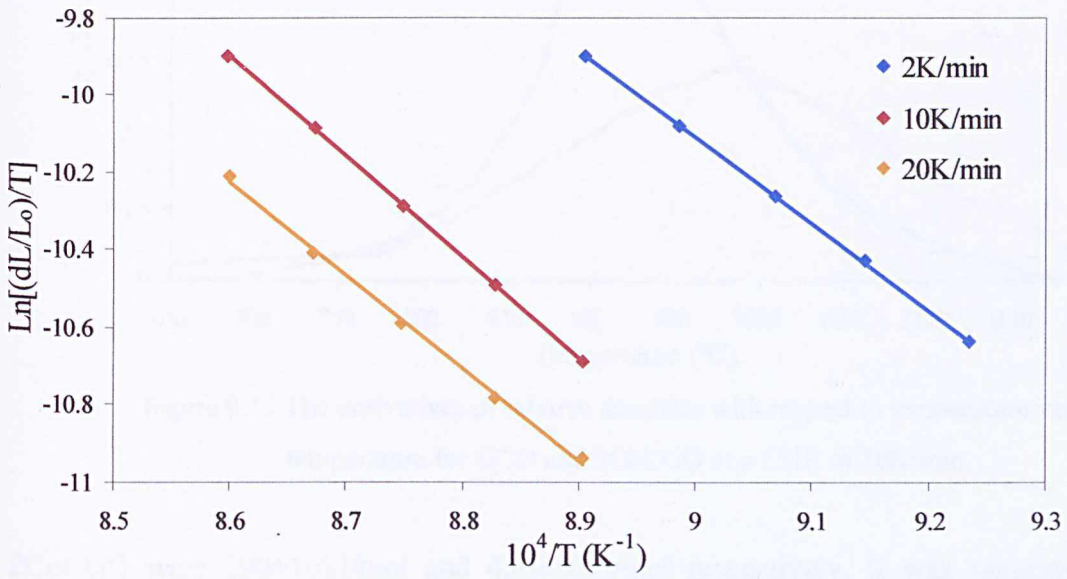


Figure 9.13 Arrhenius plot of $\Delta L/L_o$ for CGO at CHR of 2K/min, 10K/min and 20K/min.

The plots of $\ln[(\Delta L/L_o)/T]$ versus 1/T of CGO and 2CoCGO in the shrinkage range from 2-5% are presented in figures 9.13 and 9.14. From equation 9.4, the slope is equal to [-Q/(R(m+1)]. It can be seen from both figures that the three different heating rates give approximately the same slope indicating that only one sintering mechanism dominates. Using the average value m for CGO and 2CoCGO, the average value of the three slopes was used to calculate Q. The apparent activation energy of CGO and

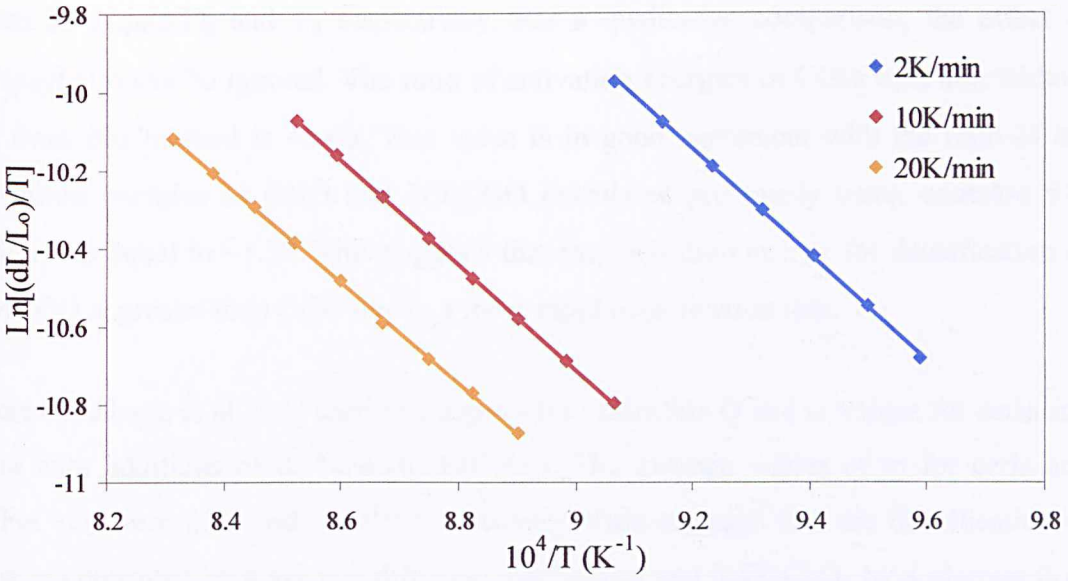


Figure 9.14 Arrhenius plot of $\Delta L/L_o$ for 2CoCGO at CHR of 2K/min, 10K/min and 20K/min.

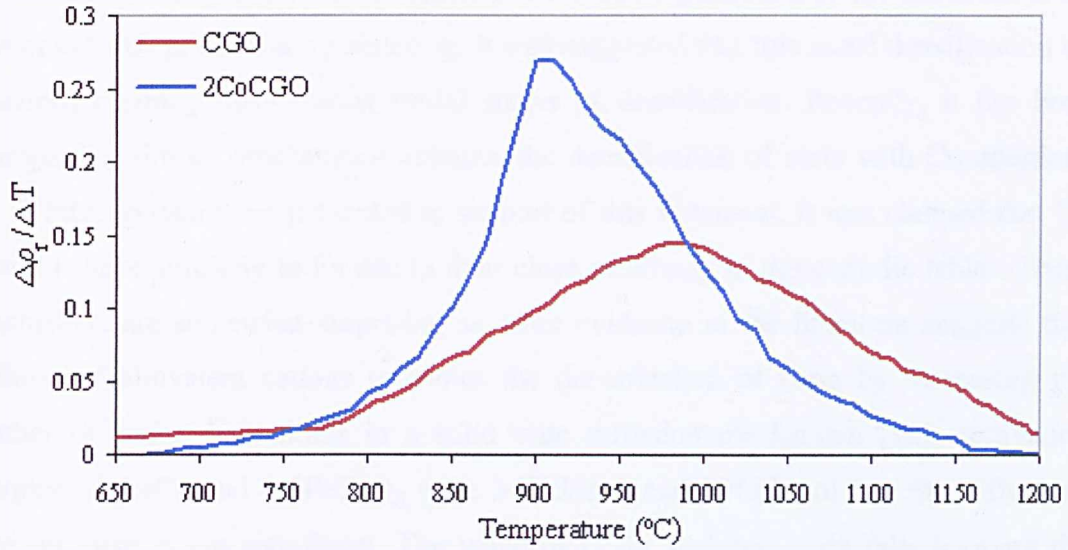


Figure 9.15 The derivatives of relative densities with respect to temperature versus temperature for CGO and 2CoCGO at a CHR of 10K/min.

2CoCGO were 290±10kJ/mol and 430±10kJ/mol respectively. It was suggested by Wang et al. [10] that Q_s is related to the densification rate by:

$$\frac{Q}{R} = T_p^2 \left(\frac{\Delta\rho}{\Delta T}\right)_p \left[\frac{-f'(\rho)}{f(\rho)}\right]_p \qquad (9.7)$$

where T is temperature and it is assumed that Q»RT and $f'(\rho)$ is the derivative of $f(\rho)$ with respect to ρ and p indicates the maximum peak value. Figure 9.15 shows the derivative of density with respect to temperature versus temperature for CGO and 2CoCGO at a CHR of 10K/min. Each curve exhibits a peak, the height and position are

given by $(\Delta\rho_r/\Delta T)_p$ and T_p respectively. For a qualitative comparison, the effect of $[f'(\rho)/f(\rho)]p$ can be ignored. The ratio of activation energies of CGO with and without Co from this method is ~1.60. This value is in good agreement with the ratio of the activation energies of CGO and 2CoCGO calculated previously using equation 9.4, which was equal to ~1.50. This suggests that the activation energy for densification of 2CoCGO is greater than CGO due to a more rapid densification rate.

Recently, Zhang et al. [11] used this approach to calculate Q and m values for ceria and ceria with additions of 0.5%Fe ($0.5FeCeO_2$). The average values of m for ceria and $0.5FeCeO_2$ were 0.97 and –0.019 respectively. This suggests that the densification of ceria is controlled by a volume diffusion mechanism and $0.5FeCeO_2$ by a viscous flow mechanism. It was proposed that the addition of Fe to ceria, which enhanced the densification, changed the surface tension of the CeO_2 grains due to the diffusion of Fe ions onto CeO_2 grains during sintering. It was suggested that this aided densification by enhanced rearrangement during initial stages of densification. Recently, it has been claimed that similar mechanisms enhance the densification of ceria with Co additions [6]. Whilst no data were presented in support of this statement, it was claimed that Co should behave similarly to Fe due to their close proximity in the periodic table. These conclusions are somewhat surprising as other evidence in the literature suggests that addition of aliovalent cations promotes the densification of ceria by increasing the number of cation interstitials in a solid state diffusion mechanism [12]. Activation energies of CeO_2 and $0.5FeCeO_2$ were 365kJ/mol and 396kJ/mol but the difference between them is not significant. The value of Q for undoped ceria falls between the values for CGO and 2CoCGO from the present study.

9.5. TEM of 2CoCGO

Samples were prepared and analysed using TEM in accordance with section 7.15. One of the samples was investigated using EDX at the University of Brisbane, Australia. The aim of which was to determine the location of the Co in CGO post sintering.

TEM revealed that the grain size of 1CoCGO sintered to high density at 1000°C ranged from approximately 20-500nm (Figure 9.16). Figure 9.17 shows the microstructure of 2CoCGO sintered at 930°C for 4 hours and has an average grain size of approximately 200nm. Both figures reveal the absence of any significant porosity. Kleinlogel and

Gauckler reported that the average grain size of 2CoCGO20 sintered to high density at 900°C was <120nm. It is presumed that the slightly higher sintering temperature required to densify CoCGO increases the average grain size. However, the grains in dense 2CoCGO are significantly finer than in dense CGO (1-3μm) as a result of the lower sintering temperature.

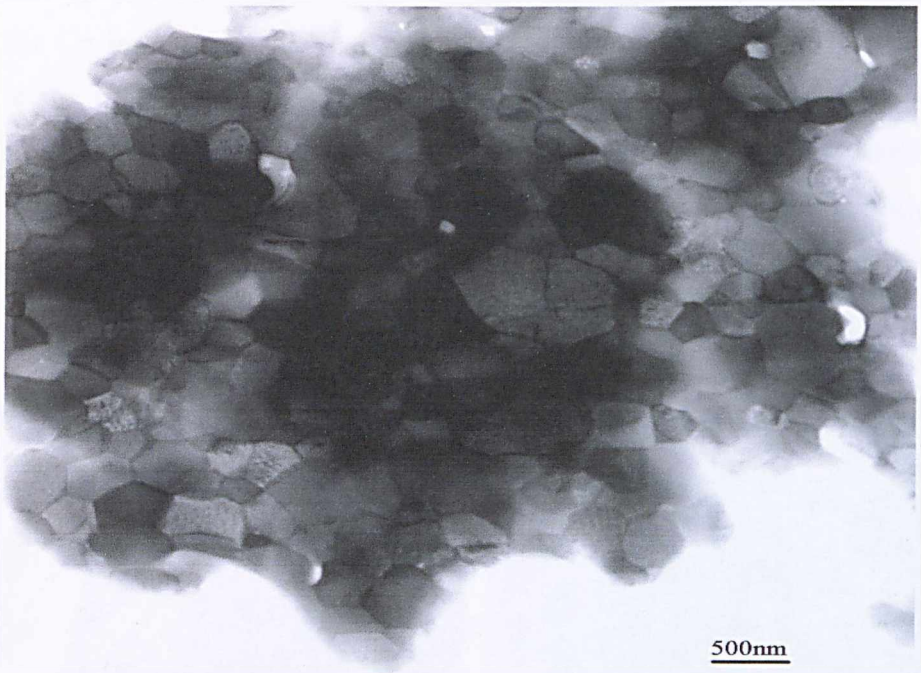


Figure 9.16 TEM micrograph of 1CoCGO sintered to high density at 1000°C for 1 hour in air.

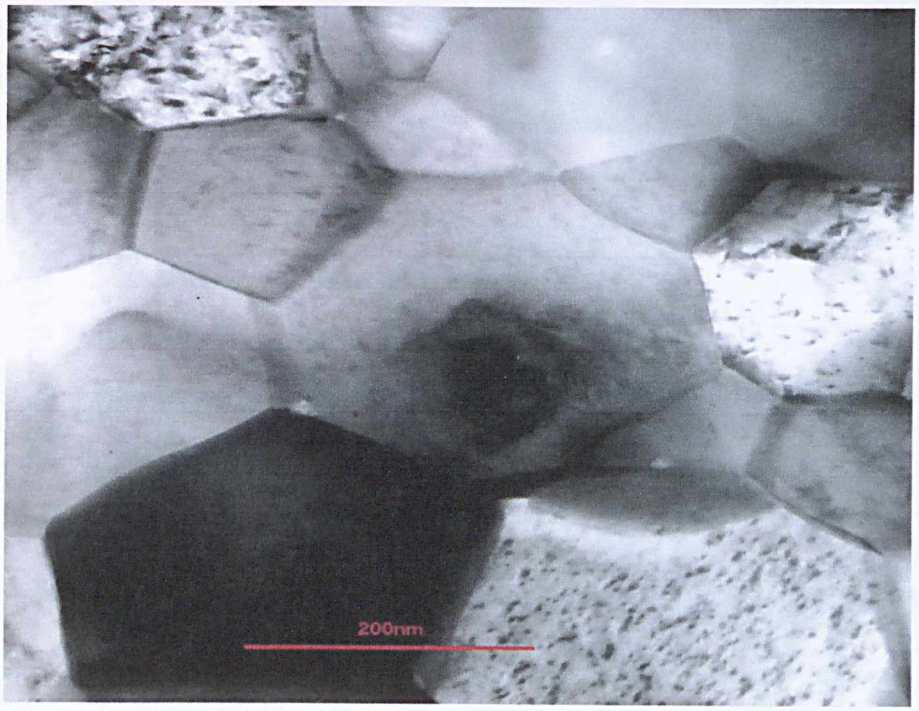


Figure 9.17 TEM micrograph of 2CoCGO sintered to high density at 930°C for 4 hours in air.

Kleinlogel and Gauckler reported the presence of an amorphous cobalt oxide grain boundary film of 2-4nm width after interrupting the sintering of 1CoCGO20 at 900°C after 10 minutes. Figure 9.18b shows an EDX map of the Co X-rays in a grain of 2CoCGO fired at 980°C for 12 hours and furnace cooled. It is clearly seen that the Co distribution is concentrated at the triple points of the grain boundaries. From figure 9.18c, the top part of the grain has a Co rich layer that is approximately 15nm thick whilst the Co layer on the bottom side of the grain is barely detected. If the Co rich phase at the grain boundary had enhanced the sintering of CGO by a liquid phase mechanism, it is expected that the entire grain boundary (or a large portion) would be wetted with Co. Figure 9.18c also shows that the Gd concentration is slightly larger in the region that is enriched in Co. On the side of the grain that has a small Co concentration, there is no evidence of Gd enrichment.

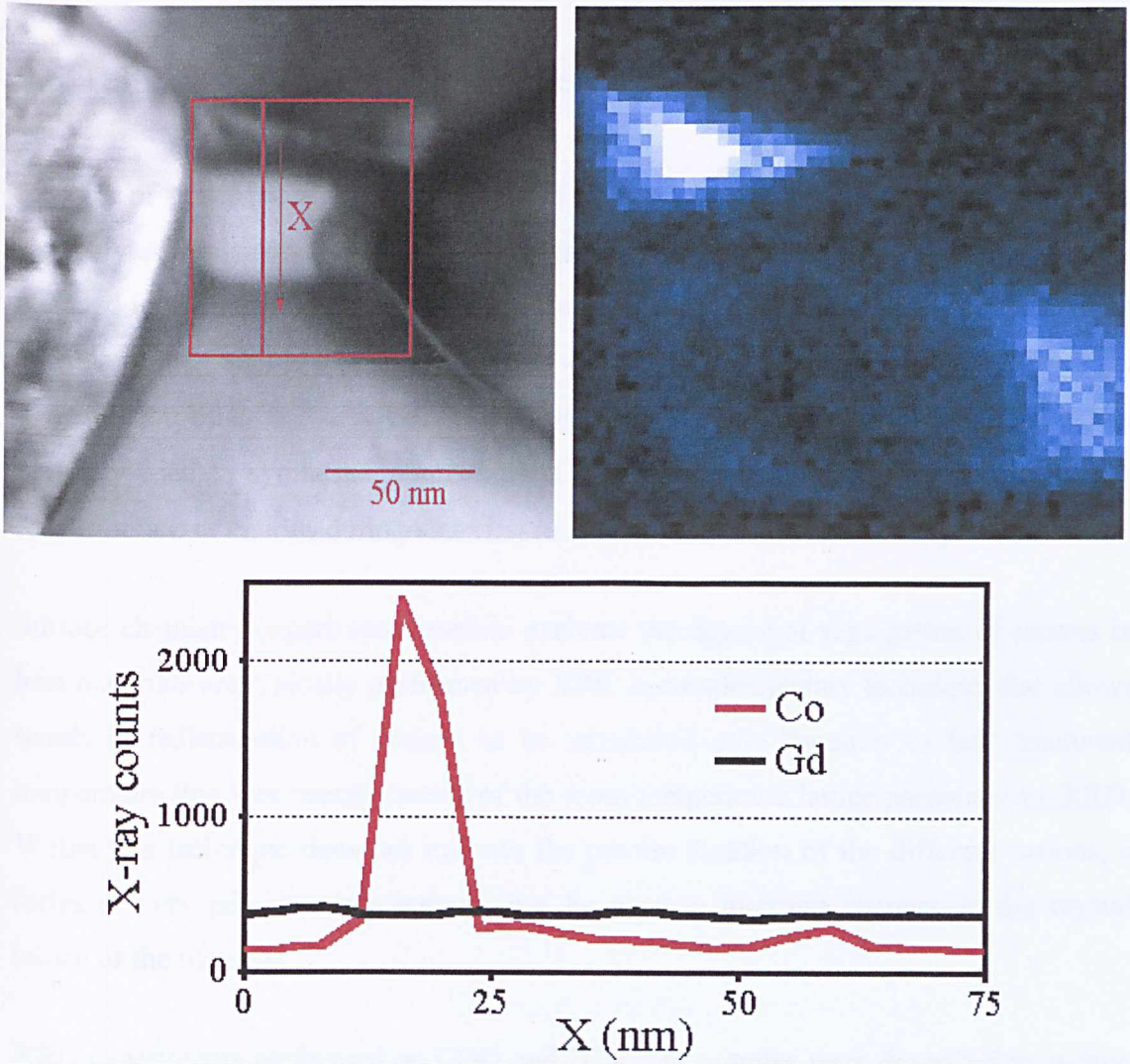


Figure 9.18 (a) TEM micrograph of grain in 2CoCGO fired at 980°C for 12 hours and furnace cooled (b) EDX map of Co X-rays inside box area in (a) (c) EDX line scan of Co and Gd concentration across grain in (a).

The relatively thin layers of electrolytes used in SOFC's are generally considered to have poor mechanical properties. The tensile fracture strength, σ_{TS}, of a ceramic is approximately:

$$\sigma_{TS} = \frac{K_{IC}}{\sqrt{\pi a}} \qquad (9.8)$$

where a is the inherent flaw size and K_{IC} is the fracture toughness. Decreasing the average grain size likewise decreases the value of a. Furthermore, K_{IC} of a ceramic material can be increased by the dispersion of particles of a second phase at the grain boundary. The advancing crack is pinned by the particles and 'bows' between them [13]. Therefore a contribution of both reduced grain size and presence of a Co rich layer on the grain boundary of 2CoCGO densified between 930-1000°C are expected to increase the tensile fracture strength of CGO (sintered at 1350°C).

9.6. Lattice Parameter Measurements of CGO and 2CoCGO

Reports of grain boundary segregation of dopants added to ceria and zirconia based electrolytes imply that there is significant redistribution of the different cation species at elevated temperatures. To the best of the author's knowledge, there is no literature that considers the effect that redistribution of dopants during sintering has on the densification of these materials. It was possible, due to the relatively low temperature typically used to synthesise commercial CGO powder (typically <600-700°C), that a redistribution of cations during sintering may influence the densification process.

Surface chemistry experiments used to evaluate the degree of segregation of cations in host materials are typically performed by XPS. A complementary technique that allows trends in redistribution of cations to be monitored as a function of heat treatment temperature involves measurements of the room temperature lattice parameter by XRD. Whilst this technique does not indicate the precise location of the different cations, a series of very precise measurements can be used to interpret changes in the crystal lattice of the material.

XRD experiments performed on CGO and 2CoCGO samples were described in section 7.18. Figure 9.19 shows a typical XRD powder diffraction pattern obtained for the

samples studied. A single cubic fluorite phase was observed for all samples studied at room temperature, with a shift in the peak angles, relative to pure ceria, to lower 2θ values. The shift in peak values is caused by dissolution of Gd and Gd+Co into the lattice for CGO and 2CoCGO respectively.

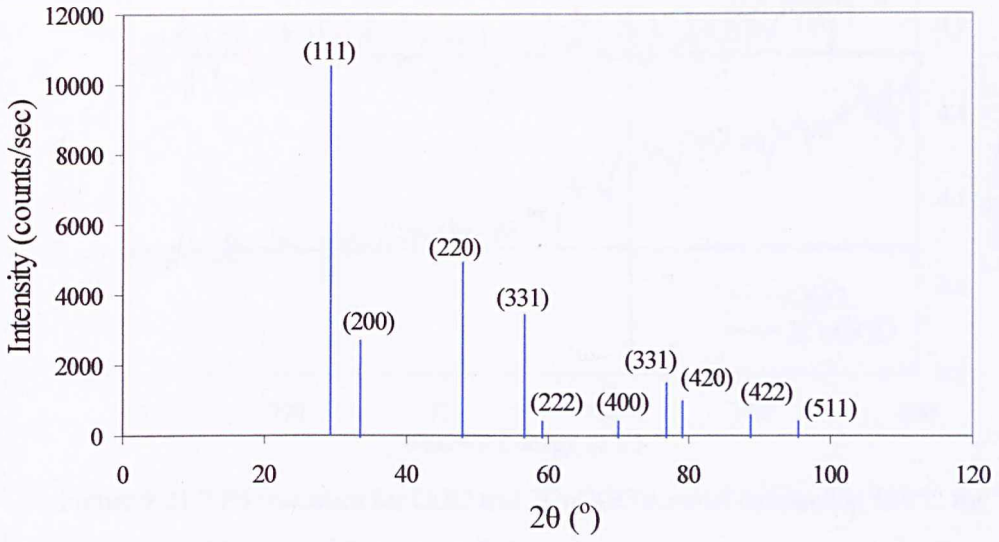


Figure 9.19 Typical XRD trace for CGO.

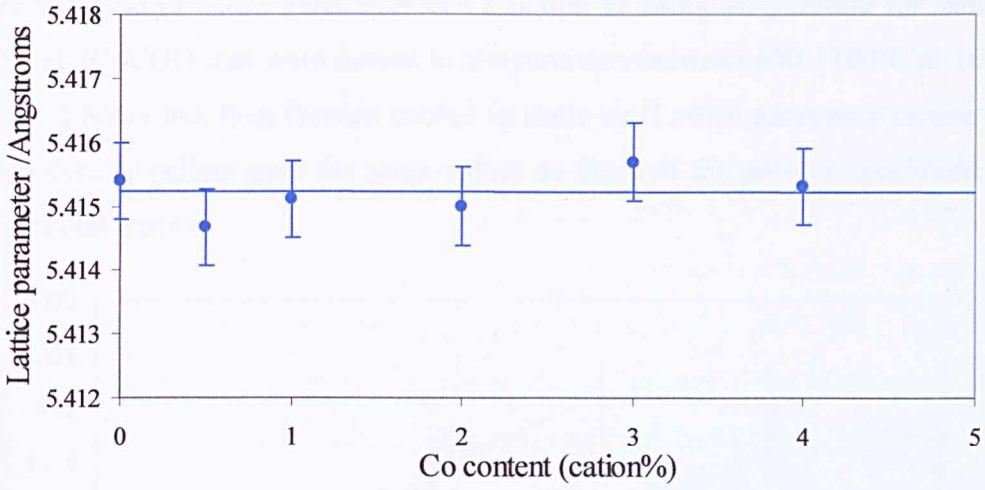


Figure 9.20 Lattice parameter of CGO and CoCGO powder (1-4%) after decomposition of ethanol/nitrate at 650°C for 1 hour.

Figure 9.20 shows the lattice parameter of CoCGO versus Co concentration prior to consolidation of the powder. Regardless of concentration, Co does not detectably alter the lattice parameter of CGO at this stage, indicating that it does not enter the CGO lattice at 650°C. Figure 9.21 displays XPS spectra, performed in accordance with section 7.17, of CGO and 2CoCGO powder calcined at 650°C for 2 hours. Due to the low Co content, it was difficult to detect Co (binding energy equal to 781eV)

unambiguously. The data do, however, suggest that there is a detectable Co concentration on the CGO surface. Figure 9.20 and figure 9.21 thus strongly suggest that Co remains segregated on the surface of the CGO powder post CoCGO powder synthesis.

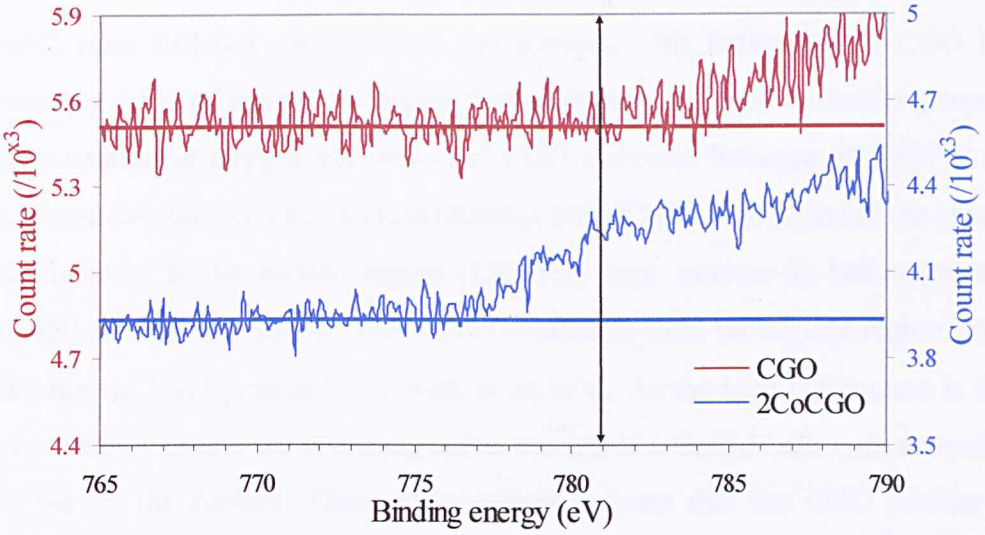


Figure 9.21 XPS spectrum for CGO and 2CoCGO powder calcined at 650°C for 2 hours and furnace cooled.

Figure 9.22 shows lattice parameter as a function of firing temperature for samples of CGO and 2CoCGO that were heated to temperatures between 650-1100°C at 10K/min, held for 2 hours and then furnace cooled in static air. Lattice parameter measurements of high density pellets gave the same values as those of the powder specimens within experimental error.

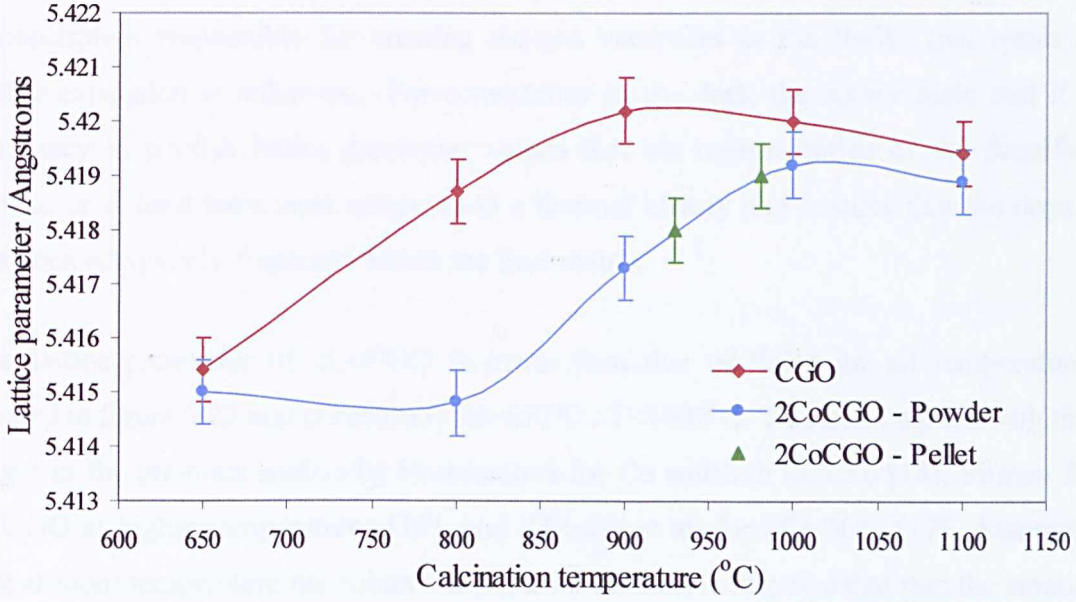


Figure 9.22 Lattice parameter of CGO and 2CoCGO powder calcined for 2 hours in air at the indicated temperature and furnace cooled.

It is widely accepted that increasing the oxygen vacancy concentration with increased additions of Gd_2O_3 (0-30mol%) results in lattice expansion of ceria. Kim [14] published a comprehensive lattice parameter review of different fluorite materials and the value of pure ceria was reported to be 5.4130Å. The lattice parameters of CGO heated to 650°C and 900°C were 5.4152Å and 5.4200Å respectively. This indicates that CGO has a higher concentration of oxygen vacancies than undoped CeO_2 and the lattice parameter (and concentration of oxygen vacancies) of CGO increases between 650-900°C. XPS studies of commercial CGO and CGO20 fired at 1000°C likewise revealed the presence of Gd enrichment at the surface region [15]. The large increase in lattice parameter between 650-1000°C thus implies that more Gd diffuses from the surface region into the bulk than the Gd level present in the bulk at <650°C. As the total Gd content is fixed, the as-received CGO powder is considered to consist of a Ce/Gd bulk with an enriched layer of Gd on the surface. These observations indicate that the CGO powder was produced at a temperature below 650°C (e.g. by hydrothermal or co-precipitation synthesis).

There is disagreement in the literature for the lattice parameter of CGO, Hong [16] reported a value of 5.4135Å whilst Kharton et al. [17] claimed it was 5.4170Å. The best value for CGO in this study is 5.4200±0.001Å. A common misconception by many workers is to quote lattice parameter for doped ceria assuming that the dopant:host ratio is uniform throughout the sample. Often, the thermal history of the specimen is not quoted. This makes it difficult to interpret the lattice parameter as the dopant concentration responsible for creating oxygen vacancies in the 'bulk' that result in lattice expansion is unknown. For consistency in the data, the author feels that it is necessary to publish lattice parameter values that are representative of the densified article, or at least have been subjected to a thermal history that ensures that the dopant has been adequately dispersed within the host matrix.

The lattice parameter of 2CoCGO is lower than that of CGO for all temperatures studied in figure 9.22 and particularly for 650°C <T<1000°C. This trend agrees with that found in the previous studies by Hartmonovà for Co addition to YSZ [18], Sirman for CoCGO at higher temperatures [19], and Kharton et al. for 2CoCGO [17]. Assuming that at room temperature the cobalt ion has a 3+ valence, it is speculated that the smaller Co^{3+} ($^{VIII}r(Co^{3+})$ =0.71Å) substitutes for the larger Ce^{4+} cation ($^{VIII}r(Ce^{4+})$ =0.97Å) resulting in a negative contribution to the lattice parameter (Equation 9.9).

$$Co_2O_3 \longrightarrow 2Co'_{Ce} + V_O^{\cdot\cdot} + 3O_O^X \qquad (9.9)$$

However, this is offset by a positive contribution from the oxygen vacancy. For temperatures between 800-1000°C, the lattice parameter of 2CoCGO increases by approximately the same amount as CGO until its plateau is established. Two possible explanations are as follows. The solubility of Co in CGO could be less than 2% and this limit is reached for 2CoCGO at ~800°C after 2 hours. Above this temperature the lattice parameter of 2CoCGO exhibits similar behaviour to CGO and increases due to Gd entering the lattice. Alternatively, some Co^{3+} could enter the CGO interstitially, resulting in an increase in the lattice parameter (Equation 6.9) as suggested by Hartmonovà for CoYSZ [18].

The redistribution of cations in both CGO and CoCGO in the temperature range where initial stage sintering of both these materials occurs makes analysis of densification kinetics more difficult to interpret (section 9.4). It is felt, however, that these studies are valid in the sense of enabling a qualitative comparison to be made.

9.7. Densification of Gd Doped Ceria

These observations suggest that the redistribution of cations may influence the densification process of CGO and CoCGO. Chen [20] noted that the grain boundary mobility and densification of undoped ceria is higher in a less oxidising atmosphere. It is generally accepted that increasing the oxygen vacancy concentration in ceria likewise increases the concentration of cation interstitials (Equations 6.5 and 6.6). As oxygen diffusion is very fast in fluorite-type oxides, cation diffusion must be the rate-limiting step for mass transportation.

From equation 4.5, CGO20 is expected to have a larger oxygen vacancy concentration and thus cation interstitial concentration compared to CGO. Figure 9.23 shows that there is no difference in the shrinkage rate between CGO and CGO20 in the temperature region where Co and Cu aid the densification of CGO. This seems to show that increasing the oxygen vacancy concentration in CGO does not enhance the densification rate. However, the CGO20 synthesised by the same procedure as the CGO, similarly can be considered to consist of a Ce/Gd bulk with a Gd rich layer on the surface and the lattice Gd concentration is not equal to the overall Gd concentration. When CGO and

CGO20 are sintered, diffusion of Gd into the bulk creates additional oxygen vacancies at temperatures below 900°C that indirectly enhance the densification compared to undoped ceria. In this study it is possible to sinter CGO and CGO20 to high density (after short sintering times) at 1150°C, whilst commercially synthesised ceria typically densifies at ~1600°C [6]. Therefore, it is speculated that Gd on the surface diffuses into the bulk of CGO at approximately the same rate as it does in CGO20.

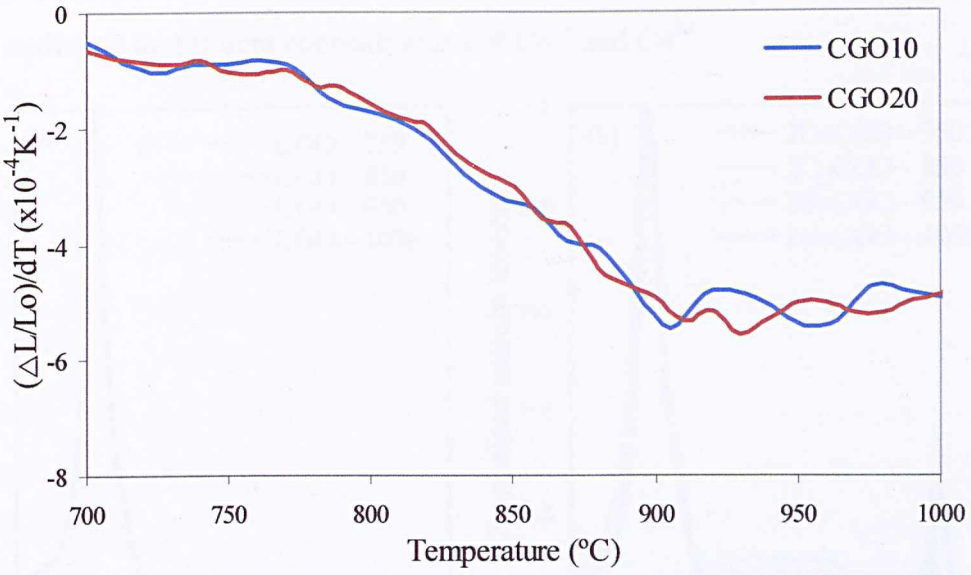


Figure 9.23 Linear differential shrinkage of CGO and CGO20 as a function of temperature fired at a CHR of 2K/min in air.

9.8. Oxygen Vacancy Concentration of CGO and 2CoCGO

So far, it has been established that the CGO powder has a surface region that is greatly enriched in Gd, or in the case of 2CoCGO both Gd and Co. The temperature required to densify CGO is approximately 450°C lower than that required to densify ceria. Furthermore, it has recently been claimed that additions of 0.25%Co can reduce the sintering temperature of ceria by ~250°C [6]. It is possible that addition of Co further aids densification of CGO by increasing the concentration of cation defects at low temperature. Raman spectroscopy was performed to investigate changes in the oxygen vacancy concentration of these materials.

Samples were prepared and tested in accordance with section 7.13. Figures 9.24 and 9.25 show the Raman spectra of CGO and 2CoCGO samples that were heat treated at the indicated temperature for 2 hours and then furnace cooled. Each spectrum was normalised by the intensity of the main band at around 460cm^{-1}. This band is the only

allowed Raman mode (F_{2g}) of fluorite metal dioxides, and can be viewed as a symmetric breathing mode of the oxygen atoms around cerium ions [21]. The broad band in the range 540-600cm^{-1} originates from the oxygen vacancies in the CeO_2 lattice. The Raman spectra of 2CoCGO have additional peaks. All samples have a peak occurring at 695cm^{-1}, the intensity of which is significantly greater for samples fired at 950°C and 1050°C. These samples have an additional peak at 525cm^{-1}, which is absent from the samples fired at 750°C and 850°C. It is believed that the additional peaks in 2CoCGO can be attributed to different concentrations of Co^{2+} and Co^{3+}.

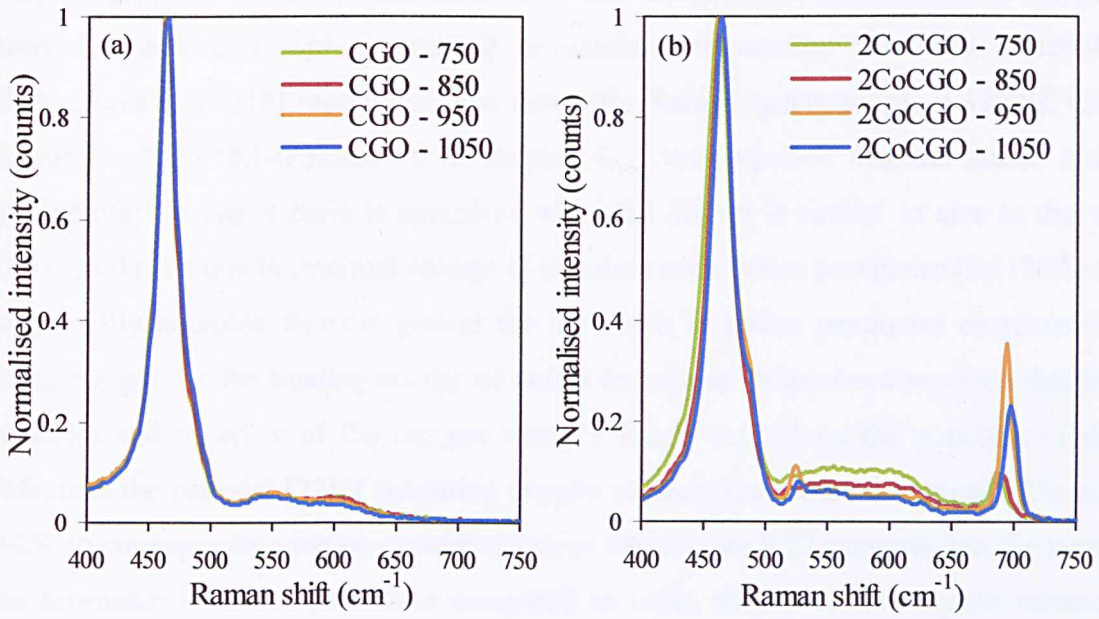


Figure 9.24 Raman spectra (400-750cm^{-1}) of (a) CGO and (b) 2CoCGO pellet fired at 750°C, 850°C, 950°C and 1050°C (2 hours in air and furnace cooled).

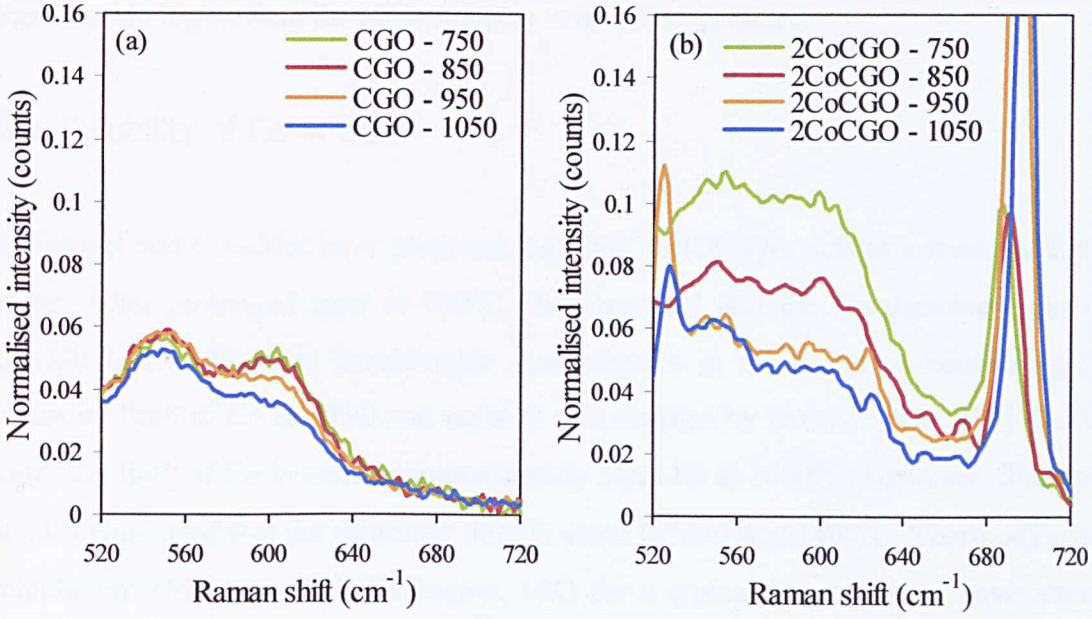


Figure 9.25 Raman spectra (520-720cm^{-1}) of (a) CGO and (b) 2CoCGO pellet fired at 750°C, 850°C, 950°C and 1050°C (2 hours in air and furnace cooled).

Figures 9.25a and 9.25b show the Raman spectra between 520-720cm^{-1} (the oxygen vacancy band region) of CGO and 2CoCGO fired at four different temperatures and furnace cooled. The oxygen vacancy intensity at room temperature in 2CoCGO fired at 750°C is approximately double the intensity of CGO fired at 750°C. It is well known that defects dissociate in CGO at temperatures above 500-600°C; however, the presence of a large oxygen vacancy concentration in the region where 2CoCGO rapidly densifies implies that the defect structure of CGO is affected by addition of small levels of Co.

Surprisingly, the intensity measured at room temperature attributable to oxygen vacancies decreases with increasing calcination temperature for both materials. Hartmanovà et al. [18] reported similar trends for Raman spectroscopy of 12YSZ with additions of Co (0.1-0.3mass%). In chapter 4, it was reported that the lattice ionic conductivity of doped ceria is optimised when the dopant is similar in size to that of Ce4+, as this results in minimal change of the ideal ceria lattice parameter (5.4130Å). It is generally accepted that the greater the mismatch in lattice parameter compared to ceria, the greater the binding energy of defect associates. It has been reported that the structure and intensity of the oxygen vacancy bands depend on the structure of the defects in the material [22]. Comparing oxygen vacancy intensities in figures 9.25a and 9.25b to corresponding lattice parameter values from figure 9.22 suggests that the larger the mismatch in lattice parameter compared to ceria, the lower the oxygen vacancy intensity due to greater defect association at room temperature. This could explain why the oxygen vacancy Raman intensity of 2CoCGO fired at 750°C and 850°C is significantly higher than the other samples at room temperature.

9.9. Solubility of Co in CGO

Kleinlogel and Gauckler have proposed that the Co rich layer acts as a transient liquid phase. After prolonged time at 900°C, they reported that the Co dissolves into the CGO20 lattice. There is considerable disagreement in the literature concerning the solubility limit of Co in CGO and ceria. It was claimed by Donstov et al. [23] that the solubility limit of Co in ceria is approximately 30mol% at 1600°C. However, Sirman et al. [19] concluded that the solubility limit is about 0.5mol% at 1400°C. Thermodynamic calculations (MTData, NPL Eddington, UK) for a typical laboratory air environment (and assuming ideal solution) predict that at 1423°C the equilibrium vapour pressure of $Co(OH)_2$ is high enough to give a loss rate of up to approximately 1.5mgcm^{-2}hr^{-1}. In the

present study it was experimentally observed that heat treatment of CoCGO under these conditions does indeed lead to the loss of most of the cobalt. It is believed that the solubility limits derived by both sets of workers are thus flawed. Studies were performed on quenched samples of CGO (CGOQ) and 2CoCGO (2CoCGOQ). It was envisaged that quenching would 'freeze' the high temperature structure, thus enabling a better understanding of the role of Co in the enhanced sintering of CGO.

Figure 9.26 shows the Raman spectra in the in the oxygen vacancy band region of CGOQ pellets fired at four different temperatures and quenched in iced water. The spectra of the CGOQ samples were almost identical to the spectra of CGO samples fired at similar temperatures and furnace cooled. The only difference being a very slight increase in oxygen vacancy intensity for the CGOQ samples. The oxygen vacancy band intensity is influenced by defect interaction within the microstructure, which inturn is influenced by dimensional changes of the lattice. These results would suggest that the defect structure of CGO heat treated between 750-1050°C is unaffected by different cooling rates. In support of this statement, it was found that the lattice parameter of CGO heated to 1000°C for 2 hours and furnace cooled and air cooled (sample removed from furnace) were identical. As Gd has an ionic radius that is comparable in size to Ce, this minimises the elastic strain on the lattice. Segregation of impurities and dopants is enhanced when the ionic radius is very different to that of the host. The relatively small elastic strain in the CGO microstructure (fired at 1050°C for 2 hours) thus results in negligible segregation of Gd during cooling.

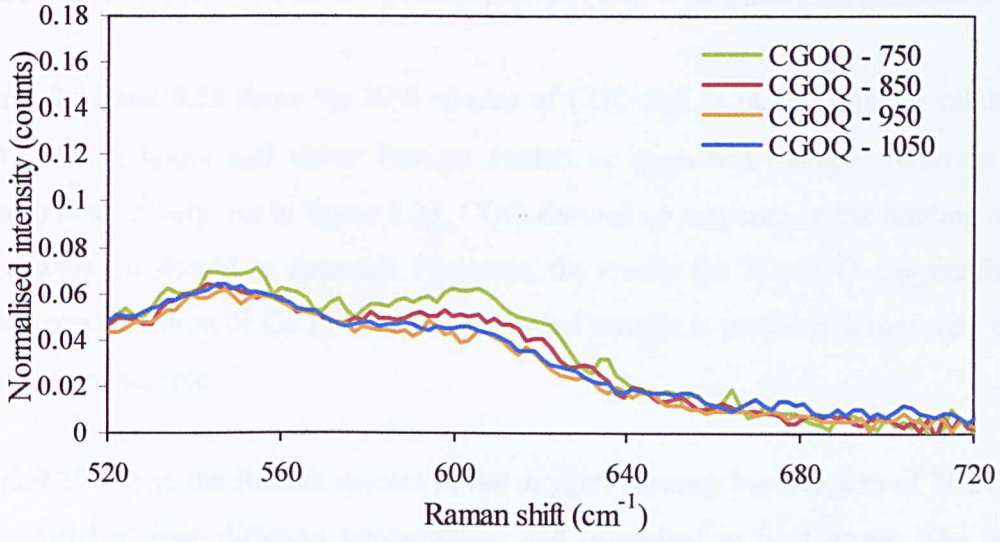


Figure 9.26 Raman spectra of CGO pellet fired at 750°C, 850°C, 950°C and 1050°C (2 hours in air and ice quenched).

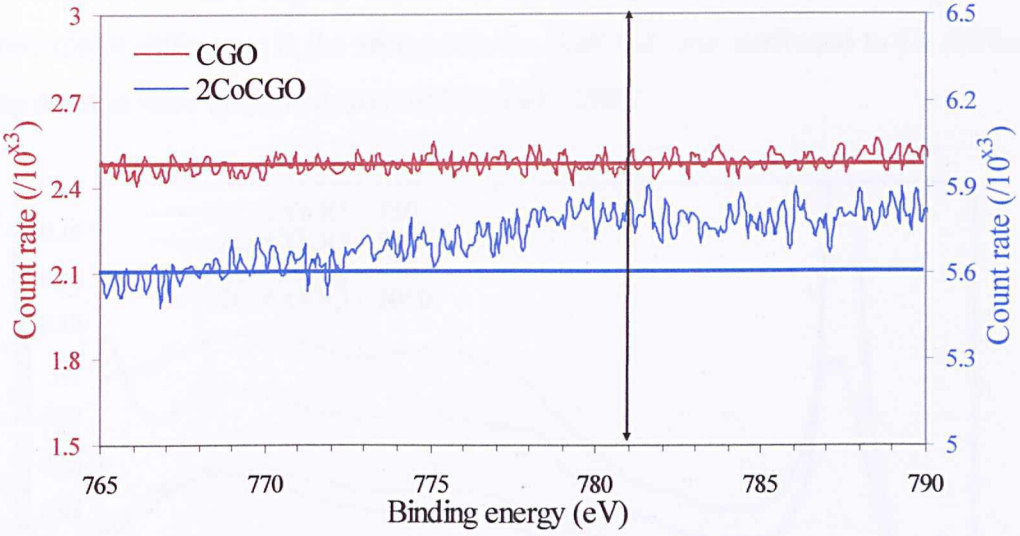


Figure 9.27 XPS spectra of CGO and 2CoCGO powder (1000°C for 2 hours and furnace cooled).

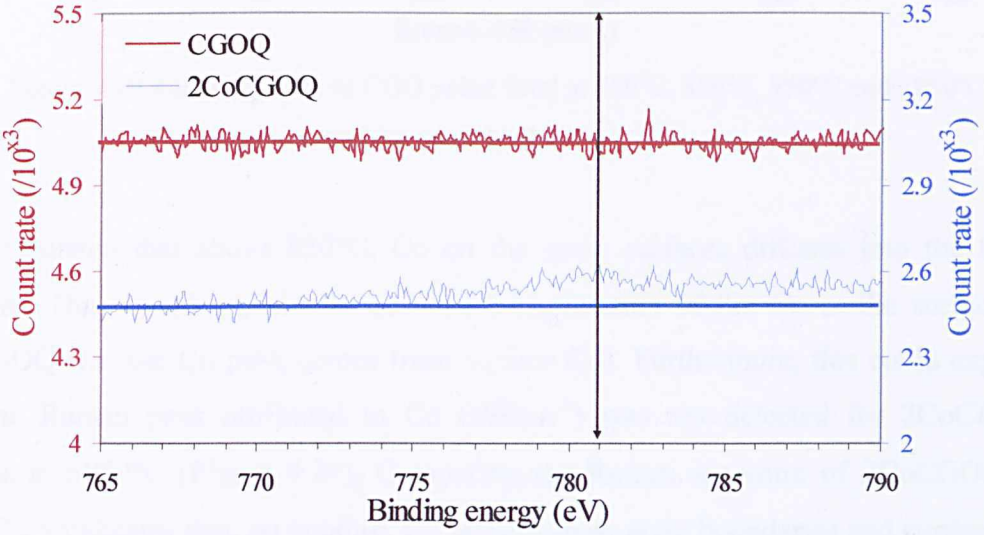


Figure 9.28 XPS spectra of CGO and 2CoCGO powder (1000°C for 2 hours and quenched in air).

Figures 9.27 and 9.28 show the XPS spectra of CGO and 2CoCGO powder calcined at 1000°C for 2 hours and either furnace cooled or quenched (sample removed from furnace) respectively. As in figure 9.21, CGO showed no response in the binding energy region were Co should be detected. However, the results for 2CoCGO suggest that the surface concentration of Co in the furnace cooled sample is probably larger than that in the quenched sample.

Figure 9.29 shows the Raman spectra in the oxygen vacancy band region of 2CoCGOQ pellets fired at four different temperatures and quenched in iced water. The Raman spectra for 2CoCGOQ samples show similar trends to furnace-cooled samples (Figure 9.25b). The oxygen vacancy Raman intensity was identical for samples quenched from

950°C and 1050°C and slightly higher for samples quenched from 750°C and 850°C. The one major difference is the absence in the peak that was attributed to Co (690cm^{-1}) in samples that were quenched from 950°C and 1050°C.

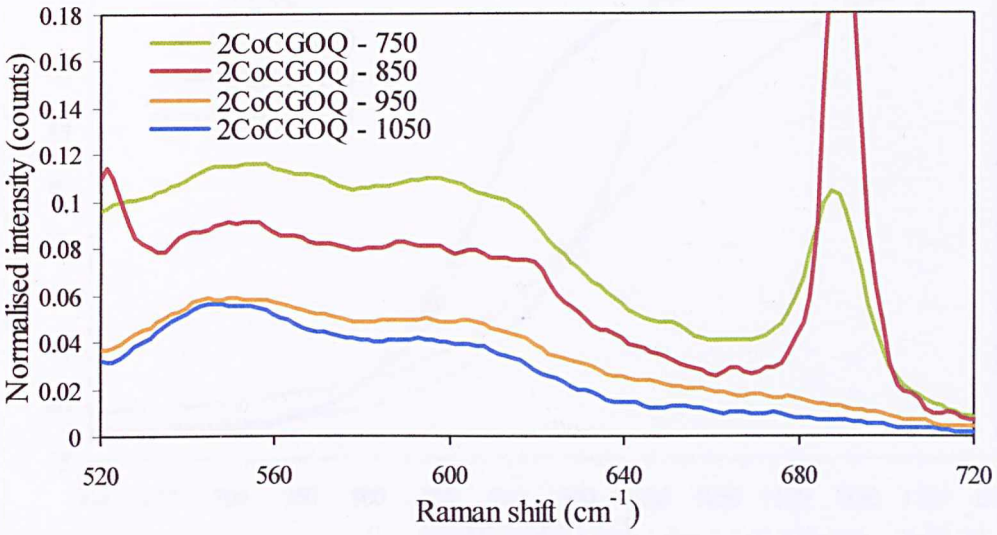


Figure 9.29 Raman spectra of CGO pellet fired at 750°C, 850°C, 950°C and 1050°C (2 hours in air and ice quenched).

It is speculated that above 850°C, Co on the grain surfaces diffuses into the CGO structure. This would explain the reduced concentration of the Co at the surface of 2CoCGOQ (i.e. the Co peak comes from surface Co). Furthermore, this could explain why the Raman peak attributed to Co (690cm^{-1}) was not detected for 2CoCGOQ samples at >850°C (Figure 9.29). Comparing the Raman spectrum of 2CoCGOQ to figure 9.25 indicates that, on cooling, Co segregates to grain boundaries and surfaces. It was previously shown that the Co concentration of a furnace cooled 2CoCGO sample was almost exclusively located at the grain boundary. These results thus partly agree with Kleinlogel and Gauckler in that there is evidence to suggest that a 2% addition of Co is soluble in the CGO lattice above 850°C. If the material cools from above 850°C relatively slowly, however, the majority of the Co segregates to the grain boundary. For reasons previously stated, the segregation of Co is due to the system relieving the large elastic strain caused by the inclusion of the much smaller Co cation.

9.10. Co Additions to CGO20: CHR Dilatometry

Kleinlogel and Gauckler [3] performed CHR dilatometry for CoCGO20 at 5K/min and reported different T_{max} values to those obtained for CoCGO in section 9.2.1. In order to

determine whether the difference resulted from the different heating rate or an increased Gd content, a CHR study of CoCGO20 was performed at 10K/min.

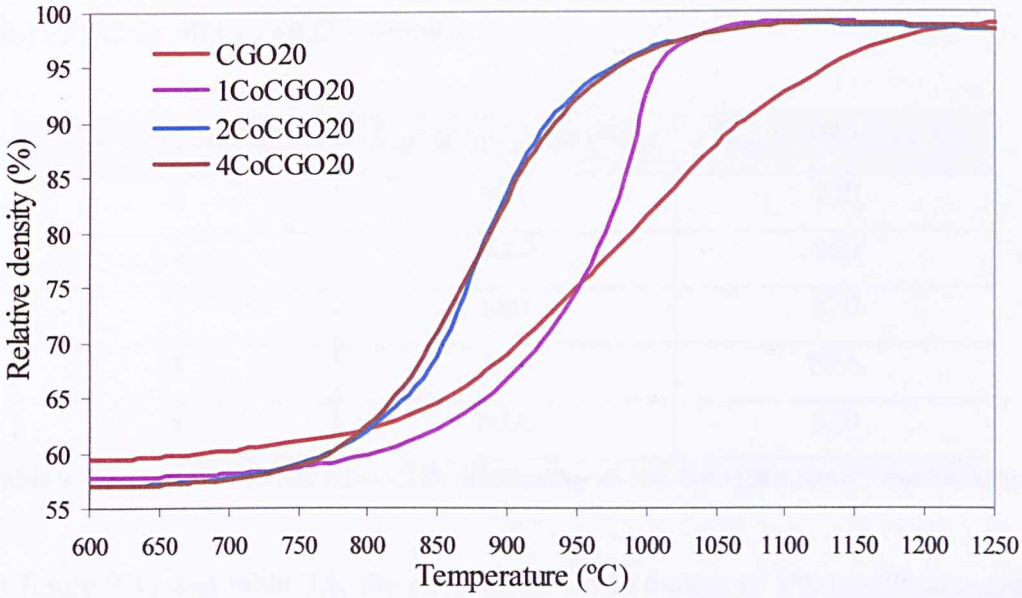


Figure 9.30 Relative density of Co additions to CGO20 by CHR dilatometry (10K/min).

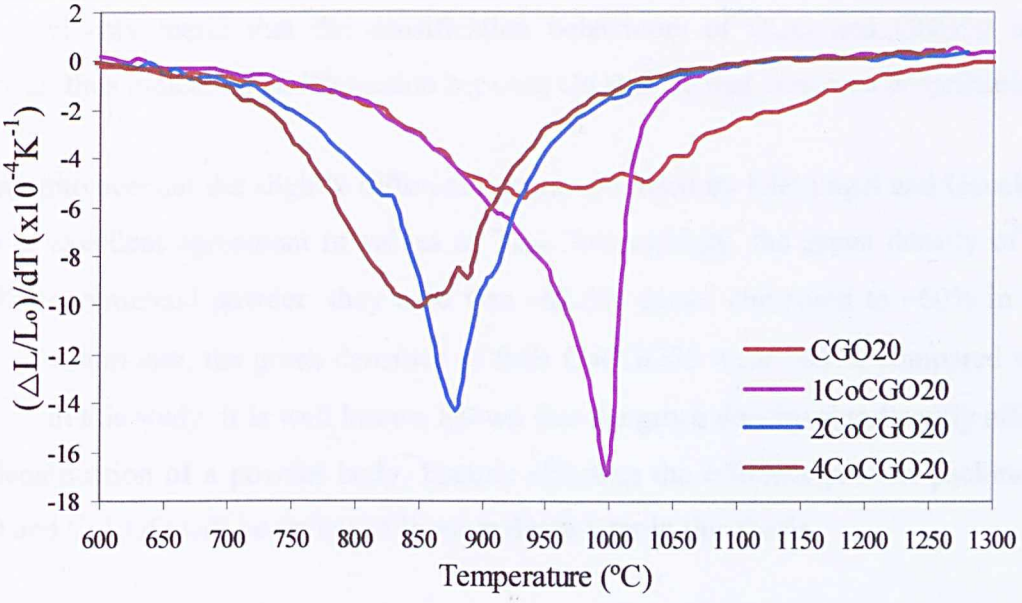


Figure 9.31 Linear differential shrinkage as a function of temperature for Co additions to CGO20.

Figure 9.30 shows that Co additions (1-4%) enhance the densification of CGO20. As for CoCGO, Co additions between 2-4% maximise the enhanced sinterability of CGO20. Figure 9.30 also shows that the green density of CGO20 is reduced as the Co content increases. The green densities of CGO20 (~60%) and CoCGO20 (~57.5%) were almost identical to those previously mentioned for CGO and CoCGO. This is unsurprising

considering the starting CGO20 powder was supplied by the same manufacturer and was probably produced by the same process, thus having similar characteristics. One difference between CoCGO20 and CoCGO is that slight 'over sintering' occurred at above 1100°C for all CoCGO20 samples.

Co addition (%)	T_{max} at 10K/min (°C)	T_{max} at 5K/min (°C)
0	931	930
1	1000	950
2	880	870
4	849	N/A
5	N/A	820

Table 9.4 T_{max} of CoCGO20 from CHR dilatometry at 10K/min (this study) and 5K/min [3].

From figure 9.31 and table 9.4, the addition of Co in excess of 1% results in a greater enhancement in the densification of CGO20 than CGO. The only difference between the preparation, treatment and characterisation of these powders was their Gd content. It was previously found that the densification behaviours of CGO and CGO20 were identical, thus indicating an interaction between Co and Gd that enhances densification.

Taking into account the slightly different heating rate used by Kleinlogel and Gauckler, there is excellent agreement in values of T_{max}. Interestingly, the green density of the CGO20 commercial powder they used was ~62.5% dense, compared to ~60% in this study. Furthermore, the green densities of their CoCGO20 were ~60%, compared with ~57.5% in this study. It is well known known that the green density significantly affects the densification of a powder body. Factors effecting the efficient powder packing of CGO and CoCGO will be reviewed in more depth later in this thesis.

9.11. Co Oxide Phase Change: Influence on Densification of CoCGO

It has been argued that Co probably enhances initial stage densification of CGO by a volume diffusion mechanism. Due to limitations in the CHR dilatometry analysis, it cannot be assumed that this mechanism is solely active throughout the entire densification process. It was observed in table 9.1 that T_{max} of 2CoCGO and 4CoCGO occur at approximately the same temperature that Co_2O_3 transforms to CoO in air (Figure 8.4). A study was performed to see whether there was a link between the

enhanced densification of 2CoCGO and the phase transformation of Co oxide at approximately 900°C. Thermodynamic calculations show that the transition of Co_2O_3 to CoO when fired in air and argon (10ppm H_2O) environments are approximately 810°C and 906°C respectively, which are in agreement with DTA (Figure 9.32). T_{max} values of 2CoCGO fired in air and argon from figure 9.33 were 865°C and 840°C respectively and are not in agreement with the reduction temperatures. This suggests that T_{max} is not related to the reduction of Co3+ to Co2+ (although reduction in the presence of CGO might be different from reduction of the pure oxide).

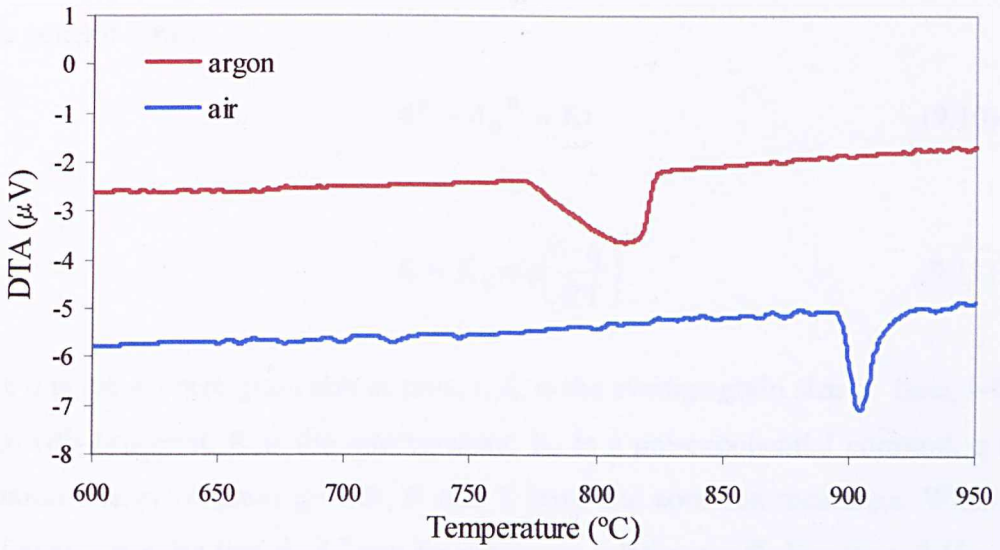


Figure 9.32 DTA of $Co(NO_3)_2.6H_2O$ dissolved in ethanol and dried at 50°C when fired in air and argon.

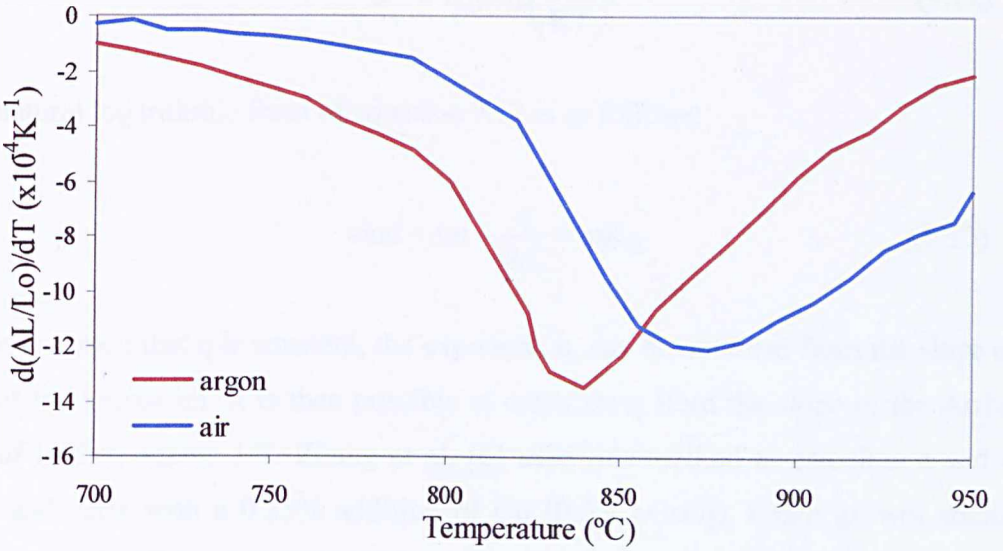


Figure 9.33 Linear shrinkage rate as a function of temperature for 2CoCGO fired in air and argon at a CHR of 2K/min.

Figure 9.33 shows that the shrinkage rate peak (maximum) of 2CoCGO shifts to lower temperatures when fired in argon. It has been argued that 2CoCGO densifies by a volume diffusion mechanism; it is therefore expected that firing in argon will promote the oxygen vacancy concentration and thus create more cation interstitials.

9.12. Grain Growth of CGO and 2CoCGO

Studies were performed to investigate the effect of Co on grain growth of CGO. Isothermal grain growth behaviour can be described with the kinetic growth equations of the general form:

$$d^n - d_o^n = Kt \qquad (9.10)$$

and

$$K = K_o \exp\left(\frac{-q}{RT}\right) \qquad (9.11)$$

where d is the average grain size at time, t, d_o is the average grain size at time, t=0, n is the growth exponent, K is the rate constant, K_o is a pre-exponential constant, q is the activation energy of grain growth, R and T have the common meanings. When d_o is significantly smaller that d, d_o^n can be neglected relative to d^n. Equation 9.10 can be simplified to:

$$d^n = K_o \exp\left(\frac{-q}{RT}\right)t \qquad (9.12)$$

The natural logarithmic form of equation 9.12 is as follows:

$$n\ln d = \ln t - \frac{q}{RT} + \ln K_o \qquad (9.13)$$

If it is assumed that q is constant, the exponent, n, can be obtained from the slope of the plot of lnd versus lnt. It is then possible to calculate q from the slope of the Arrhenius plot of $\ln(d^n/t)$ versus 1/T. Zhang et al. [6] used this method to calculate n and q for ceria and ceria with a 0.25% addition of Co ($0.25CoCeO_2$). Grain growth studies of CGO and 2CoCGO were performed, as described in section 7.14.1, such that q and n could be obtained and compared to those by Zhang. Figure 9.34 is a representative SEM micrograph, all samples had an equiaxed grain morphology.

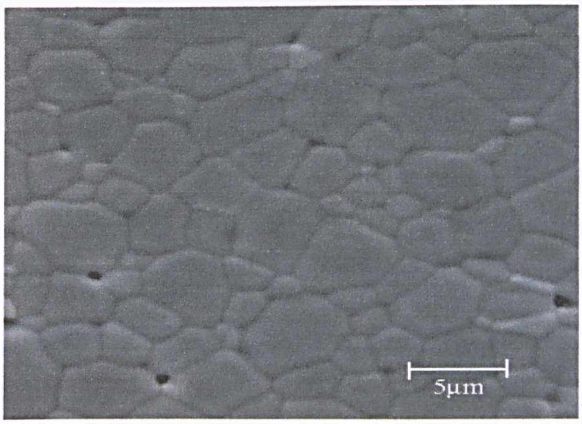


Figure 9.34 SEM micrograph of 2CoCGO fired at 1500°C for 1 hour.

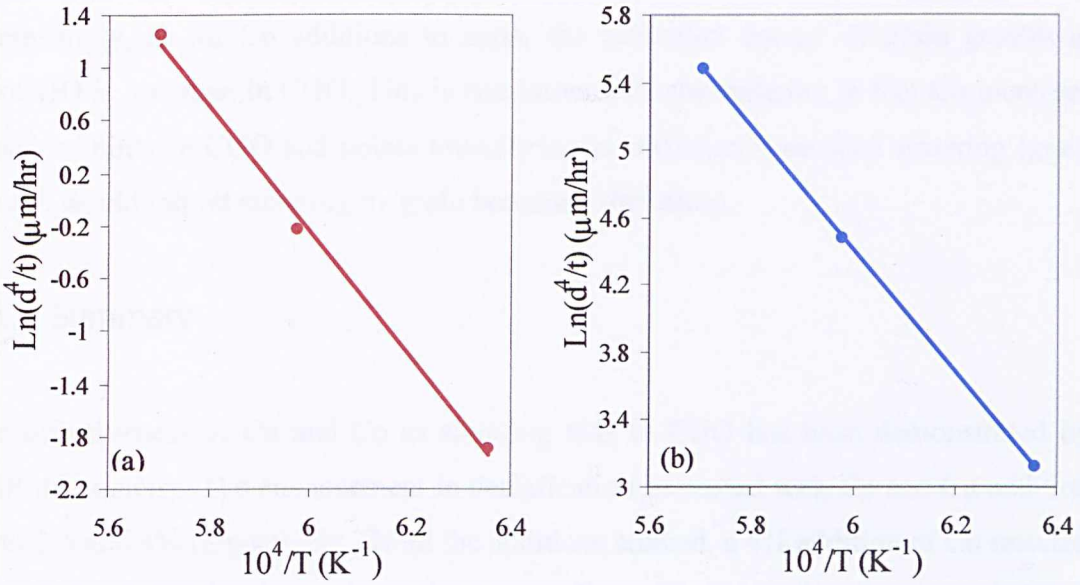


Figure 9.35 The plots of Lnd versus Lnt (a) CGO (b) 2CoCGO (Temp. in (°C)).

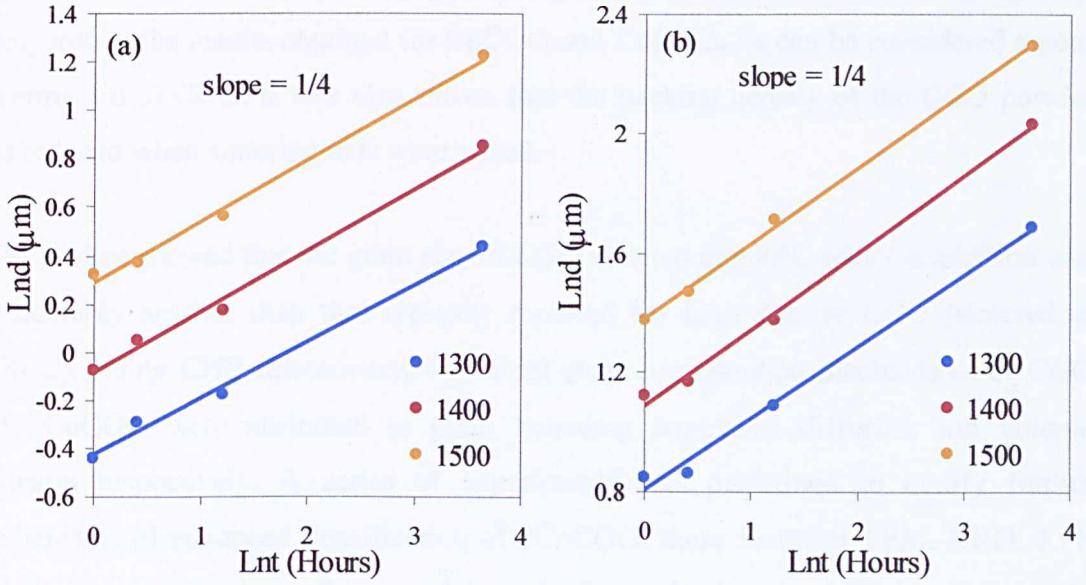


Figure 9.36 The plots of Lnd^n versus 1/T to calculate q for (a) CGO and (b) 2CoCGO.

Figure 9.35 shows the plots of lnd versus lnt for CGO and 2CoCGO. It can be seen that both CGO and 2CoCGO have the grain growth exponent, n, of approximately 4. Zhang et al. [6] obtained n values of ~3 and 4 for ceria and $0.25CoCeO_2$ respectively. Based on equation 9.12, the activation energy, q, was calculated for both materials (Figure 9.36). The activation energies for CGO and 2CoCGO were 913±40kJ/mol and 692±40kJ/mol respectively. Values of q obtained by Zhang for ceria and $0.25CoCeO_2$ were 697kJ/mol and 572kJ/mol respectively. The higher activation energy of CGO compared to ceria is consistent with the literature. Inaba [24] reported that grain growth in CGO20 was considerably less than in ceria when fired in similar conditions. The enriched layer of Gd in CGO pins the boundaries, thus resulting in inhibition of grain growth. Interestingly, as for Co additions to ceria, the activation energy of grain growth in 2CoCGO is less than in CGO. This is consistent with the sintering in that Co increases cation mobility in CGO and points towards lattice diffusion controlled sintering (grain growth would inhibit sintering by grain boundary diffusion).

9.13. Summary

The effectiveness of Cu and Co as sintering aids to CGO has been demonstrated by CHR dilatometry. The enhancement in densification increased with Co and Cu addition up to 2% and 4% respectively. Of all the additions studied, a 4% addition of Cu resulted in obtaining high density at the lowest temperature. These studies, however, indicate that 'over sintering' of CuCGO results in a significant decrease in the relative density. Arguably, Co is the more promising sintering aid, as it appears to be more forgiving. Compared to the results obtained for CoCGO and CuCGO, Fe can be considered a poor sintering aid to CGO. It was also shown that the packing density of the CGO powder was reduced when sintering aids were added.

TEM studies showed that the grain size of CGO sintered at 930°C with Co addition was considerably smaller than that typically reported for high density CGO (sintered at 1350°C). Using CHR dilatometry, the initial stage densification mechanisms of CGO and 2CoCGO were attributed to grain boundary controlled diffusion and volume diffusion respectively. A series of experiments was performed to clarify further mechanisms of enhanced densification of 2CoCGO; these included TEM, XRD, XPS and Raman spectroscopy. Prior to firing, CGO powder has a surface region greatly enriched in Gd and the lattice Gd concentration is much less than the nominal one. For

temperatures greater than 650°C, the Gd in the surface region diffuses into the bulk. More oxygen vacancies and cation interstitials are created which in turn enhances the mass transport of cations thus aiding densification when compared to ceria (Equations 4.5 and 6.6). The enhanced densification of 2CoCGO is more complex and studies have not identified the nature of the enhanced sintering unambiguously. It is speculated that Co, located on particle surfaces after preparation, diffuses into the bulk of the powder and likewise increases the rate at which Gd diffuses into the bulk of the powder at temperatures of ~750-800°C. Studies revealed that Co is relatively mobile within CGO at temperatures were the majority of shrinkage occurs. It was speculated that at temperatures greater than 850°C, Co is soluble within the CGO matrix, if cooled slowly this Co segregates to the grain boundaries and surfaces. Analysis of a sintered sample (furnace cooled) of 2CoCGO revealed that the majority of the Co additive was located at the grain boundary. This is presumably due to the high elastic strain associated with the relatively small ionic radius of Co. Grain growth studies revealed that Co enhanced the grain growth of CGO when fired under similar conditions which is consistent with Co enhancing cation mobility and densification by volume diffusion.

References

1. F.F.Lange. Ceramic Transactions. **1**, (1989), 1069.
2. J.A.Cerri, E.R.Leite, D.Gouvêa and E.Longo. J.Am.Ceram.Soc. **79**, 3, (1996), 799.
3. C.Kleinlogel and L.J.Gauckler. Adv.Mats. **13**, 14, (2001), 1091.
4. J.R.Seidensticker and M.J.Mayo. J.Am.Ceram.Soc. **79**, 2, (1996), 401.
5. T.Zhang, P.Hing, H.Huang and J.Kilner. J.Eur.Ceram.Soc. **21**, (2001), 2221.
6. T.Zhang, P.Hing, H.Huang and J.Kilner. J.Eur.Ceram.Soc. **22**, (2002), 27.
7. M.J.Bannister. J.Am.Ceram.Soc. **51**, 10, (1968), 548.
8. W.S.Young and I.B.Cutler. J.Am.Ceram.Soc. **53**, (1970), 659.
9. J.L.Woolfrey and M.J.Bannister. J.Am.Ceram.Soc. **55**, (1972), 390.
10. J.Wang and R.Raj. J.Am.Ceram.Soc. **73**, (1990), 1172.
11. T.Zhang, P.Hing, H.Huang and J.Kilner.To be Published.
12. P-L.Chen and I-W.Chen. J.Am.Ceram.Soc. **77**, 9, (1994), 2289.
13. Engineering Materials 2: An Introduction to Microstructures, Processing and Design. M.F.Ashby and D.R.H.Jones. Elsevier Science Ltd, 1994.
14. D-J.Kim. J.Am.Ceram.Soc. **72**, 8, (1989), 1415.
15. P.J.Scanlon, R.A.M.Bink, F.P.F.van Berkel, G.M.Christie, L.J.van Ijzendoorn,

H.H.Brongersma and R.Gvan Welzenis. Solid State Ionics. **112**, (1998), 123.

16. S.J.Hong and A.V.Virkar. J.Am.Ceram.Soc. **78**, (1995), 339.
17. V.V.Kharton, F.M.Figueiredo, L.Navarro, E.N.Naumovich, A.V.Kovalevsky, A.A.Yaremchenko, A.P.Viskup, A.Carneiro, F.M.B.Marques and J.R.Frade. J.Mater.Sci. **36**, (2001), 1105.
18. M.Hartmanová, F.Hanic, D.Tunega and K.Putyera. Chem.Papers. **12-15**, (1998), 12.
19. J.D.Sirman, D.Waller and J.A.Kilner. Proc. of the 5th International Symposium on SOFCs. Eds. U.Stimming, S.C.Singhal, H.Tagawa and W.Lehnert. The Electrochem.Soc. (1997), 1159.
20. P-L.Chen and I-W.Chen. J.Am.Ceram.Soc. **79**, 7, (1996), 1793.
21. X.Lin, L.Li, G.Li and W.Su. Mater.Chem.Phys. **69**, (2001), 236.
22. W.H.Weber, K.C.Hass and J.R.McBride. Phys.Rev B. **48**, 1, (1993), 178.
23. G.Donstov, G.Vitter and C.Déportes, Rev.Int.Hautes Tempér et Réfract. **9**, (1972), 147.
24. H.Inaba, T.Nakajma and H.Tagawa. Solid State Ionics. **106**, (1998), 263.

Chapter 10 – Electrical Properties of CoCGO and CuCGO

10.1. Introduction

In the last chapter it was shown that Co and Cu are effective sintering aids for CGO. Whilst the primary aim of my research has been to find a technique that densifies CGO to high density below 1000°C, arguably the most important property of the electrolyte is to efficiently conduct oxygen ions through its defect structure. This chapter will discuss the effects on the electrical properties of CGO as a result of adding such sintering aids, with particular emphasis on Co addition. Such studies make it possible to pinpoint the optimum level of Co addition that results in enhanced densification whilst maintaining an acceptable level of electrical conductivity.

As the bulk of the data presented in this chapter contains impedance plots, the impedance spectroscopy technique will be reviewed in more depth. The effect on the grain boundary and lattice conductivity of CGO with different levels of Co and Cu is then presented. The rest of the chapter concentrates solely on the Co level that has the highest electrical conductivity as determined by A.C. impedance spectroscopy. A 4 point D.C. technique was used to investigate whether Co introduces any detrimental electronic carriers into CGO at fuel cell operating conditions. The final section investigates the effect of sintering temperature and time on the electrical conductivity of Co doped CGO.

10.2. A.C. Impedance Spectroscopy of Polycrystalline Materials

The preparation of samples and analysis equipment was discussed in section 7.7. When a small sinusoidal voltage (V_t) is applied across a sample, a resulting sinusoidal current (I_t) will lead the voltage by some phase angle (ϕ). This phase difference occurs due to either the dielectric response of the bulk lattice or to polarisation effects at the grain boundaries and electrodes. The impedance of the sample (Z) is as follows;

$$Z = \frac{V_t}{I_t} \tag{10.1}$$

Unlike resistance, impedance is frequency dependent and is expressed in complex number form as;

$$Z = |Z| e^{-j\phi} \tag{10.2}$$

or in Cartesian co-ordinates;

$$Z = |Z|\cos\phi - j|Z|\sin\phi \tag{10.3}$$

where $|Z| = V_o/I_o$, V_o and I_o are the amplitude of the voltage and current respectively. The real (Z') and imaginary (Z'') impedances can thus be expressed as;

$$Z' = |Z|\cos\phi \tag{10.4}$$

$$Z'' = |Z|\sin\phi \tag{10.5}$$

rearranging equation 10.3;

$$Z = Z' - jZ'' \tag{10.6}$$

The ceramic electrolytes discussed in this thesis are all polycrystalline and thus consist of both grains (lattice) and grain boundaries. Generally, the relaxation of charged species in the lattice and grain boundary occur at different rates and it is thus possible to separate their impedances as a function of frequency. The impedance of each process will consist of a resistance (R_T) and capacitance (C_T) component in parallel and allows the impedance of the lattice relaxation to be expressed as;

$$\frac{1}{Z} = \frac{1}{R_T} + C_T j\omega \tag{10.7}$$

It has been shown that equation 10.7 is analogous to the equation of a circle, with a radius of r/2 and a centre at (r/2, 0). In all the materials studied, ω, R_T and C_T are greater than zero, thus resulting in a semi-circle on the *x* axis when plotted as a function of frequency. Both the lattice and grain boundary will produce semi-circular responses. The grain boundary response will be displaced from the lattice response depending on the relaxation rate of the charged species. It is normal to compare the relaxation rates of

different processes in terms of rate constants or relaxation times (τ), this can be defined as;

$$\tau = R_T C_T \tag{10.8}$$

In terms of the lattice rate constant, τ_l can be expressed as follows;

$$R_l = \frac{L}{A\sigma_l} \tag{10.9}$$

$$C_l = \frac{A\varepsilon_o\varepsilon_l}{L} \tag{10.10}$$

Therefore;

$$\tau_l = \frac{\varepsilon_o\varepsilon_l}{\sigma_l} \tag{10.11}$$

where R_l and C_l are the resistance and capacitance of the lattice respectively, L is the sample length, A is the cross sectional area, ε_o is the permittivity of free space and σ_l and ε_l are the electrical conductivity and relative dielectric constant of the lattice respectively.

The grain boundary relaxation time constant, τ_{gb} can be expressed as follows [1];

$$R_{gb} = \frac{\delta L}{dA\sigma_{sgb}} \tag{10.12}$$

$$C_{gb} = \frac{A\varepsilon_o\varepsilon_{gb}}{\delta}\ \frac{d}{L} \tag{10.13}$$

Therefore;

$$\tau_{gb} = \frac{\varepsilon_o\varepsilon_{gb}}{\sigma_{sgb}} \tag{10.14}$$

where R_{gb} and C_{gb} are the resistance and capacitance of the grain boundaries respectively, d is the grain size, δ is the grain boundary width and σ_{spb} and ε_{gb} are the specific grain boundary conductivity and grain boundary relative dielectric constant. The resistance of the grain boundary is normally associated with the presence of a second phase or a constriction resistance (limited grain to grain contact), which can also result in a space charge region at the grain boundary. The capacitance of this region is

thus associated with the polarisation at the interface. Typically, the capacitance of the grain boundary and lattice are in the order of 10^{-9} and 10^{-11} respectively for doped ceria materials. As a result, τ at the grain boundary is typically much higher than that of the lattice causing the two processes to be well separated on an impedance plot. It is possible to mathematically derive equation 10.7 from the impedance of a resistor and capacitor connected in parallel. Generally, the electrolyte is modelled using electrically equivalent R-C circuits connected in series. The impedance spectrum of CGO at 163°C clearly shows the lattice, grain boundary and electrode response and equivalent R-C circuit (Figure 10.1). As only the electrical conductivity of doped ceria is under consideration in this study, all electrode response data have been omitted.

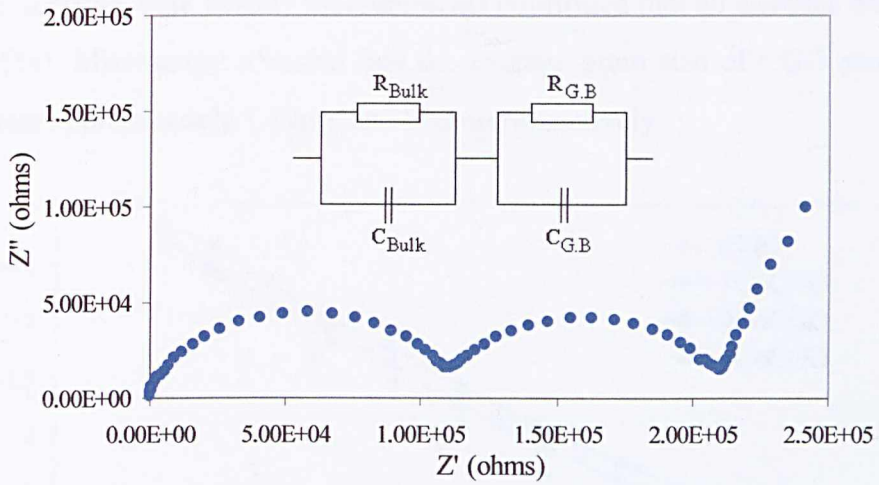


Figure 10.1 Impedance spectrum at 163°C for CGO fired at 1350°C for 4 hours in air and equivalent R-C circuit.

Using the computer program Zplot, it was possible to evaluate the resistance associated with both the lattice and grain boundary components of the material. From equation 4.8, a plot of logσT versus 1/T enables a comparison of the lattice and grain boundary conductivities of different materials. The terms lattice conductivity and grain boundary conductivity refer to the contribution of the respective region to the total conductivity. The gradient of each line can then be used to calculate the activation energy (E_a) for ionic conduction.

10.3. A.C. Impedance Spectroscopy of Materials in this Study

The electrical conductivity of CGO, CoCGO and CuCGO were studied with A.C. impedance spectroscopy in air, using the equipment described in section 7.7. The lattice

and grain boundary contributions were separated in accordance with section 10.2. Conductivity measurements of the lattice and grain boundary were restricted to below approximately 350°C and 400°C respectively. Above these temperatures, the margin of error in separating the two components was unacceptably large. The resistance of the platinum wires was tested using an empty cell and was found to be <1.5Ω below 500°C.

10.3.1. Electrical Conductivity of CoCGO

The CoCGO samples were sintered at 980°C for 1 hour (air) whilst the CGO sample was sintered at 1450°C for 4 hours (air). All samples were furnace cooled. Prior to A.C. impedance analysis, bulk density measurements confirmed that all samples were highly dense (>95%). Microscopy revealed that the average grain size of CGO and CoCGO samples were approximately 1.49μm and 200nm respectively.

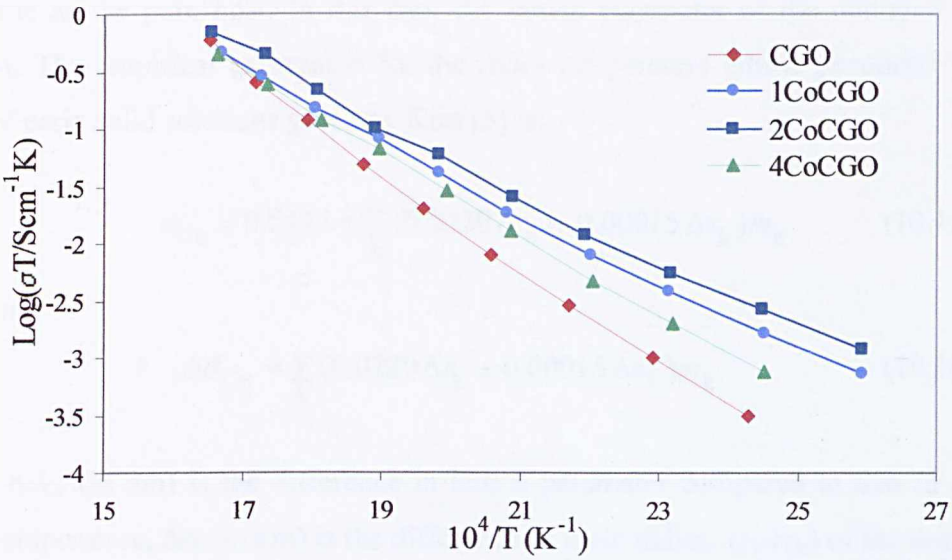


Figure 10.2 Arrhenius graph of the lattice conductivity of CGO and CoCGO.

Figure 10.2 shows the Arrhenius graph for lattice conductivity of CGO and CoCGO. As LogσT increases approximately linearly with 1/T. This strongly suggests that fully associated behaviour is being measured for all the samples. It is clear that the addition of Co enhances the lattice conductivity at temperatures below 350°C with a maximum occurring for the sample 2CoCGO. This trend agrees with the reported enhanced lattice conductivity of small additions of Co to YSZ [2]. Ralph [3] reported the existence of a convergence point at 550°C in the lattice conductivity data of various Gd doped ceria compositions. At this focus point the conductivity is independent of the dopant

concentration. In the present study a convergence point in the lattice conductivity exists at approximately 330°C for CoCGO.

The activation energy (E_a) below 350°C for the lattice conductivity of CGO, 1CoCGO, 2CoCGO and 4CoCGO is 0.80eV, 0.61eV, 0.60eV and 0.70eV respectively. The E_a of CGO is in agreement with the literature [4]. It can therefore be stated that the addition of Co to CGO clearly influences the value of activation energy with a minimum occurring for 2CoCGO. It is generally accepted that the activation enthalpy (ΔH) for ionic conduction in a rare earth (RE) doped fluorite oxide electrolyte is equal to the sum of the enthalpy of motion (ΔH_m) and association (ΔH_a) of the defect complex ($RE_{Ce'} - V_{\ddot{o}}$). In section 4.4 it was reported that ΔH_a strongly influences the activation energy of doped ceria electrolytes and is related to the mismatch in ionic radius of the dopant and host cation. Kim [5] proposed that for a given fluorite structure the ideal dopant radius that maximises the conductivity is the one that leaves the lattice parameter the same as the pure host. In this case the lattice parameter of the undoped ceria is 5.413Å. The empirical expression for the room temperature lattice parameter (d_{Ce} (in nm)) of ceria solid solutions given by Kim [5] is;

$$d_{Ce} = 0.5413 + \sum_k (0.0220\,\Delta r_k + 0.00015\,\Delta z_k) m_k \qquad (10.15)$$

therefore;

$$\Delta d_{Ce} = \sum_k (0.0220\,\Delta r_k + 0.00015\,\Delta z_k) m_k \qquad (10.16)$$

where Δd_{Ce} (in nm) is the difference in lattice parameter compared to that of ceria at room temperature, Δr_k (in nm) is the difference in ionic radius (r_k-r_{Ce}) of the dopant (r_k) and the Ce cation in eightfold coordination, Δz_k is the valency difference (z_k-z_{Ce}), and m_k is the cation percent of the dopant. Assuming that Ce is tetravalent and both Gd and Co are trivalent; r_{Ce} = 0.097nm, r_{Gd} = 0.1053nm and r_{Co} = 0.071nm [6], Δd values for CGO and 2CoCGO are $+3.26\times10^{-4}$nm and -1.096×10^{-3}nm respectively. Similarly, the theoretical cation% of Co in the lattice of CGO that prevents lattice expansion at room temperature is 0.31%. This implies that only a small lattice concentration of Co is required to optimise the lattice conductivity. Figure 10.3 shows spectra from EDXS point analysis in TEM at the grain boundary and in the lattice of 2CoCGO sintered at 980°C for 1 hour and furnace cooled. The peak occurring at 6.92 keV is from cobalt. The majority of the Co is located at the grain boundary whilst only a very low

concentration is observed in the lattice. The trends in lattice ionic conductivity for CoCGO are in excellent agreement with data presented in chapter 9.

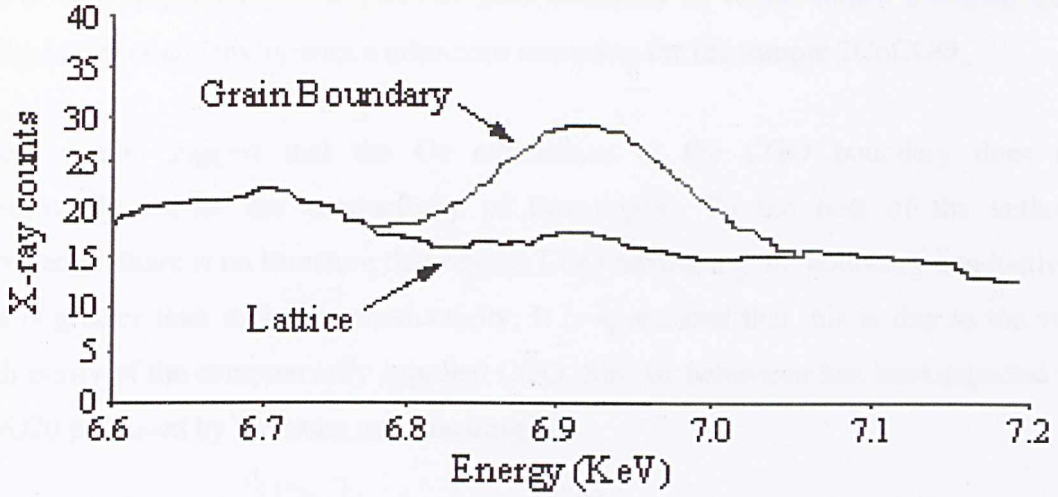


Figure10.3 EDXS spectrum for point analysis in TEM of Co content in the grain boundary and lattice of 2CoCGO sintered at 980°C for 12 hours and furnace cooled.

The conductivity of sample 4CoCGO, although greater than pure CGO, was less than the sample 2CoCGO. It is speculated that the lattice conductivity increases to a maximum as a function of Co addition and then decreases due to increased defect interaction with the oxygen vacancies.

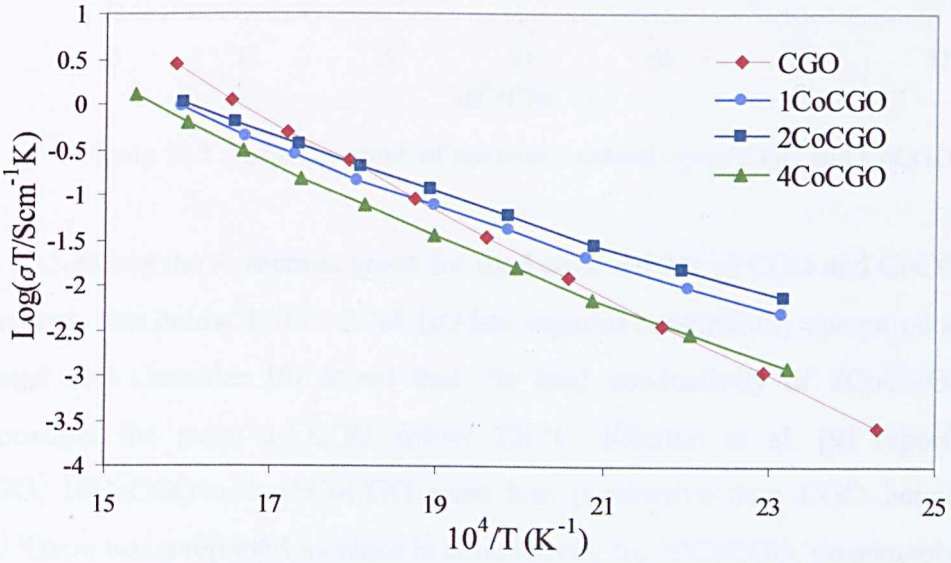


Figure10.4 Arrhenius graph of the grain boundary conductivity of CGO and CoCGO.

Figure 10.4 shows the Arrhenius graph for grain boundary conductivity of CGO and CoCGO. Below approximately 250°C, the grain boundary conductivity of CoCGO is greater than CGO. Above this temperature, the grain boundary conductivity of CGO is

larger than all CoCGO samples studied. E_a values for the grain boundary conductivity of CGO, 1CoCGO, 2CoCGO and 4CoCGO below 390°C are 0.94eV, 0.62eV, 0.60eV and 0.76eV respectively. The CoCGO grain boundary E_a values follow a similar trend to the lattice conductivity with a minimum occurring for the sample 2CoCGO.

These results suggest that the Co enrichment at the CGO boundary does not significantly reduce the conductivity of this region. To the best of the author's knowledge, there is no literature that reports CGO having a grain boundary conductivity that is greater than its lattice conductivity. It is speculated that this is due to the very high purity of the commercially supplied CGO. Similar behaviour has been reported for CGO20 produced by the same manufacturer [7].

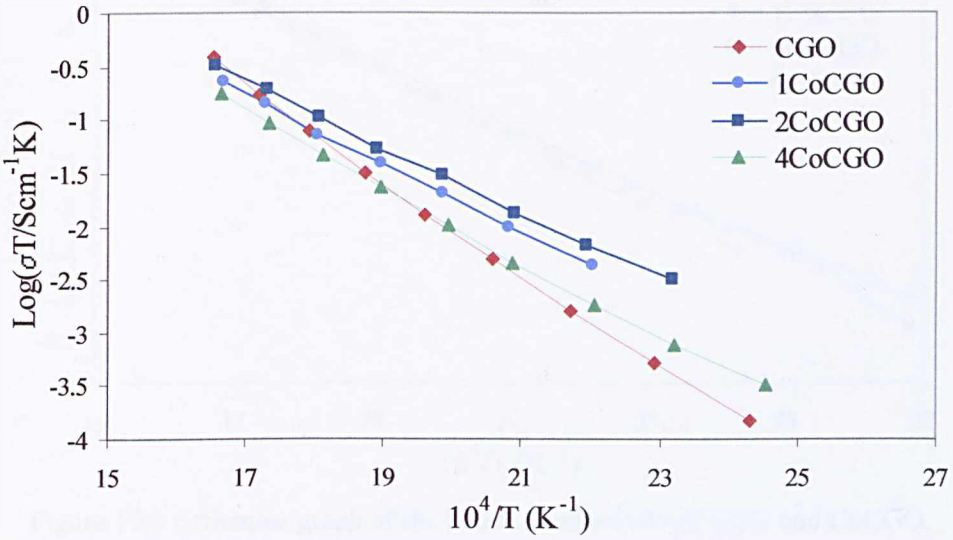


Figure 10.5 Arrhenius graph of the total conductivity of CGO and CoCGO.

Figure 10.5 shows the Arrhenius graph for total conductivity of CGO and CoCGO. The graph reveals that below 320°C, 2CoCGO has superior conductivity compared to CGO. Kleinlogel and Gauckler [8] found that the total conductivity of 2CoCGO20 was approximately the same as CGO below 320°C. Kharton et al. [9] reported that 5CoCGO, 10CoCGO and 15CoCGO were less conductive than CGO between 20-977°C. There was a reported increase in conductivity for 20CoCGO, presumably due to enhanced electronic conduction in the material. Therefore, assuming that the conductivity is solely ionic, a 2% addition of Co to CGO is the optimum additive level in the temperature range studied.

10.3.2. Electrical Conductivity of CuCGO

As for CoCGO, pellets of CuCGO were fired at 980°C for 1 hour and allowed to furnace cool. Bulk density measurements confirmed that all samples were highly dense (>95%). Figure 10.6 shows the Arrhenius plot for lattice conductivity of CGO and CuCGO. As LogσT increases approximately linearly with 1/T, this strongly suggests that fully associated behaviour is being measured for all the samples. The addition of Cu to CGO very slightly enhances the lattice conductivity below the 'convergence point' temperature occurring at 250°C.

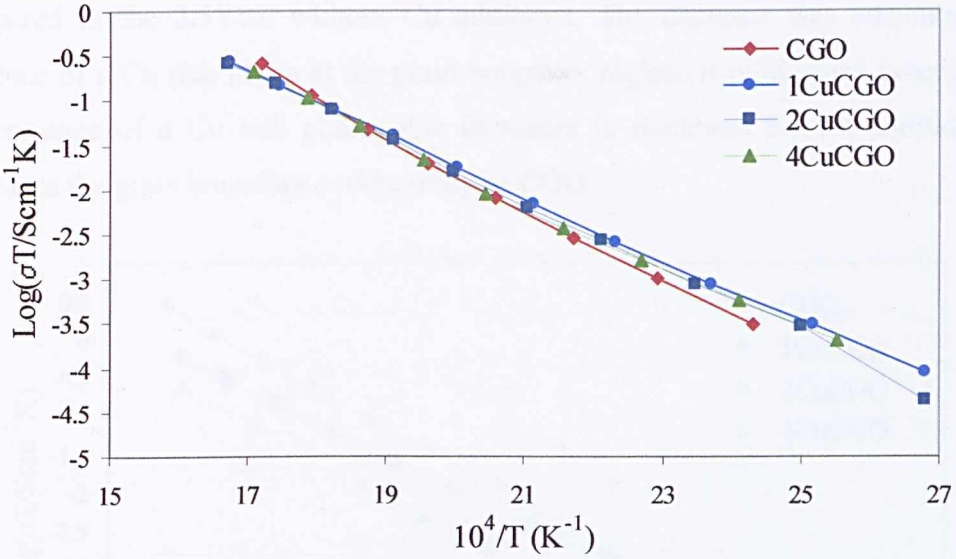


Figure 10.6 Arrhenius graph of the lattice conductivity of CGO and CuCGO.

Hartmanovà [10] reported that the lattice conductivity of 8YSZ was slightly decreased by the addition of Cu. The Cu^{2+} cations were believed to substitute for the Zr^{4+} cations thus creating extra oxygen vacancies. As the 'optimum' oxygen vacancy concentration is considered to exist in ZrO_2 when doped with ~8%Y_2O_3, the additional oxygen vacancies result in greater defect association. As it is known that CGO and CGO20 have very similar lattice ionic conductivities, an increase in oxygen vacancies in CGO is not expected to lower the lattice ionic conductivity. Lattice parameter values of 2CuCGO powder fired at 650°C, 800°C and 1100°C for 2 hours in air and furnace cooled were 5.4129Å, 5.4172Å and 5.4203Å respectively. This suggests that at 650°C Cu decreases the lattice parameter of CGO considerably. It is assumed that the Cu diffuses into the Gd/Ce bulk by a similar mechanism to that previously described for Co in CGO

(chapter 9). Between 800°C and 1100°C, where the majority of shrinkage occurs during CHR sintering, the lattice parameter is approximately the same as CGO. Therefore, as the lattice parameter of CuCGO and CGO are almost identical after heating at temperatures greater than 800°C, it is speculated that the ΔH_a is likewise similar thus explaining why there is little difference in the lattice conductivity of CGO and CuCGO. Figure 10.7 shows the Arrhenius graph for grain boundary conductivity of CGO and CuCGO. The inclusion of Cu as a sintering aid to CGO decreases the grain boundary conductivity for all additive levels investigated in this study. Bowen et al. [11] studied the impedance spectroscopy of Cu additions to 2.5YSZ. It was reported that increased additions of Cu to 2.5YSZ decreased the grain boundary conductivity of 2.5YSZ compared to the 2.5YSZ without Cu additions. The decrease was attributed to the presence of a Cu rich phase at the grain boundary region. It is likewise speculated that the presence of a Cu rich phase, that increases in thickness for Cu additions >2%, decreases the grain boundary conductivity of CGO.

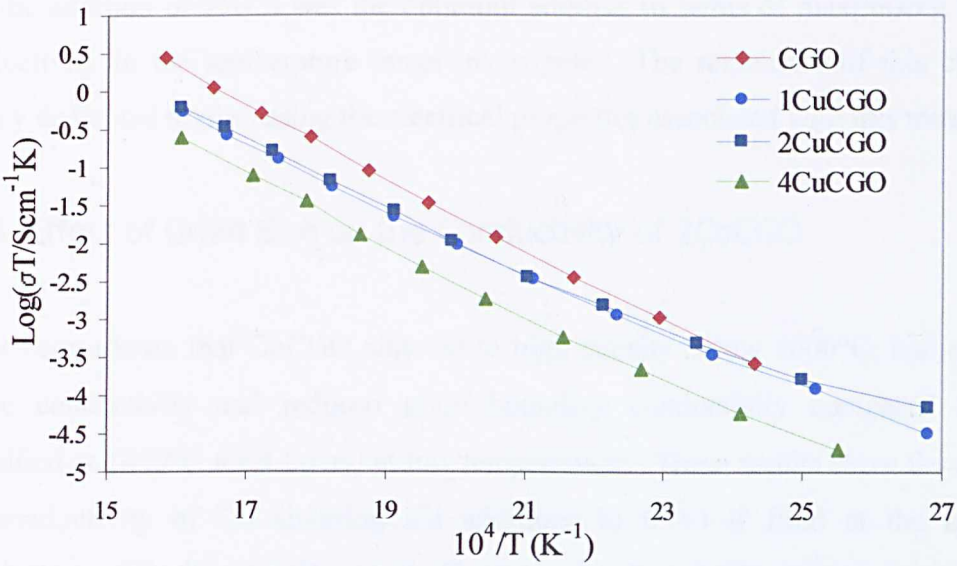


Figure 10.7 Arrhenius graph of the grain boundary conductivity of CGO and CuCGO.

Figure 10.8 shows the Arrhenius graph for the total conductivity of CGO and CuCGO. Similar to the results for CoCGO (Figure 10.5), the addition of Cu to CGO does not significantly decrease the total ionic conductivity in the temperature range studied. These studies indicate that Cu can be effectively used to densify CGO at temperatures below 1000°C with only minor adverse effects on the ionic conductivity.

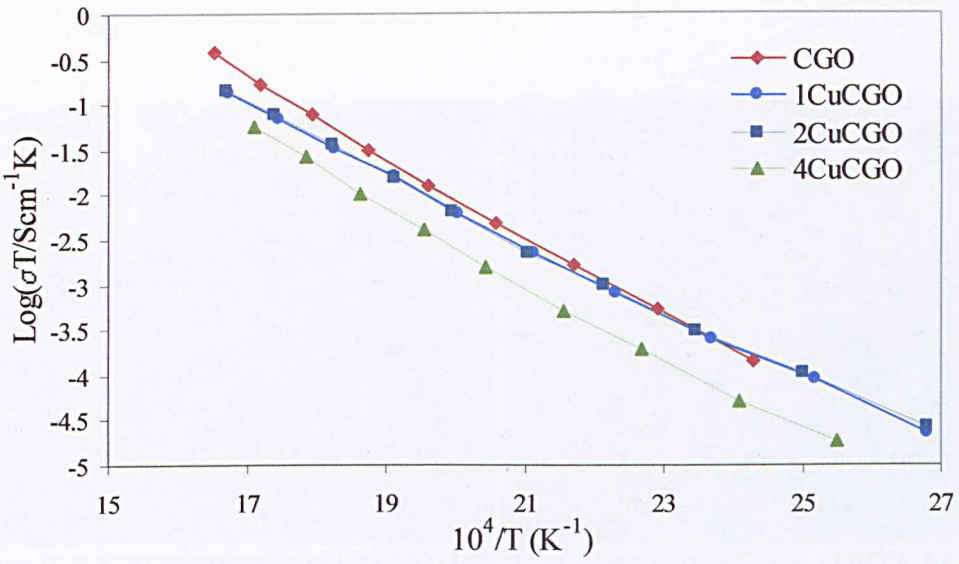


Figure 10.8 Arrhenius graph of the total conductivity of CGO and CuCGO.

A.C. impedance data of CoCGO and CuCGO materials presented in this study revealed that the addition of 2%Co was the optimum additive in terms of maximising the ionic conductivity in the temperature range investigated. The remainder of this chapter is mainly dedicated to discussing the electrical properties associated with this material.

10.4. Effect of Grain Size on the Conductivity of 2CoCGO

It has been shown that CoCGO sintered to high density below 1000°C, had enhanced lattice conductivity and reduced grain boundary conductivity compared to CGO (densified at 1450°C for 4 hours) at low temperatures. These results show the effect on the conductivity of Co sintering aid additions to CGO if fired at the annealing temperature of ferritic stainless steel. These results do not take into account the large difference in grain size between the CGO (1.49μm) and CoCGO (~200nm). A comparative study of CGO and 2CoCGO of similar grain sizes was performed to determine what effect the reduced grain size of 2CoCGO has on the ionic conductivity.

From figure 9.35b, it was possible to determine the firing schedule that would densify a 2CoCGO specimen having a similar grain size to the CGO sample used as a reference. A 2CoCGO pellet was fired at 10K/min to 1100°C and then immediately furnace cooled (2CoCGOL where L indicates large grain size). Using the linear line intercept method, the grain size of CGO and 2CoCGOL were 1.49μm and 1.73μm respectively

(Figure 10.9). The 2CoCGO sample with a grain size of ~200nm is termed 2CoCGOS in this section.

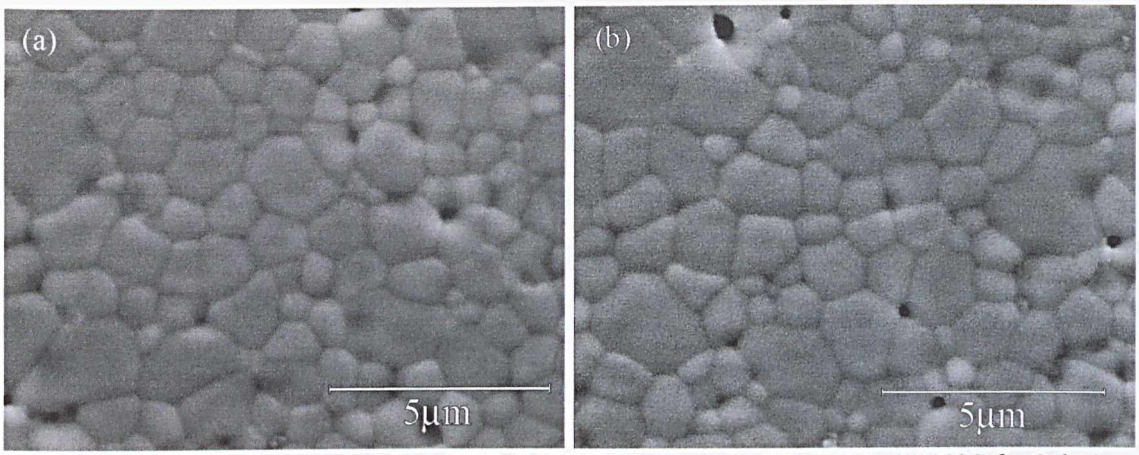


Figure 10.9 SEM micrographs of (a) CGO (1450°C for 4 hrs) (b) 2CoCGOL (1100°C for 0 hrs).

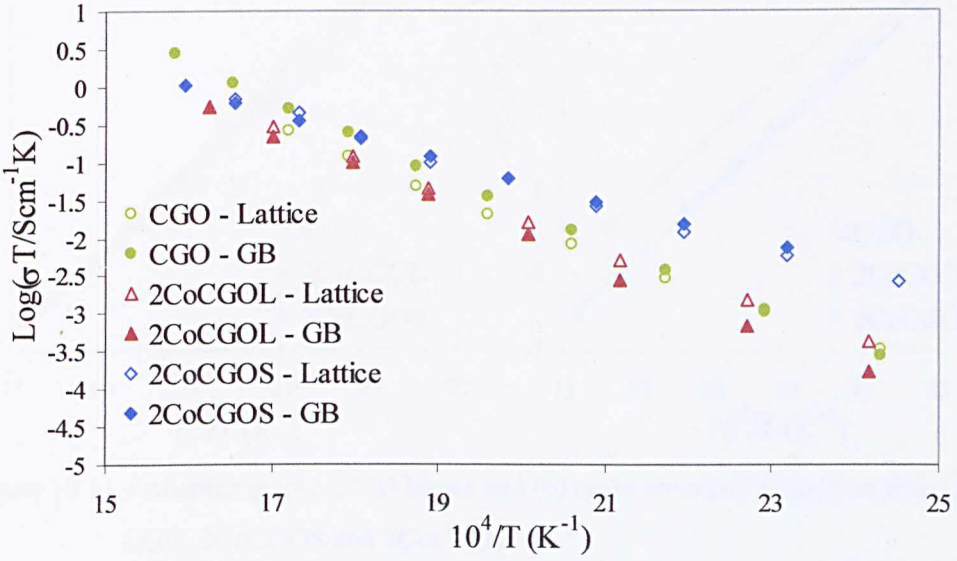


Figure 10.10 Arrhenius graph of lattice and grain boundary (GB) conductivity of CGO, 2CoCGOS and 2CoCGOL.

It is generally accepted that the lattice conductivity for a ceramic material is essentially independent of grain dimensions (provided that the lattice composition is independent of grain size). Previously, it was argued that the lattice conductivity of 2CoCGOS is higher than CGO at low temperatures due to lower ΔH_a resulting from better lattice parameter matching. Interestingly, the lattice conductivities of 2CoCGOL and CGO are approximately the same (Figure 10.10). In figure 9.22 it was shown that 2CoCGO fired in excess of 1000°C had a lattice parameter similar to that of CGO. This result further supports the argument that firing temperature dictates the lattice parameter that likewise affects the ionic conductivity of the material at low temperatures.

Figure 10.10 shows that the grain boundary conductivities of CGO and 2CoCGOL are approximately the same. Since these specimens have similar grain size, the Co rich layer at the grain boundary has had little effect on the specific grain boundary conductivity of CGO. Kharton et al. [9] reported that the grain boundary conductivity of CGO20 increases with increasing average grain size greater than 2-3μm due to a reduction in grain boundary surface area. The observation that grain boundary conductivity of 2CoCGOL is less than that of 2CoCGOS is not consistent with their relative grain sizes. Christie et al. [12] also reported an abnormally high conductivity in fine-grained samples of CGO20 (0.4-0.8μm) which they were unable to explain.

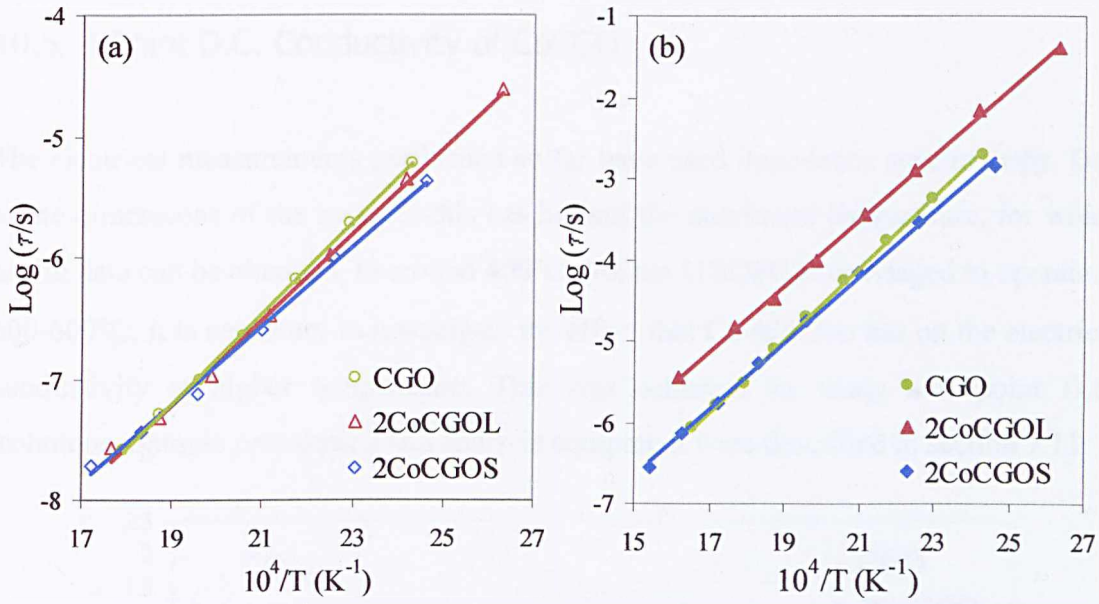


Figure 10.11 Arrhenius graphs of (a) lattice and (b) grain boundary relaxation time (τ) of CGO, 2CoCGOS and 2CoCGOL.

Figure 10.11a shows the Arrhenius plot of the lattice relaxation time (τ_l) for CGO, 2CoCGOL and 2CoCGOS. From equation 10.11, τ_l is proportional to the dielectric constant/lattice conductivity ratio. In figure 10.10 the lattice conductivity of 2CoCGOS was approximately an order of magnitude greater than CGO at low temperature, whilst figure 10.11a shows that the difference in τ_l between these two materials is significantly less than this amount. It is thus speculated that ε_l of 2CoCGOS is much larger than ε_l of CGO, thus explaining why the difference in τ_l is smaller than expected. As the lattice conductivities and the lattice relaxation times of CGO and 2CoCGOL are approximately the same, this indicates that the lattice dielectric constant of 2CoCGOL is different to that of 2CoCGOS. It is speculated that Co loss from the lattice region of 2CoCGOL when sintered at relatively high temperature decreases the dielectric constant such that it

tends towards that of CGO. Conversely, figure 10.11b shows that the grain boundary relaxation times of CGO and 2CoCGOS are approximately the same, whilst the grain boundary relaxation time of 2CoCGOL is approximately seven times as large for a given temperature. Since the grain boundary conductivity of 2CoCGOS is greater than 2CoCGOL (Figure 10.10) this indicates that the grain boundary dielectric constant of 2CoCGOL is similar in magnitude to that of 2CoCGOS. These results suggest that when 2CoCGO is sintered at 1100°C, the lattice contains only trace levels of Co as it has segregated to the grain boundary region. This may explain why the lattice parameters of CGO and 2CoCGO are almost identical when sintered at >1000°C.

10.5. 4 Point D.C. Conductivity of CoCGO

The electrical measurements performed so far have used impedance spectroscopy. Due to the dimensions of the samples this has limited the maximum temperature, for which useful data can be obtained, to around 400°C. As the ITSOFC is envisaged to operate at 500-600°C, it is necessary to investigate the effect that Co addition has on the electrical conductivity at higher temperature. This was achieved by using a 4 point D.C. technique. Sample preparation and analysis equipment were described in section 7.11.

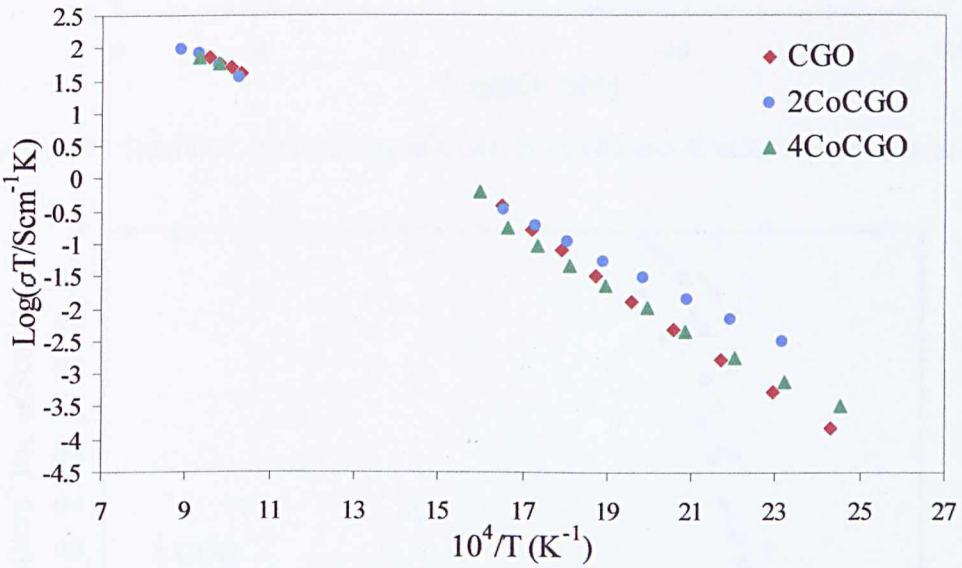


Figure 10.12 Total conductivity of CGO, 2CoCGO and 4CoCGO in air (AC and DC).

Figure 10.12 shows the combined A.C. and D.C. total conductivity in air for highly dense (>95%) samples of CGO, 2CoCGO and 4CoCGO. The region with no data represents a range in which neither technique can produce accurate results for the specimen dimensions used. The D.C. total conductivity of CGO agrees with data

published by Wang et al. [13]. Between 700-850°C, all samples have approximately the same total conductivity and E_a (0.65eV). This trend agrees with that found in the previous studies for Co additions to CGO20 [8]. The graph shows that Ea is lower in the high temperature D.C measurements. This phenomenon has been widely reported in the literature for CGO and is due to the dissociation of the defect pairs at approximately 500-550°C [4]. This enables more oxygen ions to conduct, thus resulting in a lower Ea. Although this transition occurs in the temperature range were data are lacking in the present study, it is speculated that the addition of Co does not significantly affect the 'dissociation' temperature of CGO. This is probably due to the very small Co content that was previously shown to exist in the bulk of the material.

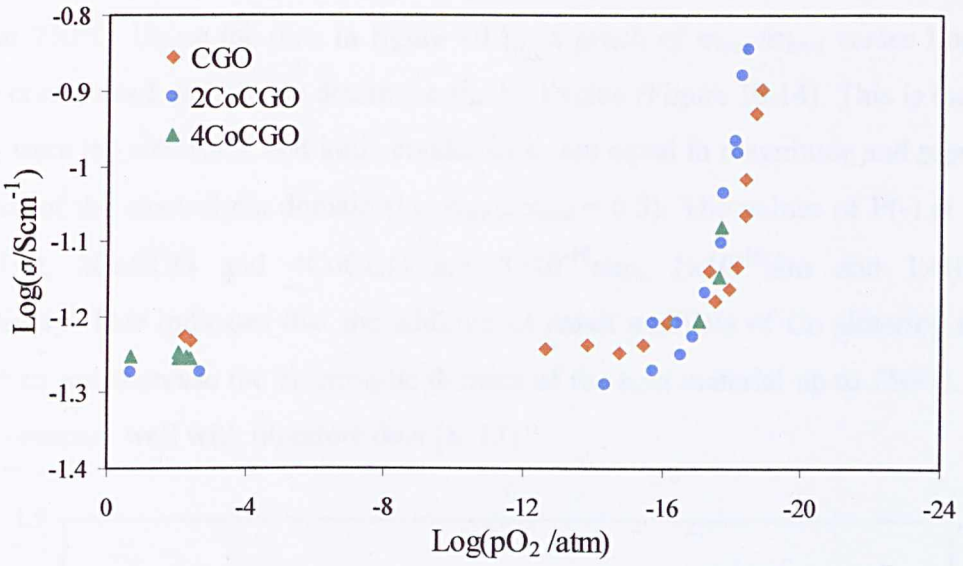


Figure 10.13 Total D.C. conductivity of CGO, 2CoCGO and 4CoCGO versus pO_2 at 750°C.

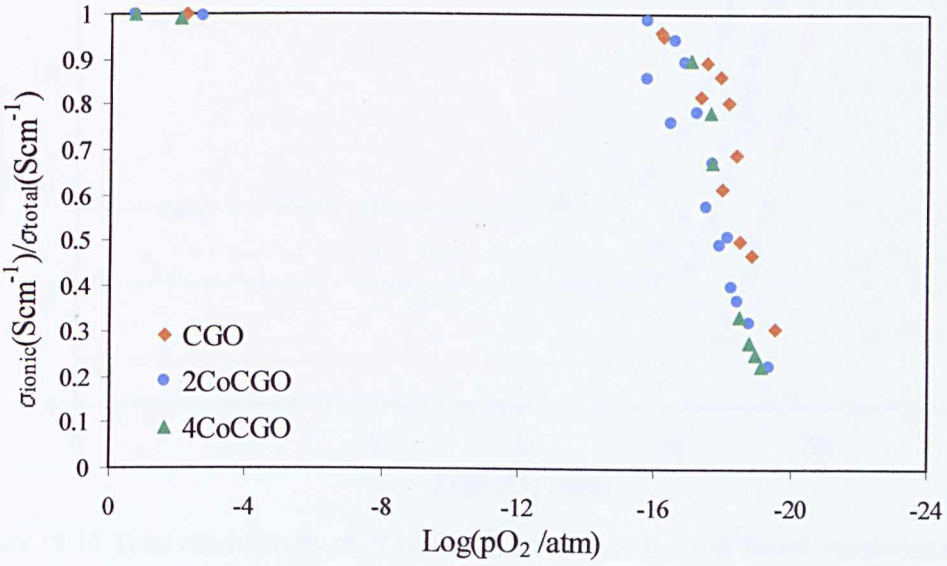


Figure 10.14 Graph showing the P(-) value for CGO and 2CoCGO at 750°C.

Figure 10.13 shows the total D.C. conductivity as a function of pO_2 for CGO, 2CoCGO and 4CoCGO at 750°C. As mentioned in section 4.8, one of the main problems associated with doped ceria electrolytes is the tendency of the Ce^{4+} cation to reduce to Ce^{3+} at low pO_2 values. At high pO_2 ($>10^{-16}$atm), the conducting mechanism of CGO is predominately ionic. For low pO_2 values ($<10^{-16}$atm) the conductivity significantly increases due to the presence of electronic charge carriers that result from the reduction of the Ce^{4+} cation. The gradient in the region where electronic conductivity dominates is approximately –0.25. This agrees with theory, which predicts that the electron concentration will be proportional to $pO_2^{-1/4}$ [14].

Importantly, both 2CoCGO and 4CoCGO show approximately the same behaviour as CGO at 750°C. Using the data in figure 10.13, a graph of $\sigma_{ionic}/\sigma_{total}$ verses $Log(pO_2)$ can be constructed, in order to determine the P(-) value (Figure 10.14). This is the value of pO_2 were the electronic and ionic conductivity are equal in magnitude and represents the limit of the electrolytic domain (i.e. $\sigma_{ionic}/\sigma_{total} = 0.5$). The values of P(-) at 750°C for CGO, 2CoCGO and 4CoCGO are 5×10^{-18}atm, 1×10^{-18}atm and 1×10^{-18}atm respectively. This indicates that the addition of small amounts of Co sintering aids to CGO does not decrease the electrolytic domain of the host material up to 750°C. These results compare well with literature data [8, 13].

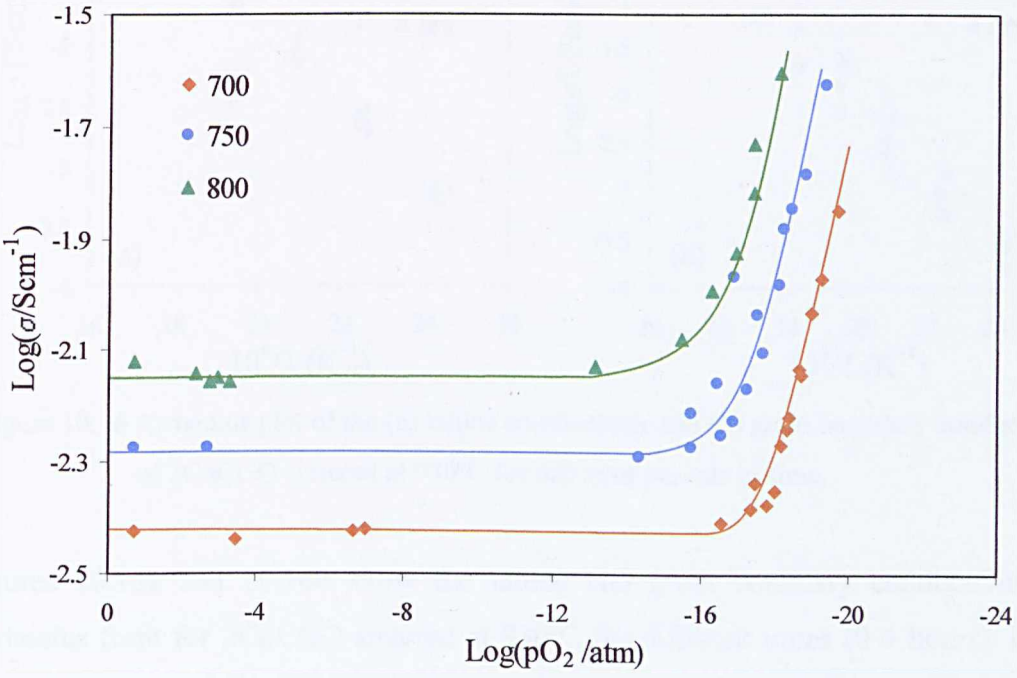


Figure 10.15 Total conductivity of 2CoCGO versus pO_2 at three different temperatures (°C).

Figure 10.15 shows the variation in D.C. conductivity as a function of pO_2 for 2CoCGO at three different temperatures: 700, 750 and 800°C. The electrolytic domain decreases as the temperature is increased because the formation of electrons is thermally activated. For the same reason as previously discussed, the gradient of each graph in highly reducing atmospheres (>10^{-18}atm) was approximately –0.25.

10.6. Effect of Sintering Time and Temperature on the Conductivity of 2CoCGO

In chapter 9 it was found that the oxygen vacancy concentration of 2CoCGO at room temperature increased when the firing temperature was decreased from 1000°C to 750°C. A series of A.C impedance measurements was performed on 2CoCGO samples fired at 930°C and 980°C for different periods of time (0, 0.5, 1, 2 and 4 hours) to assess whether the conductivity could be enhanced by carefully controlling the firing temperature and time.

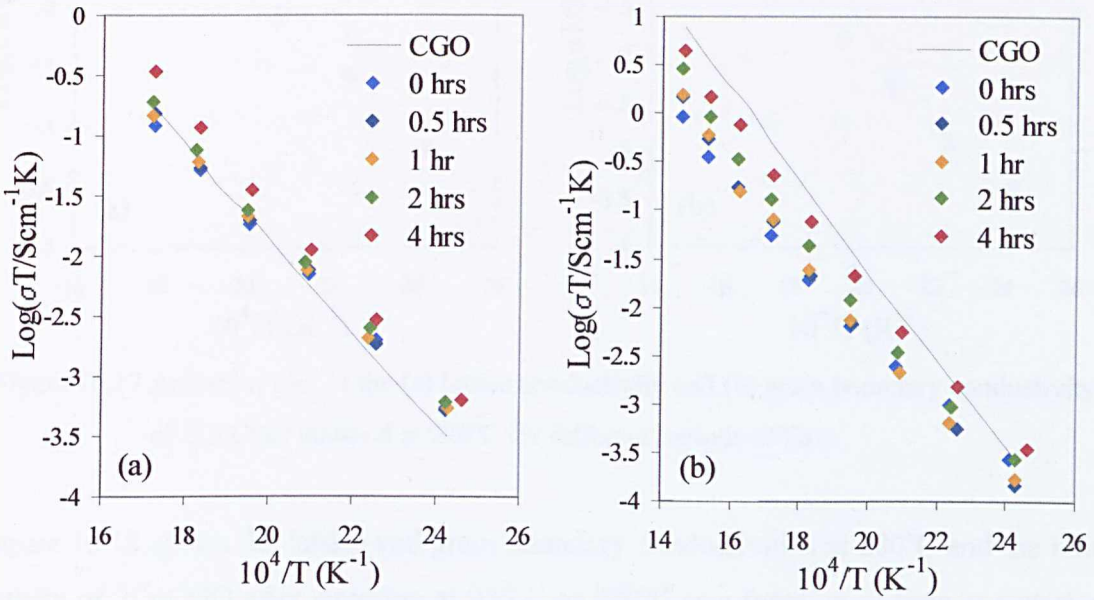


Figure 10.16 Arrhenius plot of the (a) lattice conductivity and (b) grain boundary conductivity of 2CoCGO sintered at 930°C for different periods of time.

Figures 10.16a and 10.16b show the lattice and grain boundary conductivities in Arrhenius form for 2CoCGO sintered at 930°C for different times (0-4 hours). Below approximately 240°C all 2CoCGO samples have enhanced lattice conductivity compared to CGO. Above this value only 2CoCGO specimens sintered in excess of 1 hour have enhanced lattice conductivity, with a maximum occurring for the sample

sintered for 4 hours. The equivalent grain boundary conductivity for all 2CoCGO samples is less than that of CGO. The grain boundary conductivity increases as a function of sintering time.

Figures 10.17a and 10.17b show the lattice and grain boundary conductivities in Arrhenius form of 2CoCGO sintered at 980°C for different times. All samples containing Co have an enhanced conductivity compared to CGO at temperatures below 320°C, above this temperature 2CoCGO has approximately the same conductivity as CGO regardless of sintering time. As for samples sintered at 930°C, the grain boundary conductivity of 2CoCGO sintered at 980°C is less that that of CGO but is independent of sintering time.

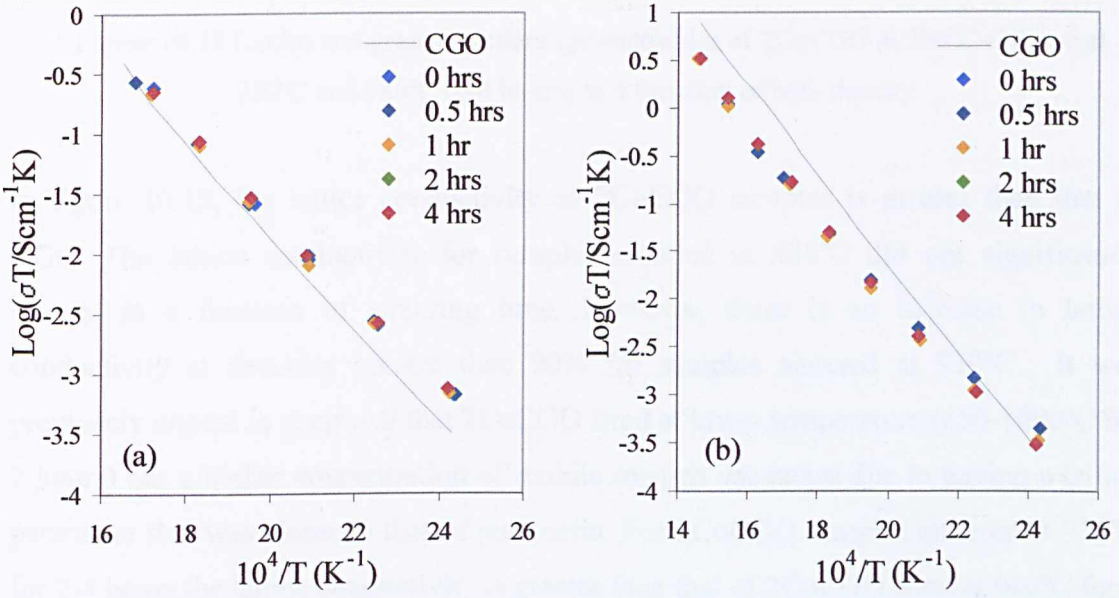


Figure 10.17 Arrhenius plot of the (a) lattice conductivity and (b) grain boundary conductivity of 2CoCGO sintered at 980°C for different periods of time.

Figure 10.18 shows the lattice and grain boundary conductivities at 200°C and the bulk density of 2CoCGO after sintering at 930°C or 980°C as a function of time at sintering temperature. The lattice and grain boundary conductivities for CGO at 200°C are 10.3×10^{-6} S cm^{-1} and 14.3×10^{-6} Scm^{-1} respectively. Increasing sintering time for samples fired at 930°C results in increased bulk density and grain boundary conductivity. It is speculated that as the material densifies there is a relative increase in the grain boundary contact surface area. Specimens sintered at 980°C show grain boundary conductivity to be approximately independent of sintering time, probably because these specimens are all close to high density.

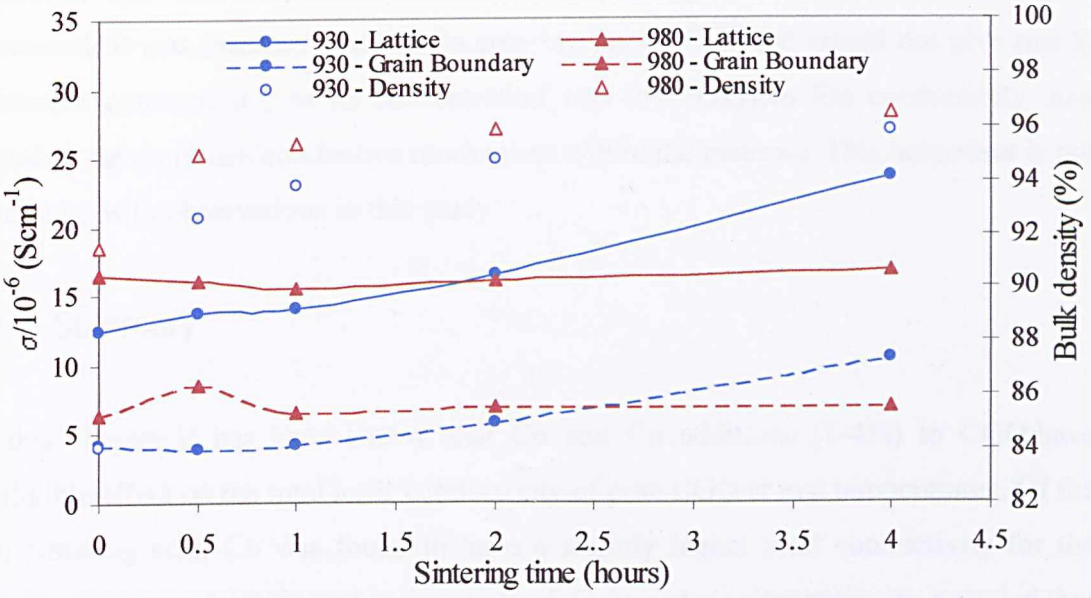


Figure 10.18 Lattice and grain boundary conductivities of 2CoCGO at 200°C sintered at 930°C and 980°C (0-4 hours) as a function of bulk density.

In figure 10.18, the lattice conductivity of 2CoCGO samples is greater than that of CGO. The lattice conductivity for samples sintered at 980°C did not significantly change as a function of sintering time. However, there is an increase in lattice conductivity at densities greater than 90% for samples sintered at 930°C. It was previously argued in chapter 9 that 2CoCGO fired at lower temperature (650-1000°C for 2 hours) has a higher concentration of mobile oxygen vacancies due to having a lattice parameter that was closer to that of pure ceria. For 2CoCGO samples sintered at 930°C for 2-4 hours the lattice conductivity is greater than that of 2CoCGO fired at 980°C for a similar time. It is speculated that the increase in lattice conductivity for 2CoCGO fired at 930°C as a function of sintering time is thus due to the slower redistribution of Co. Furthermore, firing 2CoCGO at lower temperature for extended periods of time enhances the lattice conductivity of the material by minimising the lattice parameter mismatch compared to that of pure ceria.

Kleinlogel and Gauckler [8] sintered 1CoCGO20 at 900°C for dwell times of 10 minutes, 2 hours and 50 hours. A.C impedance at 200°C of the sample sintered for 10 minutes had a single arc, this was interpreted as representing purely electronic conductivity through the Co rich layer at the grain boundary. As sintering time increased, two separated arcs formed that after sufficient annealing were similar to those of CGO20. It was proposed that as more of the Co rich grain boundary layer phase

dissolved into the lattice, the electronic conductivity associated with this region decreased. It was assumed that the Co entering the CGO lattice would not give rise to electronic conductivity, as its concentration was low. Oxygen ion conductivity now becomes the dominant conductive mechanism within the material. This behaviour is not consistent with observations in this study.

10.7. Summary

In this chapter it has been shown that Co and Cu additions (1-4%) to CGO have negligible effect on the total ionic conductivity of pure CGO at low temperatures. Of the two sintering aids, Co was found to have a slightly higher total conductivity for the temperature range investigated in this study. A.C. impedance spectroscopy revealed that a 2%Co addition gave the best conductivity in samples with additives sintered below 1000°C. A 4 point D.C technique confirmed that the conductivity of 2CoCGO was solely ionic at ITSOFC operating temperatures. Furthermore, it was shown that the addition of 2%Co and 4%Co did not significantly affect the electrolytic domain region compared to pure CGO at 750°C. Whilst the grain boundary conductivity of 2CoCGO was slightly reduced at lower temperatures, the lattice component was enhanced compared to CGO. Furthermore, it was found that densifying 2CoCGO at lower temperatures for extended periods of time resulted in enhancing the lattice conductivity compared to CGO and 2CoCGO densified at higher temperature. These findings are consistent with those reported in chapter 9 that indicate that Co diffuses into the CGO structure and minimises lattice parameter change from that of pure ceria. This results in minimising ΔH_a thus enhancing the lattice ionic conductivity. From a practical viewpoint, densifying 2CoCGO at lower temperature not only reduces production costs but results in a material with slightly enhanced ionic conductivity at low temperatures.

References

1. H.L.Tuller. Solid State Ionics. **131**, (2000), 143.
2. M.Hartmanová, F.Hanic, D.Tunega and K.Putyera. Chem.Papers. **12-15**, (1998), 12.
3. J.M.Ralph. Ph.D. Thesis. University of London, 1998.
4. B.C.H.Steele. Solid State Ionics. **129**, (2000), 95.
5. D-J.Kim. J.Am.Ceram.Soc. **72**, 8, (1989), 1415.
6. R.D.Shannon. Acta.Cryst. **A32**, (1976), 751.

7. R.Rudkin. Private Communications.

8. C.Kleinlogel and L.J.Gauckler. J.Electroceramics. **5**, 3, (2000), 231.

9. V.V.Kharton, F.M.Figueiredo, L.Navarro, E.N.Naumovich, A.V.Kovalevsky, A.A.Yaremchenko, A.P.Viskup, A.Carneiro, F.M.B.Marques and J.R.Frade. J.Mater.Sci. **36**, (2001), 1105.

10. M.Hartmonova, F.W.Poulsen, F.Hanic, K.Putyera, D.Tunega, A.A.Urusovskaya and T.V.Oreshnikova. J.Mater.Sci. **29**, (1994), 2152.

11. C.Bowen, S.Ramesh, C.Gill and S.Lawson. J.Mater.Sci. **33**, (1998), 5103.

12. G.M.Christie and F.P.Fvan Berkel. Solid State Ionics. **83**, (1996), 17.

13. S.Wang, T.Kobayashi, M.Dokiya and T.Hashimoto. J.Electrochem.Soc. **147**, 10, (2000), 3606.

14. Science and Technology of Fuel Cells. N.Q.Minh and T.Takahashi. Elsevier Press, 1995.

Chapter 11 – Factors Affecting Consolidation and Densification of 2CoCGO Powder

11.1. Introduction

In the previous chapter it was concluded that a 2% addition of Co to CGO was the 'optimum' additive level. The aim of this chapter is to explore ways in which the densification of this material can be maximised by controlling certain processing steps. It was speculated that the densification of 2CoCGO could be further enhanced if the green density of the consolidated powder was increased. The three factors that are most influential to the efficient packing of the 2CoCGO powder are; calcination temperature of the nitrate, particle size distribution and external pressure applied to consolidate the powder. A greater understanding may facilitate more reliable production of the SOFC and thus make it economically more competitive.

The selection of CGO in the Imperial planar design is partly due to having a TEC that is approximately the same as ferritic stainless steel for temperatures below 1000°C. The effect on the TEC of Co addition to CGO is thus investigated. The last section of this chapter is a brief feasibility study on the densification of 2CoCGO thick films made by tape casting and screen-printing.

11.2. Effect of Powder Calcination Temperature on Densification of 2CoCGO

The Co was added to CGO in the form of $Co(NO_3)_2.6H_2O$ dissolved in ethanol. Subsequently the water, ethanol and nitrate species were removed by calcination to form the CoCGO powder. This was considered necessary to avoid gas evolution during sintering that would be detrimental to the densification process, or in a more extreme situation result in mechanical failure of the specimen.

It was previously shown that the minimum calcination temperature of CoCGO powder is ~300°C (Figure 8.4). Figure 11.1 shows the relative density of 2CoCGO that was calcined at 300°C for 30 minutes (2CoCGOLC) compared with one calcined at 650°C for 30 minutes (2CoCGOHC) at 5K/min to 800°C and 2K/min to 1000°C in argon.

Decreasing the calcination temperature increases the green density of the consolidated powder, the green densities of 2CoCGOLC and 2CoCGOHC were 59.1% and 57.2% respectively. The green density of as-received CGO and CGO dispersed in ethanol and heat treated in a similar fashion to CoCGO were both approximately 60%. The average particle size of CGO, 2CoCGOLC and 2CoCGOHC were 0.87μm, 0.87μm and 0.94μm respectively. This indicates that calcining at 300°C results in negligible agglomeration of the powder whilst calcining at 650°C results in a limited amount of agglomeration.

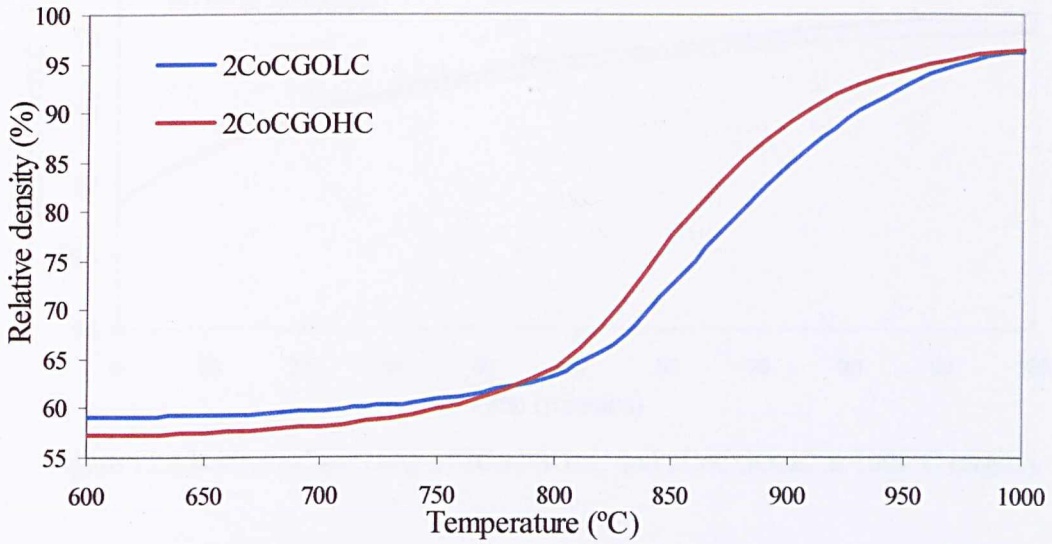


Figure 11.1 Constant rate heating of 2CoCGO calcined at 400°C for 30 minutes (2CoCGOLC) and 650°C for 30 minutes (2CoCGOHC) (5K/min to 800°C and 2K/min to 1000°C (argon)).

A surprising result from figure 11.1 is that the onset of densification for 2CoCGOHC occurs at a lower temperature than for 2CoCGOLC. The relative densities of both samples, however, were almost identical at approximately 95% when the temperature reached 1000°C.

Figure 11.2 shows the isothermal final stage sintering of 2CoCGOLC and 2CoCGOHC at 1000°C after they had been heated up at a constant rate as indicated in figure 11.1. During final stage sintering, 2CoCGOLC has a slightly higher relative density than 2CoCGOHC. It was shown by Occhionera and Halloran [1] that alumina compacts with a higher green density had a smaller mean pore size and a narrower pore size distribution. Zhao and Harmer [2] reported that increasing the green density increases the number of pores per grain and narrows the pore size distribution. A model was presented that predicted that increasing the number of pores on the grain increased the

densification rate, grain growth rate and the ratio of relative densification during the final stages of densification. This model is consistent with the final stage sintering of ceria and CGO20 [3]. It thus follows that the slightly enhanced densification of 2CoCGOLC during the final stages of sintering is due to the increased number of pores on the grain that result from its higher green density after consolidation.

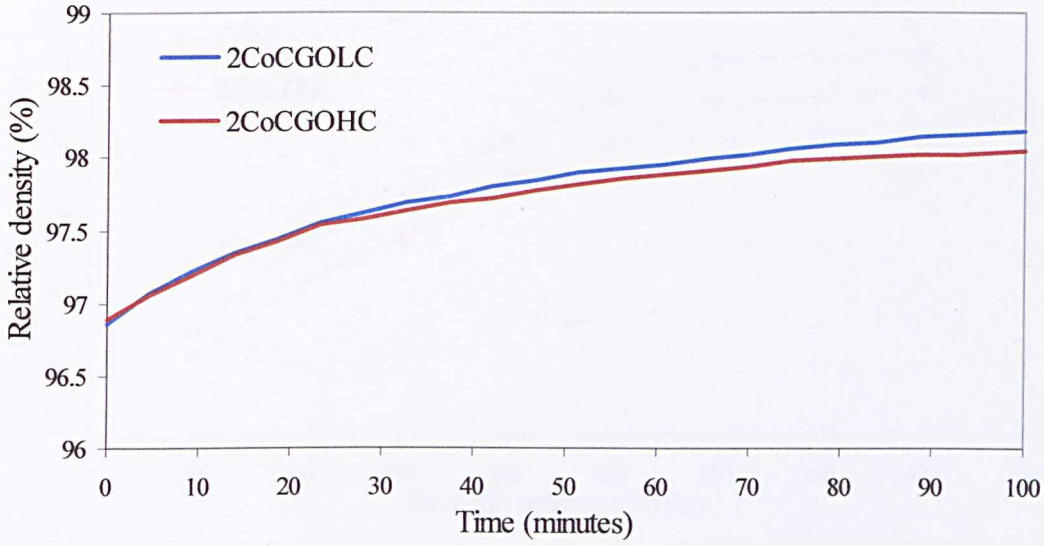


Figure 11.2 Isothermal sintering of 2CoCGOLC and 2CoCGOHC at 1000°C (argon).

From a practical viewpoint, the final density of both the materials is approximately the same, the final relative densities of 2CoCGOLC and 2CoCGOHC were 98.18% and 98.03% respectively. Therefore, the effect of calcination temperature between 300-650°C of 2CoCGO powder can be considered to have negligible effect on the overall densification at 1000°C.

11.3. Effect of Isostatic Pressure on Densification of 2CoCGO

One of the key factors that influences sintering of a powder system is applied external pressure during compaction of the powder body. Generally, the green density of a powder system is increased by isostatically pressing in order to minimise the sintering temperature required to achieve full densification. In terms of manufacture of the ITSOFC assembly being developed at Imperial College, it would be beneficial if isostatic pressing was not performed. Apart from reducing production costs, it could be beneficial to the anode and cathode performance, as these components require a large porosity to work efficiently. Furthermore, isostatic pressing requires that samples be

sealed in airtight bags. This can be particularly difficult when dealing with large objects that have sharp corners. Studies were performed in order to determine whether the enhanced densification of CGO with the addition of Co eliminated the need for isostatic pressing of the sample prior to firing.

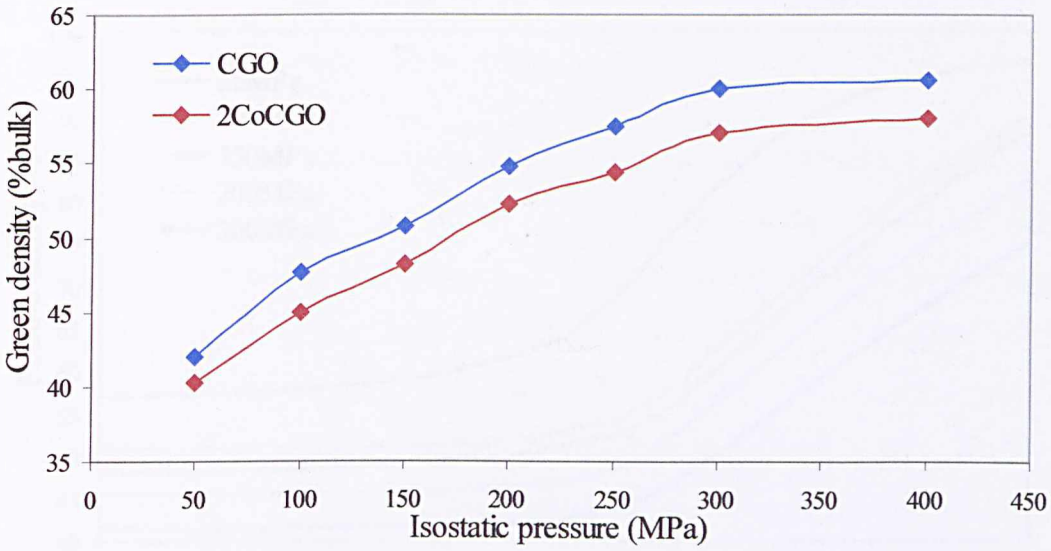


Figure 11.3 Green density (%bulk) of CGO and 2CoCGO isostatically pressed at different pressures.

Figure 11.3 shows that the green density (bulk) of both CGO and 2CoCGO increased approximately linearly with applied isostatic pressure between 50-300MPa. Further increases in applied pressure resulted in a negligible increase in the green density. Therefore, isostatically pressing CGO and 2CoCGO at 300MPa is considered sufficient to maximise the green density of the powder body.

Figures 11.4 and 11.5 show the relative density of 2CoCGO, fired by CHR sintering upto 1000°C then isothermally held for 100 minutes, as a function of isostatic pressure. The change in relative density during CHR up to 1000°C is approximately the same for all samples. The difference in relative density at 1000°C (0 minutes) is approximately the same as the difference in green density of the respective samples. After isothermally sintering at 1000°C for 100 minutes, only 2CoCGO isostatically pressed at 200MPa and 300MPa achieved >95% density. Therefore, in terms of achieving highly dense samples at 1000°C after a limited time, the green density of 2CoCGO must be equal to or greater than approximately 51%. Ultimately, the 2CoCGO powder is envisaged to be fabricated

into thick films (~15μm) by either tape casting or screen-printing. Typically, the green density of films prepared by these techniques, after binder removal, is approximately 35-45%. Therefore, isostatic pressing (>200MPa) will be required prior to firing in order to achieve dense 2CoCGO below 1000°C.

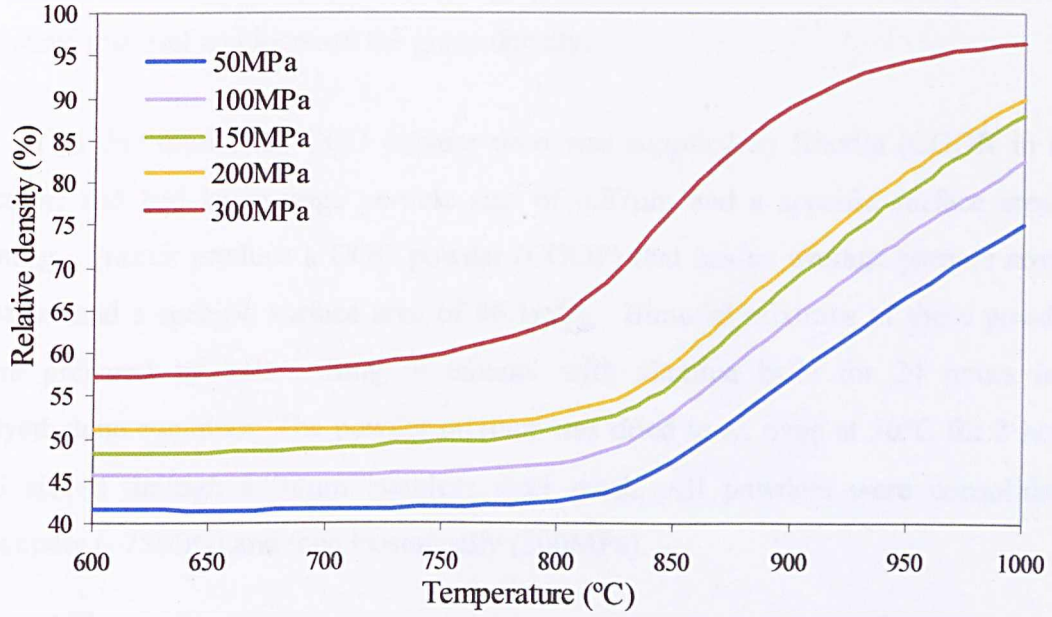


Figure 11.4 CRH dilatometry of 2CoCGO powder isostatically pressed at different pressures (5K/min to 800°C and 2K/min to 1000°C (argon)).

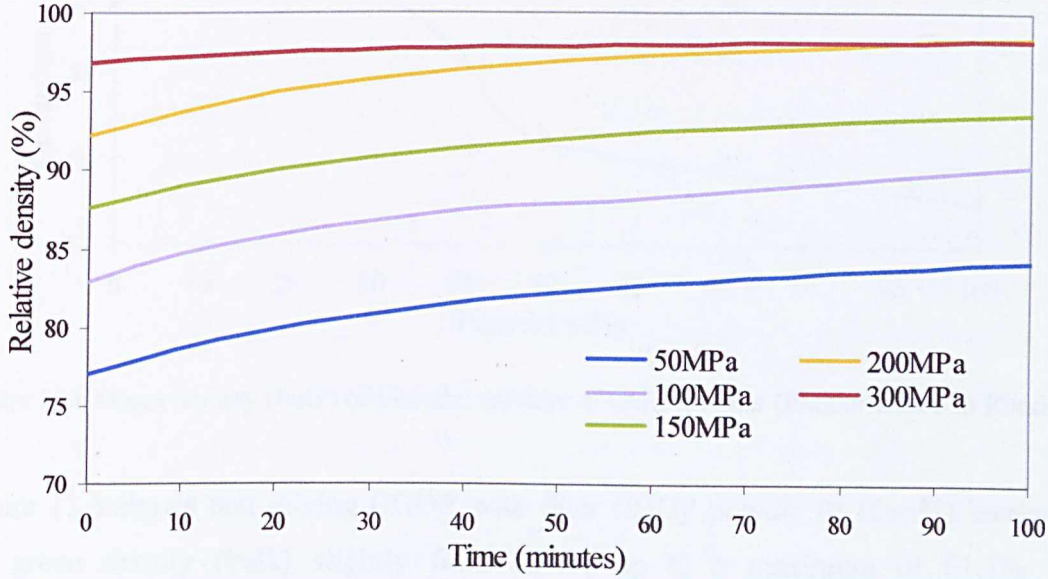


Figure 11.5 Isothermal sintering at 1000°C of 2CoCGO powder isostatically pressed at different pressures (argon).

11.4. Effect of Particle Size on Densification of CGO and 2CoCGO

In the previous section it was demonstrated that enhancing the green density likewise enhances the sinterability of 2CoCGO. A method used to increase the green density of compacts is to mix fine and coarse powders of the same material (bimodal mixtures). In principle, the interstices between the large particles are filled with smaller particles of the same material and increase the green density.

So far in this thesis, the CGO powder used was supplied by Rhodia (CGOR in this section) and had an average particle size of 0.87μm and a specific surface area of $21m^2/g$. Praxair produce a CGO powder (CGOP) that has an average particle size of 0.48μm and a specific surface area of $40.1m^2/g$. Bimodal mixtures of these powders were prepared by ball milling in ethanol with alumina balls for 24 hours in a polyethylene container. The powder mixture was dried in an oven at 50°C for 2 hours and sieved through a 38μm stainless steel mesh. All powders were consolidated uniaxially (~75MPa) and then isostatically (300MPa).

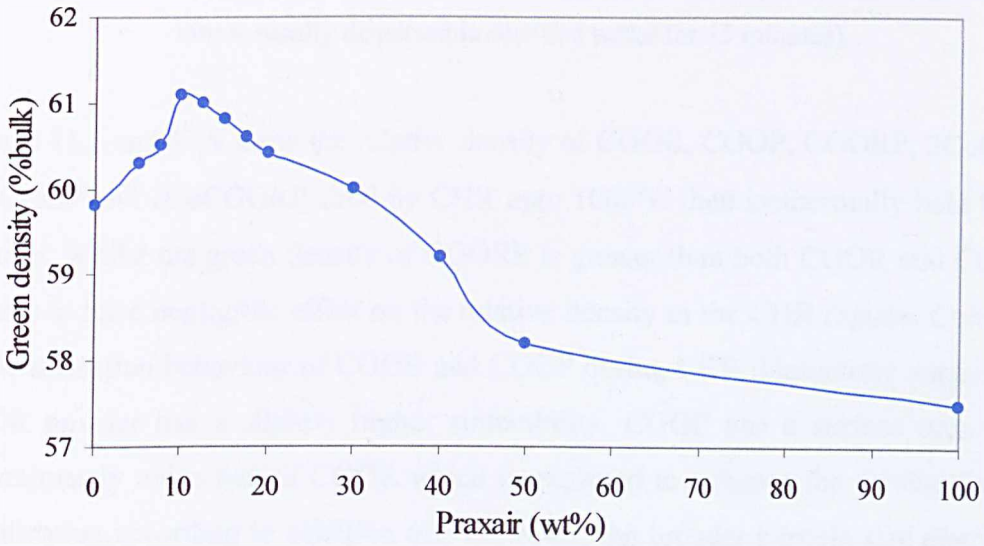


Figure 11.6 Green density (bulk) of bimodal mixture of CGO powder (Praxair added to Rhodia).

Figure 11.6 shows that mixing CGOR with finer CGOP powder (0-10wt%) increases the green density (bulk) slightly from 59.8% up to a maximum of 61.1% for 90wt%CGOR + 10wt%CGOP (CGORP). Computer simulations give a value of 63.7% as the maximum limit of packing density for the dense random packing of monosized spheres [4]. This indicates that the bulk density of the bimodal mixture is approaching maximum packing efficiency. Further additions of CGOP resulted in a decrease in

packing efficiency and green density. CGOP has a lower green density than CGOR. It is well known that the packing density of ceramic powders is enhanced as the standard deviation of the distribution increases (i.e. particle size distribution gets broader). Figures 11.7a and 11.7b show that the particle size distribution of CGOR is broader than CGOP, which might explain the more efficient powder packing of this material. However, sub-micron particles do not behave in the same way as macroscopic spheres. In particular inter-particle forces tend to dominate over gravitational forces and so packing is not easy to interpret.

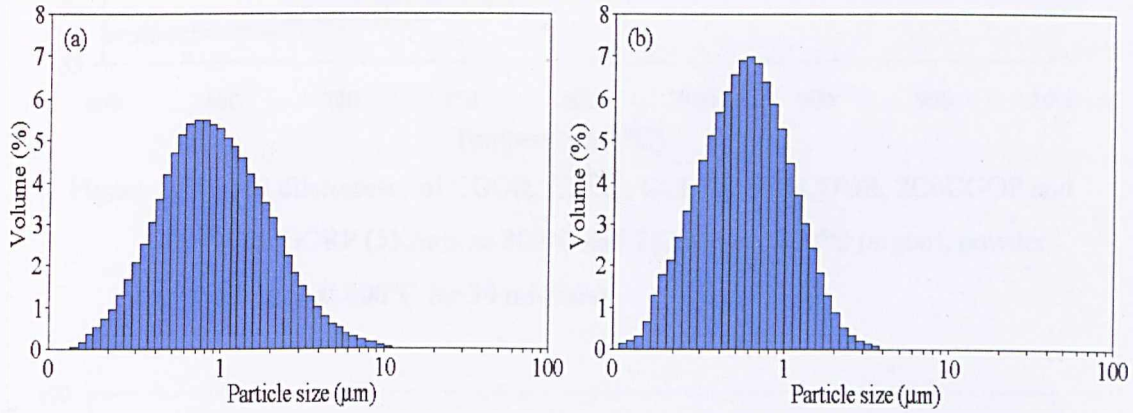


Figure 11.7 The particle size distribution for (a) CGOR and (b) CGOP (both powders ultrasonically dispersed in distilled water for 15 minutes).

Figures 11.8 and 11.9 show the relative density of CGOR, CGOP, CGORP, 2CoCGOR, 2CoCGOP and 2CoCGORP fired by CHR upto 1000°C then isothermally held for 100 minutes. Whilst the green density of CGORP is greater than both CGOR and CGOP, it appears to have negligible effect on the relative density in the CHR regime. Comparing the densification behaviour of CGOR and CGOP during CHR dilatometry suggests that CGOR powder has a slightly higher sinterability. CGOP has a surface area that is approximately twice that of CGOR which is expected to enhance the driving force for densification according to equation 6.2. However, the broader particle size distribution that enhances the green density of CGOR appears to be more influential to the densification of CGO. This result has great practical importance. The current trend amongst many ceramic producers it to produce even finer powders. Invariably this raises production costs, as techniques become more complex and time-consuming. For example, the cost of the CGO powder produced by Praxair and Rhodia used in this study is £700/kg and £450/kg respectively.

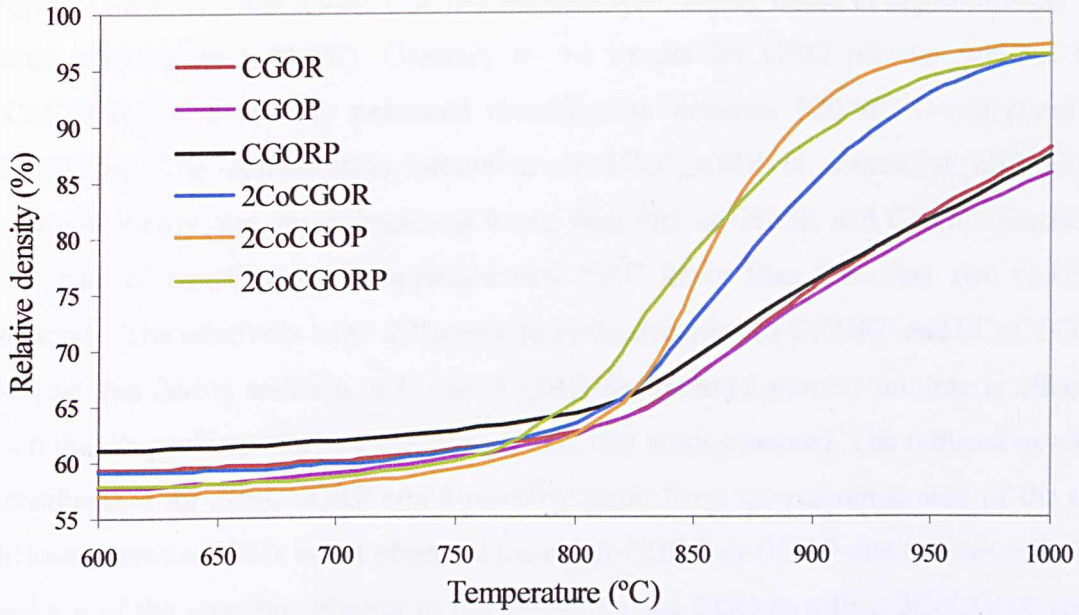


Figure 11.8 CRH dilatometry of CGOR, CGOP, CGORP, 2CoCGOR, 2CoCGOP and 2CoCGORP (5K/min to 800°C and 2K/min to 1000°C (argon), powder calcined at 400°C for 30 minutes).

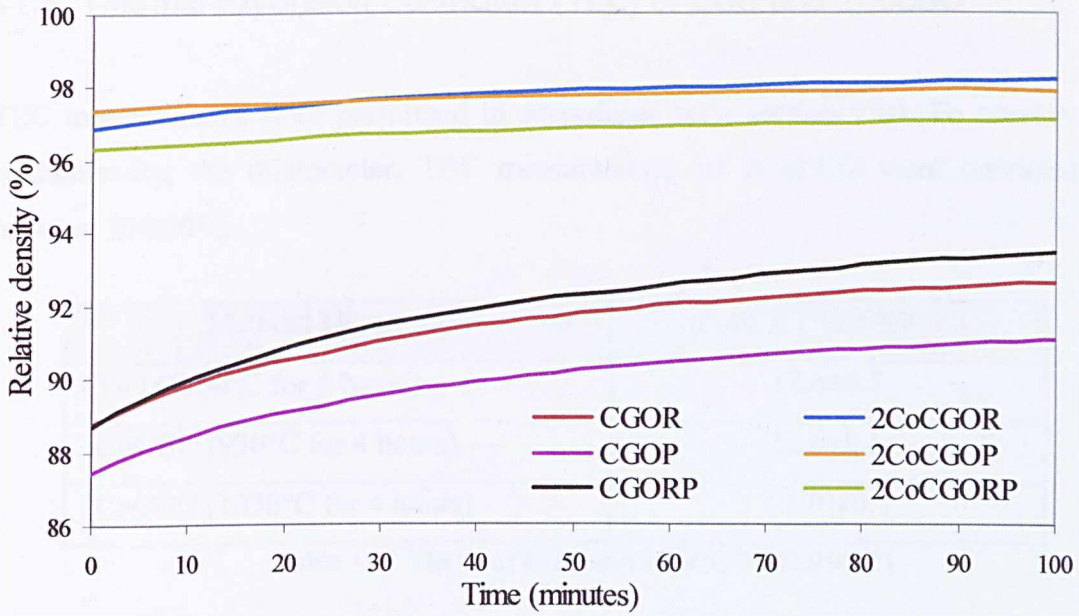


Figure 11.9 Isothermal sintering at 1000°C of CGOR, CGOP, CGORP, 2CoCGOR, 2CoCGOP and 2CoCGORP (argon).

Isothermal sintering of the three different CGO powders indicates that the final density increases with increased green density. For reasons previously discussed in section 11.2, it is speculated that a higher green density enhances the number of pores at the grain and thus increases the relative density during the later stages of densification.

Figure 11.8 shows that all the CoCGO samples were highly dense at approximately the same temperature (~960°C). Contrary to the results for CGO powder without Co, 2CoCGOP has a notably enhanced densification between 820-900°C compared to 2CoCGOR. The densification behaviour of 2CoCGORP is somewhat difficult to interpret. Firstly, the green density is lower than that of CGOR and CGOP. Secondly, the onset of densification is approximately 50°C lower than the other two CoCGO materials. The relatively large difference in green densities of CGORP and 2CoCGORP suggest that during addition of Co to CGORP, the bimodal powder mixture is affected such that its packing efficiency is reduced (i.e. less homogeneous). The reduced onset of densification for 2CoCGORP could possibly result from the rearrangement of the two different powders. This is not observed for either CGOR or CGOP due to more efficient packing of the powders. Similar to the results for the CGO powders, 2CoCGOR has a slightly enhanced relative density during the later stages of isothermal sintering due to its higher green density.

11.5. Thermal Expansion Coefficient (TEC) of CGO and 2CoCGO

TEC measurements were performed in accordance with section 7.10. To prevent Co contaminating the dilatometer, TEC measurements of 2CoCGO were restricted to between 20-950°C.

Material Description	$\alpha x10^{6}K^{-1}$ (20-950°C)
CGO (1350°C for 4 hours)	12.6±0.1
2CoCGO (930°C for 4 hours)	12.6±0.1
2CoCGO (1030°C for 4 hours)	12.70±0.1

Table 11.1 TEC's of CGO and 2CoCGO (20-950°C).

Table 11.1 lists the average TEC of CGO and 2CoCGO sintered at 930°C for 4 hours and 1030°C for 4 hours respectively. Importantly, the use of Co as a sintering aid to CGO does not alter the TEC of CGO. Furthermore, the sintering temperature of 2CoCGO does not significantly alter the TEC. As previously discussed in section 3.4.4, the selection of CGO as an electrolyte for the Imperial College planar design is primarily due to the almost exact TEC match of CGO and ferritic stainless steel. The fact that Co can significantly aid the densification of CGO yet not change the TEC is of extreme importance. Kharton et al. [5] recently reported the TEC of CGO and

CoCGO by high temperature XRD and dilatometry between 27-827°C. The TEC, measured by high temperature XRD, was $13.4\pm0.1\times10^{-6}K^{-1}$, $12.9\pm0.1\times10^{-6}K^{-1}$ and $13.1\pm0.1\times10^{-6}K^{-1}$ for CGO, 2CoCGO and 10CoCGO respectively. No measurement of TEC was performed on CGO by dilatometry but TECs of $11.7\pm0.1\times10^{-6}K^{-1}$ and $12.4\pm0.1\times10^{-6}K^{-1}$ were reported for 2CoCGO and 10CoCGO respectively. It is speculated that the difference in TEC for 2CoCGO in this study and that by Kharton et al. (using dilatometry) was due to the different temperature ranges used to obtain the data.

11.6. Tape Casting Thick Films of 2CoCGO

It is envisaged that the electrolyte will be deposited onto either the anode or cathode in the Imperial College planar ITSOFC by a colloidal processing technique, such as tape casting or screen-printing. The following two sections discuss two brief feasibility studies on densifying thick films of 2CoCGO by each of these methods.

A tape cast slurry was made according to the process shown in figure 11.10 and composition shown in table 11.2. Prior to adding the dispersant and solvent, the 2CoCGO powder was ultrasonically agitated in order to limit agglomeration. Casting was performed by careful squeezing the slurry over two glass slides of equal height (~500μm) placed on top of a plastic sheet, using a razor blade. The thick film was very carefully removed and allowed to dry at 50°C for 24 hours. The tape was fired at 1K/min to 500°C and held at this temperature for 5 hours to remove the binder. The film was isostatically pressed at 300MPa and sintered at 5K/min to 1000°C for 4 hours in argon.

Additive	Mass added (g)
2CoCGO powder	11.972
KD1	0.199
Ethanol	7.188
PVB	1.796
PEG400/PBT	0.4490/0.4490

Table 11.2 Mass of additives used to make 2CoCGO tape cast slurry: polyester resin (KD1), poly (vinyl butyral) (PVB), poly (ethylene glycol) (PEG) and poly (butyl phthalate) (PBT).

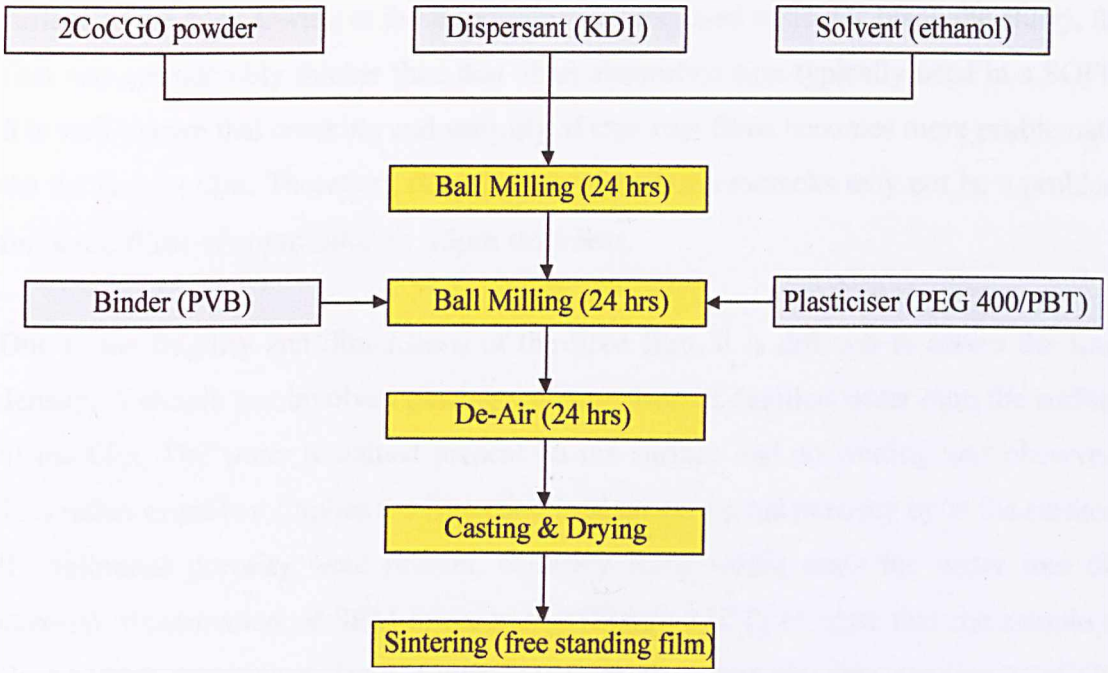


Figure 11.10 Schematic flow diagram for the tape casting of 2CoCGO.

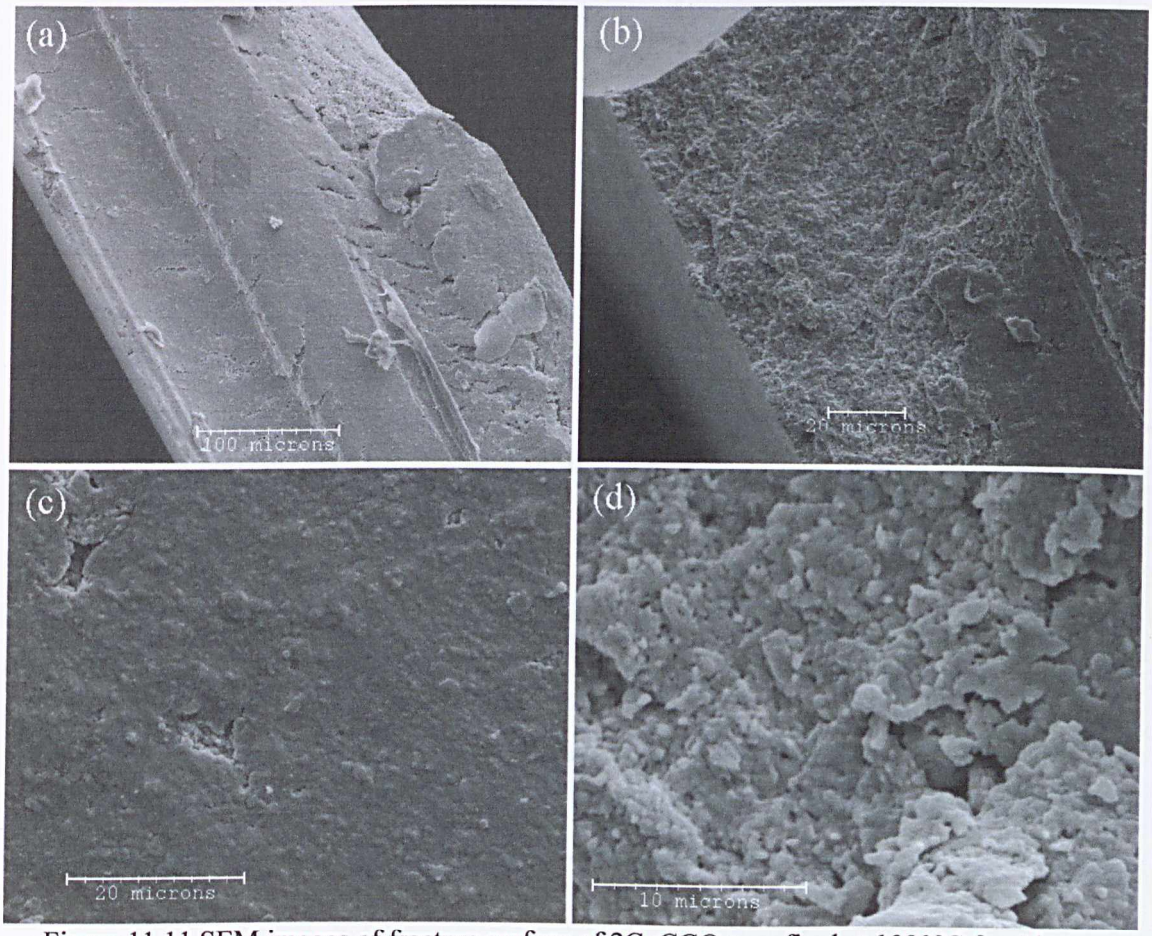


Figure 11.11 SEM images of fracture surface of 2CoCGO tape fired at 1000°C for 4 hours (argon).

After the burnout stage, visual inspection revealed the presence of microcracks on the surface of the film. Owing to the improvised method used to doctor blade the slurry, the film was considerably thicker than that of an electrolyte film typically used in a SOFC. It is well known that cracking and warping of tape cast films becomes more problematic the thicker the film. Therefore, the presence of such microcracks may not be a problem for dense films of approximately 15μm thickness.

Due to the fragility and dimensions of the fired film, it is difficult to assess the final density. A simple test involved placing a pipette drop of distilled water onto the surface of the film. The water remained present on the surface and no wetting was observed. This rather crude test implies the film contained no connected porosity by/at the surface. If continuous porosity were present, capillary force would draw the water into the material. Examination of SEM micrographs (Figure 11.11) indicate that the sample is close to high density and that it is possible to densify a tape cast free standing 2CoCGO film at 1000°C provided that it is isopressed after casting.

11.7. Screen Printing Thick Films of 2CoCGO

A screen print ink containing a 100g of 2CoCGO was prepared using a non-disclosed route by Gwent Print. The formulation of engineering ceramic screen printing inks (and tape cast slurries) is somewhat of a 'black art', it was felt that it would be too time consuming to try and prepare a screen ink as part of this PhD study. As previous results indicated that a high green density of 2CoCGO was required to achieve high density (post firing) at low temperatures, the ink was loaded with a relatively high ceramic content (~60wt%). By maximising the ceramic content, it was thought that this could result in a film with enhanced green density after the binder burn out process.

Using a DEK 1202 screen printer, the 2CoCGO ink was passed through a mask onto porous pellets of LSCF. The LSCF was pre-fired at 900°C and was approximately 80% dense. Experimentally, it was found that 5 passes of the squeegee were necessary to put a layer of 2CoCGO ink over the entire surface of the LSCF substrate. Due to the relatively high viscosity of the ink, there was a tendency for the ink to 'spring back' onto the mask. After the 2CoCGO ink was layered onto the LSCF substrate, the ink was heated at 50°C for 24 hours in an oven. Binder burnout was performed in a similar way to that for the 2CoCGO tape cast film, except that the isothermal burn out stage was

performed at 350°C. This was the recommended temperature by the manufacturers of the ink. After binder burnout, the sample was isostatically pressed (300MPa) and sintered at a CHR of 5K/min upto the designated sintering temperature and isothermally held for 4 hours in argon.

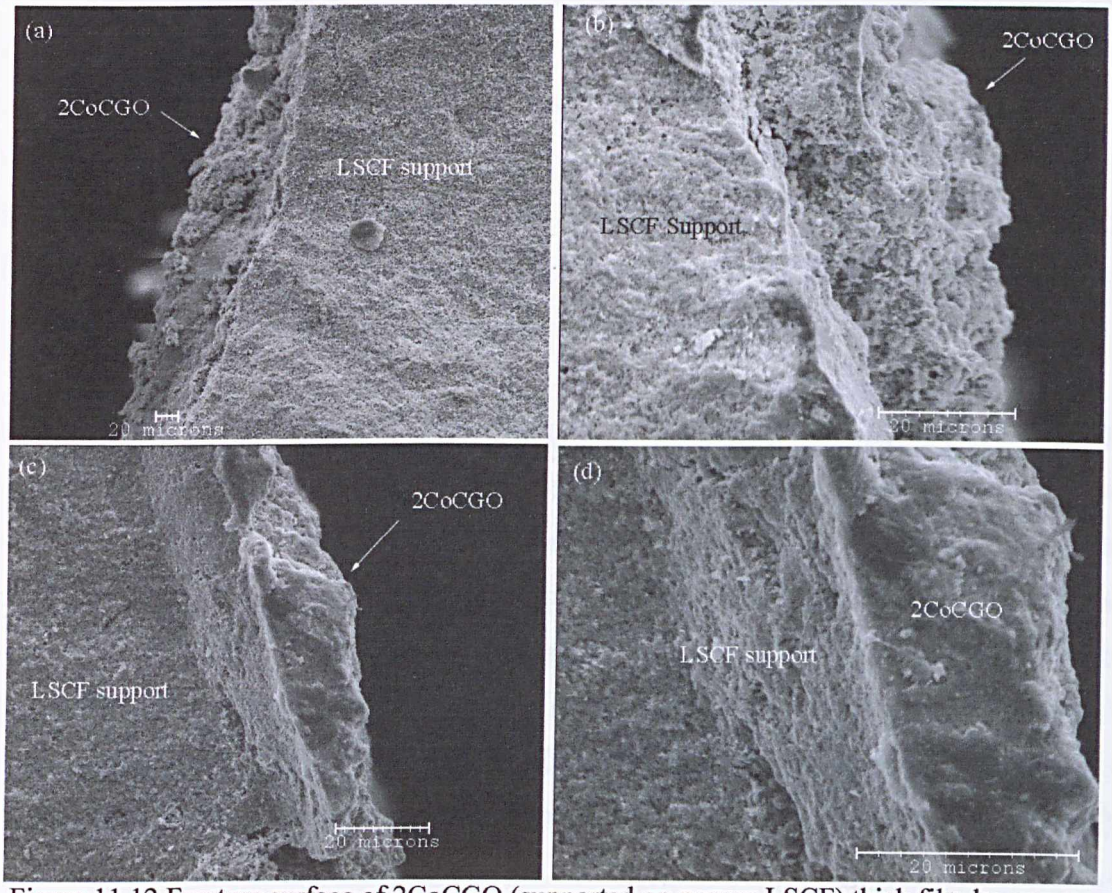


Figure 11.12 Fracture surface of 2CoCGO (supported on porous LSCF) thick film by screen printing (a-b) at 1000°C for 4 hours (Ar) and (c-d) 1100°C for 4 hours (Ar).

After the burnout stage, visual inspection revealed the presence of a significant quantity of microcracks on the surface of the film. Figure 11.12 shows the fracture surface of 2CoCGO films supported on LSCF sintered at 1000°C and 1100°C for 4 hours in argon. The electrolyte layer varied in thickness between 10-40μm. It was noted, however, that after the ink was layered onto the LSCF substrate and dried, the colour of the film was not uniform. Hence a number of passes of the squeegee was necessary to form a continuous layer over the entire substrate. The film sintered at 1000°C showed considerable porosity. Increasing the sintering temperature to 1100°C resulted in a film that was significantly more dense. It was noted, however, that regions of the film fired at higher temperature appeared to be porous whilst other areas appeared to be highly dense.

11.8. Summary

This chapter dealt with processing variables that affected the consolidation and thus densification of 2CoCGO powder. Increasing the calcination temperature from 300°C to 650°C resulted in the formation of some hard agglomerates that slightly reduced the green density of the consolidated body. It was shown that the greater the reduction in the green density of the consolidated powder, the lower the final density after firing at 1000°C for a short period of time. This was due to a reduction in the number of pores at the grain boundary that likewise decreased the driving force for elimination of porosity during the final stages of densification. Experiments revealed, however, that there was very little difference in the final density of powders calcined in the range stated.

It was shown that the green density of the consolidated 2CoCGO powder has to be equal to or greater than 51% if high density is to be achieved <1000°C. This requires isostatic pressing at a minimum of 200MPa. Interestingly, it was found that the higher green density associated with a powder with a wider particle size distribution had a higher final density than a powder with a larger surface area and narrower particle size distribution. The economic implications for mass production mean that it is not essential that the finest and therefore most expensive CGO powder be selected. Attempts to enhance the green density of 2CoCGO by bimodal mixing of two different CGO powders proved ineffective. Finally, of the two colloidal processing techniques used to fabricate thick films of 2CoCGO, the tape casting route proved more effective at fabricating dense films at the required temperature.

References

1. M.A.Occhionera and J.W.Halloran. Mater.Sci.Res. **16**, (1984), 89.
2. J.Zhao and M.P.Harmer. J.Am.Ceram.Soc. **71,** 2, (1988), 113.
3. H.Inaba, T.Nakajma and H.Tagawa. Solid State Ionics. **106**, (1998), 263.
4. Ceramic Processing and Sintering. M.N.Rahaman. Marcel Dekker, 1995.
5. V.V.Kharton, F.M.Figueiredo, L.Navarro, E.N.Naumovich, A.V.Kovalevsky, A.A.Yaremchenko, A.P.Viskup, A.Carneiro, F.M.B.Marques and J.R.Frade. J.Mater.Sci. **36**, (2001), 1105.

Chapter 12 – Co Additions to 8YSZ: Effect on Densification and Electrical Properties

12.1. Introduction

At the present time the most popular electrolyte chosen for use in SOFCs is YSZ. Typically, the temperature required to sinter YSZ to high density is between 1300-1700°C. For reasons already commented upon in section 3.6, it is beneficial to lower the sintering temperature of YSZ. The success of Co as a sintering aid to Gd doped ceria prompted an investigation to the effectiveness of Co as a sintering aid to commercially supplied 8YSZ powder. In this chapter the effect of adding small amounts of Co to 8YSZ and its effects on sintering and electrical conductivity are discussed.

12.2. Commercially Supplied YSZ

The 8YSZ powder studied in this chapter was supplied by Tosoh. ICP analysis of the powder revealed that the presence of Si (and other trace impurities) was below 30ppm. The addition of Co to the 8YSZ powder in this chapter was performed in accordance with section 7.5.

12.3. CHR Dilatometry of Co Additions to 8YSZ

To investigate the effect of Co on the sintering of 8YSZ, CHR dilatometry was performed. As described in chapter 9, the linear shrinkage was converted to relative density by equation 9.1. Figure 12.1 shows the relative density as a function of temperature for Co additions to 8YSZ powders. Due to temperature limitations of the dilatometer and the high sintering temperature required to densify all samples in figure 12.1, the plateau that indicates samples have reached their maximum density is absent.

Hartmanová et al. [1] commented that the addition of Co 'slightly' increased the density of 12YSZ. However it is obvious from the present study that Co significantly enhances the densification of 8YSZ for additions greater than 0.1%. Above this additive amount,

densification is enhanced as a function of Co content with a maximum occurring for the sample 4Co8YSZ.

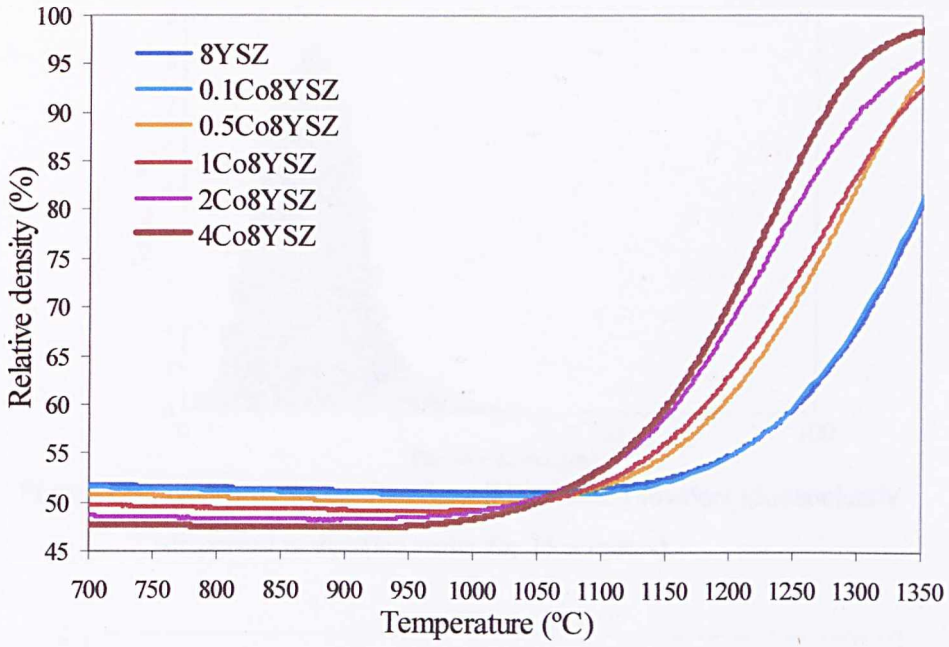


Figure 12.1 Relative density of Co additions to 8YSZ as a function of temperature by CHR dilatometry (10K/min).

Figure 12.1 also shows that the green density decreases as a function of Co content in the YSZ powder. The average particle size of the as-received powder was 0.39μm. The particle size of 0.1Co8YSZ, 0.5Co8YSZ, 1Co8YSZ, 2Co8YSZ and 4Co8YSZ were 0.40μm, 0.40μm, 0.42μm, 0.42μm and 0.44μm respectively. When uniaxially pressing the powder, it was found that samples with a relatively high Co content (i.e. 2Co8YSZ and 4Co8YSZ) consolidated poorly. It was not possible to consolidate 8YSZ with Co additions greater than 4%. Liu et al. [2] commented that the green compact density of 3YSZ is approximately linearly related to powder agglomeration under identical consolidation technique, and decreases with increasing degree of agglomeration. It is speculated that as Co content increases so to does the level of agglomeration, which reduces packing efficiency of the powder.

It is interesting to note that the green density of 8YSZ is significantly lower than that of the CGO. For powders isostatically compacted at 300MPa the green densities of 8YSZ and CGO are 53% and 60% respectively. The lower value for 8YSZ is probably due to the narrower particle size distribution associated with this material (Figure 12.2). In the last chapter it was found that the final density of 2CoCGO was higher for samples that had a higher green density. These results indicate that Co8YSZ could potentially

achieve higher final densities if initial green density can be increased (e.g. if the particle size distribution of the 8YSZ powder was made broader).

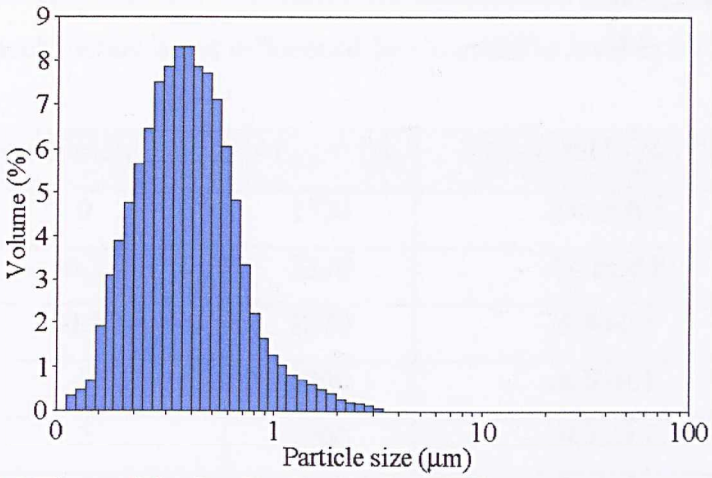


Figure 12.2 The particle size distribution for 8YSZ (powders ultrasonically dispersed in distilled water for 15 minutes).

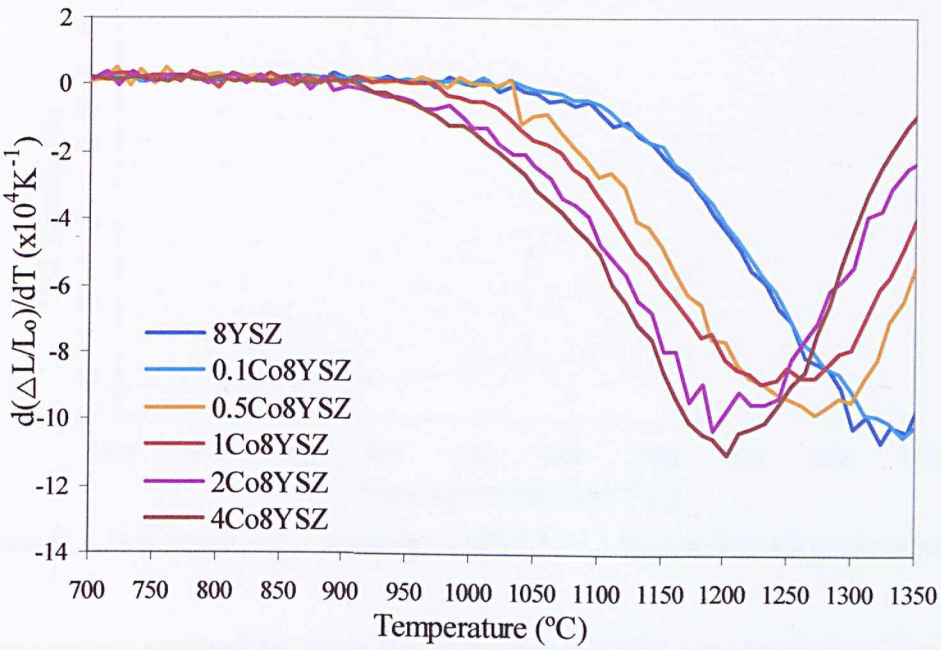


Figure 12.3 Linear differential shrinkage of Co8YSZ as a function of temperature.

Figure 12.3 shows the differential densification as a function of temperature and table 12.1 shows T_{max} values and corresponding magnitude of differential densification. The densification behaviour of 0.1Co8YSZ is almost identical to 8YSZ without additive, the values T_{max} for these materials are 1320°C and 1340°C respectively. It is speculated that the slight increase in T_{max} for 0.1Co8YSZ is due the lower value of green density. The results indicate that T_{max} decreases with increasing Co content up to 2%Co addition (1200°C), further additions do not reduce this value. Interesting, the magnitude of densification rate at T_{max} remains relatively constant as a function of Co addition.

Furthermore, for Co additions that enhance the sinterability of 8YSZ, the reduction in densification rate after T_{max} is approximately the same. This behaviour is different to Co additions to CGO and CGO20. Therefore, the transition of densifying mechanisms to nondensifying mechanisms is not influenced by Co additive level in 8YSZ (<4%Co).

Co addition (%)	~T_{max} (°C)	$d(\Delta L/L_o)/dT$ ($x10^{-4}K^{-1}$)
0	1320	-10.6±0.1
0.1	1340	-10.6±0.1
0.5	1270	-9.8±0.1
1	1220	-8.9±0.1
2	1200	-9.7±0.1
4	1200	-11.0±0.1

Table 12.1 T_{max} and magnitude for Co additions to 8YSZ powders.

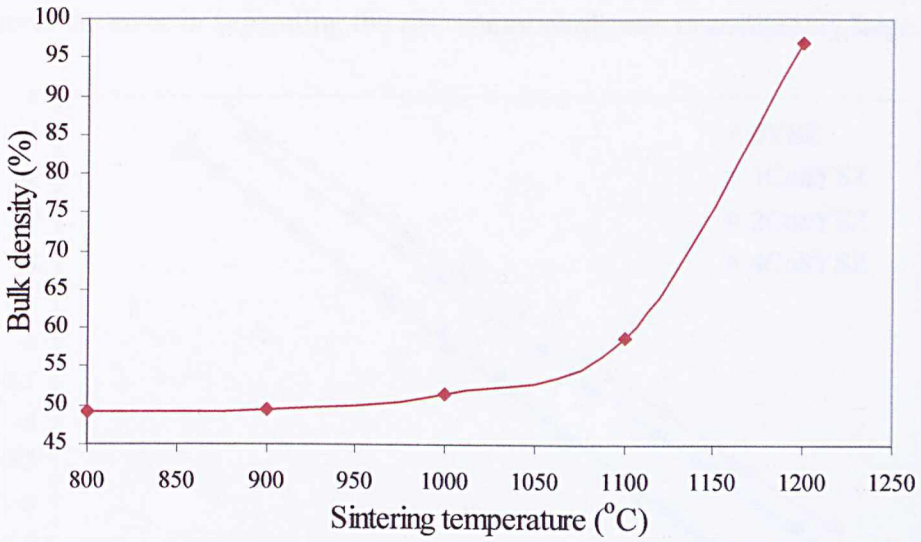


Figure 12.4 Bulk density after sintering 1Co8YSZ for 1 hour at the indicated temperature.

The temperature required to sinter the commercial 8YSZ powder to high density was 1440°C (2 hours). Figure 12.4 shows the final density of 1Co8YSZ samples after being heated at 10K/min and then held isothermally at the designated temperature for 1 hour. The results are in agreement with table 12.1, in that only the sample sintered at 1200°C reached high density as a result of its relatively large densification rate at this temperature.

To the best of the author's knowledge, no phase diagram exists for $CoO(Co_2O_3)$-Y_2O_3-ZrO_2. Seidensticker and Mayo [3] used DTA to verify that Cu additions enhanced the densification of 3YSZ by forming a liquid phase at 1144°C. In order to understand the

mechanisms that were responsible for the enhanced densification of 8YSZ with Co additions, similar studies were performed. However, similar to studies for CoCGO, this technique proved ineffective at determining whether a liquid phase was responsible for enhancements in the densification. As both CGO and 8YSZ have fluorite structures, it is speculated that the mechanism that enhances the densification by addition of small amounts of Co is probably similar.

12.4. A.C Impedance Spectroscopy of Co Additions to 8YSZ

A.C impedance measurements were performed in air on samples with Co additive sintered at 1330°C for 2 hours. The YSZ sample without additive was sintered at 1440°C for 2 hours. Measurements of the separate lattice and grain boundary contributions to conductivity were restricted to below approximately 550°C. Above this temperature, the error in separating the two components was unacceptably large.

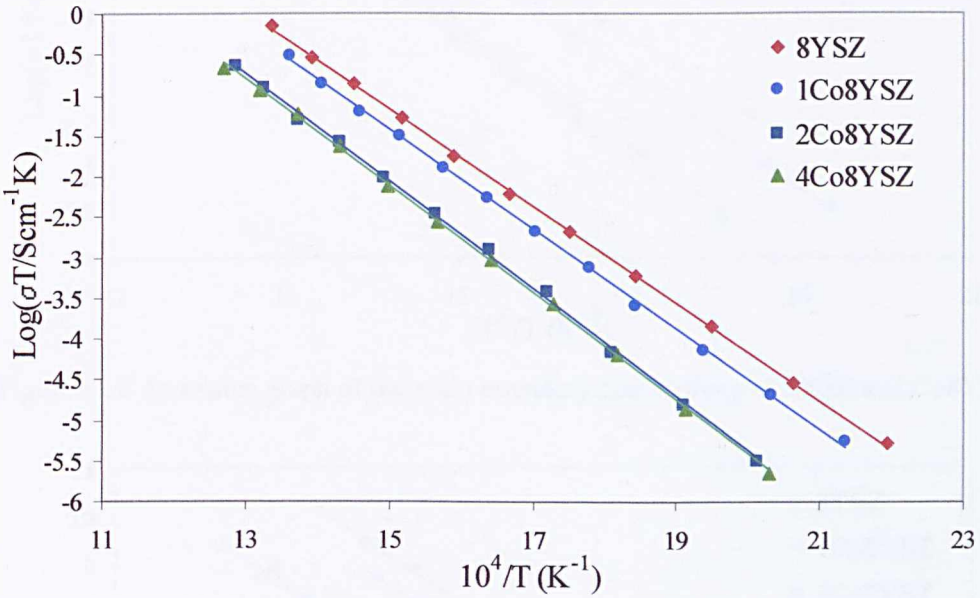


Figure 12.5 Arrhenius graph of the lattice conductivity of 8YSZ and Co8YSZ.

Hartmanová et al. [1] found that Co additions (0.1-0.5mass%) enhanced the lattice conductivity of 12YSZ. A 0.1mass%Co addition was reported to enhance the lattice conductivity by a factor of 1.65 at 275°C. This was attributed to an increase in oxygen vacancies due to the substitution of Zr^{4+} by Co^{3+} (Equation 6.8). The author finds it difficult to accept that such a large increase in ionic conductivity could occur in a material that already contains a significant concentration of oxygen vacancies. Furthermore, it has been reported that the optimal dopant level of Y_2O_3 in zirconia is

~8mol% [4]. It is expected that the creation of extra oxygen vacancies by the addition of Co to 12YSZ would thus result in increased defect association and be detrimental to the lattice ionic conductivity.

Results presented in this thesis show that the addition of Co is detrimental to the lattice ionic conductivity of 8YSZ (Figure 12.5). The activation energy for the lattice ionic conduction of 8YSZ measured in this work is 1.18eV; this value agrees well with the literature [5, 6]. The calculated activation energies for 1Co8YSZ, 2Co8YSZ and 4Co8YSZ are 1.21eV, 1.30eV and 1.31eV respectively. This trend is in agreement with impedance spectroscopy data reported for Cu additions to 2.5YSZ [7].

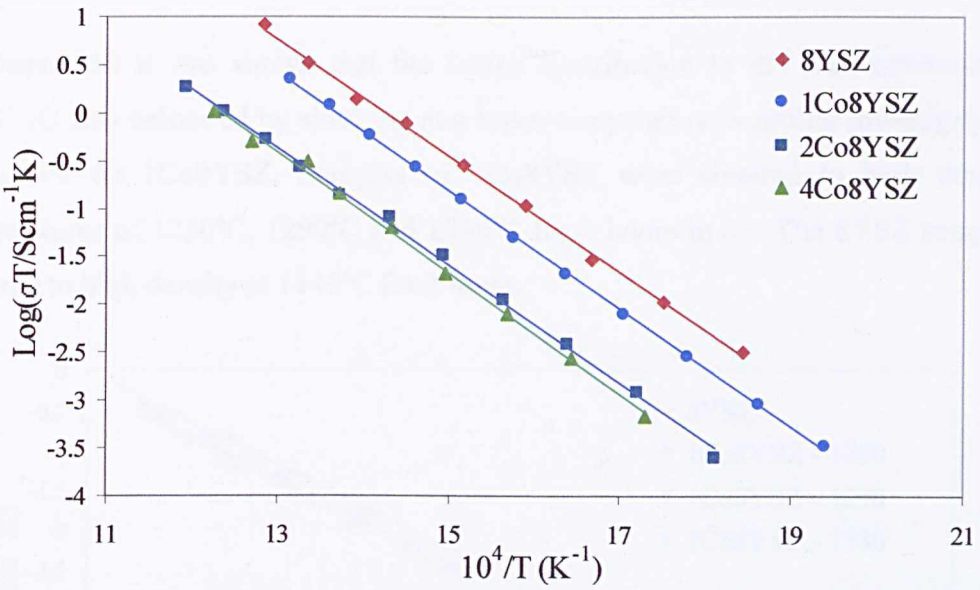


Figure 12.6 Arrhenius graph of the grain boundary conductivity of 8YSZ and Co8YSZ.

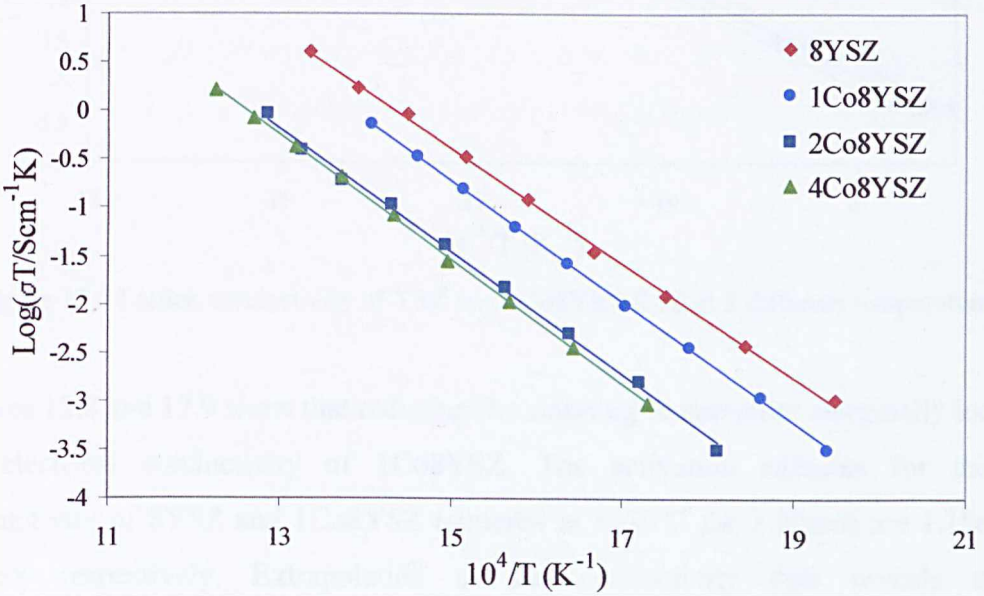


Figure 12.7 Arrhenius graph of the total conductivity of 8YSZ and Co8YSZ.

The results in figure 12.6 for changes in grain boundary conductivity are similar to the trend in lattice conductivity for Co8YSZ. The addition of Co is detrimental to the grain boundary conductivity of 8YSZ. The calculated activation energies for the grain boundary ionic conductivity of 8YSZ, 1Co8YSZ, 2CoYSZ and 4Co8YSZ are 1.21eV, 1.23eV, 1.23eV and 1.25eV respectively. These results are similar to the activation energies for grain boundary conductivity reported for Cu additions to 2.5YSZ [7]. From figure 12.7 the optimum level of Co additive that increases the sinterability of the powder, but does not significantly impair on the electrical properties, is 1%.

12.5. Effect of Sintering Temperature on the Conductivity of Co8YSZ

In chapter 10 it was shown that the lattice contribution to the total conductivity of 2CoCGO was enhanced by sintering at a lower temperature, a similar investigation was performed on 1Co8YSZ. Samples of 1Co8YSZ were sintered to high density at temperatures of 1250°C, 1290°C and 1330°C for 2 hours in air. The 8YSZ sample was sintered to high density at 1440°C for 2 hours.

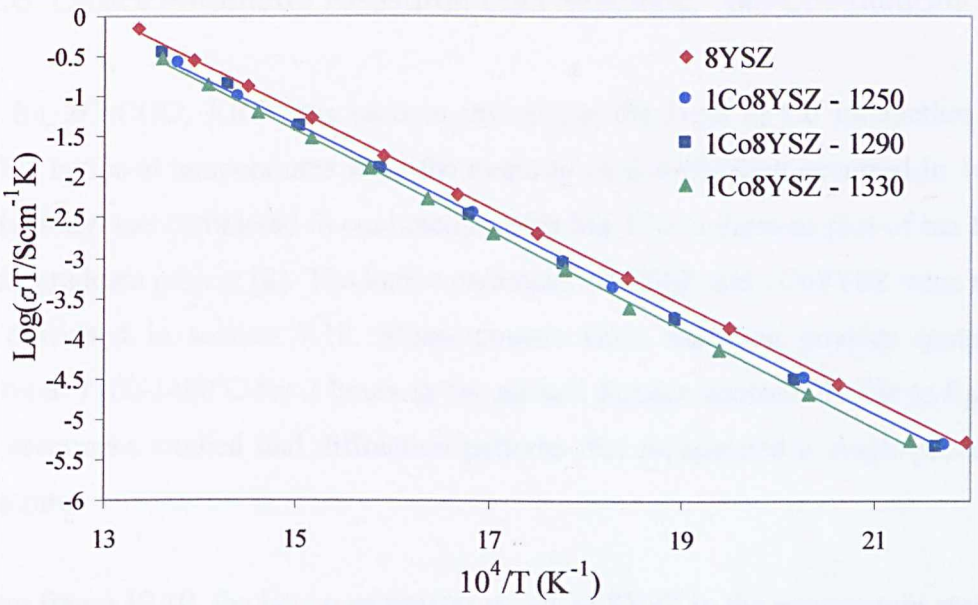


Figure 12.8 Lattice conductivity of YSZ and 1Co8YSZ fired at 3 different temperatures (°C).

Figures 12.8 and 12.9 show that reducing the sintering temperature marginally increases the electrical conductivity of 1Co8YSZ. The activation energies for the total conductivity of 8YSZ and 1Co8YSZ (sintered at 1330°C for 2 hours) are 1.18eV and 1.23eV respectively. Extrapolation of the conductivity data reveals that at approximately 700-750°C the total conductivity of the sample with additive would be

the same as YSZ sintered at a higher temperature without additive. This has important implications for fuel cell development as 700°C is considered to be the minimum operating temperature for SOFCs incorporating a YSZ electrolyte.

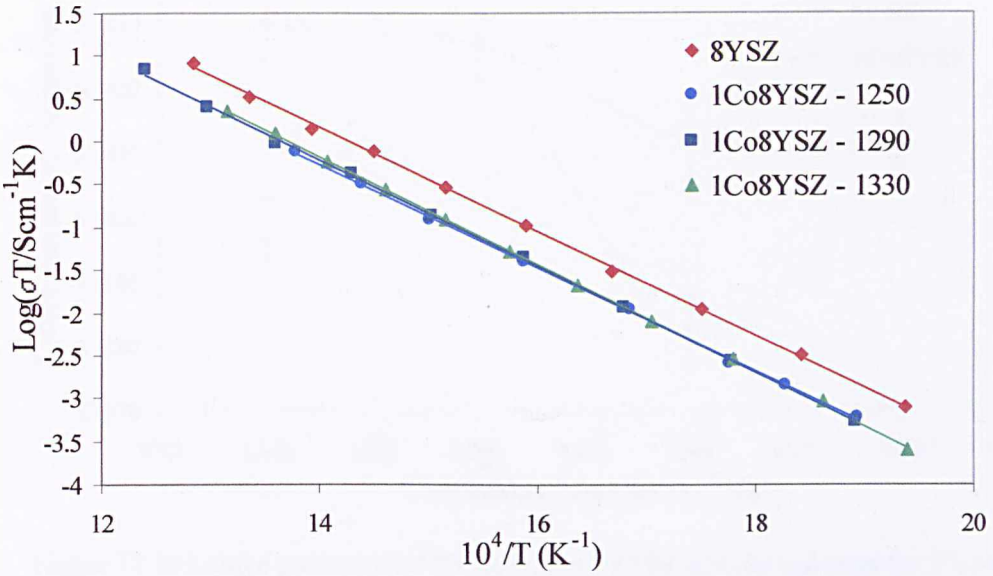


Figure 12.9 Grain Boundary conductivity of YSZ and 1Co8YSZ fired at 3 different temps (°C).

12.6. Lattice Parameter Measurements Resulting from Co Additions to 8YSZ

As for 2CoCGO, XRD was used to investigate the level of Co interaction with the 8YSZ lattice at temperatures were the majority of densification occurred in 1Co8YSZ. This study was completed in conjunction with Ms. Claire Press as part of her final year undergraduate project [8]. The lattice parameter of 8YSZ and 1Co8YSZ were measured as described in section 7.18. Measurements were made on powder samples fired between 1100-1400°C for 2 hours in dry air and furnace cooled. Similar to figure 9.19, all specimens studied had diffraction patterns that represented a single-phase fluorite structure.

From figure 12.10, the lattice parameter trends of 8YSZ in the temperature range where Co additions significantly aid densification are very different to those previously discussed for CGO (Figure 9.22). Between 1100-1200°C the lattice parameter of 8YSZ remains constant at approximately 5.1430Å, this value is in good agreement with published literature [9, 10]. For temperatures greater than 1200°C, the lattice parameter of 8YSZ decreases (~5.1410Å). This could indicate that the oxygen vacancy concentration decreases, thus suggesting that yttria is lost to the surroundings [11].

Therefore in the temperature range studied these results suggest that there is negligible diffusion of yttria from the particle surfaces into the bulk.

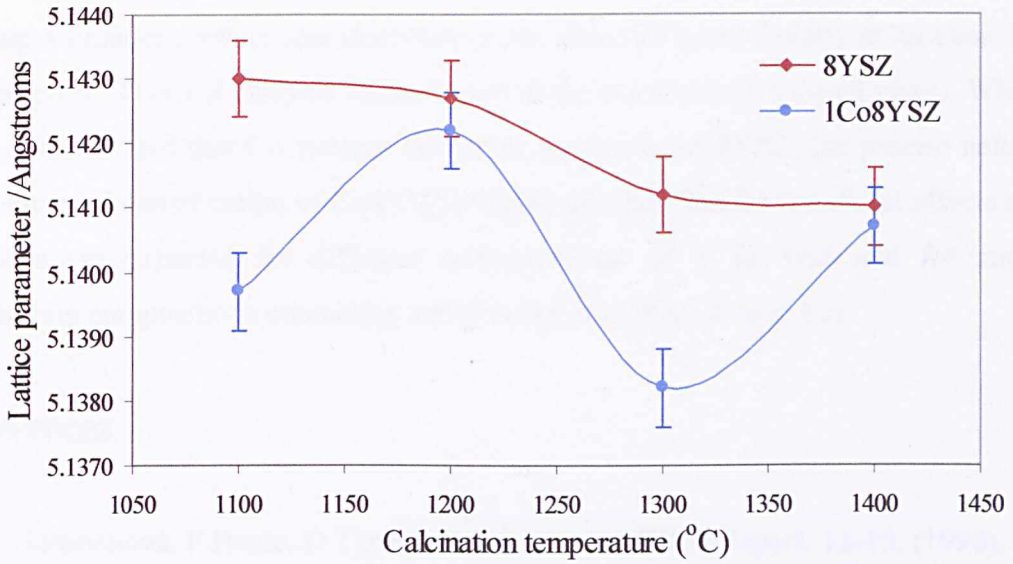


Figure 12.10 Lattice parameter of 8YSZ and 1Co8YSZ powder calcined for 2 hours in dry air at the indicated temperature and furnace cooled [8].

The lattice parameter of 1CoYSZ is lower than that of YSZ for temperatures in the range 1100-1400°C, agreeing with the trend previously reported by Hartmonovà for Co additions to 12YSZ [1]. It was claimed that the reduction in lattice parameter of 12YSZ for small additions of Co was due to the formation of a substitutional solid solution, the larger Zr^{4+} cation in the fluorite type structure of YSZ being replaced with the Co cation with the smaller effective radius. It is generally accepted that the ionic conductivity of YSZ as a function of yttria content is assumed to attain its maximum value around 8mol%Y_2O_3. The creation of more oxygen vacancies beyond the 8mol% level will, therefore, be expected to lead to a decrease in the oxygen ion conductivity (Equation 6.8). This is due to increased association of the vacancies with dopant ions at higher concentrations [12]. This is consistent with the A.C. impedance measurements of Co8YSZ (Figure 12.5) that show that Co additions lower the lattice conductivity of 8YSZ.

12.7. Summary

It has been demonstrated that Co is an effective sintering aid for 8YSZ. For the particular 8YSZ powder used the optimum level of additive was approximately 1% Co.

This level of additive reduced the sintering temperature by approximately 250°C and maintained a conductivity approximately equal to that of YSZ sintered at the higher temperature without additive. It is speculated that if the green density was increased by having a broader particle size distribution, the material could densify at an even lower temperature. Thermal analysis failed to reveal the existence of a liquid phase. Whilst it was demonstrated that Co reduces the lattice parameter of 8YSZ, the precise nature of the enhanced densification of Co8YSZ remains unclear. Similar beneficial effects of Co additive are expected for different concentrations of Y in YSZ and for zirconia electrolyte compositions containing substituents other than Y (e.g. Sc).

References

1. M.Hartmanová, F.Hanic, D.Tunega and K.Putyera. Chem.Papers. **12-15**, (1998), 12.
2. D-M.Liu, J-T.Lin and W.H.Tuan. Ceramics International. **25**, (1999), 551.
3. J.R.Seidensticker and M.J.Mayo. J.Am.Ceram.Soc. **79**, 2, (1996), 401.
4. M.Filal, C.Petot, M.Mokchah, C.Chateau and J.L.Carpentier. Solid State Ionics. **80**, (1995), 27.
5. S-J.Kim, K-H.Kim, S-J.Oh, T-K.Kang and I-H.Kuk. Solid State Ionics. **72**, (1994), 279.
6. X.Guo and J.Maier. J.Electrochem.Soc. **148**, 3, (2001), E121.
7. C.Bowen, S.Ramesh, C.Gill and S.Lawson. J.Mater.Sci. **33**, (1998), 5103.
8. C. Press. Masters Thesis. University of London, 2001.
9. M.O.Zacate, L.Minervini, D.J.Bradfield, R.W.Grimes and K.E.Sickafus. Solid State Ionics. **128**, (2000), 243.
10. R.P.Ingel and D.Lewis. J.Am.Ceram.Soc. **69**, 4, (1986), 325.
11. R.W.Grimes. Private Communications.
12. M.Hartmanová, F.W.Poulsen, F.Hanic, K.Putyera, D.Tunega, A.A.Urusovskaya and T.V.Oreshnikova. J.Mater.Sci. **29**, (1994), 2152.

Section 4

Conclusions

And

Future Work

Conclusions

Over the past 20 years many highly ionically conducting novel materials have been investigated for application as SOFC electrolytes. The review of the literature concentrated mainly on the development of doped ceria electrolytes. Arguably, gadolinia doped ceria (CGO) has the highest ionic conductivity between 500-600°C and has given rise to the concept of the intermediate temperature solid oxide fuel cell (ITSOFC) working in this temperature range. This system is considered a highly efficient and economical energy device intended for small-scale electrical power or combined heat and power applications. Commercially available CGO powders have to be sintered at approximately 1300°C to achieve high density. Reducing the densification temperature to between 900-1000°C enables the fuel cell to be fabricated on a stainless steel substrate. The benefits are improved mechanical reliability of the cell and significant cost reductions in both materials and processing. This thesis concentrated on reducing the densification temperature of CGO.

A procedure that involves the addition of Co or Cu nitrate precursors to commercially produced CGO was devised that has enabled CGO to be sintered to high density at <1000°C. Using dilatometry it was shown that the enhancement in densification increased with Co and Cu addition up to 2% and 4% respectively. Arguably, Co is the more promising sintering aid as 'over sintering' of CuCGO resulted in a significant decrease in the relative density. Heat treatment of the doped powder prior to consolidation resulted in the formation of some hard agglomerates that slightly reduced the green density of the consolidated body compared to CGO without the sintering aid. Isostatically pressing (>200MPa) the consolidated body was required before firing to enable high density to be achieved at <1000°C.

The mechanism of initial stage densification of CGO without additive is controlled by grain boundary diffusion. The commercially received CGO powder has a surface region greatly enriched in Gd and the lattice Gd concentration is much less than the nominal one. At temperatures greater than 650°C, the Gd in the surface region diffuses into the bulk, thus creating more oxygen vacancies and cation interstitials. This enhances the diffusion of cations thus aiding densification when compared to undoped ceria. The

densification of CoCGO was considerably more difficult to interpret due to the high mobility of Co in CGO at temperatures were the majority of densification occurs. It is speculated that Co located on the CGO particle surface after preparation diffuses into CGO and increases the rate at which Gd diffuses into the lattice at temperatures of ~750-800°C. Lattice parameter measurements and TEM observations indicated that at >850°C, Co is soluble within the CGO matrix but when furnace cooled the Co re-segregates to the grain boundaries and surfaces. CHR dilatometry and grain growth studies suggest that the initial stage densification of CoCGO is controlled by volume diffusion. TEM studies showed that the grain size of CoCGO sintered <1000°C was considerably smaller than that typically reported for high density CGO sintered at 1300°C. Grain growth experiments indicated that this was mainly due to the reduced temperature and not to a reduction in grain boundary mobility by the segregated Co.

Importantly, it has been found that Co and Cu additions to CGO studied in this thesis have negligible effect on the total ionic conductivity of pure CGO at low temperatures nor do they generate significant electronic conductivity under typical SOFC operating conditions. Of the two sintering aids, 2%Co was considered the optimum addition. The grain boundary conductivity of 2CoCGO sintered to high density <1000°C was slightly increased below 300°C but was reduced between 300-400°C compared to CGO without additive. The lattice conductivity of 2CoCGO sintered to high density <1000°C was greater than CGO without additive for all temperatures studied using A.C. impedance spectroscopy. Lattice parameter and XPS studies at room temperature suggest that trace levels of Co in the CGO structure minimise the lattice parameter change from that of pure ceria, thus reducing defect association and enhancing the lattice ionic conductivity. As the distribution of Co depends on sintering temperature and time, these parameters influence the lattice conductivity of 2CoCGO. Attempts to sinter (at 1000°C) a 2CoCGO film screen printed onto a substrate proved to be unsuccessful because of its low green density.

It has also been shown that Co can likewise reduce the densification temperature of 8YSZ by approximately 250°C; from 1450°C to 1200°C. The optimum level of additive in terms of reducing the sintering temperature and maintaining an acceptably high level of electrical conductivity was 1%Co. Similar beneficial effects of Co additive are expected for different concentrations of Gd in CGO and Y in YSZ and for ceria and

zirconia electrolyte compositions containing substituents other than Gd and Y (e.g. Sm and Sc respectively).

Suggestions for Future Work

This study presents many avenues for further research into the low temperature sintering of doped ceria electrolytes. There are, however, four particular areas where further experiments could prove particularly beneficial. The first of these areas is to perform an open circuit cell voltage test of a SOFC incorporating a 2CoCGO electrolyte. This would enable the electrical performance of 2CoCGO to be characterised under 'real' ITSOFC operating conditions.

Unsuccessful attempts were made at densifying a constrained 2CoCGO film prepared by screen-printing and tape casting in this study. Experiments need to be performed that devise a procedure that could commercially be scaled up to economically fabricate films of 2CoCGO at ~1000°C.

This study highlighted the mobile nature of the Co cation during firing. Furthermore the microstructure, and thus electrical conductivity, of 2CoCGO is sensitive to the level and location of Co. Ageing studies need to be performed that ascertain how Co behaves in the CGO matrix over an extended period of time at ITSOFC operating temperatures.

Tracer diffusion studies of both Co and O in CGO and CoCGO would be useful to help interpret the densification mechanism and the effect of Co on lattice diffusion of oxygen.

Perform a series of isothermal sintering studies of CoCGO and CuCGO at different pO_2 levels. This could help in the understanding of the enhanced sintering of CoCGO and CuCGO.